CMS Draft Analysis Note

The content of this note is intended for CMS internal use and distribution only

2023/07/17
Archive Hash:
Archive Date:

Central exclusive production of charged hadron pairs in proton-proton collisions at $\sqrt{s} = 13$ TeV

Part I: Study of the nonresonant continuum

Ferenc Siklér
Wigner Research Centre for Physics, Budapest, Hungary

Abstract

The central exclusive production of charged hadron pairs in pp collisions at a centre-of-mass energy of 13 TeV is examined. Events are selected by requiring both scattered protons detected in the TOTEM roman pots, exactly two oppositely charged identified particles in the CMS silicon tracker, and the energy-momentum balance of these four particles. In this part of the exploration, the nonresonant continuum processes are studied with the invariant mass of the centrally produced two-hadron system in the resonance-free region, $m < 0.7\,\text{GeV}$ or $m > 1.8\,\text{GeV}$. Differential cross sections as functions of the azimuth angle between the surviving protons and several squared four-momenta are measured in a wide region of scattered proton transverse momenta $0.2\,\text{GeV} < p_{1/2,T} < 0.8\,\text{GeV}$ and for hadron rapidities $|y| < 2$ for pions, and < 1.6 for kaons. A rich structure of interactions related to double pomeron exchange emerges. The dynamics of nonresonant continuum is determined and compared to models. With help of model tuning, various physical quantities related to the pomeron cross section, proton-pomeron and hadron-pomeron form factors, trajectory slopes and intercepts, as well as coefficients of diffractive eigenstates of the proton are determined.

PDFAuthor: “376“377“000F“000e“000r“000e“000n“000c“000“040“000S“000i“000k“000l“000e“000r
PDFTitle: “376“377“000C“000e“000n“000t“000r“000a“000l“000“040“000e“000x“000c“000l“000u“00
“000p“000r“000o“000t“000o“000n“000“040“000c“000o“000l“000l“000i“000s“000i“000o“0
PDFSubject: “376“377“000C“000M“000S
PDFKeywords: “376“377“000C“000M“000S“000,“000“040“000p“000h“000y“000s“000i“000c“000s“000,“0

Contents

1 Introduction

The cross sections of pp and $p\overline{p}$ interactions steadily rise with centre-of-mass energy and approach each other at high energies [1]. This observation was early on explained with the exchange of state [2] with vacuum quantum numbers, a Regge trajectory, the pomeron. Such an object is now seen as a sum of ladder-type diagrams (multi-peripheral model [3]) composed of spin-one gluons. Pomeron physics, its nonperturbative characteristics and its relations to theory of the strong interaction (QCD), is a topic of ongoing research with broad experimental and theoretical literature [4].

In collisions of protons, the exclusive central production of a few particles offers a clean laboratory for the study of various specific phenomena [5]. At high energies, the exchange of reggeons is suppressed and, for not too small momentum transfers, these processes are dominated by double pomeron exchange. Among others, they might provide a gluon-rich environment potentially important for the creation of hadrons that are free of valence quarks, the glueballs [6].

Double pomeron exchange processes in pp collisions were intensively studied at CERN in the 1990s [7, 8] at $\sqrt{s} = 12.7$, 23.8 and 29 GeV, with the most convincing results published by the WA102 Collaboration [9–12]. That research programme concluded that pomeron exchange had a vector-like behaviour. With the advent of record energy collider data, there is a renewed interest in the study of central exclusive production, especially in double pomeron exchange processes. Measurements in $p\overline{p}$ collisions at $\sqrt{s} = 0.9$ and 1.96 TeV were provided by the CDF Collaboration [13] at the Tevatron, with a recent publication by the STAR Collaboration [14] at $\sqrt{s} = 0.2$ TeV at RHIC.

The CMS Collaboration has recently published a study on the central exclusive $\pi^+\pi^-$ production at $\sqrt{s} = 5.02$ and 13 TeV [15], with a rather limited statistics and using only the kinematics of the centrally produced pion pair in the analysis. The present study at $\sqrt{s} = 13$ TeV is based on a high statistics sample where both the forward scattered protons and the centrally produced charged hadron pair are detected and identified with high efficiency, and measured with great precision.

Details of the theoretical background can be found in CMS AN-22-092. It deals with the single- and double-pomeron exchange, and a model tuning effort using measured data on central exclusive production of charged hadron pairs in pp collisions.

1.1 The CMS and TOTEM detectors

The central feature of the CMS apparatus is a superconducting solenoid of 6 m internal diameter, providing a magnetic field of 3.8 T. Within the solenoid volume are a silicon pixel and strip tracker, a lead tungstate crystal electromagnetic calorimeter, and a brass and scintillator hadron calorimeter, each composed of a barrel and two endcap sections. Forward calorimeters extend the pseudorapidity coverage provided by the barrel and endcap detectors. Muons are detected in gas-ionisation chambers embedded in the steel flux-return yoke outside the solenoid. Forward calorimeters, made of steel and quartz-fibres, extend the pseudorapidity coverage provided by the barrel and endcap detectors.

The silicon tracker measures charged particles within the pseudorapidity range $|\eta| < 2.5$. During the LHC running period when these data were recorded, the silicon tracker consisted of 1856 silicon pixel and 15 148 silicon strip detector modules. For nonisolated particles of $1 < p_T < 10$ GeV the track resolutions are typically 1.5% in p_T and 20–75 μm in the transverse impact parameter [16]. A more detailed description of the CMS detector, together with a definition of the coordinate system used and the relevant kinematic variables, can be found in Ref. [17].

The proton spectrometer of the TOTEM experiment consists of two sets of telescopes, known as roman pot (RP) stations that are located close to the beamline. The arms are referred to as "arm 1" (in sector 45) and "arm 2" (in sector 56) for positive and negative η, respectively. An RP that contains silicon strip detectors can approach the LHC beam to a distance of a few millimetres without affecting the LHC operation. The RPs are used to detect protons deflected at scattering angles of only a few microradians relative to the beam. Before being detected, the trajectories of protons that have lost a small amount of their original momentum slightly deviate from the beam trajectory, with the deviation dependent on the momentum of the proton. The intact proton kinematics are reconstructed after modelling the transport of the protons from the interaction point to the RP location. The TOTEM detector is described in Refs. [18, 19].

1.2 Kinematics

The CMS experiment uses a right-handed coordinate system, with the origin at the nominal interaction point (IP), the z axis along the counterclockwise-beam direction, the x axis pointing toward the centre of the accelerator ring, and the y axis pointing vertically "upward". The initial momentum of protons hitting RP-left is $p_{1,z} = +6.5\,\mathrm{TeV}$ in the z direction, while those hitting RP-right have $p_{2,z} = -6.5\,\mathrm{TeV}$.

The energy of a scattered proton is well approximated by its longitudinal momentum, because $p_z \gg p_\mathrm{T}$ and m_p, hence

$$E = \sqrt{p_z^2 + p_\mathrm{T}^2 + m_p^2} \approx p_z + \frac{p_\mathrm{T}^2 + m_p^2}{2p_z} \approx p_z. \tag{1}$$

The $p_{1/2,x}$ and $p_{1/2,y}$ components of the scattered proton momenta are measured using the roman pots, with the assumption that the longitudinal momenta ($p_{1/2,z}$) are unchanged. In reality, both scattered protons lose momentum

$$p_{1,z} \to p_{1,z} + \Delta p_{1,z}, \qquad p_{2,z} \to p_{2,z} + \Delta p_{2,z}, \tag{2}$$

and energy

$$p_{1,z} \to p_{1,z} + \Delta p_{1,z}, \qquad -p_{2,z} \to -p_{2,z} - \Delta p_{2,z}. \tag{3}$$

The momentum change of the surviving protons is such that $\Delta p_{1,z} < 0$ and $\Delta p_{2,z} > 0$.

The z-component of momenta has to be corrected, is recalculated, during data processing. The relative correction is at or below the permille level, as shown later. (The relative corrections to the x and y components are neglected since they are also at or below the permille level.) We require the conservation of energy and all three momentum components as

$$\Delta p_{1,z} - \Delta p_{2,z} + \sqrt{p_3^2 + m^2} + \sqrt{p_4^2 + m^2} \approx 0, \tag{4}$$

$$p_{1,x} + p_{2,x} + p_{3,x} + p_{4,x} = 0, \tag{5}$$

$$p_{1,y} + p_{2,y} + p_{3,y} + p_{4,y} = 0, \tag{6}$$

$$\Delta p_{1,z} + \Delta p_{2,z} + p_{3,z} + p_{4,z} = 0, \tag{7}$$

Equations (4) and (7) are used to approximate the momentum losses $\Delta p_{1,z}$ and $\Delta p_{2,z}$ in each event,

$$\Delta p_{1,z} = -\left(\sqrt{p_3^2+m^2}+\sqrt{p_4^2+m^2}\right)/2 - \left(p_{3,z}+p_{4,z}\right)/2, \tag{8}$$

$$\Delta p_{2,z} = +\left(\sqrt{p_3^2+m^2}+\sqrt{p_4^2+m^2}\right)/2 - \left(p_{3,z}+p_{4,z}\right)/2. \tag{9}$$

Equations (5) and (6) are employed for selecting signal events by requiring that $|\sum p_x|$ and $|\sum p_y|$ are both small.

Invariants. A four-momentum (energy-momentum four-vector) p has the form $p = (E, \vec{p})$, where E is the energy, $\vec{p}$ is three-vector of momentum. The product of two four-vectors is $p_1 p_2 = E_1 E_2 - \vec{p_1}\vec{p_2}$, it is invariant under Lorentz-transformation. The square of a four-momentum $p^2 = E^2 - \vec{p}^2 = m^2$, it is the mass squared if the particle is real (on-shell).

The squared energy-momentum t of the pomeron is

$$t = q^2 = (\Delta E)^2 - (\Delta\vec{p})^2 \approx \Delta p_z^2 - (\Delta p_z^2 + p_T^2) = -p_T^2 < 0, \tag{10}$$

hence $t_1 \approx -p_{1,T}^2$ and $t_2 \approx -p_{2,T}^2$. For the third invariant,

$$\begin{aligned} t_{12} = q_1 q_2 = -2\Delta p_{1,z}\Delta p_{2,z} - \vec{p_{1,T}}\vec{p_{2,T}} = \\ = \left[m^2 + (p_{3,T}^2 + p_{4,T}^2)/2 + E_3 E_4 - p_{3,z}p_{4,z}\right] - \vec{p_{1,T}}\vec{p_{2,T}}. \end{aligned} \tag{11}$$

A linear combination of t_1, t_2, and t_{12} is the invariant mass-squared of the central $\mathrm{h}^+\mathrm{h}^-$ system,

$$m^2 = (p_3 + p_4)^2 = (q_1 + q_2)^2 = q_1^2 + q_2^2 + 2q_1 q_2. \tag{12}$$

With that, we can write down helpful relations between momentum losses of the protons, transverse masses ($m_T^2 = m^2 + p_T^2$) and rapidities (y) of the central $\mathrm{h}^+\mathrm{h}^-$ system,

$$\Delta p_{1,z}\Delta p_{2,z} = -\frac{m^2 + p_\mathrm{T}^2}{4} = \frac{m_\mathrm{T}^2}{4}, \tag{13}$$

and

$$\Delta p_{1,z} = -\frac{E+p_z}{2} = -\frac{m_\mathrm{T}}{2}e^{y}, \qquad \Delta p_{2,z} = \frac{E-p_z}{2} = \frac{m_\mathrm{T}}{2}e^{-y}. \tag{14}$$

The last equations are used for fast event generation during the calculation of combined efficiency corrections, with uniform y distribution. The momentum losses are usually below 5 GeV which is in line with the seen transverse masses ($m_T < 3\,\mathrm{GeV}$) and our rapidity acceptance ($|y| < y_\mathrm{max}$), thus Δp_z is indeed a permille level correction to p_z.

In summary,

$$t_1 \equiv q_1^2 \approx -p_{1,T}^2, \qquad t_2 \equiv q_2^2 \approx -p_{2,T}^2, \qquad t_{12} \equiv q_1 q_2 \approx \frac{m^2 + p_{1,T}^2 + p_{2,T}^2}{2}. \tag{15}$$

1.3 Limitations and analysis strategy

The measurement has several limitations.

- The roman pots detect scattered protons in the transverse momentum range[1]

$$0.175\,\text{GeV} < |p_{1/2,y}| < 0.670\,\text{GeV}, \tag{16}$$

  their acceptance is not azimuthally symmetric. The acceptance maps of RP-left and RP-right are correlated since signals from both roman pots are used for triggering. In addition, their detection efficiencies depend on low-level strip efficiencies, and these also change with time (run number).
- The silicon tracker has a limited acceptance, $|\eta| < 2.5$. It translates to windows of rapidity acceptance for the central hadrons as $|y| < y_{\max}$ where $y_{\max} = 2.0$ in the case of $\pi^+\pi^-$, and $y_{\max} = 1.6$ for $\mathrm{K^+K^-}$ and $\mathrm{p\overline{p}}$. Tracking is efficient for $p_\mathrm{T} > 0.1\,\text{GeV}$, but the particle identification capabilities are substantially reduced for high momenta. This way, the acceptance for the central system is $0 < p_\mathrm{T} < 1.2\,\text{GeV}$ in the case of $\pi^+\pi^-$ and $\mathrm{K^+K^-}$, while it is $0.3\,\text{GeV} < p_\mathrm{T} < 1.2\,\text{GeV}$ for $\mathrm{p\overline{p}}$.

Event selection. A taken event is processed if fulfils all of the selection criteria below.

- The scattered protons in roman pots:
  - both of them have $0.175\,\text{GeV} < |p_y| < 0.670\,\text{GeV}$ (Eq. (16));
  - the difference of their estimated location of origin has $|x_1^* - x_2^*| < 80\,\mu\text{m}$.
- The charged hadrons in central tracker:
  - the pair is clearly identified (being a specific $\mathrm{h^+h^-}$ is at least 10 times more probable than any other same-type combination);
  - they are not part of the same looping particle ($|\sum \vec{p}|/m > 0.2$);
  - both of them come from the primary interaction ($|r| < 1\,\text{cm}$, $|z - z_0| < 4\sigma_z$ where σ_z includes the uncertainty of the reconstructed z position, in addition to the size of the interaction region);
  - both of them have a reasonable reconstruction efficiency ($|\eta| < 2.5$ and $p_\mathrm{T} > 0.1\,\text{GeV}$, efficiency above 0.1);
  - the two-hadron system has a rapidity of $|y| < y_{\max}$.
- The event must be classified as either signal (weight 1) or sideband (weight -1).

[1] See Fig. 37 in CMS AN-21-162.

Corrections. Our goal is to publish fully corrected quantities, not using generators or models of high-energy physics, except those describing low-energy phenomena (GEANT4) needed for tracking efficiency correction. The corrections are detailed below.

- The scattered protons in the roman pots:
  - the p_y-acceptance and the elastic trigger veto of the roman pots, both determined from data. The acceptance correction takes advantage of the azimuthal symmetry around the beam axis. The combined correction is given in bins of $(p_{1,\mathrm{T}}, p_{2,\mathrm{T}}, \phi)$.
  - the joint tracklet reconstruction efficiency in the roman pots, based on the hit structure of each tracklet at the strip-level.
- The charged hadrons in central tracker:
  - the trigger, reconstruction and particle identification efficiencies of the charged hadron pair in the silicon tracker. The first two are constructed using a realistic detector simulation of single track events in $(\eta, p_\mathrm{T}, \phi)$ with a proper combination of information on pixel layer occupancy (at least 5 clusters on 3 layers) in the barrel.
    This combined tracker correction is applied in bins of $(p_{1,T}, p_{2,T})$, where in each of them a four-dimensional correction table $[\phi, m, (\cos\theta, \varphi)_\mathrm{GJ}]$ is employed based on a kinematic simulation. Here GJ refers to the Gottfried-Jackson frame[2] in the centre-of-mass of the centrally produced hadron pair.

The corrections are applied for each event separately in the form of products of independent weight factors (roman pots and tracker). This is possible, since the verification of the above corrections reveals that there are *no efficiency holes* in the $[\phi, m, (\cos\theta, \varphi)_\mathrm{GJ}]$ space of the two-hadron system in our rapidity window.

Goals. Physics processes are studied in windows of rapidity $|y| < y_\mathrm{max}$ for the central system (as mentioned above), and as functions of

- the pairs of four-momentum transfers (t_1, t_2), or equivalently of $(p_{1,T}, p_{2,T})$;
- the angle ϕ between the momentum vectors of two scattered protons in the transverse plane;
- the invariant mass m of the central two-hadron system;
- and in the subsequent study (CMS AN-20-183 "Part II: Study of resonance production"), the polar and azimuthal angles $(\vartheta, \varphi)_\mathrm{GJ}$ of the positively charged hadron.

[2]GJ frame: the z-axis is in the direction of the resonance in the laboratory frame; the y-axis is perpendicular to both z and the incoming proton direction; $\hat{x} = \hat{y} \times \hat{z}$

2 Data-taking, conditions

The data were taken in a special, high $\beta^* = 90\,\mathrm{m}$ run of LHC, in the period 2-7 July, 2018. Some important details are listed at `https://twiki.cern.ch/twiki/bin/view/TOTEM/90m2018`.

Beam crossing angle. The half crossing-angle was 60 μrad (the proton beams cross in the horizontal plane at Point 5). At 6.5 TeV beam energy, the crossing angle results in a 390 MeV transverse momentum for both protons. This corresponds to a negligible ($\beta_x = p_x/E = -0.39/6500 = -6 \cdot 10^{-5}$) transverse boost in the horizontal plane, pointing outwards from the accelerator ring. In the following the effect of crossing angle is disregarded, in other words all quantities are calculated in the centre of mass system of the colliding protons.

Streams. The data streams are related to specific RP trigger configurations, they are

- TOTEM1X: double arm (all topologies),
- TOTEM2X: exclusive diagonal configurations and not elastic,
- TOTEM3X: elastic collisions,
- TOTEM4X: exclusive parallel configurations,

where "diagonal" refers to cases where RP detectors on opposite side (top-bottom or TB, bottom-top or BT) fired, while the "parallel" configuration refers to same side (top-top or TT, bottom-bottom or BB) detectors. Only the exclusive not elastic streams TOTEM2X and TOTEM4X are used in the following.

Bunches. LHC injection schemes used during the data taking are listed in Table 1. Fills, bunch spacing, number of filled bunches are shown along with modifier labels. These latter correspond to reduced or full readout of bunch crossings in the case of the diagonal configuration. The list of fills, number of colliding bunches, runs, along with the lumisection (LS) ranges, recalculated recorded integrated luminosity are given in Table 2. Some beam-related specialties of the fills and runs are listed below:

- fills 6877-6882 have 100 ns bunch spacing, while fills 6884-6892 had 50 ns;
- during the fills 6877-6884, all bunch crossings were recorded, with the exception of the first part of run 319159 where only data from 2/3 out of the 732 colliding bunches were taken;
- starting with fill 6885, for the diagonal (TB or BT) roman pot trigger configurations, only part of the bunch crossings were recorded, while the parallel (TT or BB) ones were left untouched. The reason for that was to keep the readout rate below a rea-

Table 1: LHC injection schemes used during the data taking. Fills, bunch spacing, number of filled bunches are shown along with modifier labels. These latter correspond to reduced or full readout of bunch crossings in the case of the diagonal configuration.

Fills	Bunch spacing	Number of bunches	Modifiers
6877	100 ns	86b	–
6879	100 ns	302b	–
6881-6882	100 ns	734b	–
6884	50 ns	302b	–
6885	50 ns	734b	487 (or 2/3)
6890-6892	50 ns	1452b	1_2, 2_3, 3_4, 4_5, 5_6, 6_7, full

Table 2: List of fills, number of colliding bunches, runs, lumisection ranges, recalculated integrated luminosities, and the fraction of selected bunch crossings in the case of the diagonal RP trigger configuration.

Fill	Coll. bxs	Run	LS range	Int. lumi. [pb^{-1}] diag.	Int. lumi. [pb^{-1}] para.	[LS-, fraction of bxs selected for diag.]
6877	84	319104	22-181	0.012	0.012	all
6879	300	319124	149-277	0.028	0.029	all
		319125	1-207	0.042	0.041	all
6881	732	319159	202-618	0.182	0.179	[202-, 2/3*] [250-, all]
		319160	1-479	0.185	0.183	all
6882	732	319174	23-72	0.023	0.024	all
		319175	1-139	0.064	0.064	all
		319176	1-1799	0.636	0.635	all
		319177	11-233	0.059	0.059	all
6884	300	319190	39-316	0.087	0.086	all
6885	732	319222	191-294	0.030	0.063	[191-, 2/3] [233-, 1/3*]
		319223	5-132	0.049	0.074	[5-, 2/3]
6890	1450	319254	168-263	0.045	0.071	[168-, 2/3]
		319255	1-164	0.082	0.120	[1-, 2/3]
		319256	1-726	0.397	0.501	[1-, 2/3], [40-, 3/4] [417-, all] [530-, 3/4]
		319260	1-132	0.067	0.088	[1-, 3/4]
		319262	1-359	0.183	0.232	[1-, 3/4] [87-, 4/5]
		319263	1-365	0.179	0.222	[1-, 4/5]
		319264	1-57	0.026	0.033	[1-, 4/5]
		319265	1-396	0.203	0.249	[1-, 4/5]
		319266	1-27	0.012	0.015	[1-, 4/5]
		319267	1-204	0.104	0.129	[1-, 4/5]
		319268	1-467	0.244	0.299	[1-, 4/5] [186-, 5/6]
		319270	1-206	0.109	0.128	[1-, 6/7]
6891	1450	319300	48-1133	0.552	0.780	[48-, 1/3] [210-, 4/5] [603-, 5/6] [870-, 6/7] [987-, all]
6892	1450	319311	50-1733	0.937	1.204	[50-, 1/2] [58-, 3/4] [76-, 4/5] [274-, 1/2] [300-, 2/3] [528-, 3/4] [838-, 4/5] [1237-, 5/6] [1495-, 6/7]
Total recorded ($\sum L_{\mathrm{int}}$)				4.54-4.57	5.52	
Total efficient ($\sum L_{\mathrm{eff}}$)				3.89-3.92	4.73	

* reduction is for both (diagonal and parallel) configurations.

sonable limit. Usually the reduction corresponds to 1/2, 2/3, 3/4, 4/5, 5/6, or 6/7 of all the provided bunch crossings;

- the actual numbers of selected bunch crossings along with their starting lumisection values are given in the last column of Table 2.

The reduction of the selected bunches does not simply translate to the reduction of the recorded luminosity since the bunch-by-bunch luminosity can greatly vary: bunches can have differing numbers of protons, and their orbits may vary slightly as well. This effect is striking for fill 6890, where the luminosity in the selected bunches is decisively smaller than the average. In summary, a detailed, bunch- and lumisection-level recalculation of the integrated luminosity was needed and performed. These are done separately for the diagonal and the parallel trigger configurations of the RPs, further details are given in Sec. 2.2.

Hadronic forward calorimeter. The HF threshold has been slightly varied (setting of 9 for fills 6877-6882, 17 for fill 6884, and 12 for fills 6885-6892), but that has a negligible influence on rates (through the `L1_NotMinimumBiasHF0` trigger path). The effect of out-of-time pileup in HF, the correlation of event losses with bunch-train configurations, is not seen in data.

Triggers. L1 and high-level triggers (HLT) for the TOTEM20 dataset, as an example, are detailed in Table 3.

Conditions and settings are listed below:

- software version used for both measured and simulated data: `CMSSW_10_1_7`;
- era: `Run2_2018_highBetaStar`;
- global tag for measured data: `101X_dataRun2_Prompt_v11`;
- global tag for simulated data: `101X_upgrade2018_realistic_v7`;
- L1 menus `L1Menu_Special2018_1_1_0`;
- HLT configuration: `/cdaq/special/90m/Test/HLT/V1[1-8]`.

The high-level trigger has the following major components:

Table 3: L1 and HLT triggers for the TOTEM20 dataset as an example.

HLT trigger / L1 seed
HLT_TOTEM_2_AND_PixelClusterCounting_BPixNClu5NLay3_part0_v1
L1_NotMinimumBiasHF0_AND_BptxAND_TOTEM_2 OR L1_TOTEM_2 OR L1_NotMinimumBiasHF0_OR_BptxAND_TOTEM_2
HLT_TOTEM_2_AND_PixelClusterCounting_BPixNClu5NLay4_part0_v1
L1_NotMinimumBiasHF0_AND_BptxAND_TOTEM_2 OR L1_TOTEM_2 OR L1_NotMinimumBiasHF0_OR_BptxAND_TOTEM_2
HLT_TOTEM_2_AND_PixelClusterCounting_BPixNClu6NLay3_part0_v1
L1_NotMinimumBiasHF0_AND_BptxAND_TOTEM_2 OR L1_TOTEM_2 OR L1_NotMinimumBiasHF0_OR_BptxAND_TOTEM_2
HLT_TOTEM_2_AND_PixelClusterCounting_BPixNClu6NLay4_part0_v1
L1_NotMinimumBiasHF0_AND_BptxAND_TOTEM_2 OR L1_TOTEM_2 OR L1_NotMinimumBiasHF0_OR_BptxAND_TOTEM_2
HLT_TOTEM_2_AND_PixelClusterCounting_BPixNClu7NLay3_part0_v1
L1_NotMinimumBiasHF0_AND_BptxAND_TOTEM_2 OR L1_TOTEM_2 OR L1_NotMinimumBiasHF0_OR_BptxAND_TOTEM_2
HLT_TOTEM_2_AND_PixelClusterCounting_BPixNClu7NLay4_part0_v1
L1_NotMinimumBiasHF0_AND_BptxAND_TOTEM_2 OR L1_TOTEM_2 OR L1_NotMinimumBiasHF0_OR_BptxAND_TOTEM_2
HLT_TOTEM_2_AND_PixelTrackCounting_BPixOnly_Mult1_part0_v1
L1_NotMinimumBiasHF0_AND_BptxAND_TOTEM_2 OR L1_TOTEM_2 OR L1_NotMinimumBiasHF0_OR_BptxAND_TOTEM_2
HLT_TOTEM_2_AND_PixelTrackCounting_BPixOnly_Mult2_part0_v1
L1_NotMinimumBiasHF0_AND_BptxAND_TOTEM_2 OR L1_TOTEM_2 OR L1_NotMinimumBiasHF0_OR_BptxAND_TOTEM_2
HLT_TOTEM_2_AND_PixelTrackCounting_BPixOnly_Mult3_part0_v1
L1_NotMinimumBiasHF0_AND_BptxAND_TOTEM_2 OR L1_TOTEM_2 OR L1_NotMinimumBiasHF0_OR_BptxAND_TOTEM_2
HLT_TOTEM_2_AND_PixelTrackCounting_Mult1_part0_v1
L1_NotMinimumBiasHF0_AND_BptxAND_TOTEM_2 OR L1_TOTEM_2 OR L1_NotMinimumBiasHF0_OR_BptxAND_TOTEM_2
HLT_TOTEM_2_AND_PixelTrackCounting_Mult2_part0_v1
L1_NotMinimumBiasHF0_AND_BptxAND_TOTEM_2 OR L1_TOTEM_2 OR L1_NotMinimumBiasHF0_OR_BptxAND_TOTEM_2
HLT_TOTEM_2_AND_PixelTrackCounting_Mult3_part0_v1
L1_NotMinimumBiasHF0_AND_BptxAND_TOTEM_2 OR L1_TOTEM_2 OR L1_NotMinimumBiasHF0_OR_BptxAND_TOTEM_2

- the pixel activity filter `hltPixelActivityFilterBPixNCluXNLayY` requires at least `X` pixel clusters and at least `Y` layers with pixel clusters in BPix;
- the pixel track filter `hltPixelTrackFilterBPixNY` requires at least `Y` pixel tracks in BPix;
- the pixel track filter `hltPixelTrackFilterNY` requires at least `Y` pixel tracks.

Datasets. The reconstructed datasets are

- `/TOTEM2[0-3]/Run2018B-22Feb2019-v1/RECO`,
  these four datasets are triggered by diagonal RP configurations TB or BT;
- `/TOTEM4[0-3]/Run2018B-22Feb2019-v1/RECO`,
  these four datasets are triggered by parallel RP configurations TT or BB.

The data are also available through
`/eostotem//eos/totem/data/cmstotem/2018/90m/RECO_copy/TOTEM[2,4][0-3]/`.

Beamspot. The location of the beamspot centre (Fig. 1) is stable throughout the whole running period, while the Gaussian widths of the beamspot (Fig. 2) show some slight, but expected variations. The beamspot parameters used in the simulation have been determined based on these conditions. They are as follows:

```
Totem90m2018CollisionVtxSmearingParameters = cms.PSet(
    Phi = cms.double(0.0),
    BetaStar = cms.double(9121.0),
    Emittance = cms.double(0.12e-7),
    Alpha = cms.double(0.0),
    SigmaZ = cms.double(4.1),
    TimeOffset = cms.double(0.0),
    X0 = cms.double(0.0965),
    Y0 = cms.double(0.119),
    Z0 = cms.double(-0.35)
)
```

Pileup. The time dependence of the average pileup is shown in Fig. 3, it is in the range $0.1 - 0.3$. In fact, because of complications connected to bunch selections, these values are not used in the analysis, but they are recalculated based on the actual detected and selected instantaneous luminosity and the visible cross section.

In events with more than one pp collision the exclusivity of the final state is spoiled, they are rejected. We need to sum the "clear" total recorded luminosity taking into account the expected pileup.

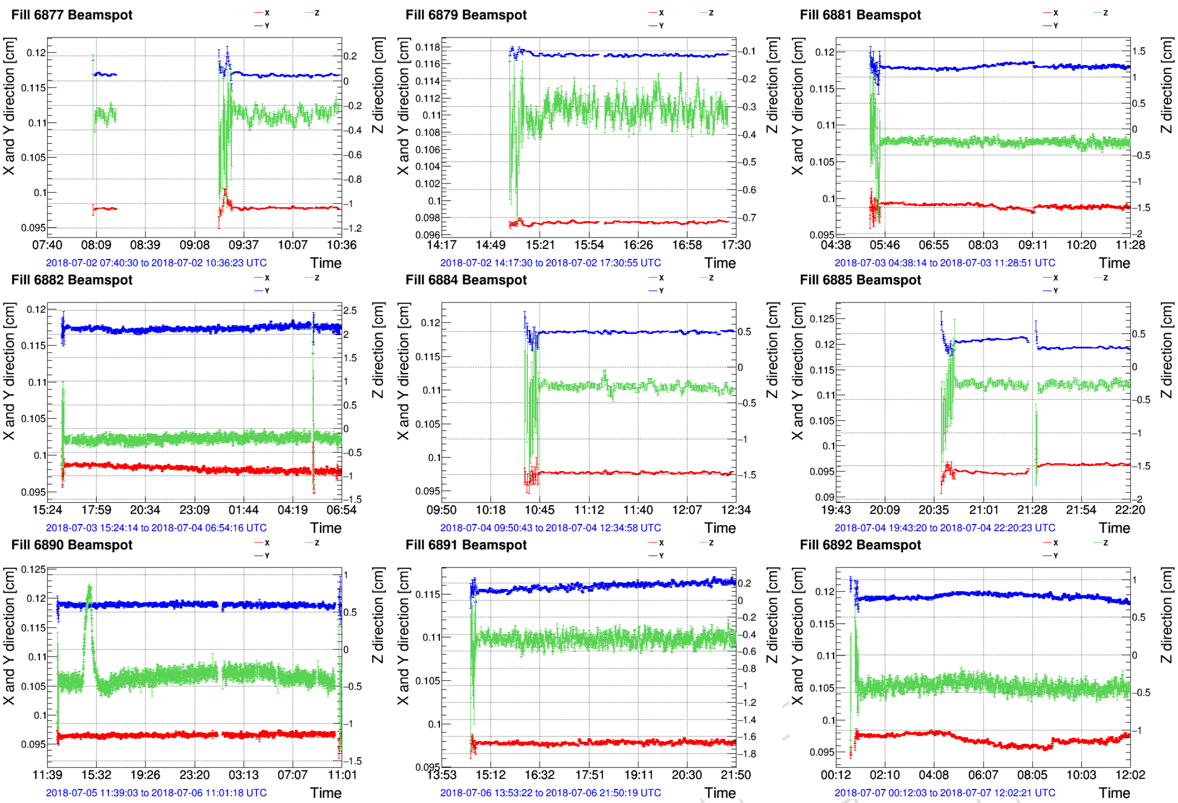

Figure 1: Position of the beamspot centre as a function of time for the analysed fills (from CMS Web Based Monitoring).

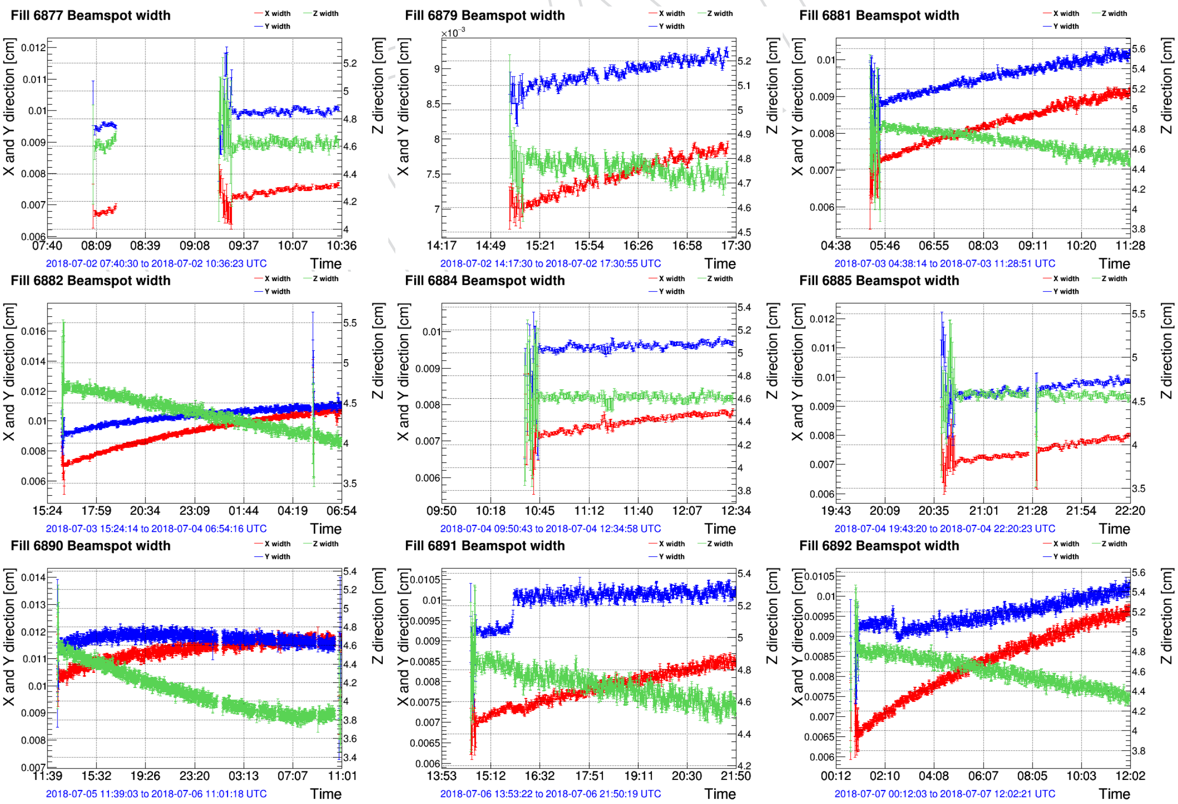

Figure 2: Gaussian width of the beamspot as a function of time for the analysed fills (from CMS Web Based Monitoring).

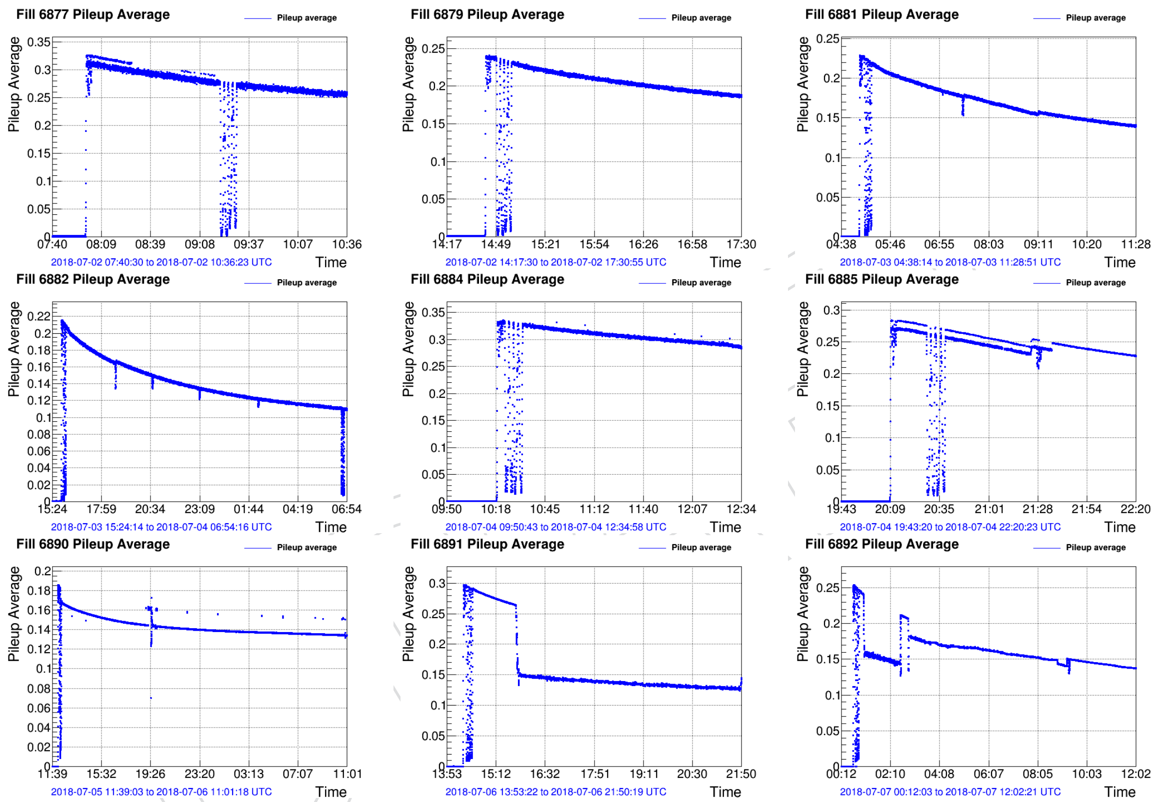

Figure 3: Average pileup as a function of time for the analysed fills (from CMS Web Based Monitoring).

2.1 Cross section and verification of corrections

There are several physics processes that could take place between two colliding protons: elastic or inelastic interactions, the latter composed of central exclusive (CE), single- (SD) and double-diffractive (DD), nondiffractive (ND) processes. Our detector-level signatures for the studied $\mathrm{p(h^+h^-)p}$ process are

- two slightly scattered but intact protons,
- two oppositely charged centrally produced hadrons,
- and the sum of their momenta being close to zero.

In fact, the situation is more complicated since sometimes more than one pp collision happens in a bunch crossing (pileup). The detection probability is the product of Poissonian $P(n) = \mu^n \exp(-\mu)/n!$ factors. We want

- exactly one detectable $\mathrm{p(h^+h^-)p}$ process,
- no other central exclusive, single-, double-diffractive or nondiffractive collisions (they would be visible in the tracker or in the calorimeters),
- no visible elastic collisions (that is, no detectable scattered protons in RPs),
- but allow for any number of undetectable elastic or $\mathrm{p(h^+h^-)p}$ collisions.

In summary, the probability of such circumstances is

$$\begin{aligned}
&\underline{P_\mathrm{selected}} = \\
&\quad = P_\mathrm{el,det}(0) \cdot P_\mathrm{p(h^+h^-)p,det}(1) \cdot P_\mathrm{CE,SD,DD,ND}(0) \cdot \sum_{j=0}^{\infty} P_\mathrm{el,undet}(j) \cdot \sum_{k=0}^{\infty} P_\mathrm{p(h^+h^-)p,undet}(k) = \\
&\qquad = \mu_\mathrm{p(h^+h^-)p,det} \exp(-\mu_\mathrm{el,det}) \exp(-\mu_\mathrm{p(h^+h^-)p,det}) \exp(-\mu_\mathrm{CE,SD,DD,ND}) = \\
&\qquad\qquad = \underline{\mu_\mathrm{p(h^+h^-)p,det} \exp(-\mu_\mathrm{vis})}, \qquad (17)
\end{aligned}$$

where μ_vis is the average number of "visible" collisions which is the sum of detectable elastic and $\mathrm{p(h^+h^-)p}$, other central exclusive, single-, double-diffractive or nondiffractive collisions:

$$\mu_\mathrm{vis} = \mu_\mathrm{el,det} + \mu_\mathrm{p(h^+h^-)p,det} + \mu_\mathrm{CE,SD,DD,ND}. \qquad (18)$$

This average of μ_vis is calculable from the overall integrated luminosity L_int as

$$\langle \mu_\mathrm{vis} \rangle (L_\mathrm{int}) = \langle L_\mathrm{int,bunch} \rangle \, \sigma_\mathrm{vis} = \frac{L_\mathrm{int}}{n_\mathrm{bunch} n_\mathrm{orbit}} \, \sigma_\mathrm{vis}, \qquad (19)$$

where $L_\mathrm{int,bunch}$ is the average integrated luminosity per bunch crossing, n_bunch is the number of selected bunch crossings, n_orbit is the number of orbits in a time period (in our case, in a so called lumisection, it has a value of 2^{18}). Here σ_vis is the cross section of visible collisions, such as detectable elastic and $\mathrm{p(h^+h^-)p}$, other central exclusive, single-, double-diffractive or nondiffractive collisions,

$$\sigma_\mathrm{vis} = \sigma_\mathrm{el,det} + \sigma_\mathrm{p(h^+h^-)p,det} + \sigma_\mathrm{CE,SD,DD,ND}. \qquad (20)$$

Table 4: List of measured pp inelastic cross-sections at $\sqrt{s} = 13\,\text{TeV}$.

experiment	σ_{inel} [mb]	$\sigma_{\text{min.bias}}$ [mb]
ATLAS [20]	78.1 ± 2.9	
CMS [21]		69.2
LHCb [22]	75.4 ± 5.4	
TOTEM [23]	79.5 ± 1.8	
average	78.8 ± 0.8	

Finally, the number of expected selected events in a given time period is

$$\begin{aligned}\underline{n_{\text{selected}}} = P_{\text{selected}} \cdot n_{\text{bunch}} n_{\text{orbit}} = L_{\text{int}}\, \sigma_{\text{p}(\text{h}^+\text{h}^-)\text{p,det}} \cdot \exp(-\langle \mu_{\text{vis}} \rangle) = \\ = \underline{L_{\text{int}}\, \sigma_{\text{p}(\text{h}^+\text{h}^-)\text{p,det}} \cdot \exp\left(-\frac{L_{\text{int}}}{n_{\text{bunch}} n_{\text{orbit}}}\, \sigma_{\text{vis}} \right)}.\end{aligned} \tag{21}$$

The weight for a detected $\text{p}(\text{h}^+\text{h}^-)\text{p}$ event is

$$1/\left(\sum L_{\text{eff}}\right), \tag{22}$$

where the sum is over all the lumisections, while the effective luminosity is

$$L_{\text{eff}} \equiv L_{\text{int}} \exp[-\langle \mu_{\text{vis}} \rangle (L_{\text{int}})]. \tag{23}$$

What are the values to be taken for σ_{vis}? Most of the elastic pp collisions are rejected by the RP proton-pair trigger (Sec. 3.1), while large fraction of $\text{p}(\text{h}^+\text{h}^-)\text{p}$ is selected. This way the inelastic pp cross section is a good approximation for the visible cross section,

$$\sigma_{\text{vis}} \approx \sigma_{\text{inel}}. \tag{24}$$

There are several measurements of the inelastic pp cross section at $\sqrt{s} = 13\,\text{TeV}$ at LHC, they are listed in Table 4. For reference, the "minimum bias" cross section recommended by CMS is also indicated. We use the average as $\sigma_{\text{vis}} = 79 \pm 5\,\text{mb}$ where the systematic uncertainty is estimated from the difference to the minimum bias value, its half is taken. That is propagated to the final differential cross sections through the pileup correction factor $\exp(-\mu)$, With the value of the average pileup $\mu \approx 0.15$ the above 5 mb translates to a $0.15 \cdot 5/79 \approx 1\%$ systematic uncertainty.

2.2 Comparison of the number of detected and expected events

The run- and lumisection-dependent beam-related (instantaneous luminosity, bunch crossing selection) and detector-related (acceptance, triggering, efficiency) characteristics can be tested by comparing the number of observed and the number of expected events (Eq. (21)), in all RP trigger configurations (TB, BT, TT, and BB) separately. We have in each lumisection n_{selected} from reconstructed data, but it can be calculated from other sources since L_{int} is provided, n_{bunch} and n_{orbit} are known, σ_{vis} is fixed from other data. The systematic uncertainty of the integrated luminosity (L_{int}, per lumisection) is 2.5% [24]. The number of observed events is corrected for trigger and reconstruction efficiencies in the roman pots and the central tracker by weighting each event with the reciprocal of the actual efficiencies, also signed according to their event classification (signal with 1, sideband with -1, otherwise 0).

It is important to emphasise that in the reconstruction we employ all corrections, to be discussed in the following sections: corrections related to the trigger acceptance (Sec. 3.1) and detection efficiency of the proton-pair (Sec. 3.2), event classification and removal of the non-exclusive background (Sec. 6), the efficiency of high level triggering on central charged hadrons and their reconstruction efficiency (Sec. 5.1), as well as the efficiency of their identification (Sec. 5.2). In this sense, the study presented here is an important verification and demonstration of the soundness of all the corrections, notably of those related to the roman pots which are not azimuthally symmetric.

The real unknown is the cross section of the $\mathrm{p(h^+h^-)p}$ process $\sigma_{\mathrm{p(h^+h^-)p}}$, more precisely the dynamics and internal correlations of the "two protons and two oppositely charged central hadrons" system. For the rough estimation of the combined acceptance+triggering+detection efficiency we employ the DIME (v1.07) Monte Carlo event generator [25] in the dominant $\pi^+\pi^-$ channel. The event generator is run with plausible settings, exponential meson-pomeron form factor with $\Lambda_{\mathrm{off}} = 1.0\,\mathrm{GeV}$, and soft model DIME -1. Both in data and in simulation, the rapidity of the central hadrons is required to be $|y| < y_{\mathrm{max}}$.

The percentage of accepted, triggered, and detected events for the diagonal configuration is estimated as 3.9%, while for the parallel one it is 6.9%. The detected and expected number of events match if the cross section for the diagonal trigger configuration is set to 15.2 μb, and to 12.4 μb for the parallel configuration.

Data taking issues. List of specific data taking issues and problems per lumisection are listed in Table 5. Part of the roman pot system is labelled as

- "off": there are no reconstructed events since part of the detector was off;
- "low": consistently reduced data taking efficiency (for concrete values see later), likely because of reconstruction issues by one out of four data sub-streams.

These either apply to all detectors, only diagonal or parallel configurations, or in some cases to RP-left bottom (1B) and RP-right top (2T) detector parts.

Another special issue complicates the processing of run 319260 where the source for the calculation integrated luminosity was switched from the default source, the hadronic forward calorimeter (HFOC), to the pixel detector (PXL). This resulted in inconsistent data which were fixed by using a linear extrapolation based on the first 29 lumisections, separately for the diagonal and parallel trigger configurations.

Table 5: List of specific data taking issues and problems per lumisection. Configurations mentioned: diag = TB and BT; para = TT and BB; all = TB, BT, TT, and BB. Possible status: "off" (or missing, 0%), "low" ($\approx$ 75%).

Run	Config.	Status	Lumisection ranges
319104	all	off	177-179
319124	diag	off	149-150
	all	low	187-188 190-191
319125	all	off	17-19 192-194
	para	off	7-10
319600	para	low	51-56 390-392 395-396
319174	para	low	31 34-37
319175	para	low	45-50
319176	1B	low	1789-1799
	para	low	235-240 360-365
	all	low	471 1331
319177	all	off	224-226
319190	all	off	310-312
319222	all	off	191
	para	low	231
319254	diag	off	168-173
	para	low	168-169
319256	diag	low	422 449 453 457 482 490 508-510 515 681 518-519 521 528-529
	para	low	16-18 39-40 482-485
319260	all	off	132
	1B	low	53
319262	1B	low	157-176 339-359
	all	low	89
319263	2T	off	113-141
	1B	low	329-364
319264	diag	low	5
	1B	low	20-57
319265	1B	low	385-394
319267	para	low	184
319268	diag	low	465-466
	1B	low	136-156
	para	low	199 173-176 199 326 329 342 344-346 423-426 435-438
	para	off	463-467
319270	para	low	32-33
319300	diag	off	48-52
	para	low	55 79 163 198 872 660-662 664
	para	off	48-49
	all	low	1128
319311	all	off	1714-1716
	diag	low	830-831 835 837
	para	low	277-276 527-528 831-832 835 837-838 1017-1020 1577-1580
	para	off	50-59
	all	low	77

The comparison. The observed and expected number of $\mathrm{p(h^+h^-)p}$ events in each lumisection for fills or fill ranges are shown separately for the four RP trigger configurations (TB, BT, TT, and BB) in Figs. 4-24. Overall there is a very nice agreement, all details of observed changes in the conditions and characteristics of data taking are properly reflected in the expected number of detected events.

The distribution of the ratio of detected over expected two-track central exclusive events in a lumisection, plotted for "normal" and "low" lumisections, shown separately for all four configurations (TB, BT, TT, and TB) in Fig. 25. In addition to the measured values, results of Gaussian fits are plotted and their mean values are indicated. The ratios for normal events are nicely centred around one, the observed Gaussian-like spread meets the expectations for a Poissonian distribution with counts in the several hundreds. The reduced efficiency events indeed consistently show a 75% efficiency. About 2-3% of the lumisections belong here, meaning about 0.5% estimated systematic uncertainty.

The ratio of detected over expected two-track central exclusive events in a lumisection as a function of the average number of simultaneous visible (inelastic) pp collisions μ, are shown in Fig. 26 separately for all four configurations (TB, BT, TT, and TB). There are no obvious μ-dependencies visible. The number of detected two-track central exclusive events as a function of expected events in a lumisection, are shown in Fig. 27 separately for all four configurations. The lumisections nicely populate the $\pm 2\sigma$ band between the $n \pm 2\sqrt{n}$ lines as expected. The effective integrated luminosity as function of date/time is shown in Fig. 28.

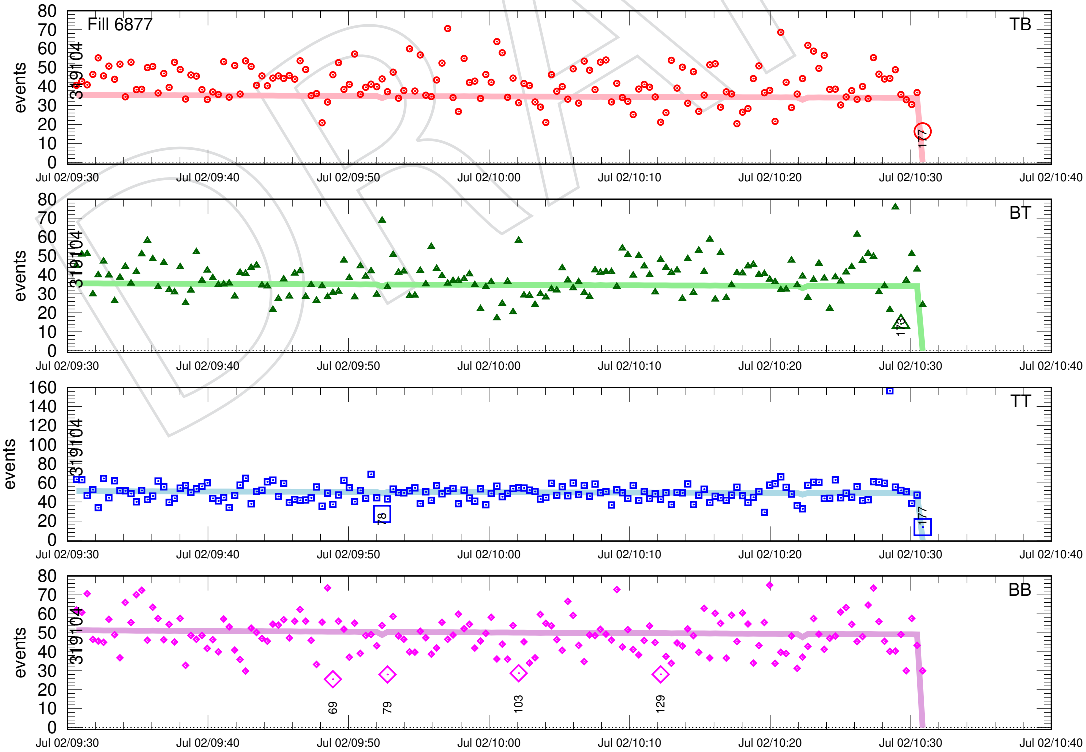

Figure 4: Observed (points) and expected (bands) number of $\mathrm{p(h^+h^-)p}$ events in each lumisection for fill (or fill-range) 6877, shown separately for the four RP trigger configurations (TB, BT, TT, and BB).

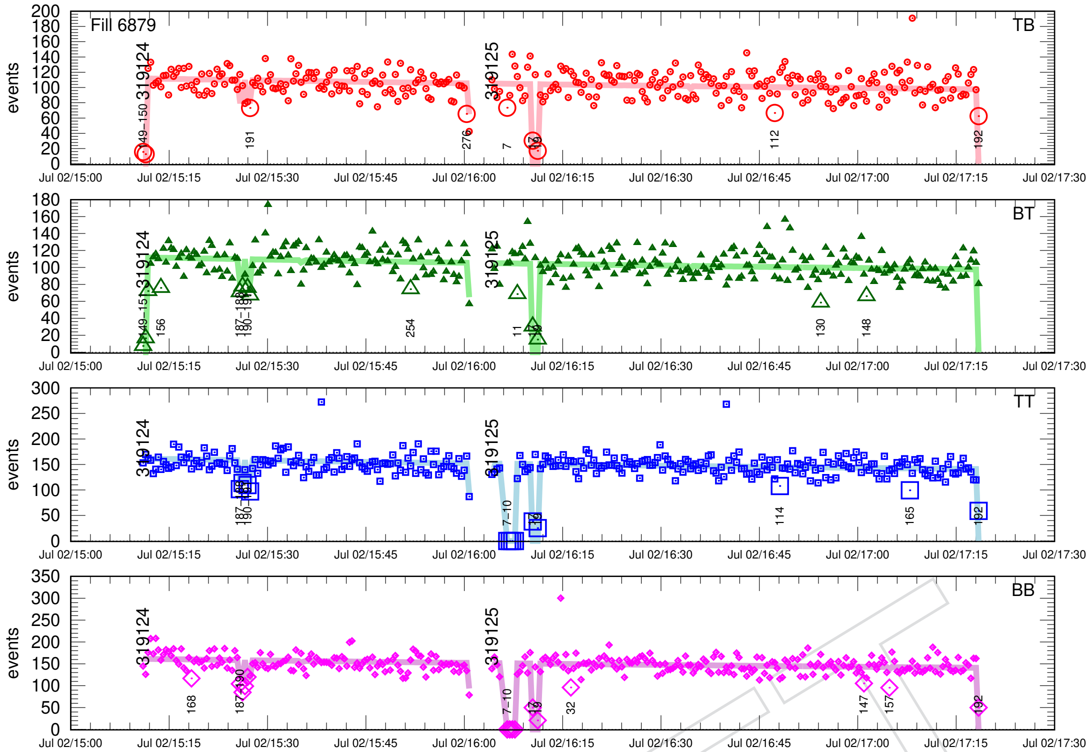

Figure 5: Observed (points) and expected (bands) number of $p(h^+h^-)p$ events in each lumisection for fill (or fill-range) 6879, shown separately for the four RP trigger configurations (TB, BT, TT, and BB).

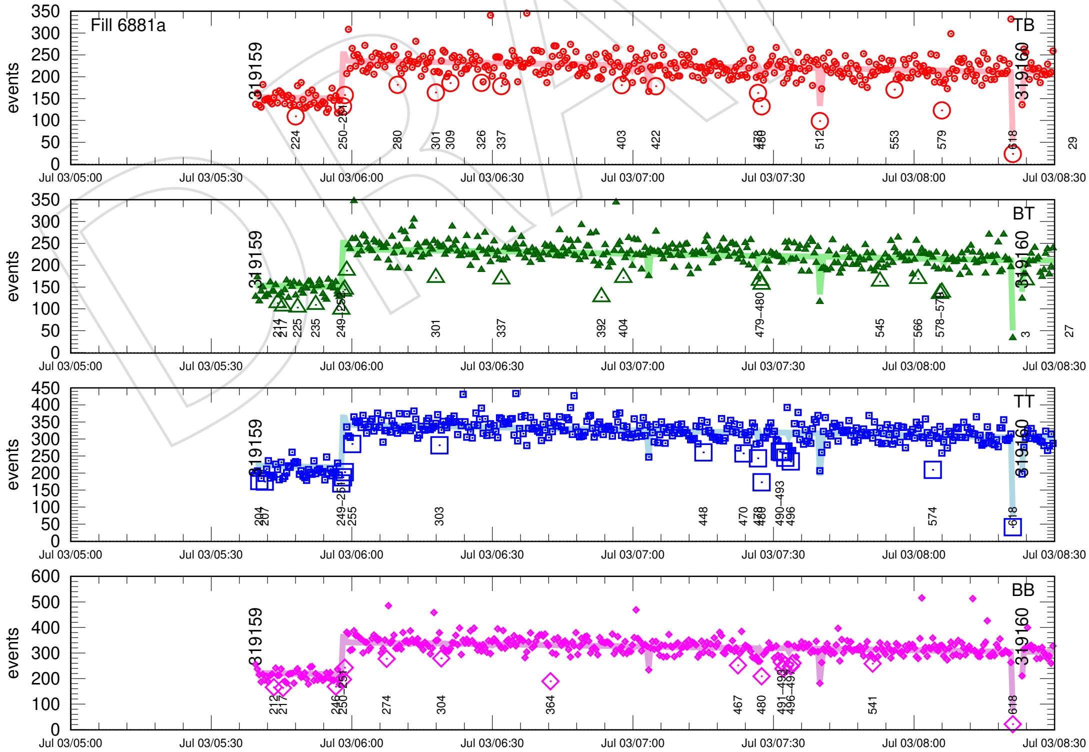

Figure 6: Observed (points) and expected (bands) number of $p(h^+h^-)p$ events in each lumisection for fill (or fill-range) 6881a, shown separately for the four RP trigger configurations (TB, BT, TT, and BB).

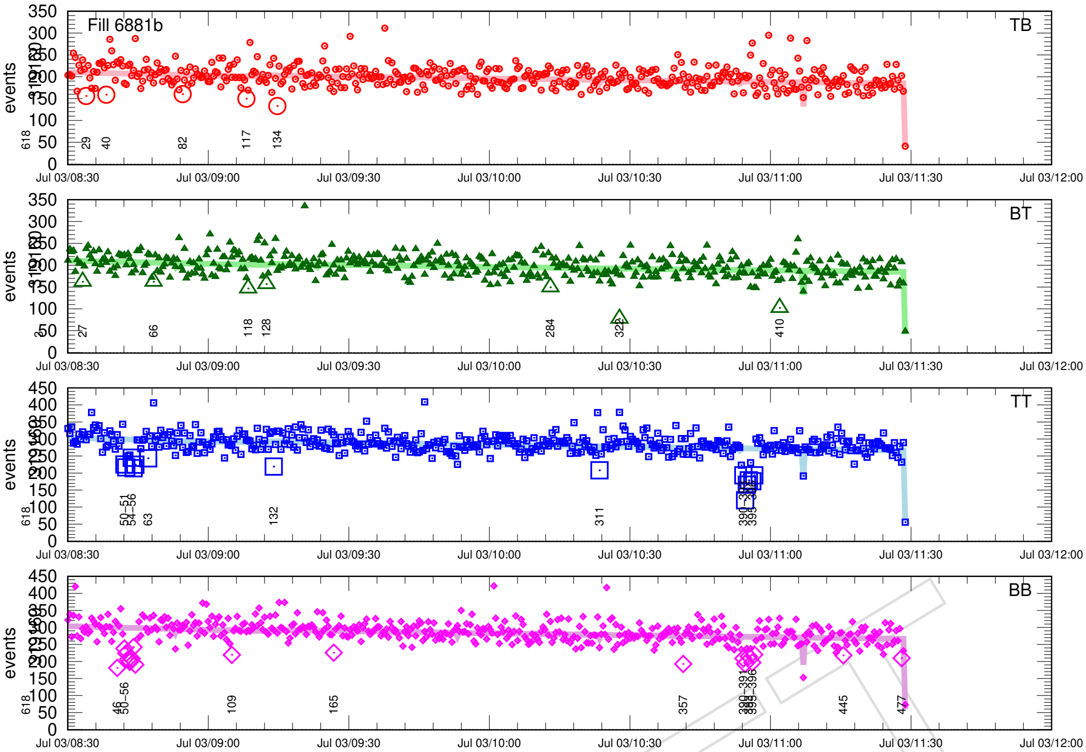

Figure 7: Observed (points) and expected (bands) number of $p(h^+h^-)p$ events in each lumisection for fill (or fill-range) 6881b, shown separately for the four RP trigger configurations (TB, BT, TT, and BB).

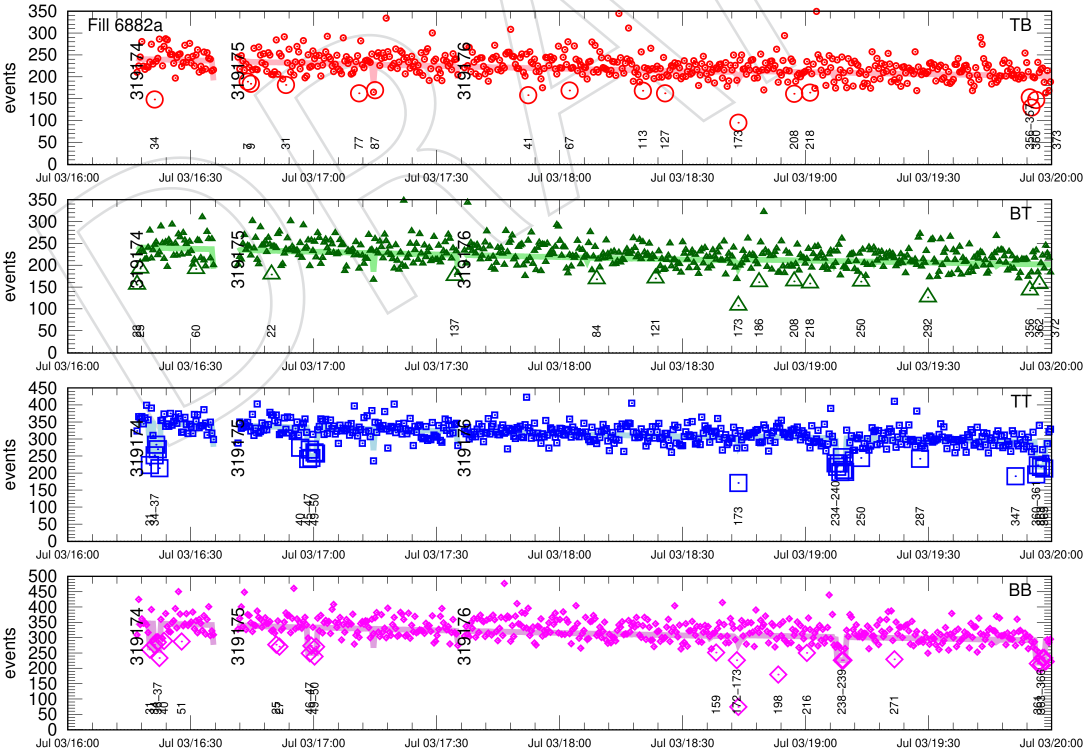

Figure 8: Observed (points) and expected (bands) number of $p(h^+h^-)p$ events in each lumisection for fill (or fill-range) 6882a, shown separately for the four RP trigger configurations (TB, BT, TT, and BB).

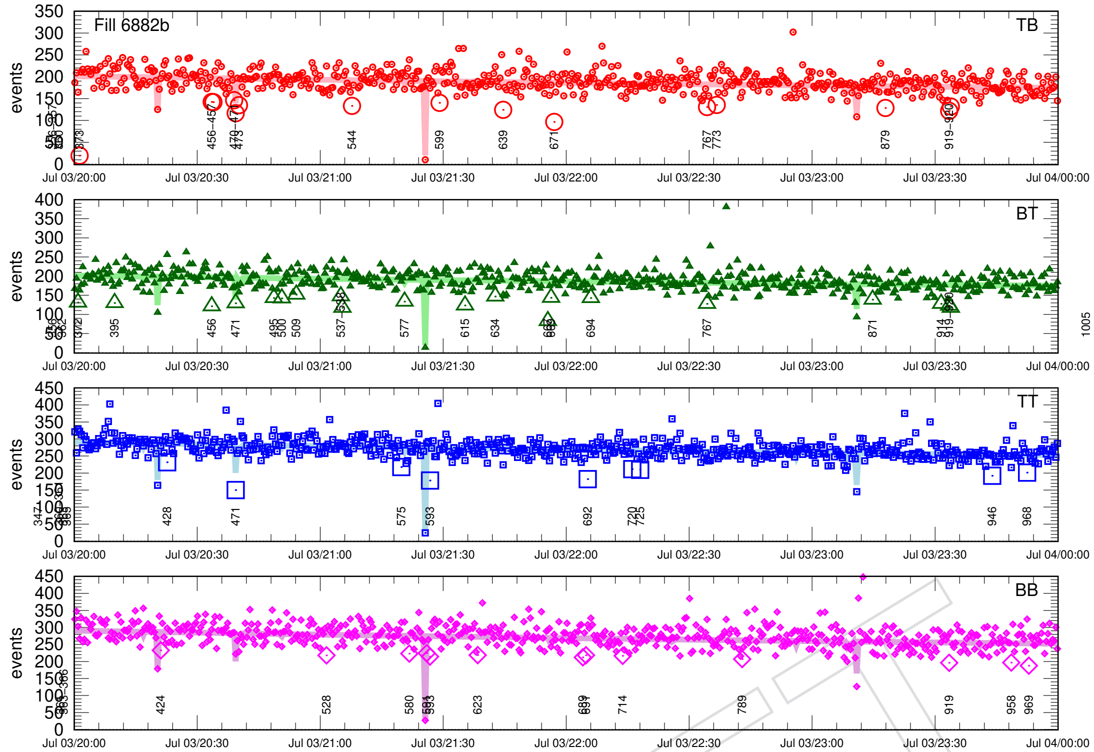

Figure 9: Observed (points) and expected (bands) number of $p(h^+h^-)p$ events in each lumisection for fill (or fill-range) 6882b, shown separately for the four RP trigger configurations (TB, BT, TT, and BB).

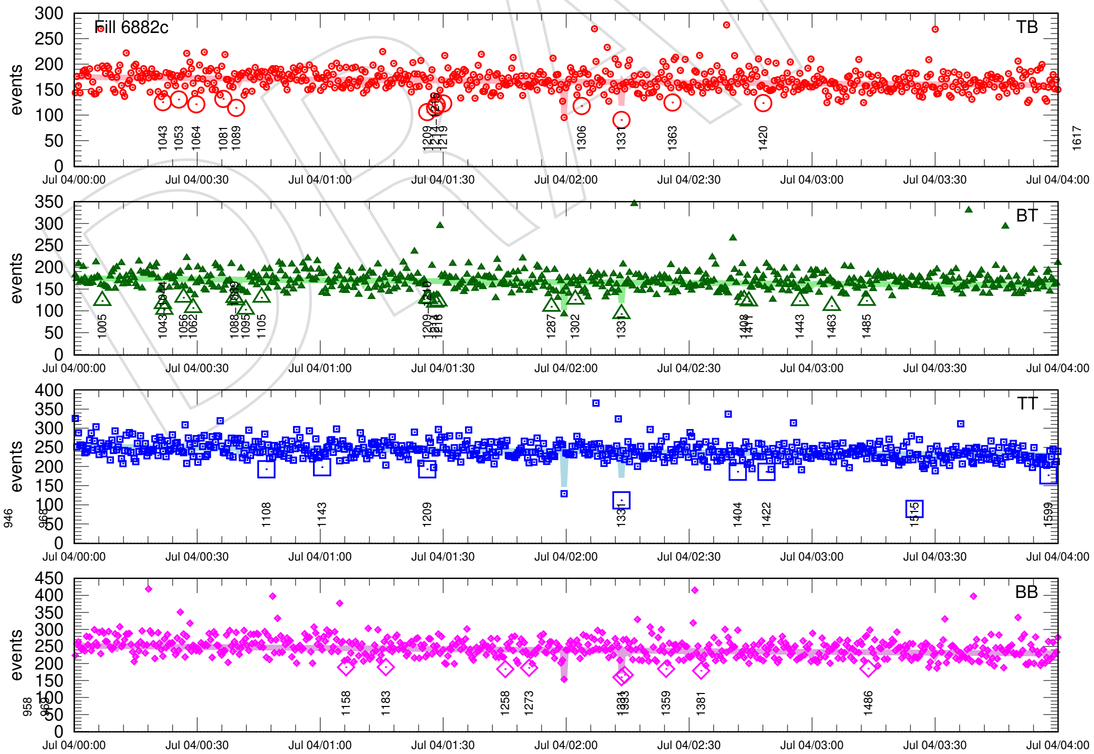

Figure 10: Observed (points) and expected (bands) number of $p(h^+h^-)p$ events in each lumisection for fill (or fill-range) 6882c, shown separately for the four RP trigger configurations (TB, BT, TT, and BB).

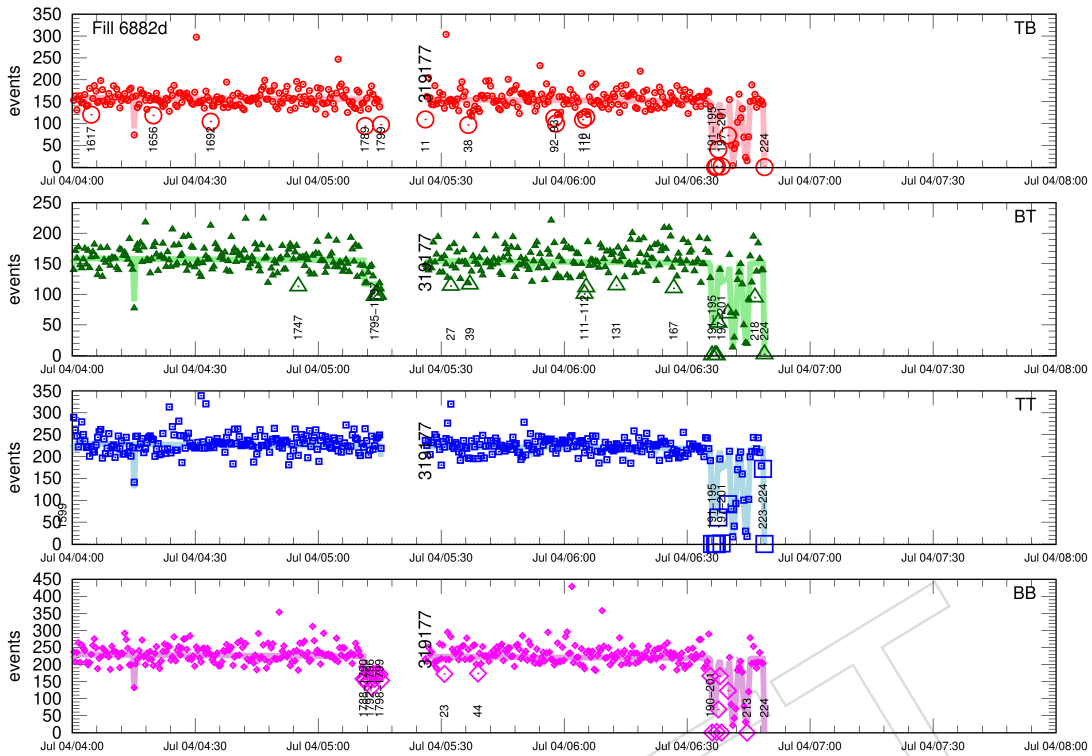

Figure 11: Observed (points) and expected (bands) number of $p(h^+h^-)p$ events in each lumisection for fill (or fill-range) 6882d, shown separately for the four RP trigger configurations (TB, BT, TT, and BB).

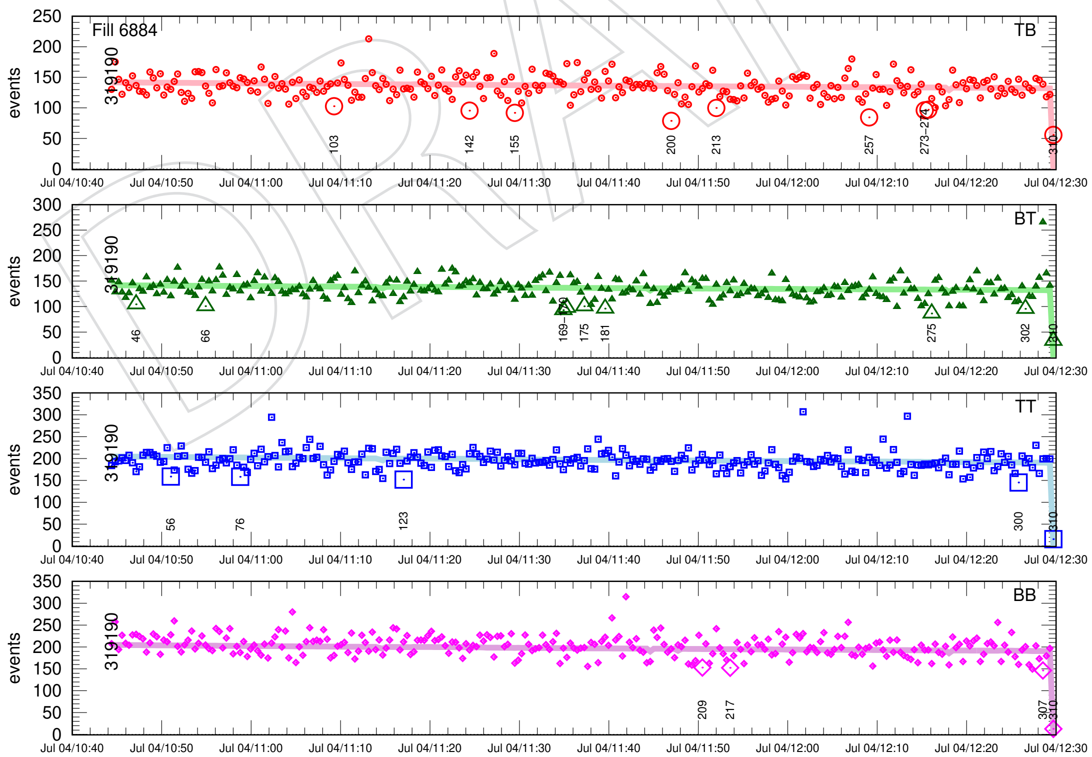

Figure 12: Observed (points) and expected (bands) number of $p(h^+h^-)p$ events in each lumisection for fill (or fill-range) 6884, shown separately for the four RP trigger configurations (TB, BT, TT, and BB).

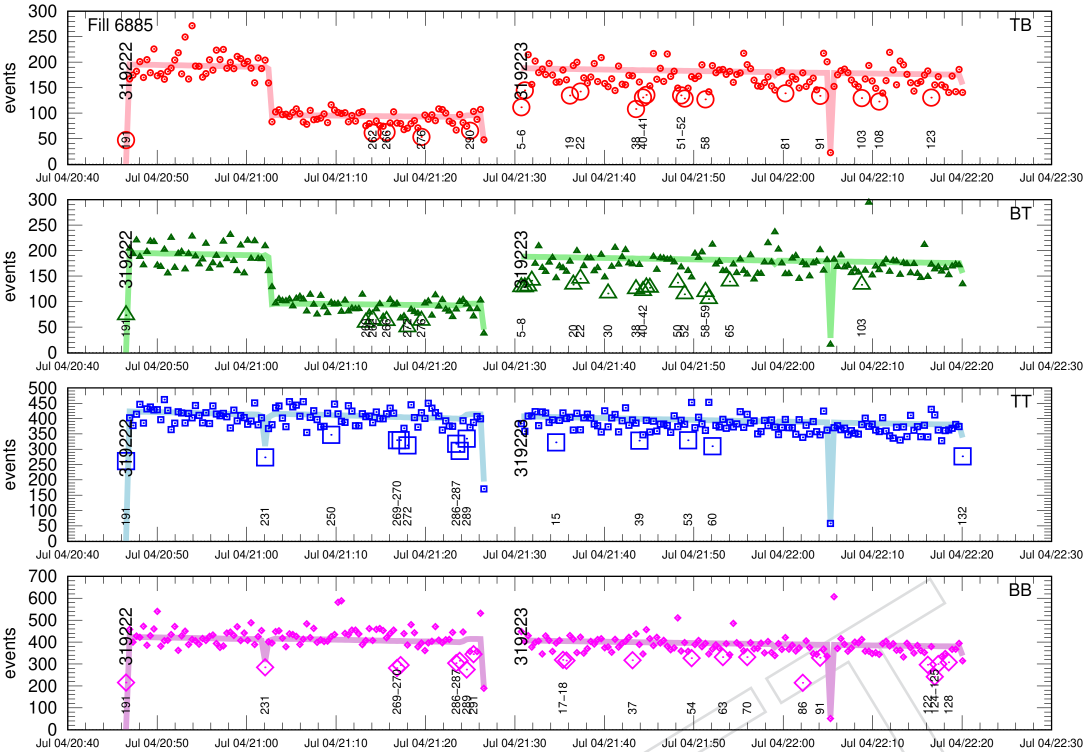

Figure 13: Observed (points) and expected (bands) number of $p(h^+h^-)p$ events in each lumisection for fill (or fill-range) 6885, shown separately for the four RP trigger configurations (TB, BT, TT, and BB).

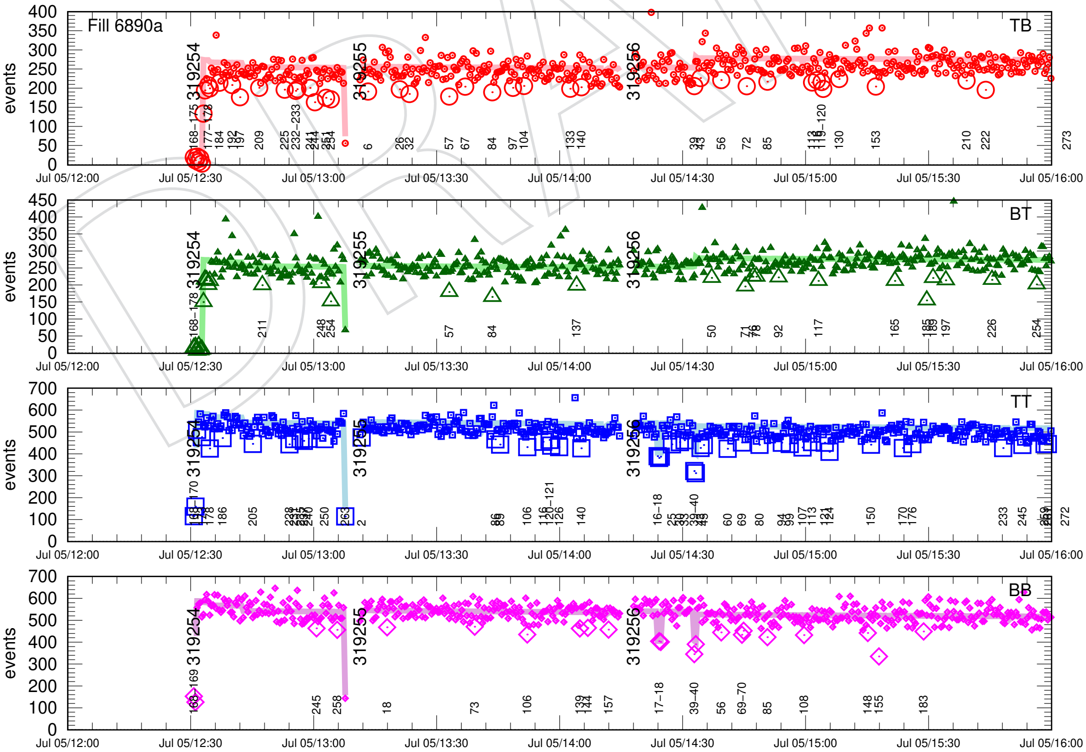

Figure 14: Observed (points) and expected (bands) number of $p(h^+h^-)p$ events in each lumisection for fill (or fill-range) 6890a, shown separately for the four RP trigger configurations (TB, BT, TT, and BB).

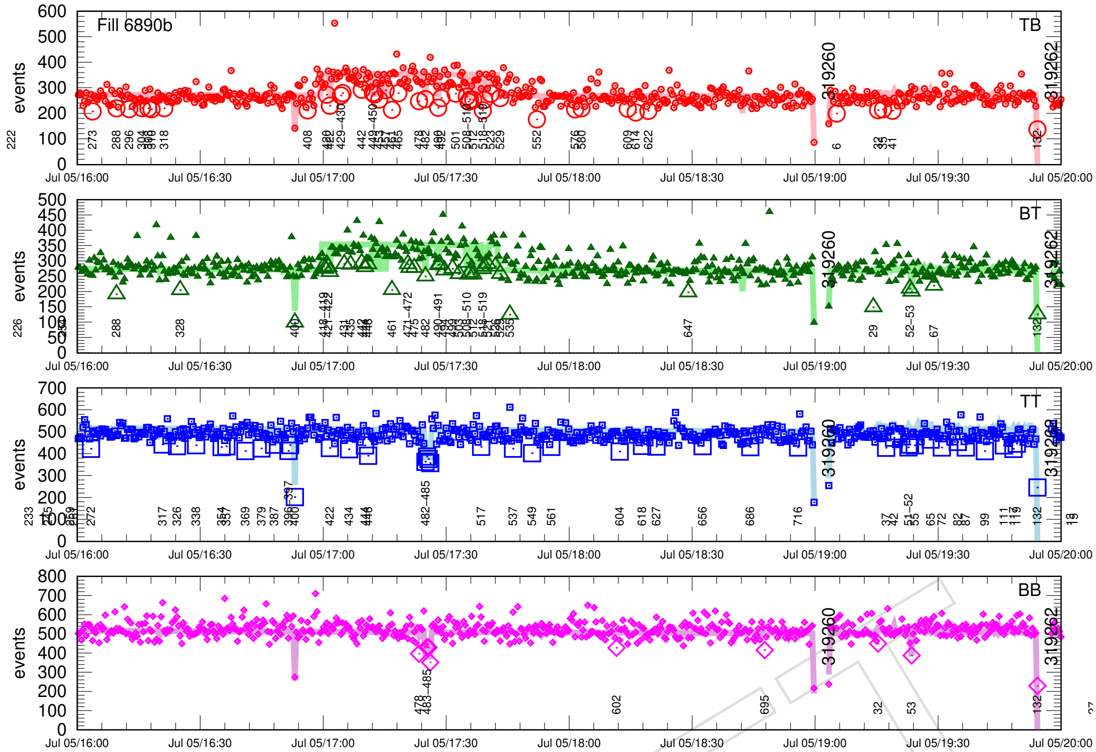

Figure 15: Observed (points) and expected (bands) number of $p(h^+h^-)p$ events in each lumisection for fill (or fill-range) 6890b, shown separately for the four RP trigger configurations (TB, BT, TT, and BB).

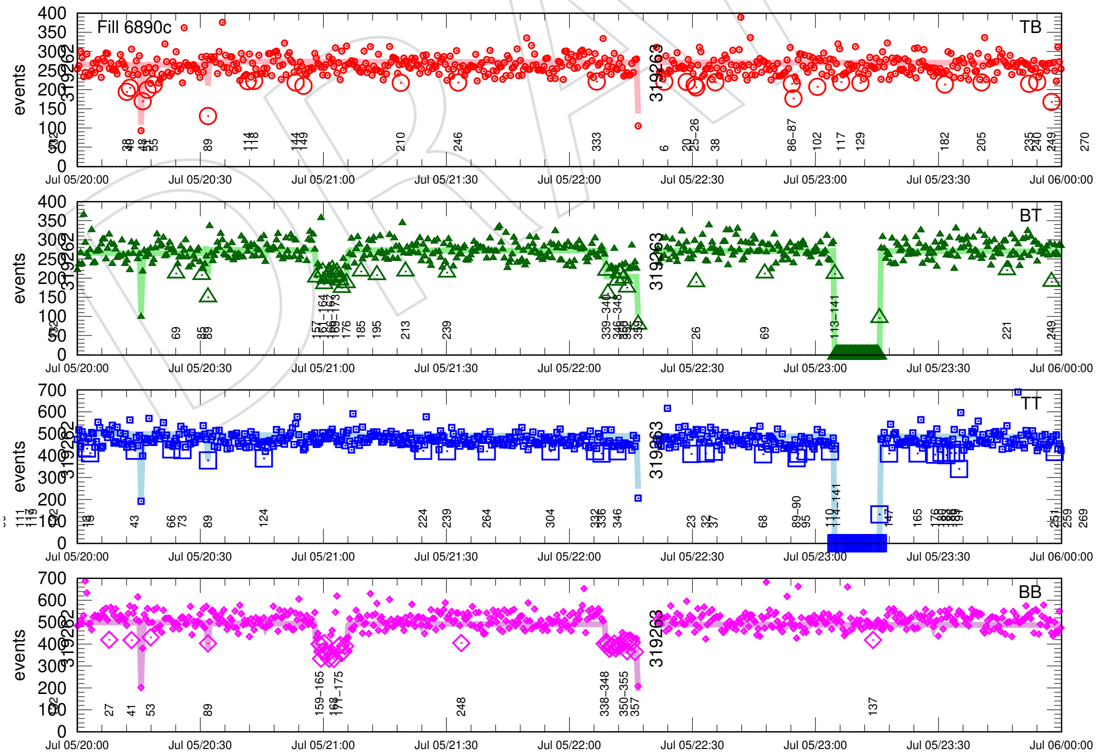

Figure 16: Observed (points) and expected (bands) number of $p(h^+h^-)p$ events in each lumisection for fill (or fill-range) 6890c, shown separately for the four RP trigger configurations (TB, BT, TT, and BB).

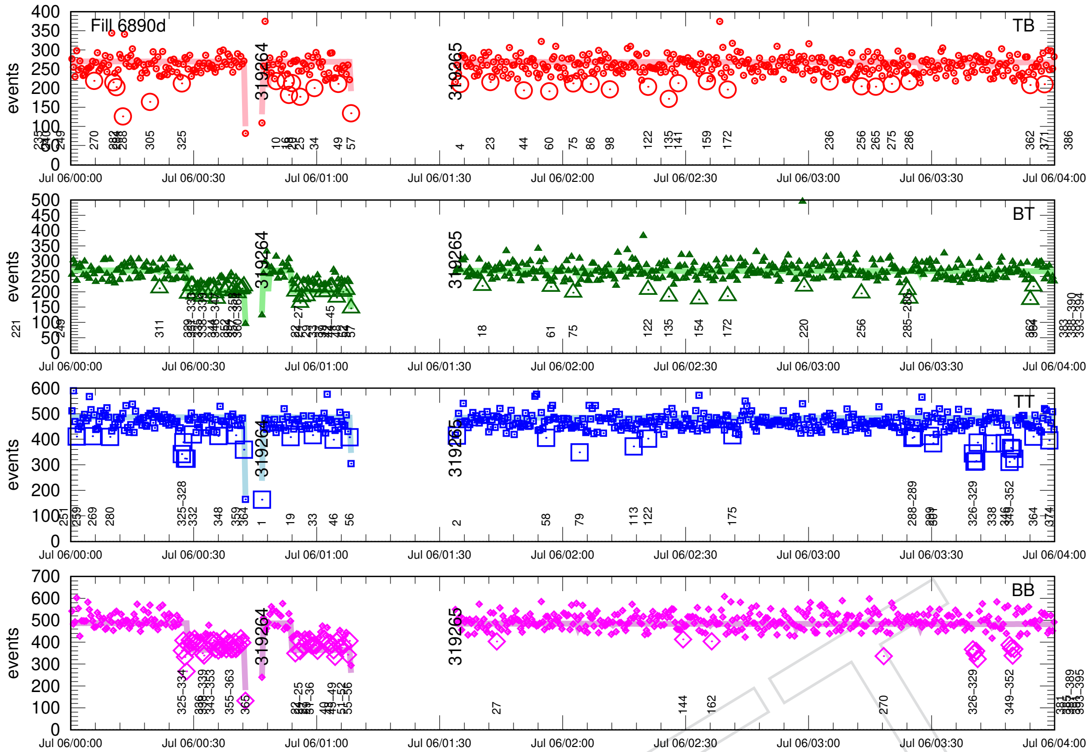

Figure 17: Observed (points) and expected (bands) number of $p(h^+h^-)p$ events in each lumisection for fill (or fill-range) 6890d, shown separately for the four RP trigger configurations (TB, BT, TT, and BB).

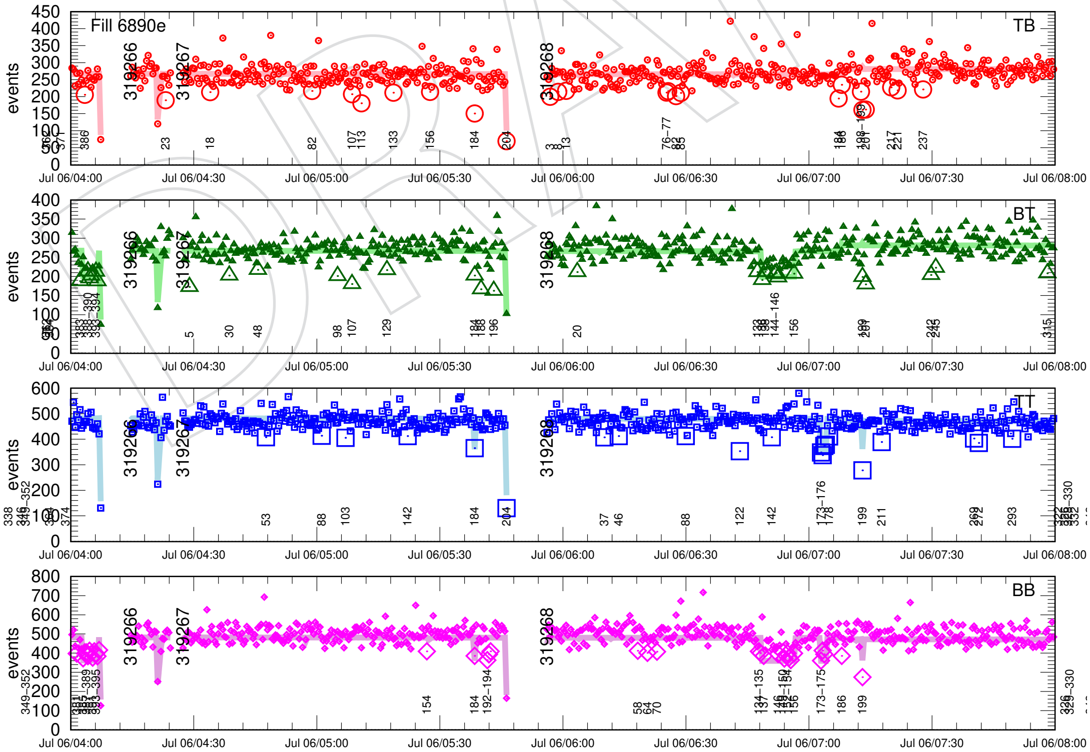

Figure 18: Observed (points) and expected (bands) number of $p(h^+h^-)p$ events in each lumisection for fill (or fill-range) 6890e, shown separately for the four RP trigger configurations (TB, BT, TT, and BB).

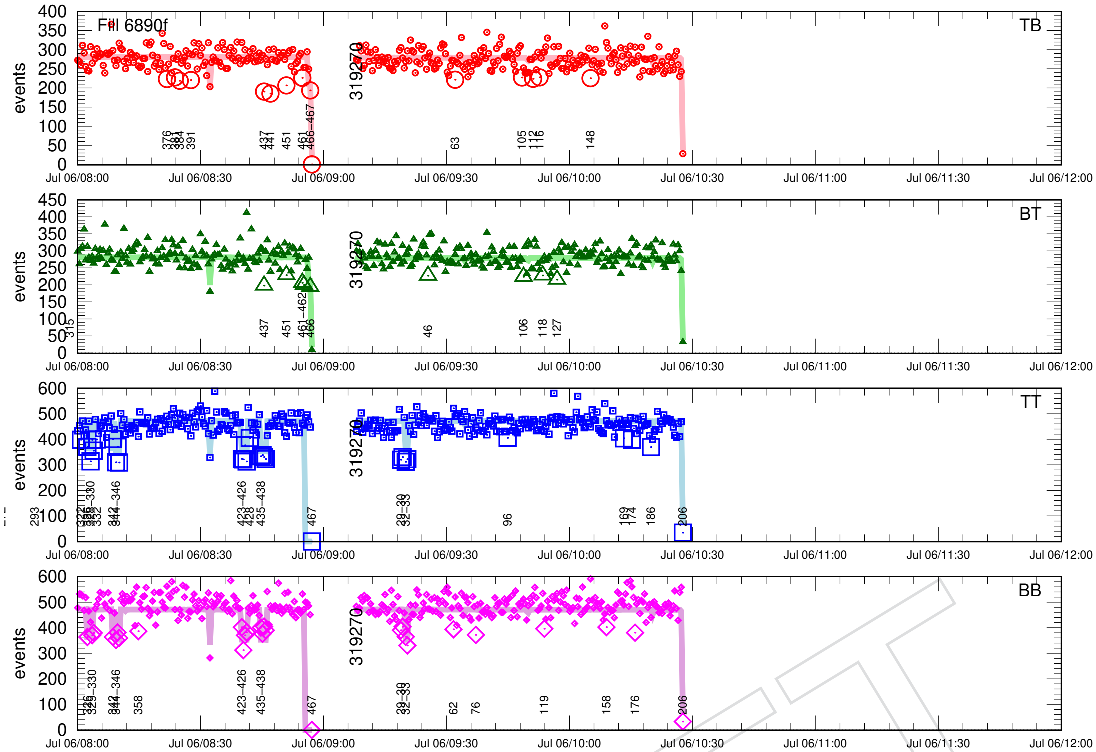

Figure 19: Observed (points) and expected (bands) number of $p(h^+h^-)p$ events in each lumisection for fill (or fill-range) 6890f, shown separately for the four RP trigger configurations (TB, BT, TT, and BB).

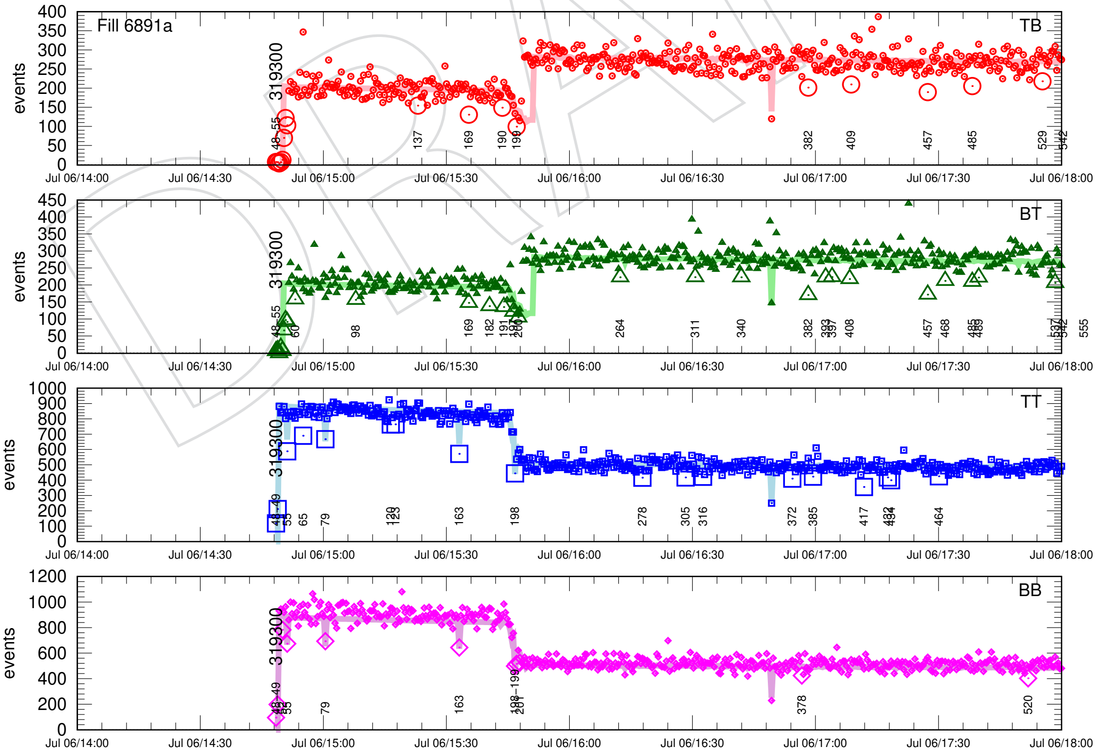

Figure 20: Observed (points) and expected (bands) number of $p(h^+h^-)p$ events in each lumisection for fill (or fill-range) 6891a, shown separately for the four RP trigger configurations (TB, BT, TT, and BB).

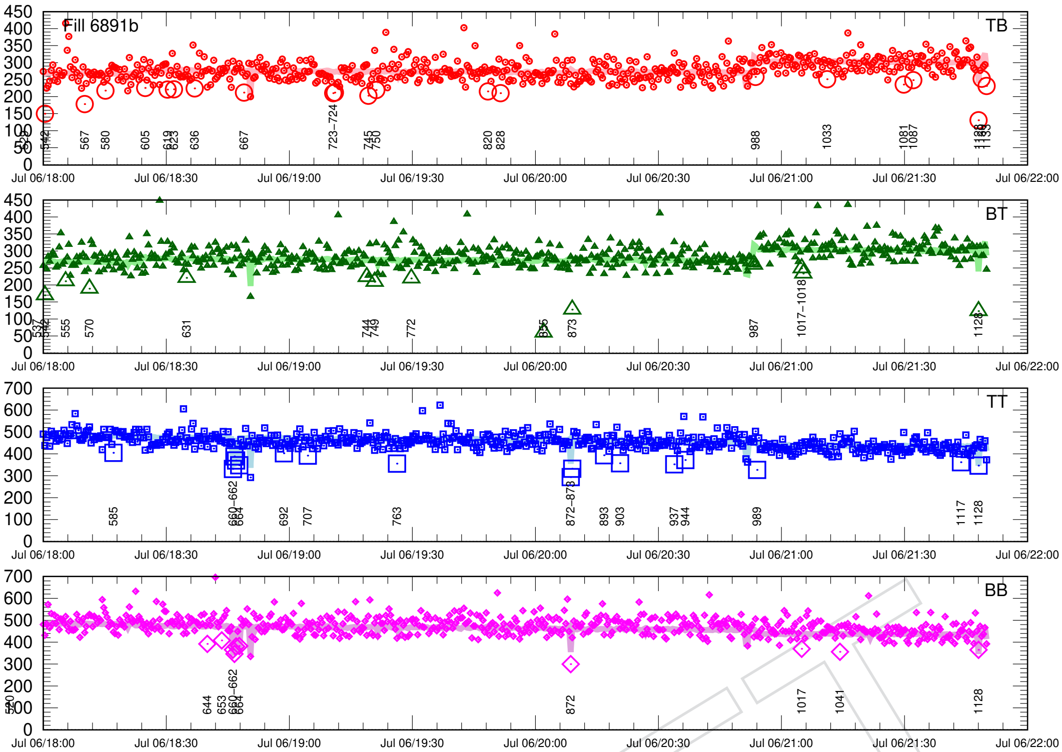

Figure 21: Observed (points) and expected (bands) number of $p(h^+h^-)p$ events in each lumisection for fill (or fill-range) 6891b, shown separately for the four RP trigger configurations (TB, BT, TT, and BB).

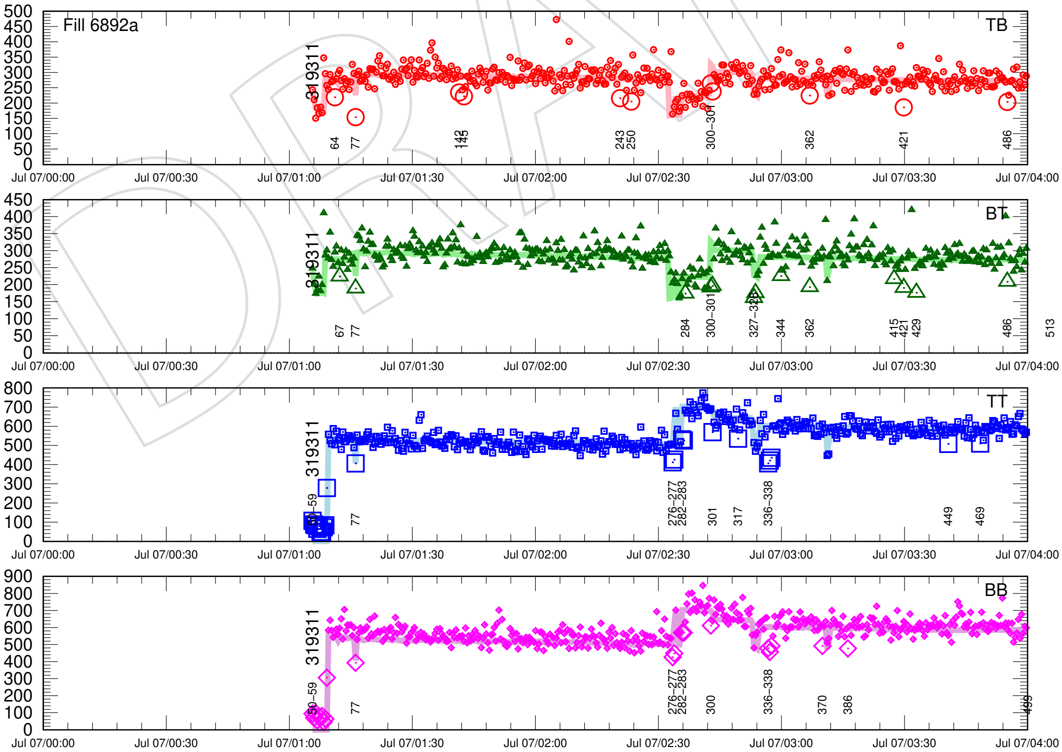

Figure 22: Observed (points) and expected (bands) number of $p(h^+h^-)p$ events in each lumisection for fill (or fill-range) 6892a, shown separately for the four RP trigger configurations (TB, BT, TT, and BB).

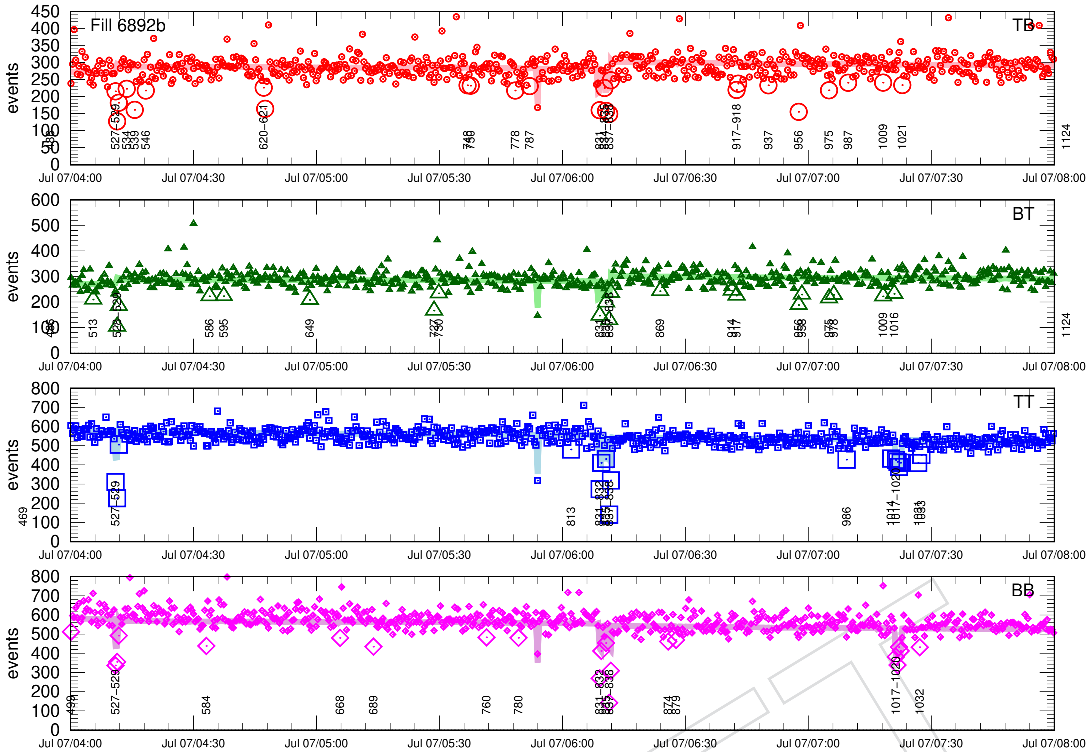

Figure 23: Observed (points) and expected (bands) number of $p(h^+h^-)p$ events in each lumisection for fill (or fill-range) 6892b, shown separately for the four RP trigger configurations (TB, BT, TT, and BB).

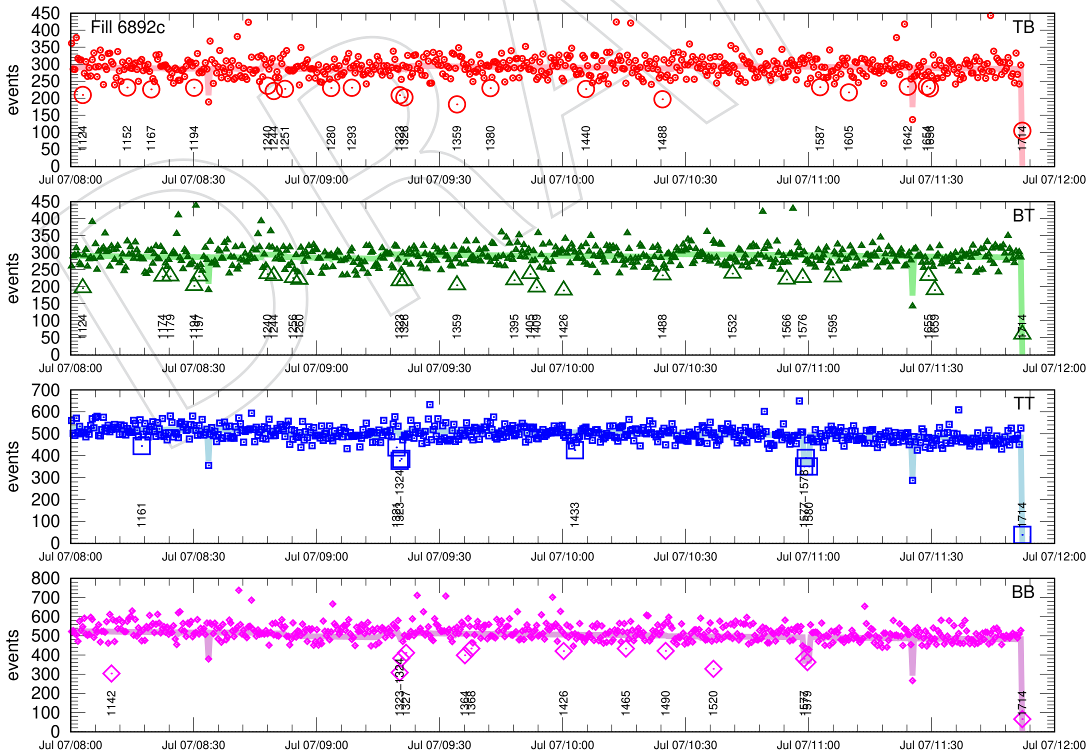

Figure 24: Observed (points) and expected (bands) number of $p(h^+h^-)p$ events in each lumisection for fill (or fill-range) 6892c, shown separately for the four RP trigger configurations (TB, BT, TT, and BB).

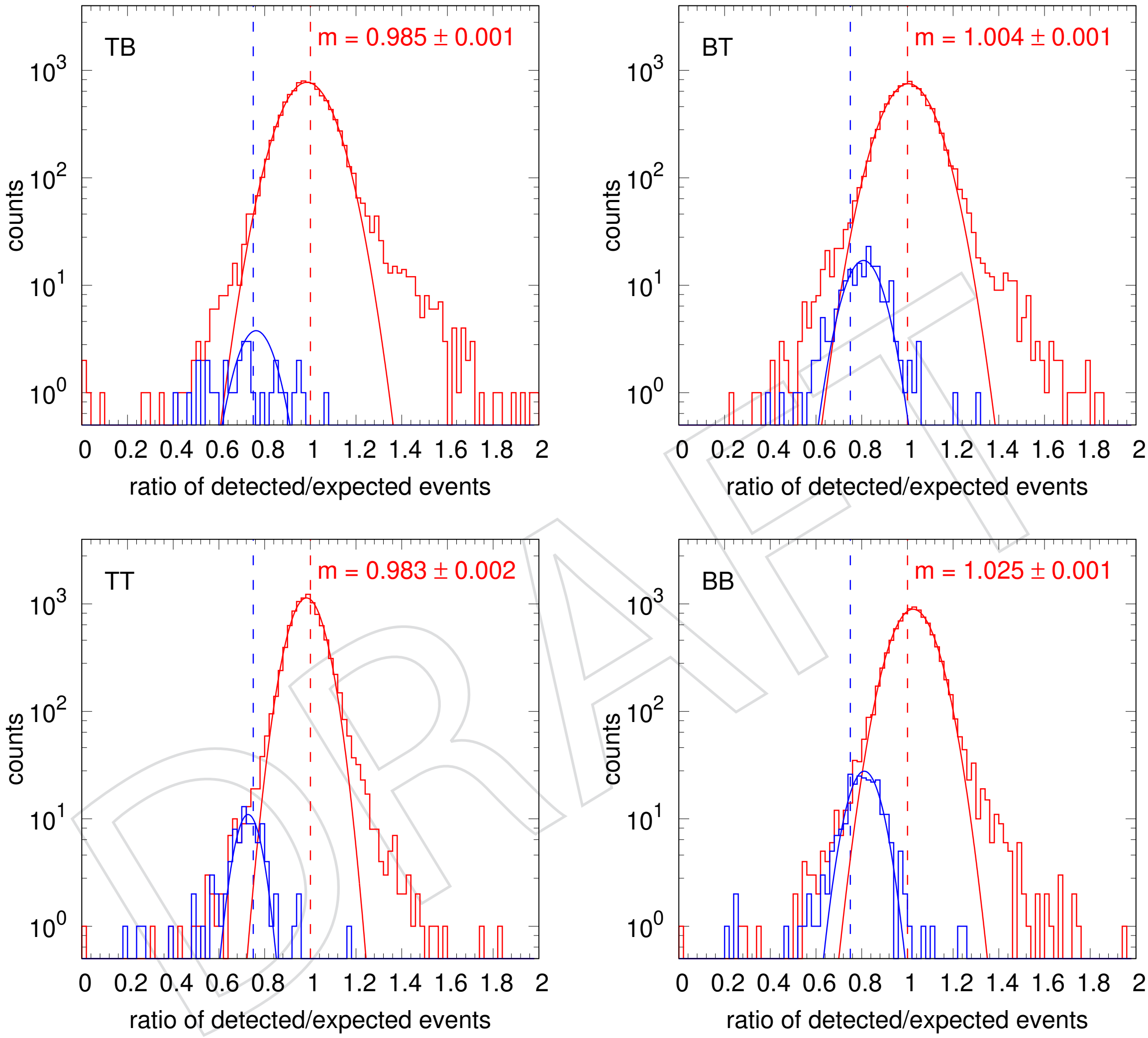

Figure 25: The distribution of the ratio of detected over expected two-track central exclusive events in a lumisection, plotted for "normal" (red) and "low" lumisections, shown separately for all four configurations (TB, BT, TT, and TB). In addition to the measured values (histograms), results of Gaussian fits are plotted (curves) and their mean values are indicated.

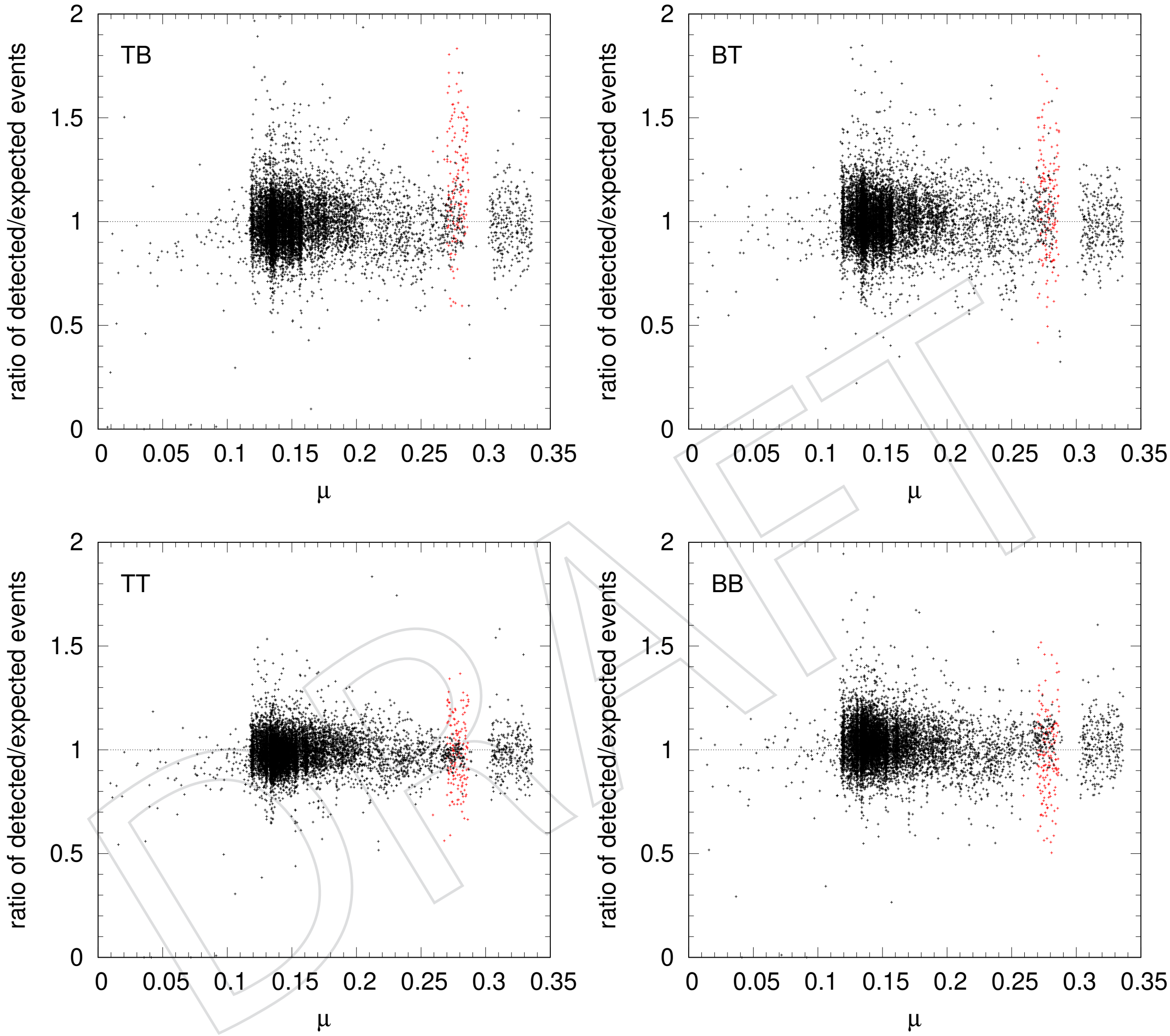

Figure 26: The ratio of detected over expected two-track central exclusive events in a lumisection as a function of the average number of simultaneous visible (inelastic) pp collisions μ, shown separately for all four configurations (TB, BT, TT, and TB). Lumisections of fill 6877 are plotted with red, while others are in black.

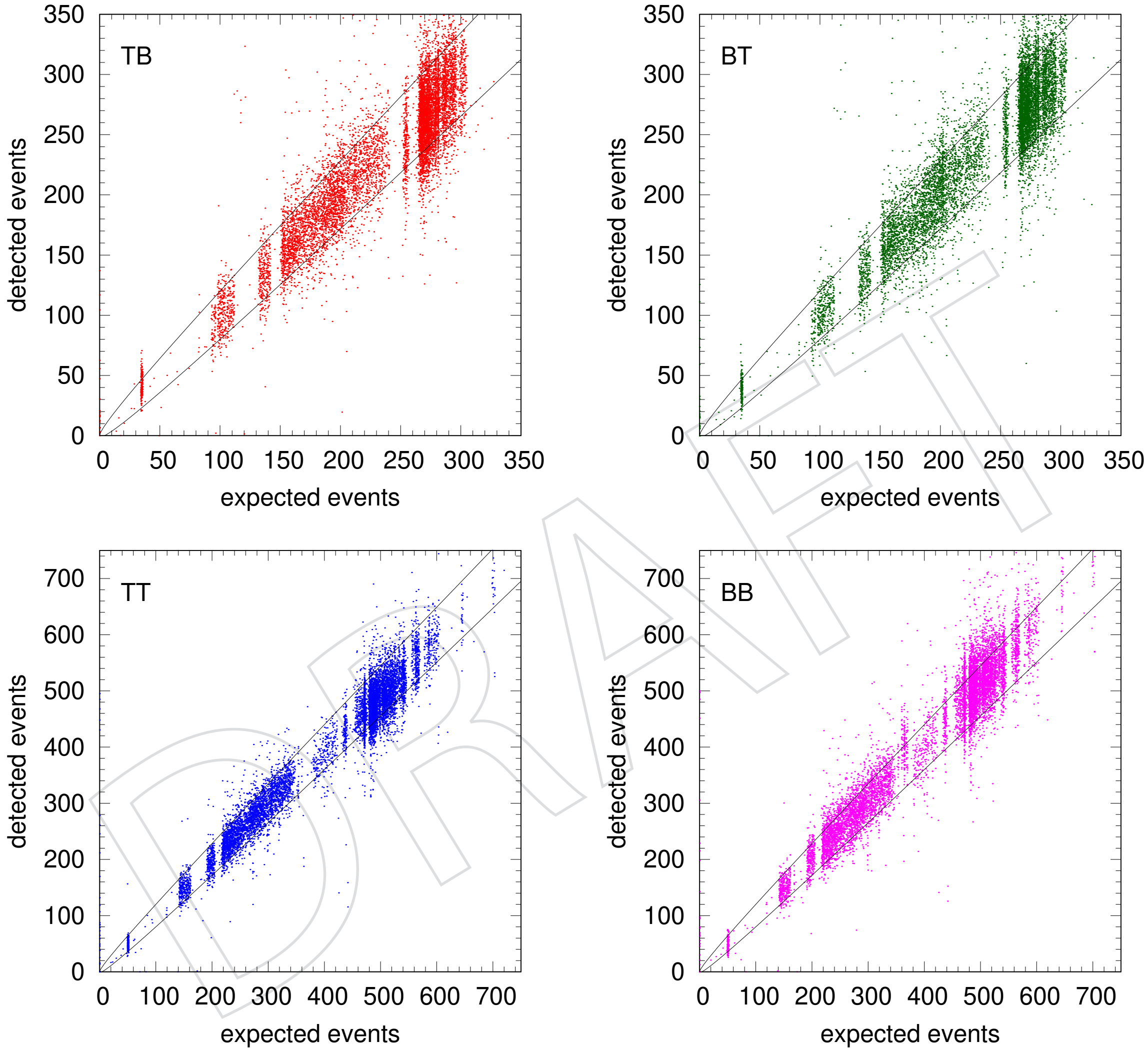

Figure 27: The number of detected two-track central exclusive events as a function of expected events in a lumisection, shown separately for all four configurations (TB, BT, TT, and TB).

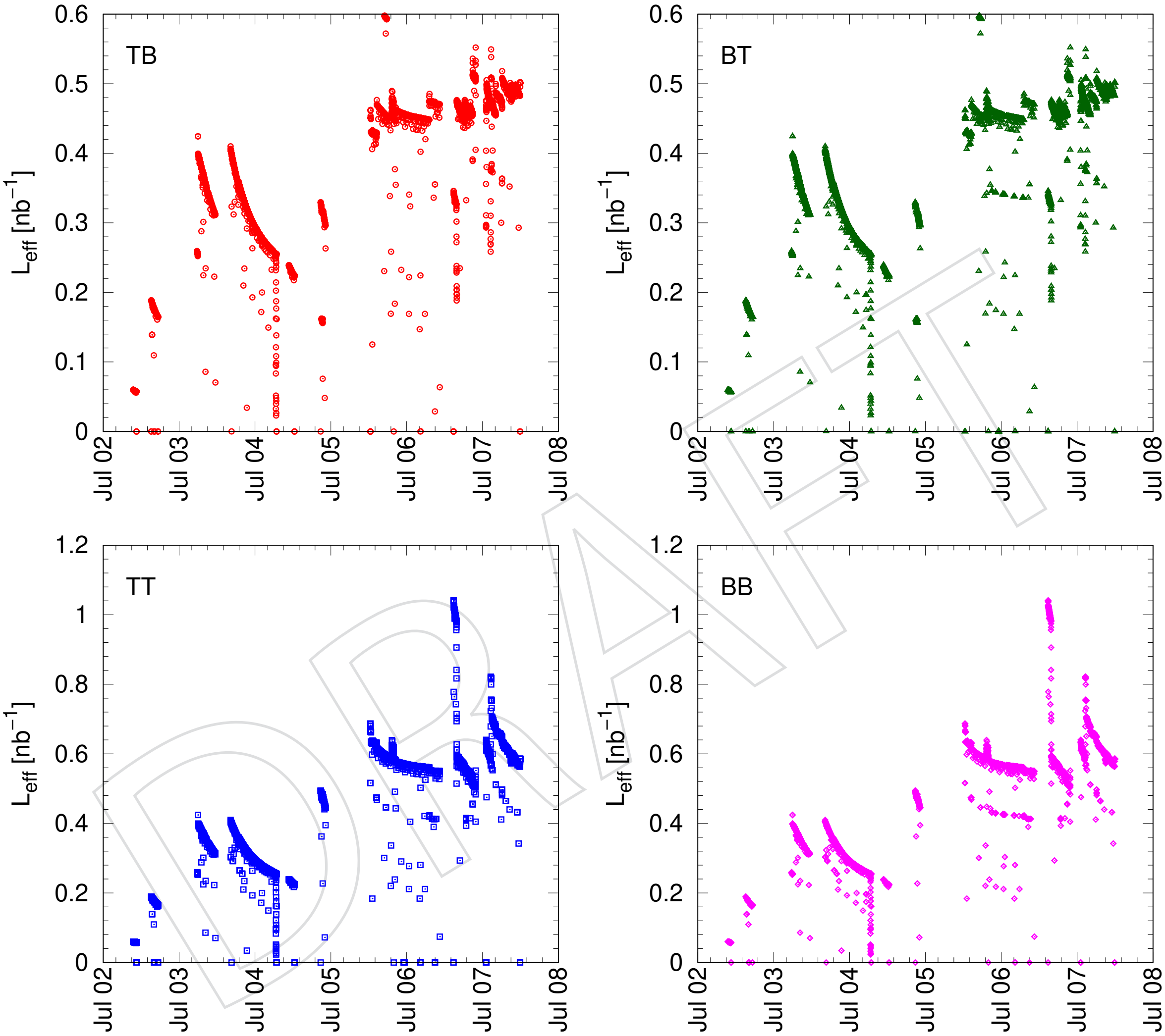

Figure 28: The effective integrated luminosity as function of date/time, shown separately for all four configurations (TB, BT, TT, and TB). Each point corresponds to a lumisection.

3 Scattered protons in the roman pots

Details of a study on the proton reconstruction using the roman pots can be found in CMS AN-21-162. It deals with the basics of strip clusters, details of proton tracklet and track reconstruction, problems of reduced strip-level efficiencies, and a precise detector alignment.

3.1 Proton-pair trigger acceptance (elastic veto)

The data taking during the special $\beta^* = 90\,\mathrm{m}$ run was dominated by elastic collision events, saturating the bandwidth of data acquisition. This way, elastic events needed to be vetoed using information from the roman pots.

Triggering is based on “trigger strips”, each of them consisting of 32 silicon strips. Since there are 512 strips on a u/v oriented plane, we have 16 trigger strips for each orientation. The trigger bit is set if at least three planes have the same trigger strip fired (performed locally by coincidence chip).

For the elastic veto, a region of interest is defined as the intersection of 6 u-oriented and 6 v-oriented consecutive trigger strips (Fig. 29). Within that region a “trigger map” (or t-map), a subset containing 15 square zones, is selected. The location of the region of interest is adjustable through software, through small integer shifts (δ_x). The t-maps coming from paired roman pots of diagonal configuration are compared. If there is at least one common trigger bit on both t-maps, a veto is generated. In total there are four diagonal veto bits: 1nT-2nB, 1nB-2nT, 1fT-2fB, and 1fB-2fT, but during data taking only the pairs for far pots were used. The two t-maps can be shifted by small integers granting a fine vertical tuning (δ_y).

In practice, an elastic veto is issued if

- in both arms

$$|t_u - t_v - \delta_x| \leq 1, \tag{25}$$

  where the horizontal shift δ_x can be topology dependent; it appears to be $\delta_x = -1$ for TB, and $\delta_x = 1$ for BT;

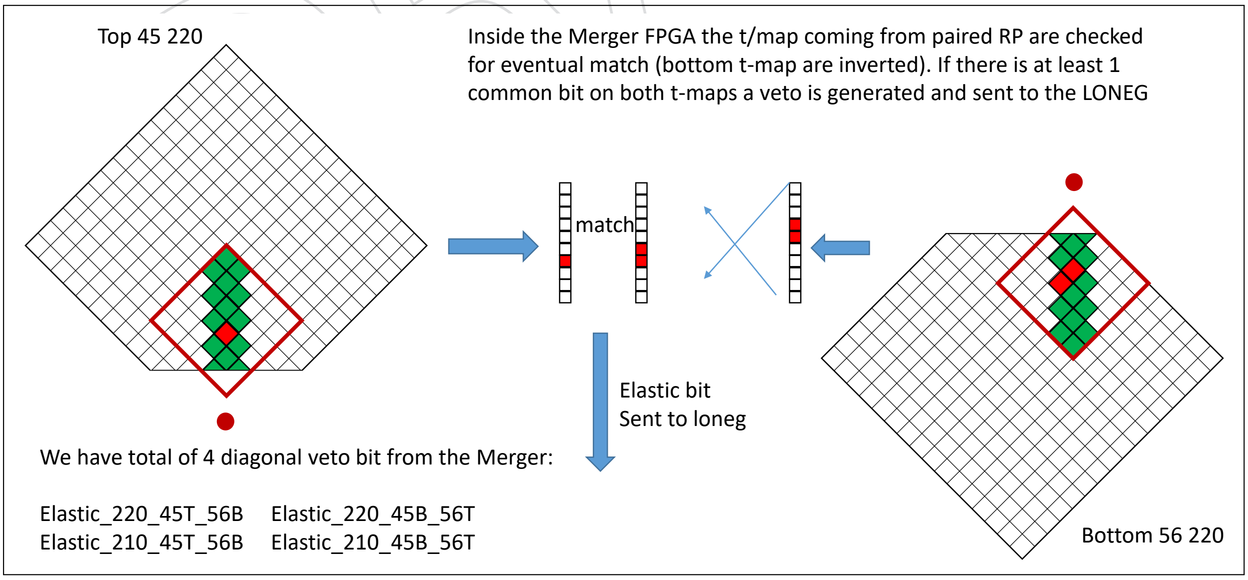

Figure 29: A page from the presentation of Eduardo Bossini (trigger report 10/09/2018).

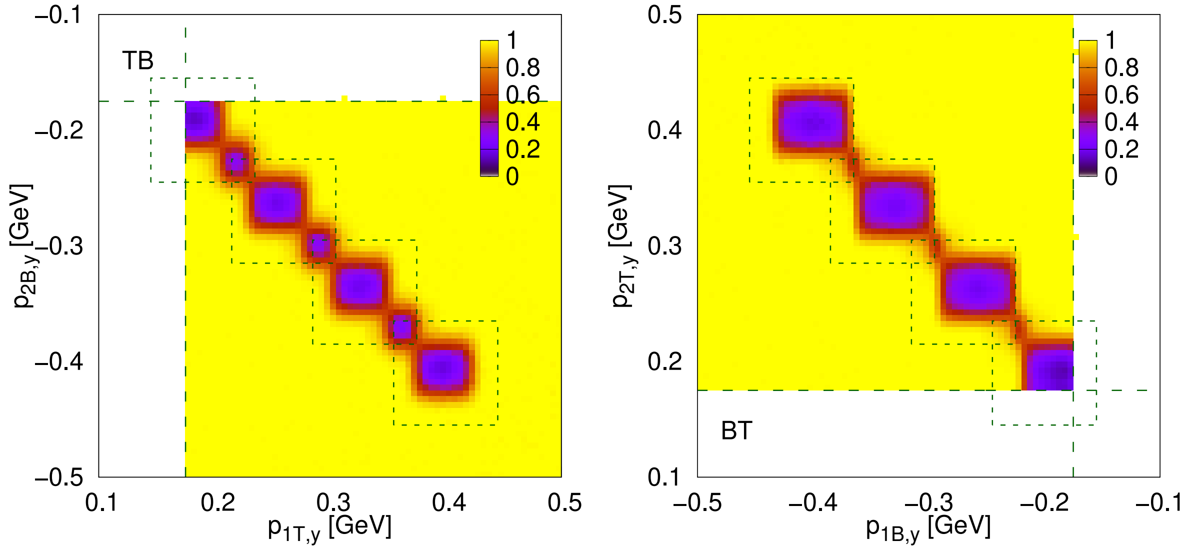

Figure 30: Suppression efficiency of elastic-like events as functions of p_y in arms 1 and 2, shown here for the TB (left) and the BT (right) trigger configuration. Limits of single-proton acceptance are shown with long dashed line. Boxes with short dashed lines indicate regions not taken into account in the comparison of the expected and detected number of events. (Sec. 2.2).

- and for the $y = 25 - (t_u + t_v)$ position of the trigger in the two arms

$$y_1 \leq 7, \qquad y_2 \leq 7, \tag{26}$$

$$y_1 - y_2 - \delta_y = 0, \tag{27}$$

  where δ_y is the vertical shift; it appears to be $\delta_y = 0$ for both diagonal trigger configurations.

For the emulation of the elastic veto we use proton tracklets and tracks from events with parallel trigger configuration (TT and BB). Track from a TT event is combined with another track from a BB event, the combined TB and BT event is checked for the above detailed veto conditions. In the end an efficiency table is constructed as functions of $(p_{1,y}, p_{2,y})$, to be used later for the calculation of roman pots related corrections (Sec. 3.2). The suppression efficiency of elastic-like events as functions of p_y in arms 1 and 2 is shown in Fig. 30 for the diagonal trigger configurations. It compares well with the actual measurement of $(p_{1,y}, p_{2,y})$ correlations for diagonal trigger configurations (TB and BT), as shown in Fig. 31.

3.2 Calculation of coverage and trigger acceptance

The combined acceptance and efficiency of roman pots with regard to triggering and detection are calculated in bins of $(p_{1,\mathrm{T}}, p_{2,\mathrm{T}}, \phi)$ using 400 million simulated two-proton events. These events are generated with

- uniform and independent $p_{1,\mathrm{T}}$ and $p_{2,\mathrm{T}}$ distributions in the range $[0, 1.0\,\mathrm{GeV}]$ with a 50 MeV binwidth;
- uniform ϕ distribution in the range $[0, \pi]$;
- using the above deduced single-proton (Eq. (16)) and proton-pair trigger acceptances.

Calculated detection efficiencies for the pair of scattered protons, as a function of their transverse momenta $(p_{1,\mathrm{T}}, p_{2,\mathrm{T}})$, in 18 bins of the proton-proton angle ϕ in the transverse plane are shown in Figs. 32, 33, and 34. While the four plots in each row show the efficiencies for each

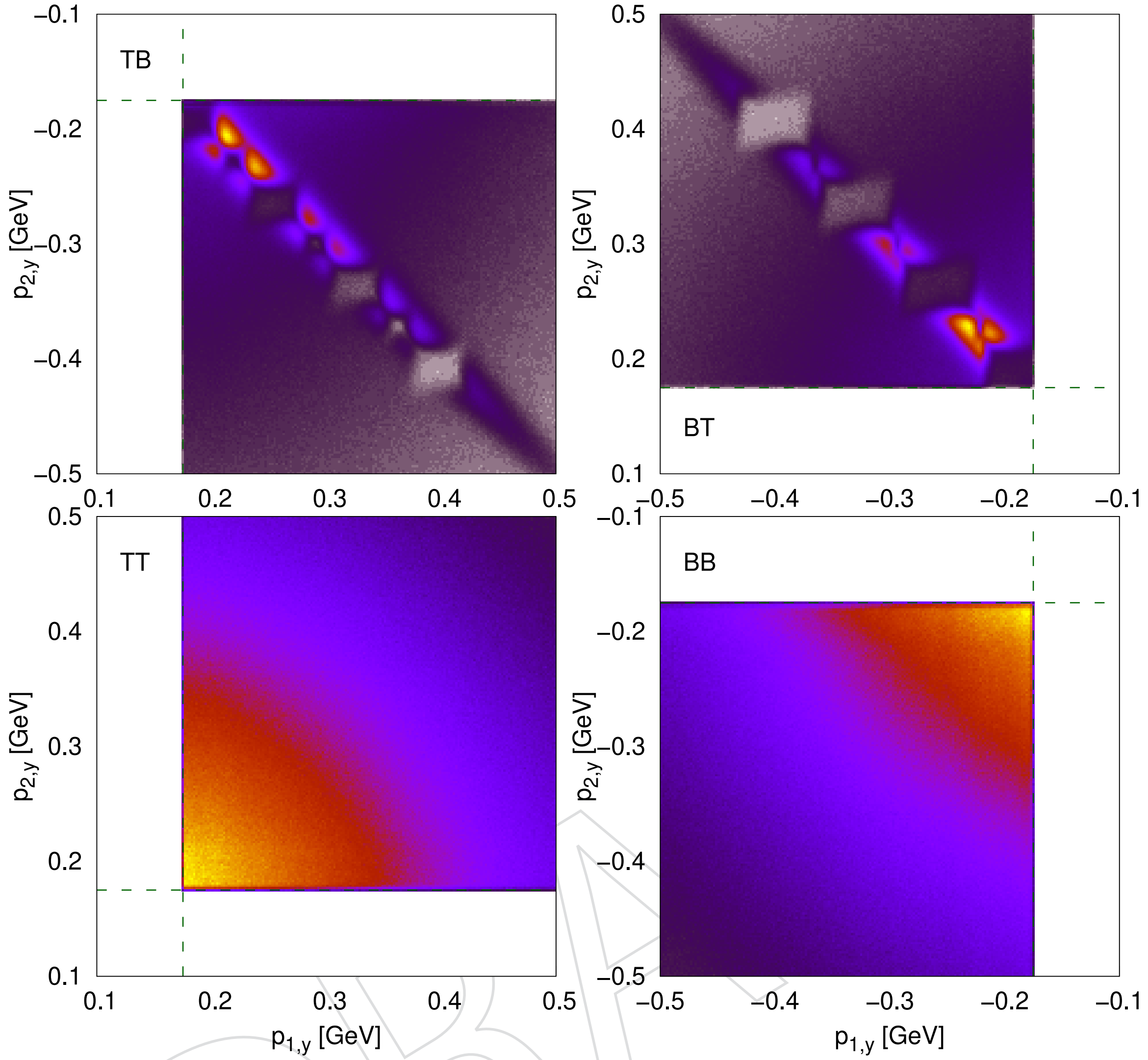

Figure 31: Correlation of detected proton momenta $(p_{1,y}, p_{2,y})$ in arm 1 vs arm 2. Limits of single-proton acceptance are shown with long dashed line.

trigger configuration (TB, BT, TT, and BB), the rightmost plot displays the coverage of the measurement. The not covered area (blue) is shown along with the ones covered by not more than one configuration (red), and those covered by all configurations (yellow). The lines corresponding to 0.2 GeV are drawn in the plots. In general we have a nice coverage, large regions are populated by all four configurations. Some corners of phase space are not covered, they are

- at very high $p_{1,\mathrm{T}}$ and very low $p_{2,\mathrm{T}}$ (and vice versa), if $\phi < 20^\circ$ or $\phi > 160^\circ$;
- at very low $p_{1,\mathrm{T}}$ and $p_{2,\mathrm{T}}$, if $70^\circ < \phi < 110^\circ$;
- and at very high $p_{1,\mathrm{T}}$ and $p_{2,\mathrm{T}}$, if $80^\circ < \phi < 100^\circ$.

Regions with roman pot-related coverage below 2% are not used in the analysis.

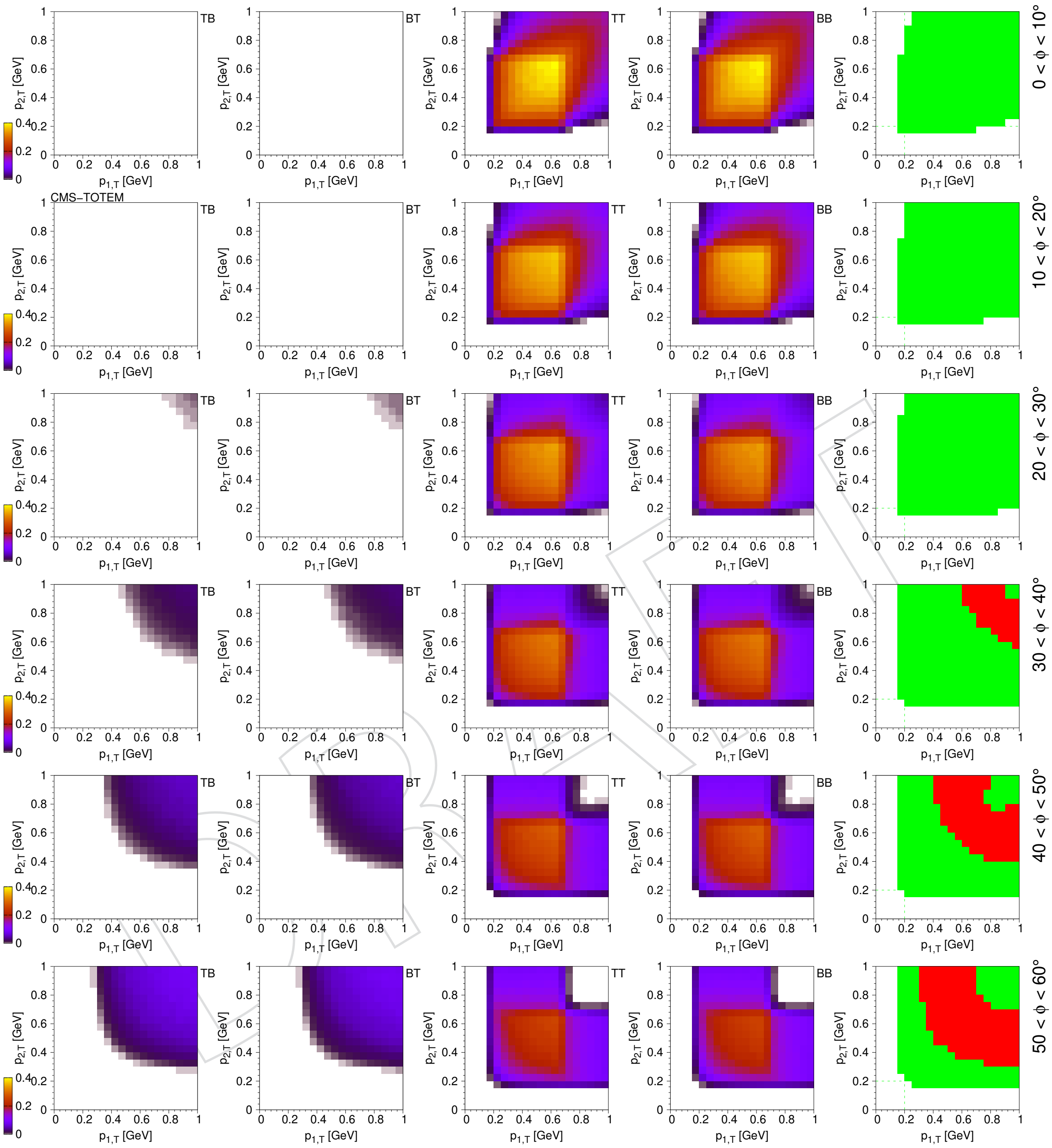

Figure 32: Calculated coverage and trigger acceptance for the pair of scattered protons as a function of their transverse momenta $(p_{1,T}, p_{2,T})$, in bins of the proton-proton angle ϕ in the transverse plane (indicated on the right side of each row). While the four plots in each row show the efficiencies for each trigger configuration (TB, BT, TT, and BB), the rightmost plot displays the coverage of the measurement with colour codes (blue: not covered; green: covered by at least one configuration; red: covered by all configurations). The lines corresponding to 0.2 GeV are drawn in the plots.

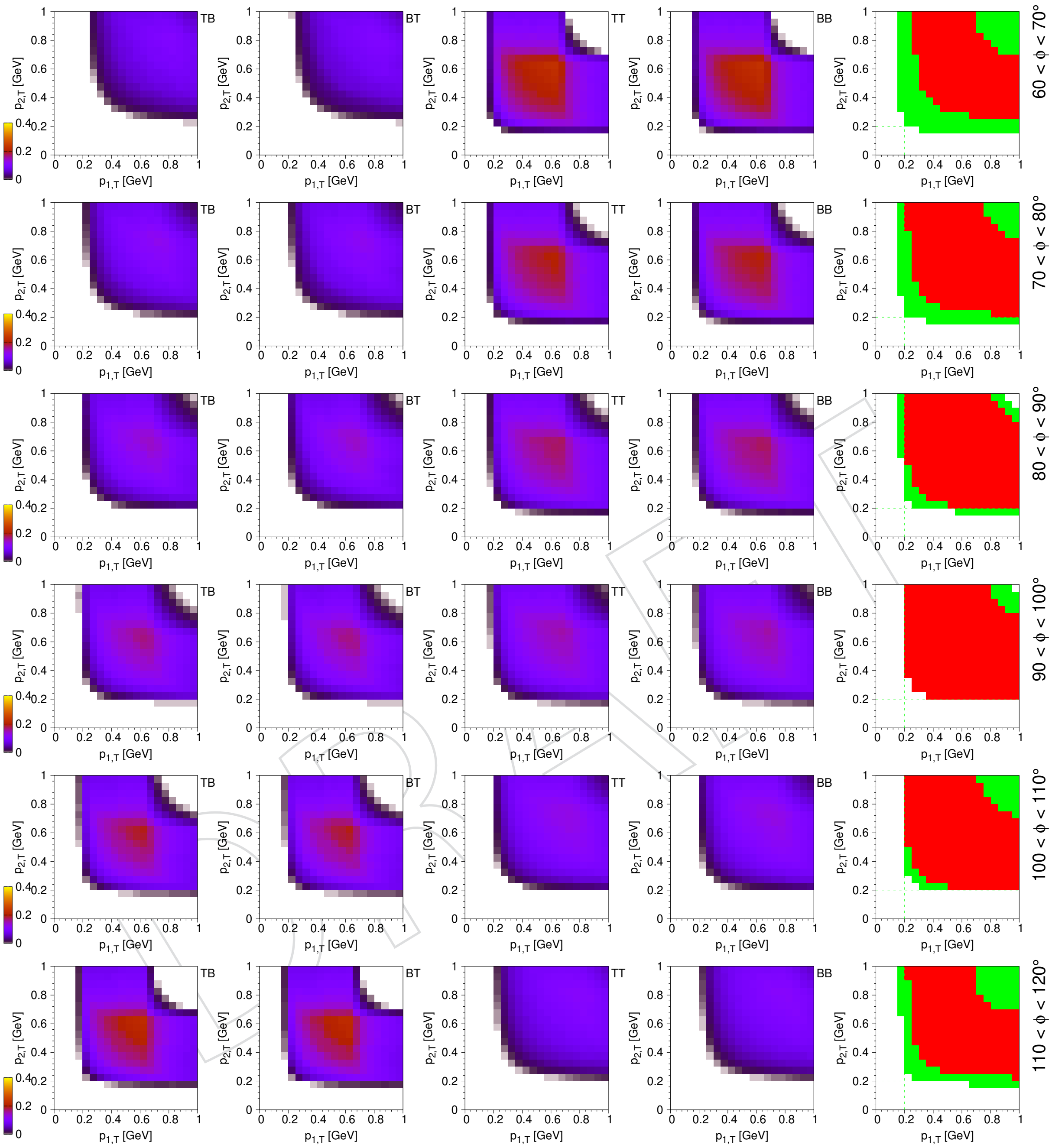

Figure 33: Calculated coverage and trigger acceptance for the pair of scattered protons as a function of their transverse momenta $(p_{1,T}, p_{2,T})$, in bins of the proton-proton angle ϕ in the transverse plane (indicated on the right side of each row). While the four plots in each row show the efficiencies for each trigger configuration (TB, BT, TT, and BB), the rightmost plot displays the coverage of the measurement with colour codes (blue: not covered; green: covered by at least one configuration; red: covered by all configurations). The lines corresponding to 0.2 GeV are drawn in the plots.

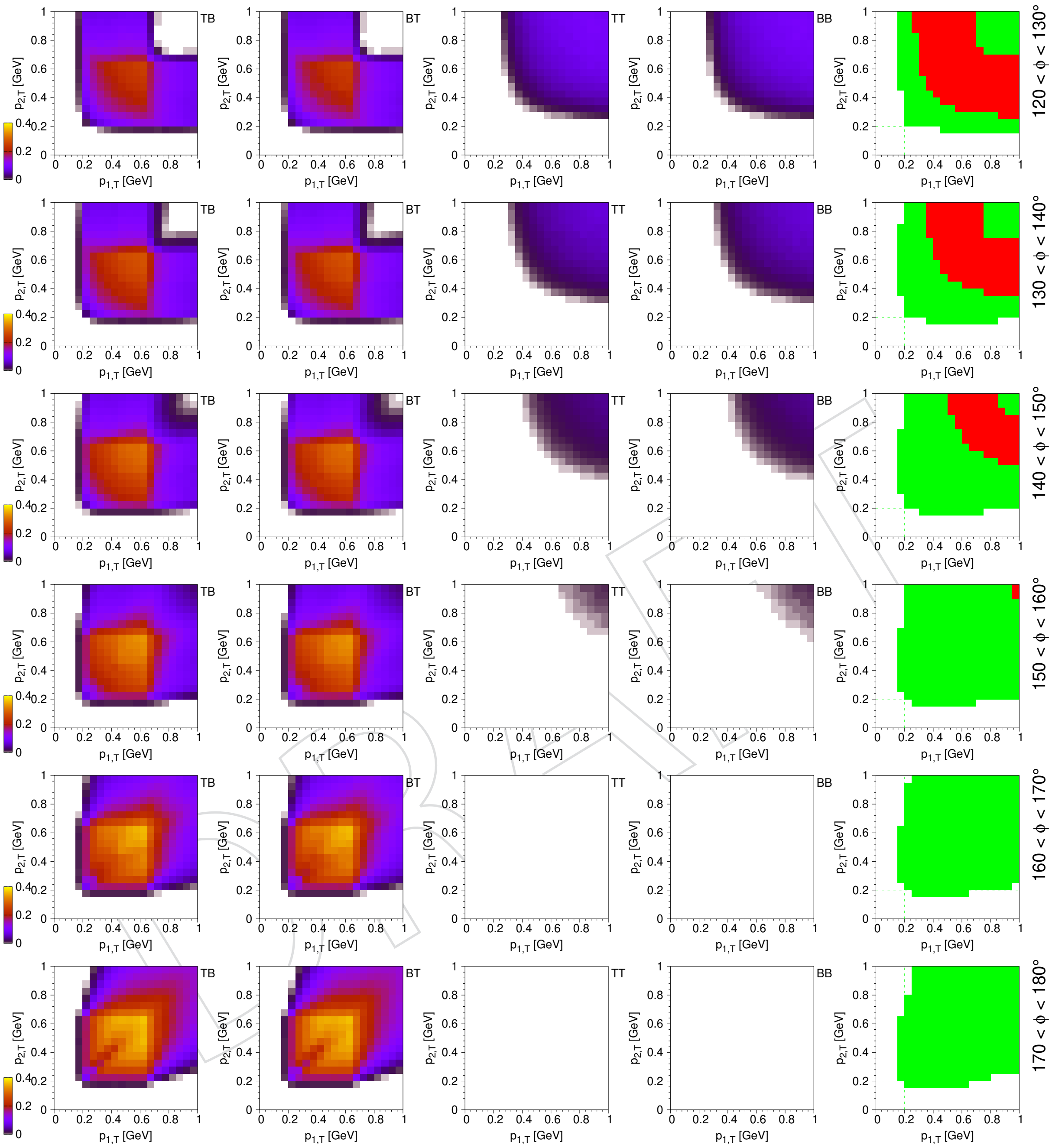

Figure 34: Calculated coverage and trigger acceptance for the pair of scattered protons as a function of their transverse momenta $(p_{1,T}, p_{2,T})$, in bins of the proton-proton angle ϕ in the transverse plane (indicated on the right side of each row). While the four plots in each row show the efficiencies for each trigger configuration (TB, BT, TT, and BB), the rightmost plot displays the coverage of the measurement with colour codes (blue: not covered; green: covered by at least one configuration; red: covered by all configurations). The lines corresponding to 0.2 GeV are drawn in the plots.

4 Energy deposits and estimation of energy loss rate

The identification of charged particles is often based on the special relationship between energy loss rate and total momentum. It is not always obvious how to choose the proper energy loss measure. If the detector has thick layers (with track path-lengths l_i) and many sensitive volumes, we can sample the energy loss distribution of a particle (with energy deposits y_i) many times and with good resolution. Hence for a track, the plain arithmetic average of the measured y_i/l_i values already gives a good estimate of the average energy loss rate ("dE/dx"), according to the central limit theorem. This average (restricted) energy loss gives the familiar Bethe-Bloch curves [1].

If the layers are thin, the individual energy deposits will not be Gaussian-distributed but will show a long tail towards higher values. Even then, the y_i/l_i values can be used but with more involved averaging methods such as harmonic, or in general, power mean[3]. The power mean estimator with power -2 was used in some CMS publications [26]. Another possibility is called truncated mean where measured y_i/l_i values are first sorted into increasing order ($y_i/l_i \leq y_{i+1}/l_{i+1}$) and the upper half of the values, or some fix percentage of the lowest and highest ones, is suppressed and only the rest of the values is averaged. It is even possible to optimise the weights for best particle-type separation and give universal prescriptions for semiconductor and gaseous detectors, independent of particle momentum.

Ideally the estimates of energy loss rate should not depend on path lengths and detector details. Unfortunately with power means or weighted means this is not the case. Although some of the dependencies could be compensated, in case of tracks with varying path length distribution only a method based on the proper knowledge of the underlying physical processes would perform appropriately. If the applied model is precise and robust, it can used for the estimation of energy loss rate values, with help of maximum likelihood estimation (MLE). In addition, such a framework is of great use for detector gain calibration (created charge wrt deposited energy or measured ADC value) of the detector elements.

The energy loss of charged particles in silicon can be approximated by a simple analytical parametrisation [27]. With help of measured charge deposits in individual channels of hit clusters their position and energy is estimated. Deposits below threshold and saturated values are treated properly, resulting in a wider dynamic range, giving improvements on both hit position and energy residuals. The model is successfully applied to track energy loss rate estimation and to detector gain calibration tasks. Therefore in this analysis we will estimate the most probable energy loss rate ε at a given reference path length of $l_0 = 450\,\mu$m, calculated with help of hits created along the particle trajectory, that is, energy deposits in sensitive elements of the pixel and strip silicon detectors. More details can be found in [28].

Since the estimation of ε does not involve the measured momentum of the particle, neither possible momentum bias nor the momentum resolution is important. As a charged particle traverses more and more sensitive silicon layers, support structures and cabling, it loses momentum (and of course energy). In the low momentum region less momentum means higher energy loss. Hence the later energy deposits are shifted towards higher values.[4] Still, this effect does not play a role because during fitting $\ln \varepsilon$ distributions the shape of the functions (templates) used are obtained from a specific simulation (regeneration of energy deposit) where the momentum loss for each hit is taken into account. In case of strips the observed signals

[3] In fact arithmetic and harmonic means are special cases of the power mean with powers 1 and -1, respectively.

[4] The momentum measurement could be also effected, but that is largely compensated by the fact that the momentum is estimated at the creation point by the Kalman filter, taking into account the momentum losses occurring at later stages.

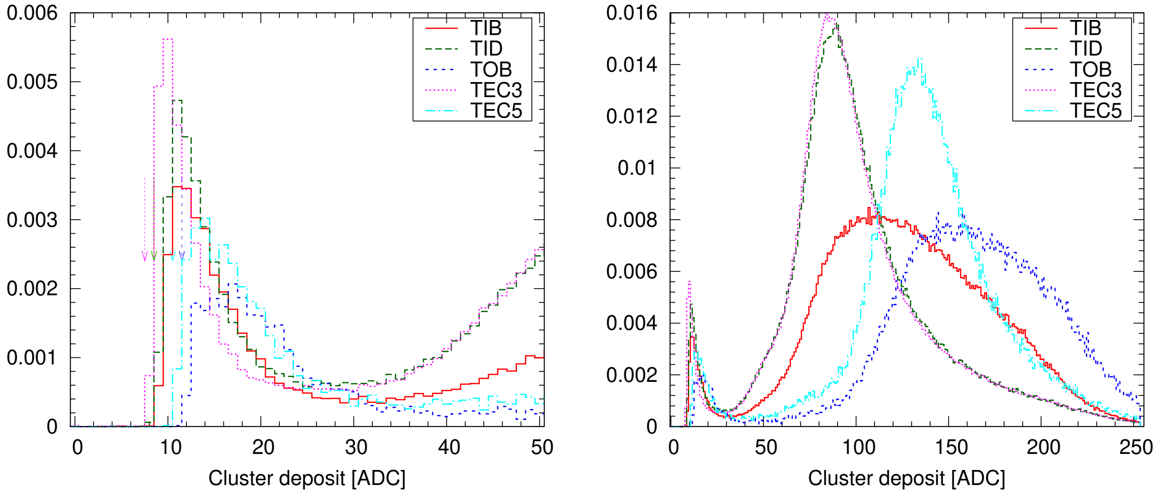

Figure 35: Distributions of cluster deposits for different strip detector types. In the left plot the horizontal scale was truncated at 50, while the right plot shows the complete spectrum. The vertical arrows indicate the chosen threshold values.

are correlated due to the capacitive coupling of the neighbouring strips and cross-talk. This is unfolded during the reconstruction of cluster deposit.

The calibration is based on a fraction of available data from the dataset `/TOTEM[20,21,22,23]/Run2018B-v1/RAW`, using runs 319267 and 319268.

4.1 Determination of basic strip properties

We have to determine the threshold t, the coupling α, and the standard deviation σ of the Gaussian noise using data. In order to reflect the differences between the various detector parts, there parameters are estimated separately for TIB, TOB, TID, TEC3 (width of about 300 μm) and TEC5 (width of about 500 μm). Those hits are collected which contain at most three strips and the expected cluster width is smaller than 0.1 in pitch units.[5] The width is predicted using the local direction of the fitted particle trajectory, also taking into account the modified charge drift direction due to the $\vec{E} \times \vec{B}$ effect.

The threshold is estimated by looking at the distribution of the sum of ADC values. Usually a value corresponding to the half maximum of the leading slope is chosen (Fig. 35). For the estimation of α and σ two- and three-strip clusters are used. In case of two strips the one with highest ADC is regarded as the main deposit, while in case of three strips it is the one in the middle. A two-dimensional histogram with values of coupled vs main deposits is filled (Fig. 36), if

- in case of thin sensors (TIB, TID and TEC3): the main deposit is equal to or greater than 30, but smaller than 254, and the coupled deposit is smaller than 0.1 times main deposit plus 20,
- in case of thick sensors (TOB and TEC5): the main deposit is equal to or greater than

[5] Picking clusters with width 0.1 was possible, there were enough of them to make this study. In the barrel, due to the $\vec{E} \times \vec{B}$ effect, narrow clusters do not primarily come from high p_{T} particles, but from lower p_{T} ones: we get narrow clusters if the particle trajectory inside the silicon is about parallel with the local drift direction. This way the charge is drifted on a single strip. In TID, TEC3, and TEC3, where $\vec{E} \times \vec{B}$ is small, normal incidence is more common, giving enough cluster samples.

50, but smaller than 254, and the coupled deposit is smaller than 0.2 times the main deposit plus 20.

At a given main deposit x_i the coupled deposits x'_j are expected to follow a normal distribution with mean $\alpha/(1-2\alpha)x_i$ and standard deviation σ. The resulted t, α and σ values are given in Table 6. We get coupling values $\alpha = 0.05 - 0.09$ and noise RMS $\sigma = 6 - 8$ ADC.

4.2 Detector gain calibration with tracks

In order to determine the multiplicative gain correction g for a detector element (in our case a chip), negative log-likelihood terms should be summed for collected hits and the sum minimised by varying g [28].

The calibration was performed in the following steps:

1. With help of a preliminary gain calibration estimate ε for each track, select pion-like tracks and collect the values of expected ε,[6] path length and deposit of each hit, and store them for every chip separately. For each chip minimise the joint chi-square of all selected hits by varying the gain.

2. Using the updated gains select only those tracks which are certainly pions, kaons, protons. Collect their hits for every chip separately and minimise again the joint chi-square chip by chip by varying the gains with similar methods as above.

The dataset already has the gains of silicon strips calibrated, according to the official calibration workflow. The multiplicative gain correction applied in the present analysis means an additional correction. If the previous calibration would suit our needs, all newly determined factors would be one. As we will see, this is not the case.

In order to perform the calibration and to reach a reasonable gain resolution, only about a fraction of data was used. Particle identification was done with a loose selection: a track was identified to be pion, kaon or proton if its momentum p and most probable energy loss rate ε satisfied the tight requirements listed in Table 7. In addition, those particles that fulfilled $p > 2\,\mathrm{GeV}$ or $\varepsilon < 3.2\,\mathrm{MeV/cm}$ were taken to be pions. These additions were important to increase the number of available hits for chips at larger radii but keeping the purity of the sample at high levels.

Distribution of number of hits on chip used for gain calibration (Fig. 37), the multiplicative gain correction (Fig. 38), and standard deviation of gain estimate (Fig. 39) are displayed, for pixel

[6] The expected ε is calculated with a model [1], using the density correction δ according to [29].

Table 6: Properties of several strip detectors in peak mode evaluated using hits with close to normal incidence, from charge sharing.

Detector	t [ADC]	α	σ [ADC]
	0.0		0.0
	0.0		0.0
	0.0		0.0
	0.0		0.0
	0.0		0.0

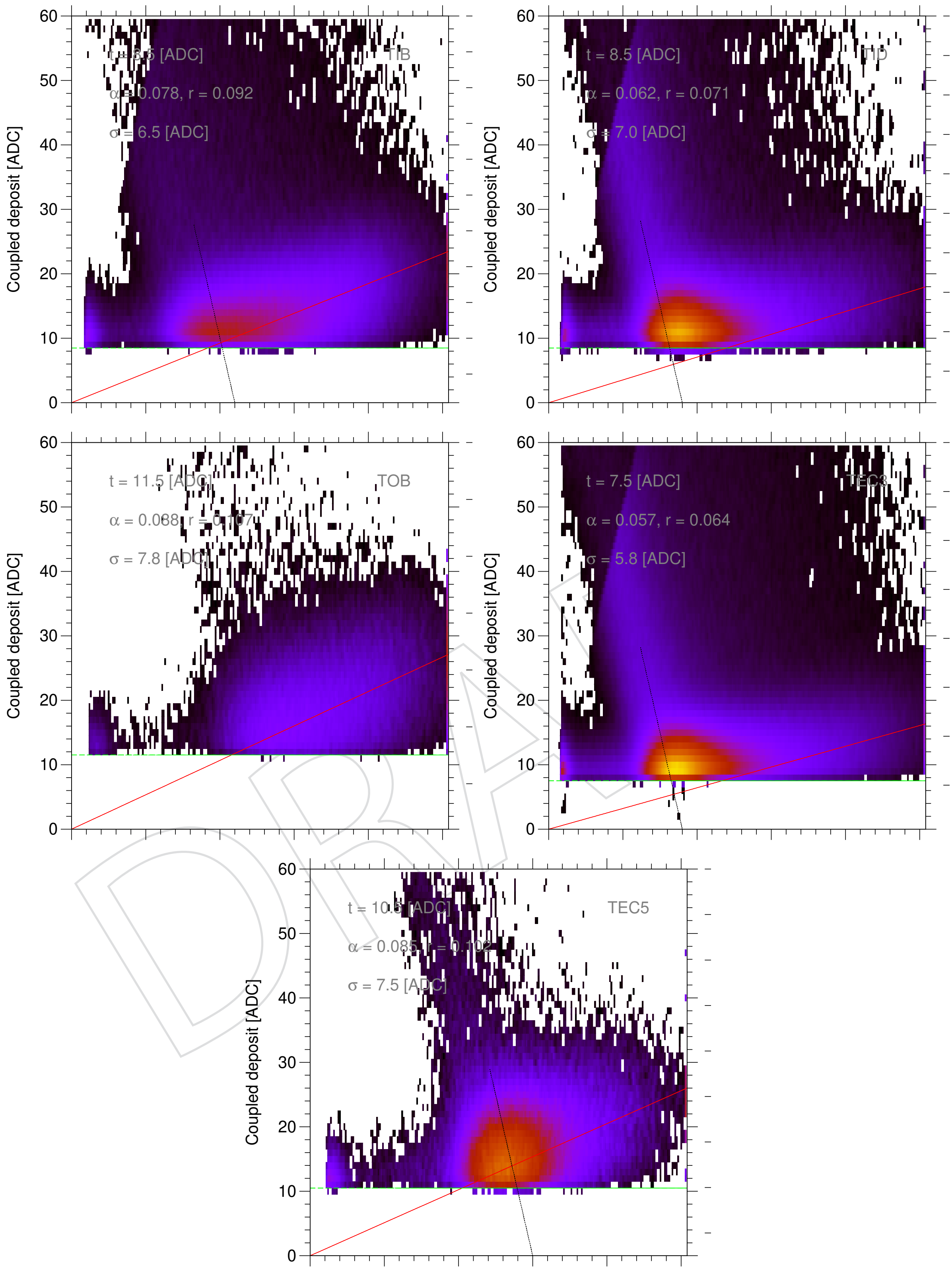

Figure 36: Two-dimensional histograms filled with main and coupled deposits, in case of thin (TIB, TID, TEC3) and thick (TOB, TEC5) sensors. The horizontal dashed green line indicates the location of the threshold while solid red line shows the result of the fit. For details see the text.

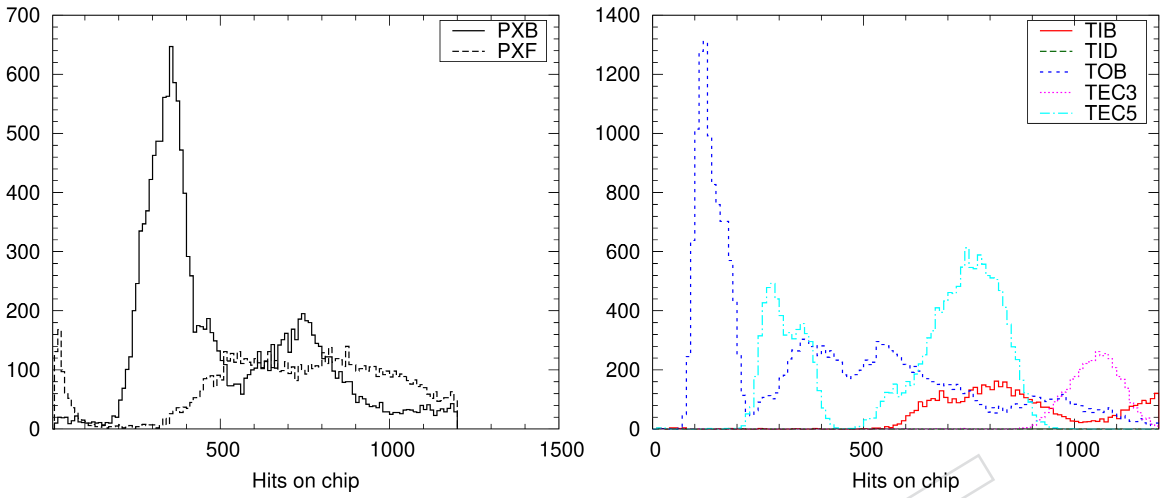

Figure 37: Distribution of the number of hits on chip used for gain calibration. Pixel detectors (PXB, PXF) are shown on the left, strip detectors (TIB, TID, TOB, TEC3, TEC5) are on the right. Each entry in the histograms represents a chip.

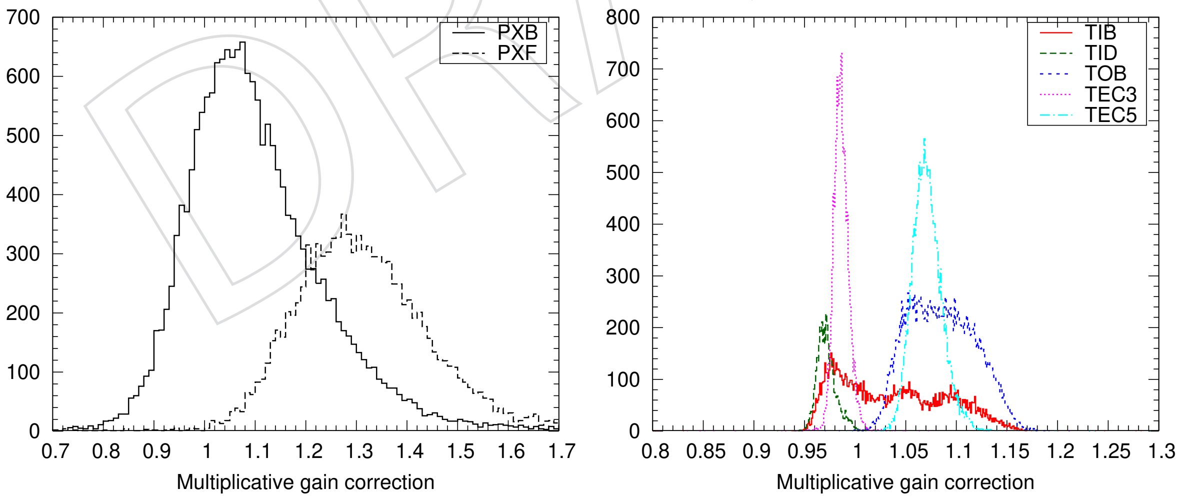

Figure 38: Distribution of the multiplicative gain correction. Pixel detectors (PXB, PXF) are shown on the left, strip detectors (TIB, TID, TOB, TEC3, TEC5) are on the right. Each entry in the histograms represents a chip.

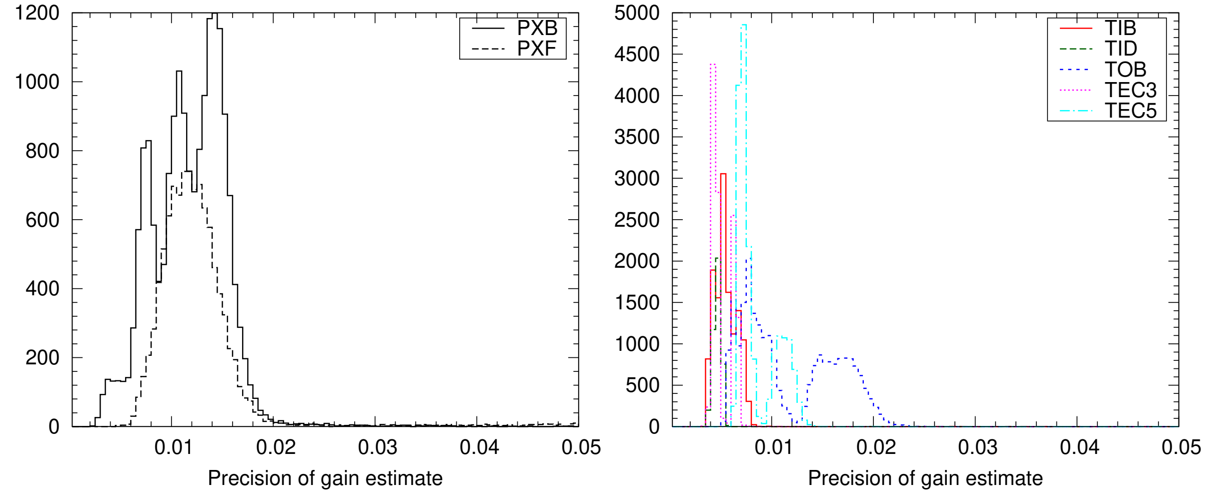

Figure 39: Distribution of standard deviation of gain estimate. Pixel detectors (PXB, PXF) are shown on the left, strip detectors (TIB, TID, TOB, TEC3, TEC5) are on the right. Each entry in the histograms represents a chip.

detectors (PXB, PXF) and strip detectors (TIB, TID, TOB, TEC3, TEC5) separately. Each entry in the histograms represents a chip. The distribution of the multiplicative gain correction is quite wide for pixels. For strips it is narrower since the standard gain calibration was already applied beforehand, although there are sizeable shifts up to 0.1 and 0.2 for TIB, TOB and TEC5. The precision of gain estimates are in the range 0.2-1% for pixel chips, while for strips it depends on the local position of the chip: it is around 0.4% for TIB, but it goes up to 1.5% for TOB. TEC5 values are relatively precise because of their larger thickness.

4.3 Model validation and hit-level residual corrections

After detector gain calibration, it is important to check and validate the energy loss model, the deposit estimates and their uncertainties with help of data. While the model gives a satisfactory description of the low-level elementary processes, the channel noise and effects of below threshold and saturation losses are reasonably described (especially for strips), there could be remaining issues that simply cannot be covered within this analysis. For this study those particles (electrons, pions, kaons, and protons) are selected with the loose selection discussed above.

Multi-dimensional histograms are filled with $\beta\gamma = p/m$, path-length (l), deposit and deposit uncertainty. These latter are calculated from estimated cluster noise for pixels, and using the estimated uncertainty for strips. The chosen binning is the following: $-1.25 < \log(\beta\gamma) < 1.75$ with 0.04 width; $270 < l < 900\,\mu$m with $10\,\mu$m wide bins; $y < 1\,$MeV with 5 keV binwidth.

Table 7: Tight requirements for approximate particle identification. Note that all ε values are functions of p. Subscripts e, π, K and p refer to the most probable value for a given particle species, as expected from simulation.

Particle	Momentum	Differential energy loss
electron	$p < 0.16\,$GeV	$\varepsilon < (\varepsilon_e + \varepsilon_\pi)/2$
pion	$0.16 < p < 0.70\,$GeV	$\varepsilon < (\varepsilon_\pi + \varepsilon_K)/2$
kaon	$p < 0.70\,$GeV	$(\varepsilon_\pi + \varepsilon_K)/2 < \varepsilon < (\varepsilon_K + \varepsilon_p)/2$
proton	$p < 1.40\,$GeV	$(\varepsilon_K + \varepsilon_p)/2 < \varepsilon$

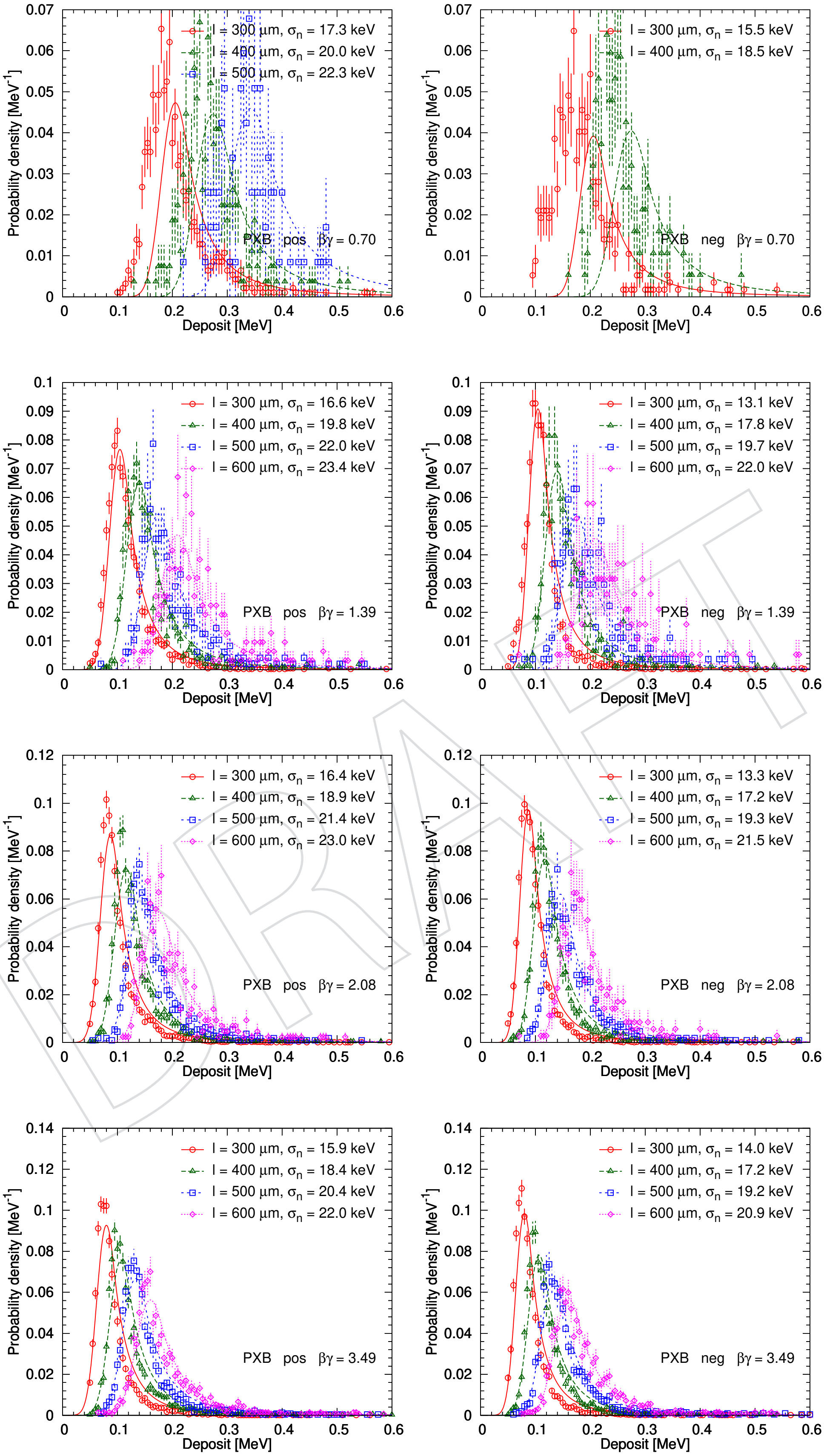

Figure 40: Validation of energy deposit model for PXB. Measured energy deposit distributions of surely identified hadrons at $\beta\gamma = 0.70$, 1.39, 2.08 and 3.49 for positives (left column) and negatives (right column) are shown. Values are given at path lengths of $l = 270$, 300, 400, 500, 600, 750, and 900 μm silicon, shown together with model predictions. The average cluster noise σ_n is also given. Missing plots indicate insufficient data for those path-lengths.

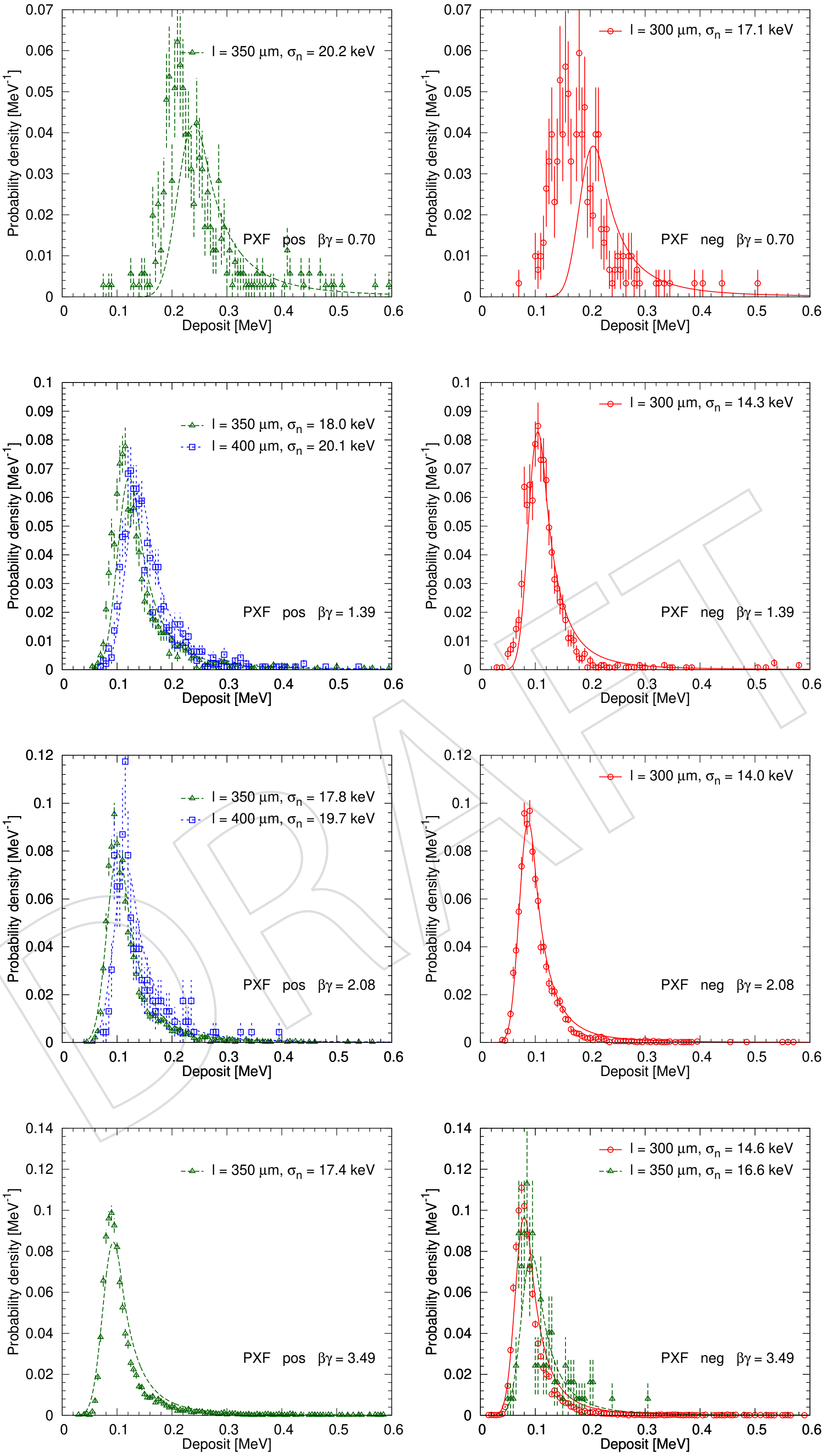

Figure 41: Validation of energy deposit model for PXF. Measured energy deposit distributions of surely identified hadrons at $\beta\gamma = 0.70$, 1.39, 2.08 and 3.49 for positives (left column) and negatives (right column) are shown. Values are given at path lengths of $l = 270$, 300, 400, 500, 600, 750, and 900 μm silicon, shown together with model predictions. The average cluster noise σ_n is also given. Missing plots indicate insufficient data for those path-lengths.

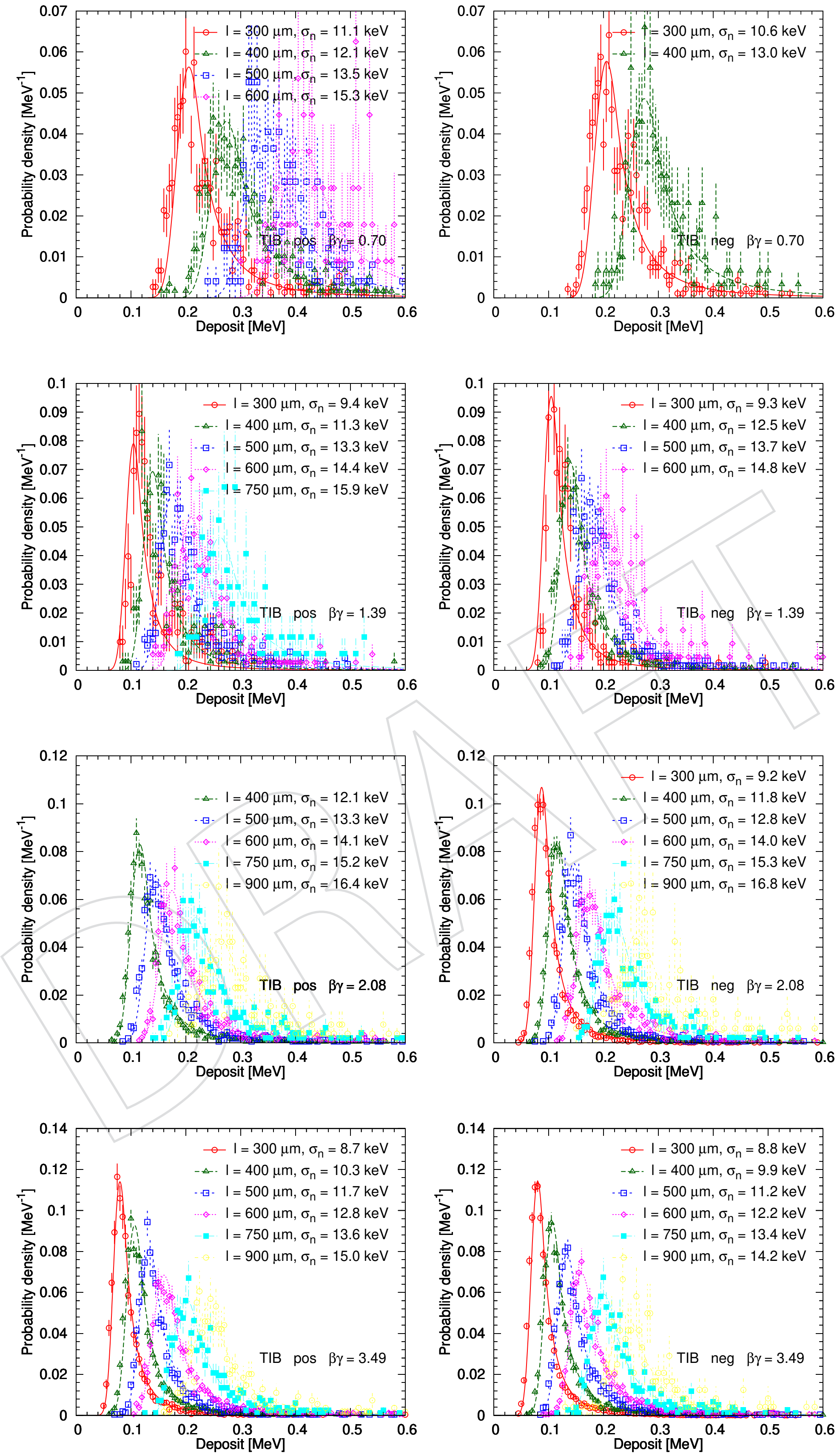

Figure 42: Validation of energy deposit model for TIB. Measured energy deposit distributions of surely identified hadrons at $\beta\gamma = 0.70$, 1.39, 2.08 and 3.49 for positives (left column) and negatives (right column) are shown. Values are given at path lengths of $l = 270$, 300, 400, 500, 600, 750, and 900 μm silicon, shown together with model predictions. The average cluster noise σ_n is also given. Missing plots indicate insufficient data for those path-lengths.

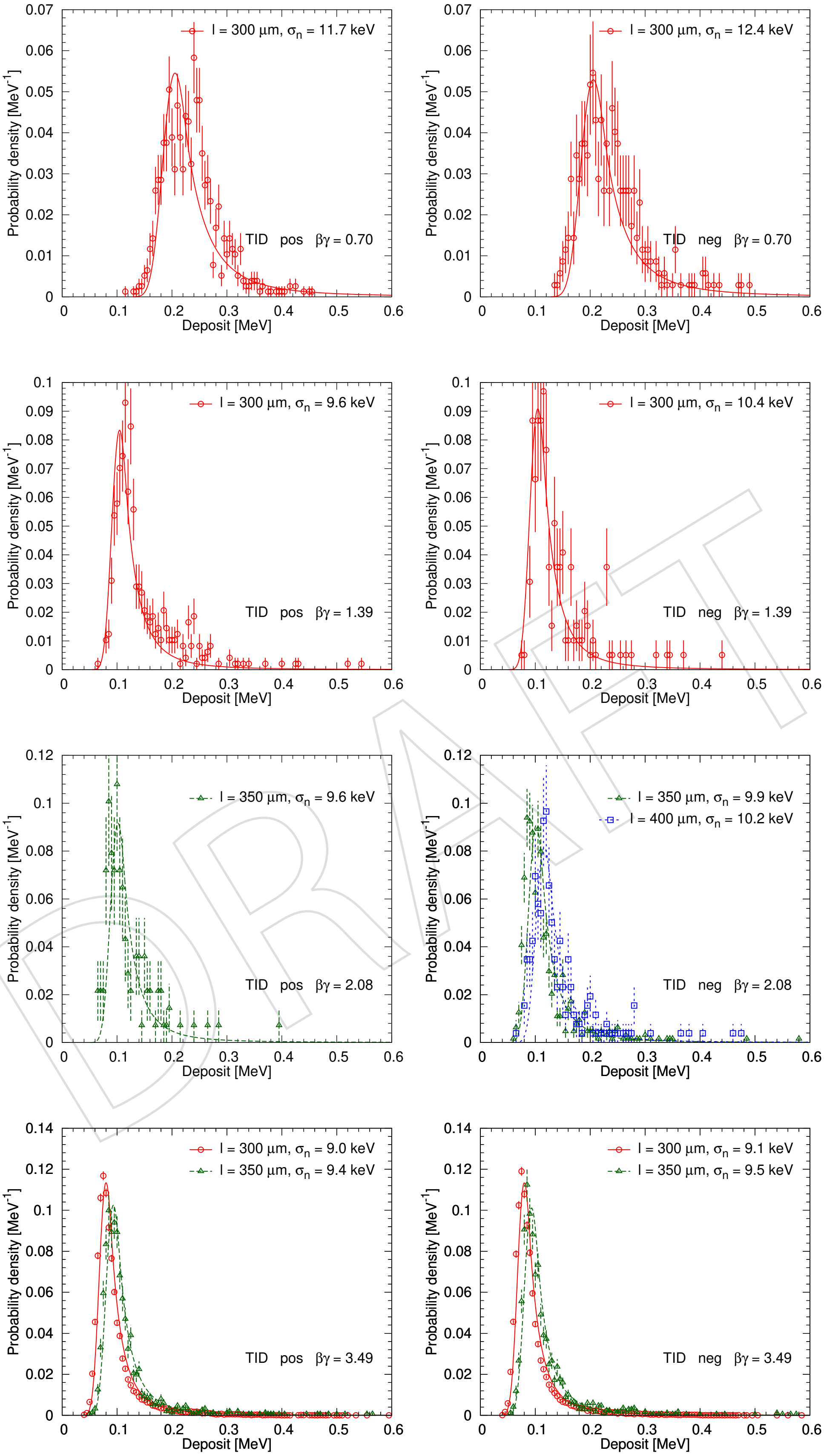

Figure 43: Validation of energy deposit model for TID. Measured energy deposit distributions of surely identified hadrons at $\beta\gamma = 0.70$, 1.39, 2.08 and 3.49 for positives (left column) and negatives (right column) are shown. Values are given at path lengths of $l = 300$, 400, 500, 600, 750, and 900 μm silicon, shown together with model predictions. The average cluster noise σ_n is also given. Missing plots indicate insufficient data for those path-lengths.

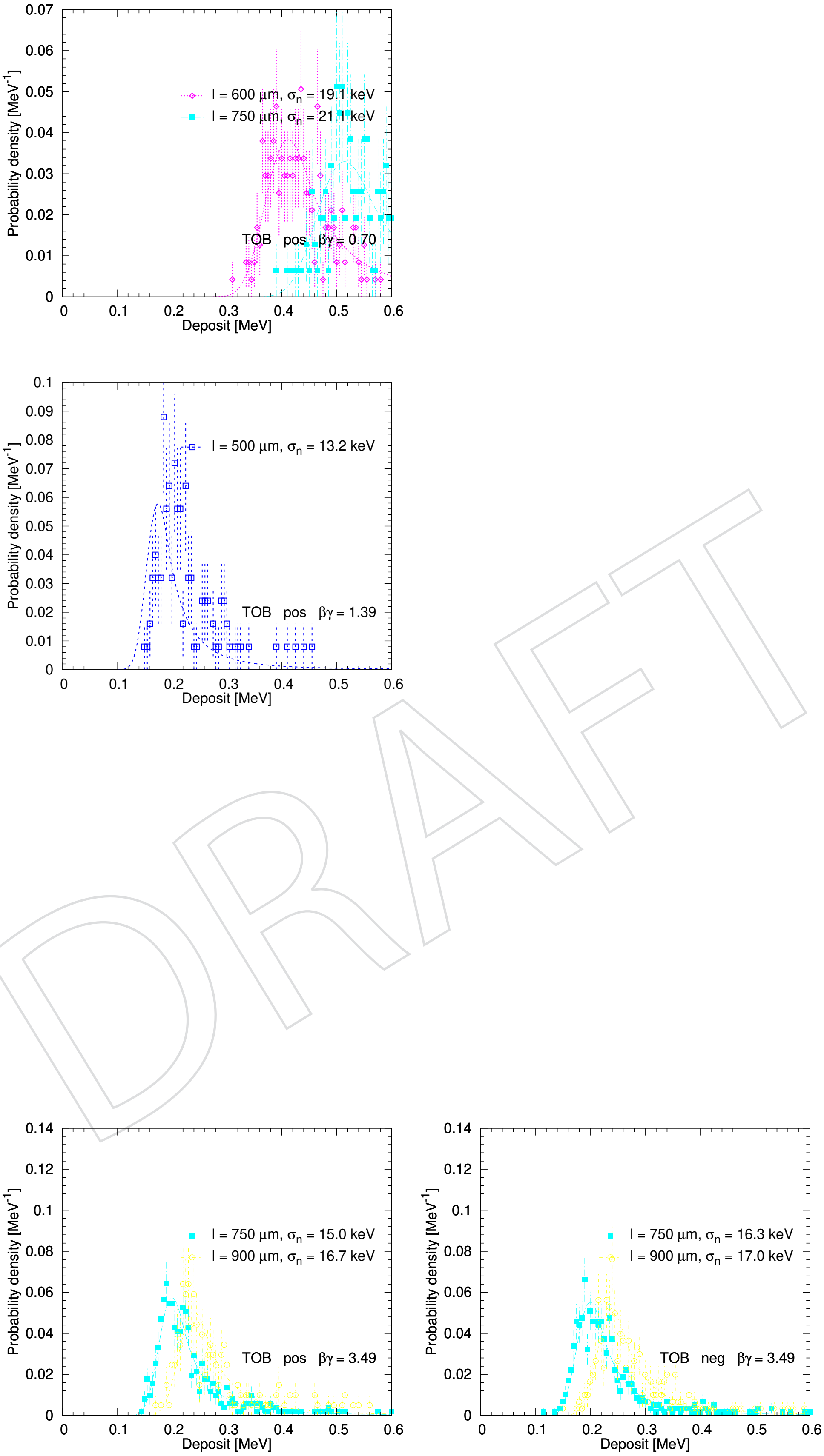

Figure 44: Validation of energy deposit model for TOB. Measured energy deposit distributions of surely identified hadrons at $\beta\gamma = 0.70$, 1.39, 2.08 and 3.49 for positives (left column) and negatives (right column) are shown. Values are given at path lengths of $l = 300$, 400, 500, 600, 750, and 900 μm silicon, shown together with model predictions. The average cluster noise σ_n is also given. Missing plots indicate insufficient data for those path-lengths.

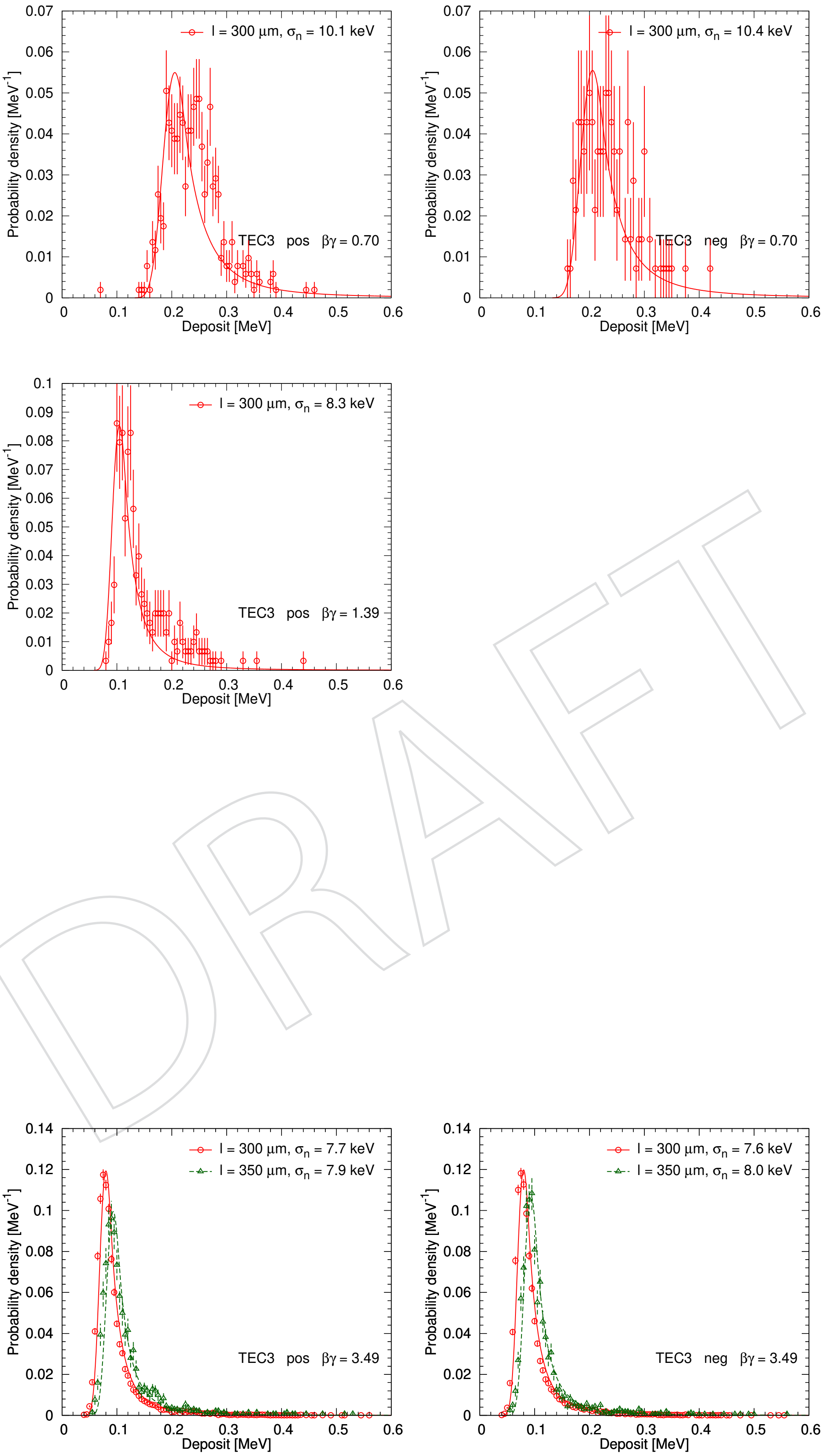

Figure 45: Validation of energy deposit model for TEC3. Measured energy deposit distributions of surely identified hadrons at $\beta\gamma = 0.70$, 1.39, 2.08 and 3.49 for positives (left column) and negatives (right column) are shown. Values are given at path lengths of $l = 300$, 400, 500, 600, 750, and 900 μm silicon, shown together with model predictions. The average cluster noise σ_n is also given. Missing plots indicate insufficient data for those path-lengths.

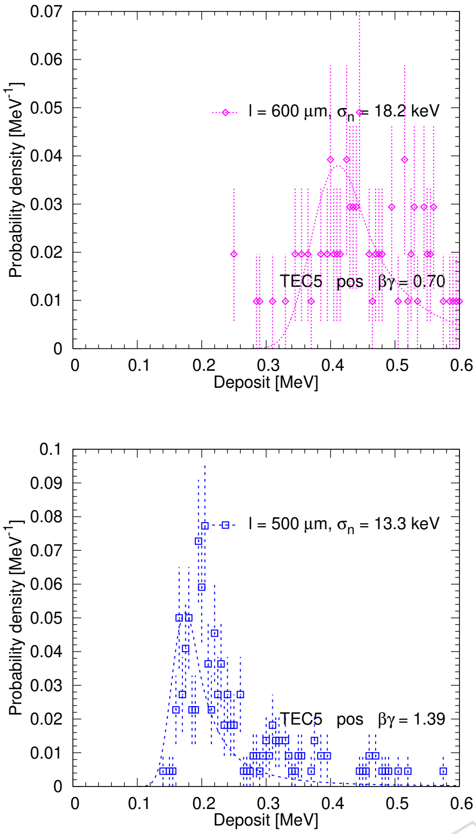

Figure 46: Validation of energy deposit model for TEC5. Measured energy deposit distributions of surely identified hadrons at $\beta\gamma = 0.70$, 1.39, 2.08 and 3.49 for positives (left column) and negatives (right column) are shown. Values are given at path lengths of l = 300, 400, 500, 600, 750, and 900 μm silicon, shown together with model predictions. The average cluster noise σ_n is also given. Missing plots indicate insufficient data for those path-lengths.

As examples, measured energy deposit distributions of surely identified hadrons at $\beta\gamma = 0.70$, 1.39, 2.08 and 3.49 for positives and negatives are shown for all detector types in Figs. 40, 41, 42, 43, 44, 45 and 46. Values are given at path lengths of $l = 270$ or 300, 400, 500, 600, 750, and 900 μm silicon, shown together with predictions of the applied model. For these theoretical curves the average of the cluster noise σ_n was used, its value is also given in the legend. Empty plots indicate missing path lengths. Note that the uncertainty of the measured track momentum, present at low momentum due mostly to multiple scattering, was not taken into account. Each track contributed to its $\beta\gamma$ bin according to its measured momentum. That could lead to wider measured deposit distributions in data.

Despite of the large $\beta\gamma$ and path-length range, and detector types studied, the model gives a fairly good description.

4.4 Estimation of most probable energy loss rate for tracks

Having the proper hit energy deposits y_i, the next step is to estimate the most probable energy loss rate ε for the whole trajectory. The joint chi-squared to minimise is

$$\chi^2(\varepsilon) = \sum_i \chi^2_{y_i} \left(\Delta(\varepsilon, l_i)\right).$$

Since the association of hits to trajectories is not always unambiguous, some hits do not belong to the actual track. Most of those hits are noise clusters, especially in the strip detector, where the threshold is relatively low. (Even if a hit is real, thus the measured deposit is correct, the calculated path length can be false.) Assuming that there is at most one false hit on a trajectory it can be detected and removed. Only those tracks are considered that have at least 3 hits and for which $\chi^2 > 1.3\, n_{\text{hits}} + 4\sqrt{1.3\, n_{\text{hits}}}$. If the exclusion of a hit decreases the joint chi-square of the trajectory by a considerable amount, in our case the condition $\chi^2_{\text{removed}} < \chi^2_{\text{orig}} - 12$ is checked, then the hit is removed. According to detailed studies if there is an outlier then it is usually the hit with the lowest y/l value. Thus, in order to save processing time, only the hit with the lowest y/l value is considered for removal.

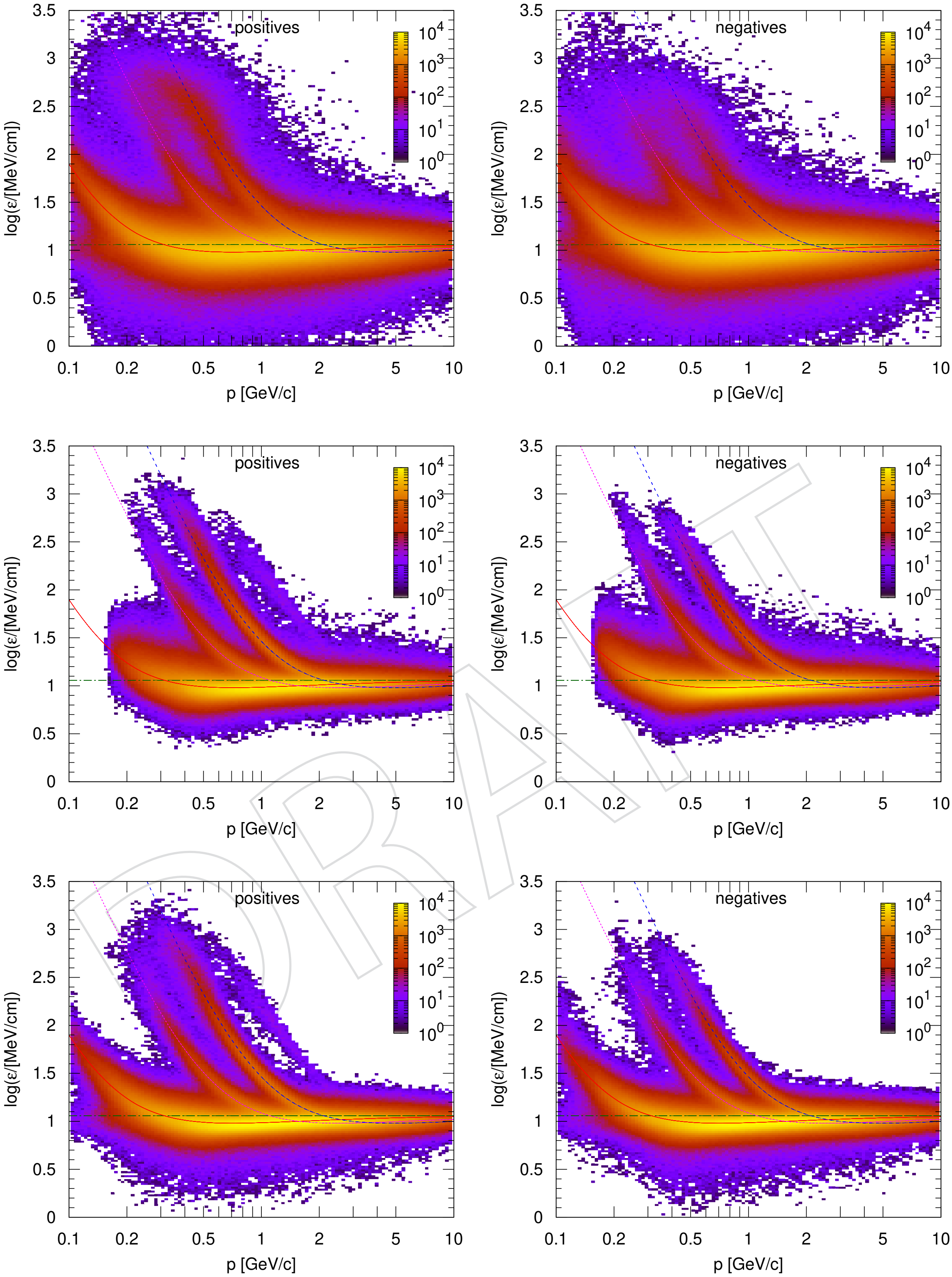

Figure 47: Distribution of $\ln\varepsilon$ values as a function of total momentum p. Note that the colour scale is logarithmic. The left (right) column displays results using positive (negative) particles. The rows give the distribution of $\ln\varepsilon$ estimated with pixel, strip, and all hits, respectively. The curves show the most probable values for electrons, pions, kaons and protons.

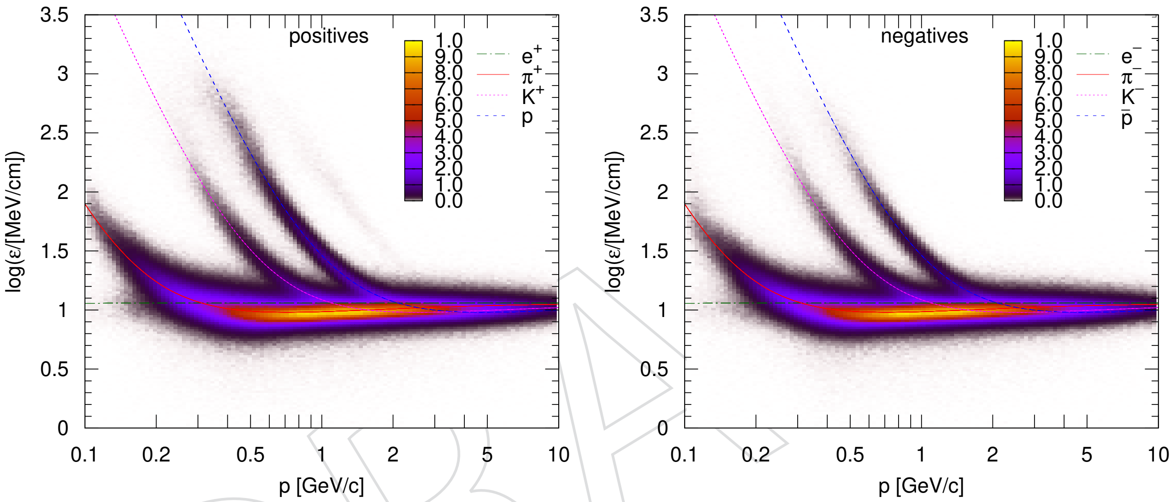

Figure 48: Distribution of $\ln \varepsilon$ values as a function of total momentum p for positive (left) and negative (right) particles. Note that the colour scale is linear. The curves show the most probable values for electrons, pions, kaons and protons.

5 Produced particles in the central region

The finding and fitting of the charged particles in the silicon tracker are performed with official tools, they contain the results of an optimisation for low momentum particles from previous studies. In the following we discuss some single-track and some two-track parameters using events with exactly two oppositely charged reconstructed particles.

The distribution of the z coordinate of reconstructed charged particles at their closest approach to the beam-line is shown in Fig. 49-left. The histogram shows data, while the curve indicates the a Gaussian fit with mean value of $m_z = -0.37$ cm and standard deviation $\sigma_z = 4.63$ cm. The distribution of the transverse impact parameter of reconstructed charged particles is shown in Fig. 49-right. The histogram shows data, while the curve indicates a fit with the Cauchy distribution with $\Gamma = 0.046$ cm. The distribution of the normalized difference of Δz of the reconstructed charged particle pair is shown in Fig. 50-left. A Gaussian centred around zero with unit standard deviation is plotted (dashed blue).

Low transverse momentum particles looping in the solenoidal magnetic field might rarely be reconstructed as two oppositely charged particles with closely opposite momentum vectors. Their contribution is visible in Fig. 50-right, where the distributions of the variable $|\vec{p}_3 + \vec{p}_4|/m$ for pions-, kaon-, and proton-pairs are plotted: they populate the peak near zero. It is interesting that we see hardly any K^+K^- pairs from loopers. During analysis, events containing loopers are removed by requiring $|\vec{p}_3 + \vec{p}_4|/m > 0.2$. The corresponding event loss is very small and is neglected.

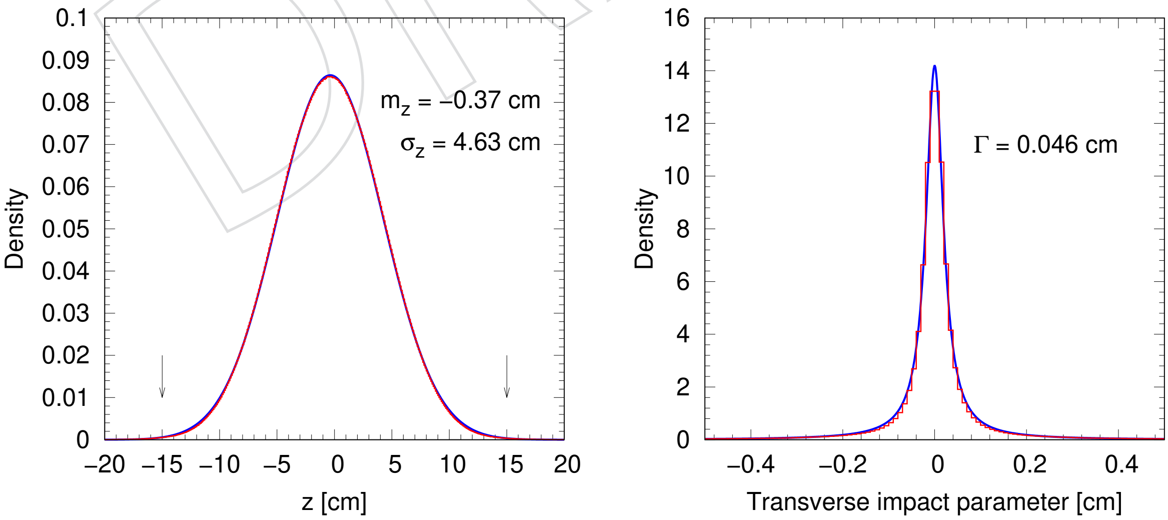

Figure 49: Left: distribution of the z coordinate of reconstructed charged particles at their closest approach to the beam-line. The histogram shows data, while the curve indicates a Gaussian fit. Right: distribution of the transverse impact parameter of reconstructed charged particles. The histogram shows data, while the curve indicates a fit with the Cauchy distribution.

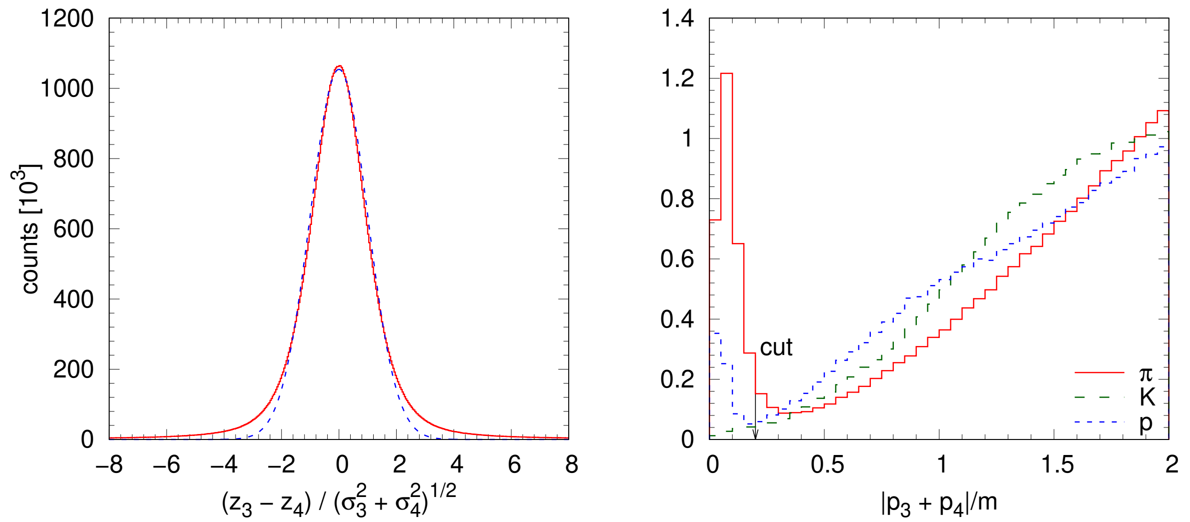

Figure 50: Left: distribution of difference between the z coordinates of the two central charged hadrons, normalised by the standard deviation of the Gaussian expectation. A Gaussian centred around zero with unit standard deviation is plotted (dashed blue). Right: distribution of the variable $|\vec{p}_3 + \vec{p}_4|/m$ for pions-, kaon-, and proton-pairs. A cut at 0.2 to remove loopers is indicated by the downward pointing arrow.

The decision on maximal rapidity $y_{\max}$ (2.0 for $\pi^+\pi^-$, 1.6 otherwise) was based on the rapidity distribution of the central two-hadron system. It is shown separately for $\pi^+\pi^-$, K^+K^-, and $p\overline{p}$ pairs in Fig. 51 using reconstructed central exclusive events with particle identification.

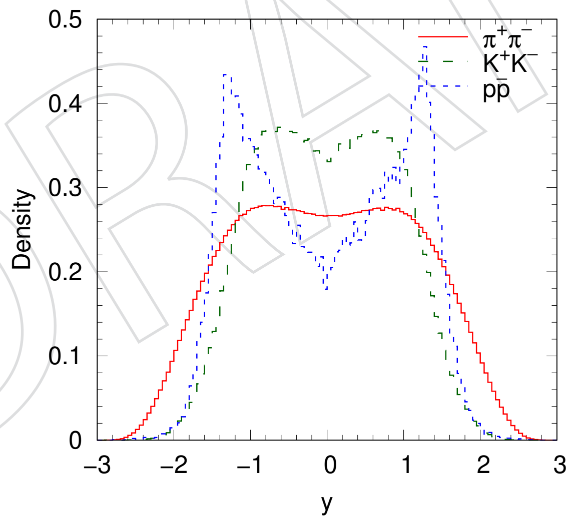

Figure 51: Rapidity distribution of the central two-hadron system, shown separately for $\pi^+\pi^-$, K^+K^-, and $p\overline{p}$ pairs using reconstructed central exclusive events with particle identification.

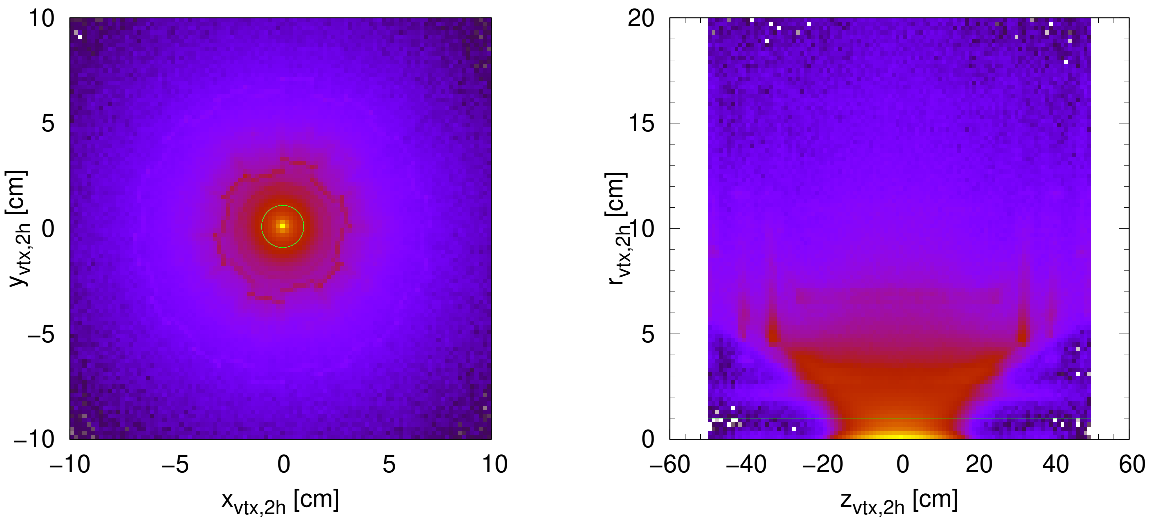

Figure 52: Distribution of event vertices in the transverse $x - y$ plane (left) and in the $z - r$ system (right). The continuous distribution of $\mathrm{K^0_S}$ decays and the discrete outlines of photon conversions on the beam pipe and pixel layers are well visible. The green circle and line indicate $r = 1\,\mathrm{cm}$.

Distribution of event vertices in the transverse $x - y$ plane and in the $z - r$ system are shown in Fig. 52. The continuous distribution of $\mathrm{K^0_S}$ decays and the discrete outlines of photon conversions on the beam pipe and pixel layers are well visible. The green circle and line indicate $r = 1\,\mathrm{cm}$.

Events are selected if the z values of both tracks satisfy $|z - m_z| < 4\sigma_z$, while their vertex is closer to the beamline than 1 cm. The latter cut eliminates photon conversions on the beam pipe and pixel tracker layers while significantly reducing the contribution of long-lived decays.

Track-fit χ^2 distributions of identified charged hadrons (π, K, and p) for selected number of degrees of freedom (ndf) values are shown in Fig. 53. (Details of particle identifications are given in Sec. 5.2.) Histograms show data, while curves indicate the expected chi-squared distributions. The match between data and expectation is fair but acceptable.

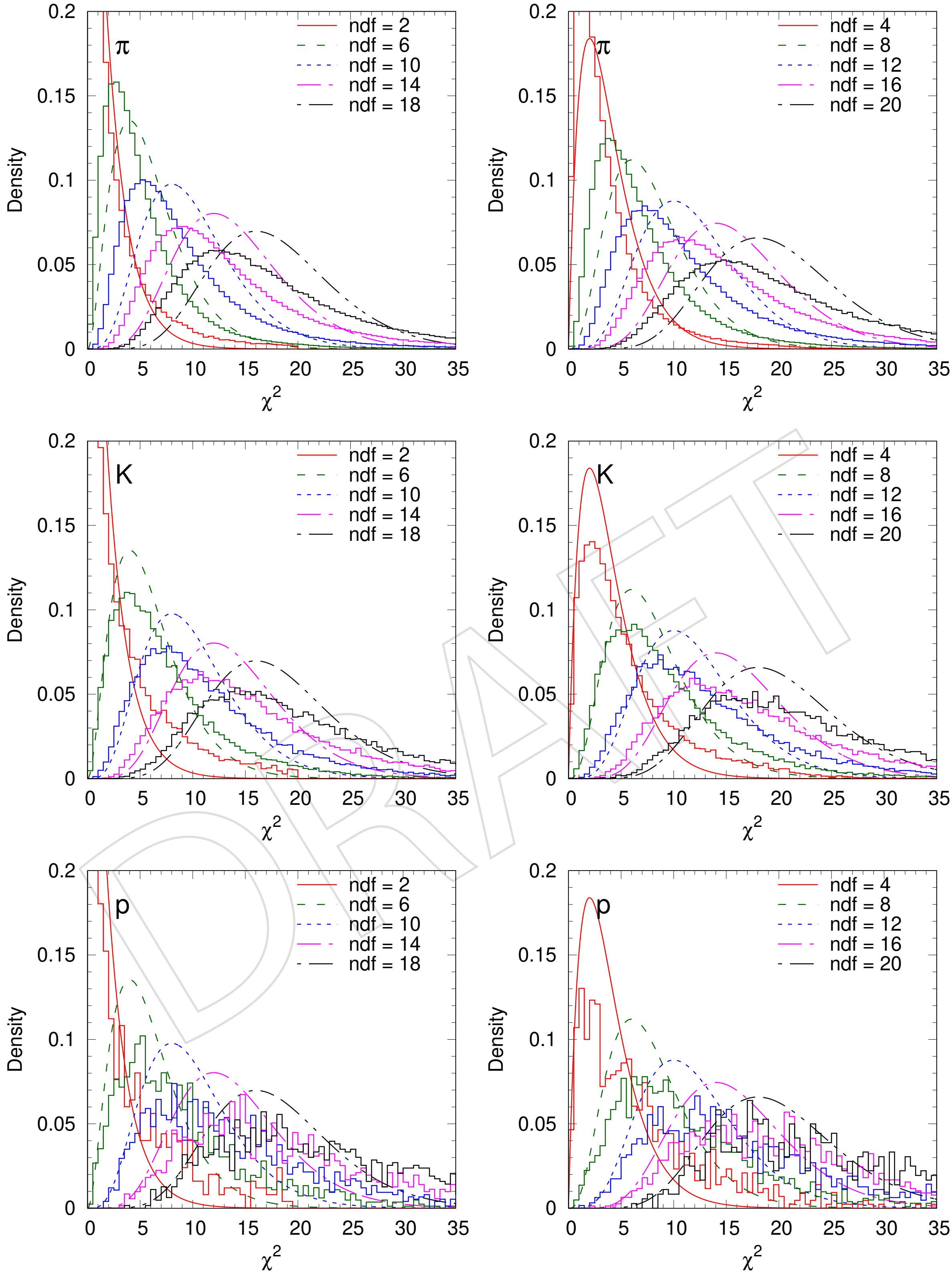

Figure 53: Track-fit χ^2 distributions of identified charged hadrons (π: top row, K: centre row, p: bottom row) for selected number of degrees of freedom (ndf) values. Histograms show data, while curves indicate the expected χ^2 distributions.

5.1 High level trigger and tracking efficiency

Distributions of positively (left) and negatively (right) charged particles in the (η, p_T) plane are shown in Fig. 54. The "valleys" correspond to inefficiencies at lower p_T and are present because the high-level trigger contains pixel activity filters and various pixel track filters (Sec. 2). It is obvious that having a simple single-track tracking efficiency table is not satisfactory. Instead, we have to deal with a combined "track-pair high-level trigger and tracking" efficiency.

We have simulated and fully reconstructed (through CMSSW) single charged hadrons, π^+ or π^- or K^+ or K^- or p or $\overline{\mathrm{p}}$, 30 M events each. They were generated uniformly in the kinematic range $-3 < \eta < 3$, $0.01\,\mathrm{GeV} < p_\mathrm{T} < 2\,\mathrm{GeV}$, all ϕ. Besides collecting reconstruction efficiency information in bins of $(\eta, p_\mathrm{T}, \phi)$, the distribution of hit patterns in the pixel layers is also recorded. The combination of these is used to determine the high level trigger and reconstruction efficiency of two-track events (Sec. 2). An event is taken, the high level trigger would fire, if

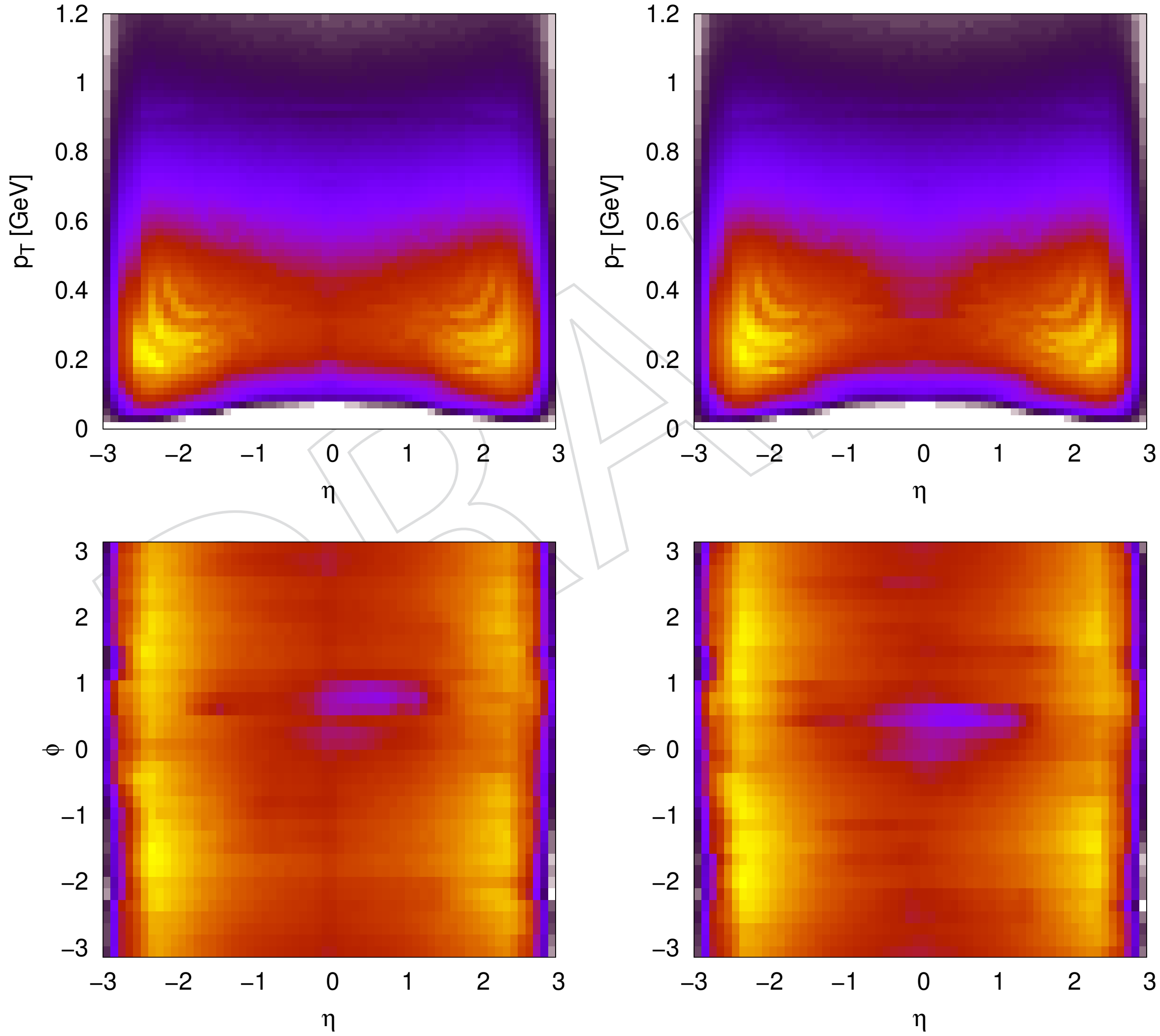

Figure 54: Top row: Distributions of positively (left) and negatively (right) charged particles in the (η, p_T) plane. The "valleys" corresponding to inefficiencies at lower p_T are well visible. Bottom row: Distributions of positively (left) and negatively (right) charged particles in the (η, ϕ) plane. The efficiency holes in the region $0 < \phi < 1$ are well visible.

- the pixel activity filter (`hltPixelActivityFilterBPixNCluXNLayY`) requires at least 5 pixel clusters and at least 3 layers with pixel clusters in BPix;
- the pixel track filter (`hltPixelTrackFilterBPixNY`) requires at least 1 pixel track in BPix;
- the pixel track filter (`hltPixelTrackFilterNY`) requires at least 1 pixel tracks;

The systematics uncertainty of the single particle tracking efficiency in the relevant low momentum regions is 1.4%, based on a data-driven study [30].

The extracted single-particle reconstruction efficiencies (reconstructed exactly once), for positively and negatively charged pions, kaons, and protons as functions of (η, p_T) are shown in Fig. 55. The distributions clearly show the acceptance edge near $\eta \approx 2.5$ and the efficiency losses at low total momenta because of multiple Coulomb scattering and energy loss. The curves indicate constant total momentum at $p = 0.1$ GeV for pions, 0.16 GeV for kaons, 0.25 GeV for protons.

Probabilities of reconstructing a charged particle more than once (multiple reconstruction) are shown in Fig. 56 projected on the (η, p_T) plane. Such particles are concentrated at $\eta \approx 0$ for pions, and around $\eta \sim 2$, but their frequency at or below the percent level.

The combined probabilities of reconstruction of, and firing HLT by, a charged particle are shown in Fig. 57, projected on the (η, p_T) plane. The plots show a significant decrease of efficiency in the region of barrel-endcap transition due to few pixel clusters or layers with pixel hits.

The ϕ dependence of the single-particle combined reconstruction and HLT-efficiency is demonstrated in Fig. 58 for $p_T < 1$ GeV, projected on the (η, ϕ) plane. The efficiency holes in the region $0 < \phi < 1$ and $|\eta| < 1$ are well visible.

Calculation of event-by-event two-track corrections. Detailed measures of single-particle reconstruction are available for the ranges $-3 < \eta < 3$ [60 bins], $p_T < 2$ GeV [40 bins], $-\pi < \phi < \pi$ [36 bins]. More precisely, in each bin we know the probability of being reconstructed, of firing HLT, and the distribution of pixel layer occupancies in case of not firing HLT.

In an event, the combined efficiency of reconstruction and HLT of the charge hadron pair is deduced, taking into account hat

- both hadrons must be reconstructed;
- either one of the hadrons should be able to fire HLT, or the ensemble of their clusters should fire HLT (realised by addition and bitwise or operations).

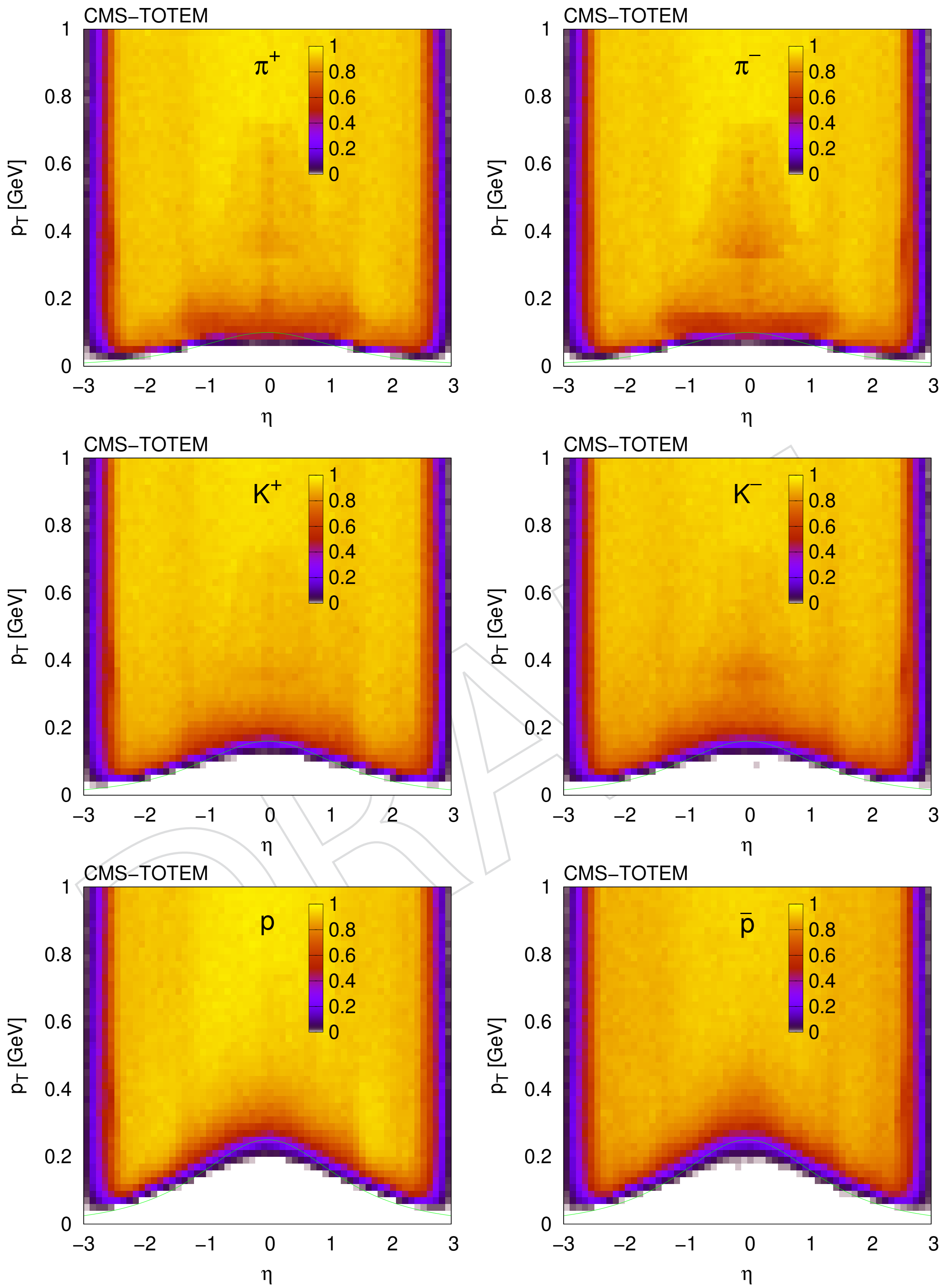

Figure 55: Extracted single-particle reconstruction efficiency (reconstructed exactly once), for positively and negatively charged pions, kaons, and protons as functions of (η, p_{T}). Curves indicate constant total momentum ($p = 0.1\,\mathrm{GeV}$ for pions, $0.16\,\mathrm{GeV}$ for kaons, $0.25\,\mathrm{GeV}$ for protons).

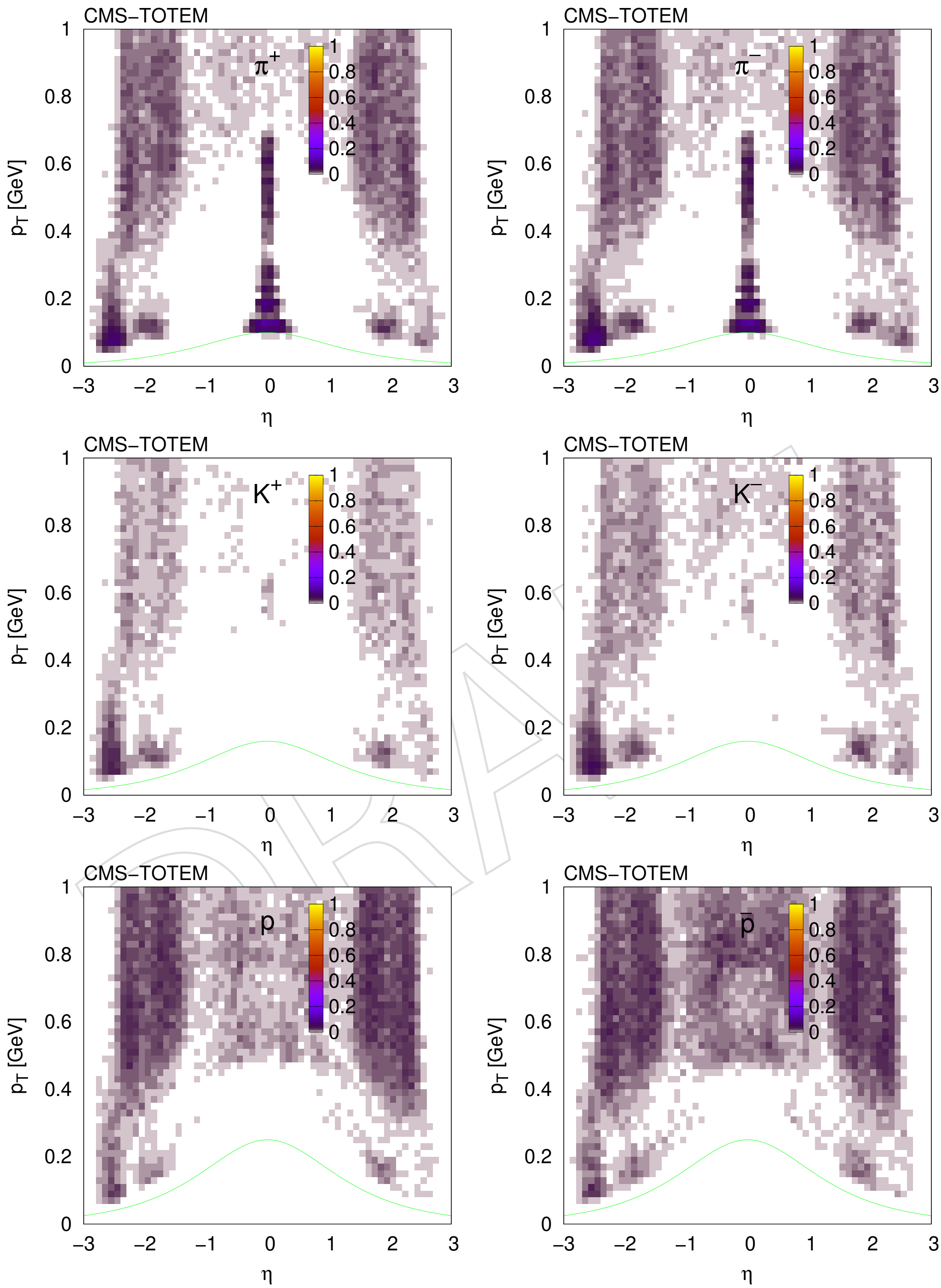

Figure 56: Extracted single-particle reconstruction efficiency (reconstructed more than once), for positively and negatively charged pions, kaons, and protons as functions of (η, p_T). Curves indicate constant total momentum ($p = 0.1\,\text{GeV}$ for pions, $0.16\,\text{GeV}$ for kaons, $0.25\,\text{GeV}$ for protons).

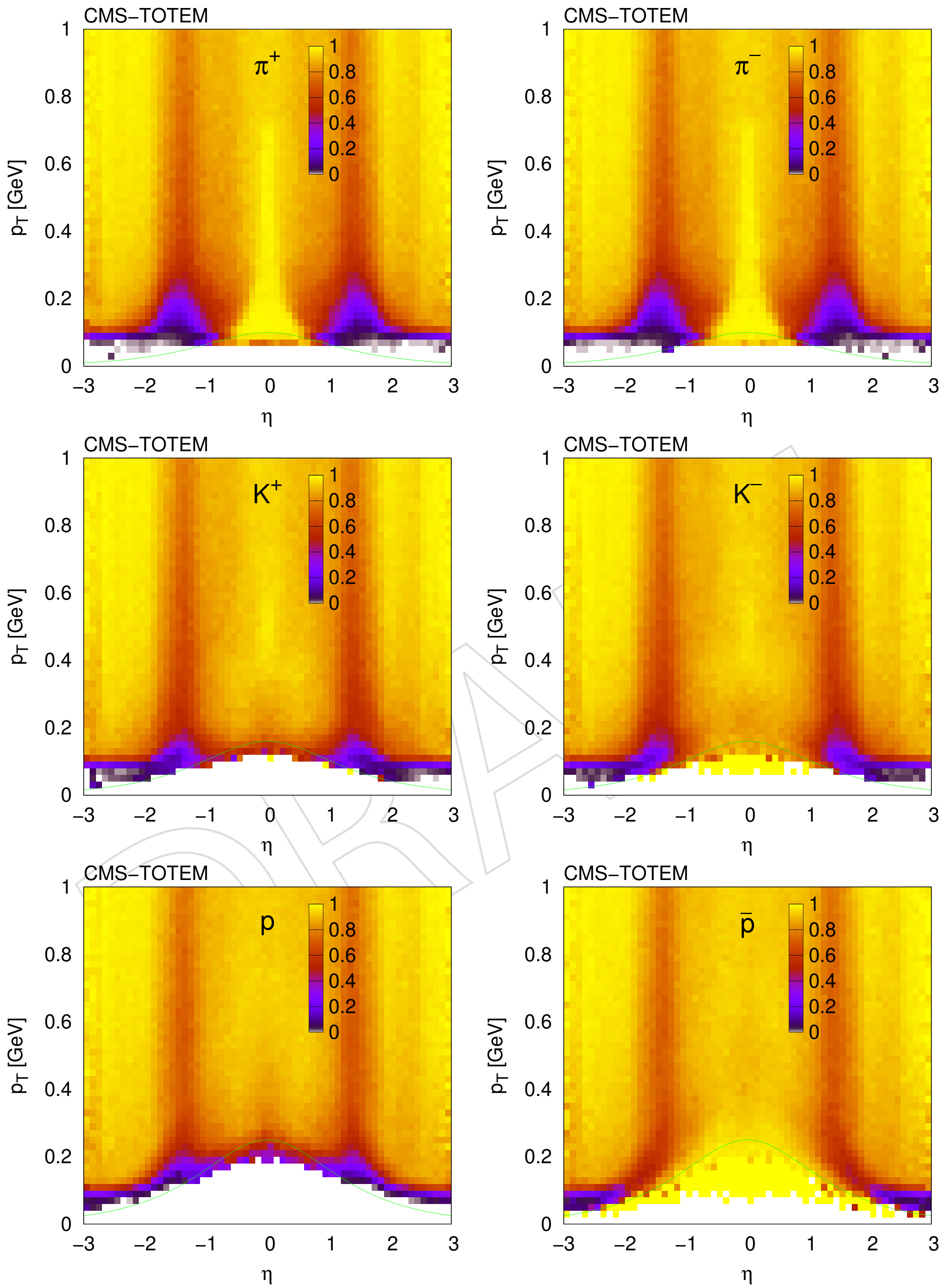

Figure 57: Extracted single-particle HLT efficiency (reconstructed and fired HLT), for positively and negatively charged pions, kaons, and protons as functions of (η, p_T). Curves indicate constant total momentum ($p = 0.1$ GeV for pions, 0.16 GeV for kaons, 0.25 GeV for protons).

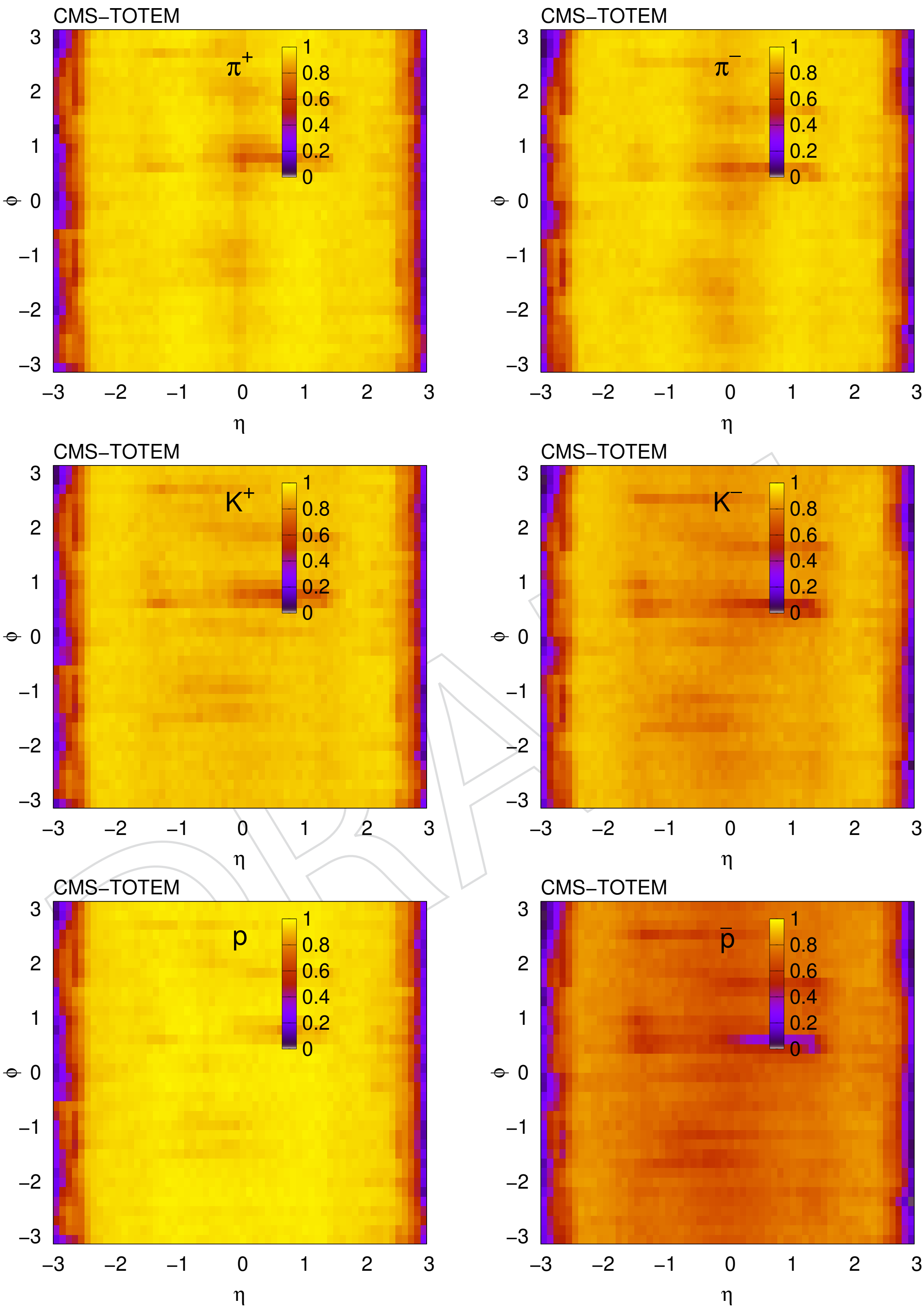

Figure 58: Extracted single-particle HLT efficiency (reconstructed and fired HLT) if $p_T < 1\,\mathrm{GeV}$, for positively and negatively charged pions, kaons, and protons as functions of (η, ϕ). The efficiency holes in the region $0 < \phi < 1$ and $|\eta| < 1$ are well visible.

5.2 Particle identification

Details on the data-based determination of basic silicon strip properties, detector gain calibration, model validation, and on the estimation of the most probable energy loss rate (or its logarithm, $\ln\varepsilon$), and its variance $\sigma^2_{\ln\varepsilon}$, for tracks were given in Sec. 4.

The distributions of $\ln\varepsilon$ as a function of total momentum p, for charged reconstructed particles in selected two-track events (signal, sideband, identified $\pi^+\pi^-$, $\mathrm{K}^+\mathrm{K}^-$, $\mathrm{p}\overline{\mathrm{p}}$) are shown in Fig. 59. The curves show the expected $\ln\varepsilon$ for electrons, pions, kaons, and protons (Eq. (34.12) in Ref. [1]). While the sideband region displays a reasonable amount of pions, kaons, and protons, the signal region reveals only very few protons in the sample (Fig. 59, upper row). This is expected since the exclusive production of $\mathrm{p}\overline{\mathrm{p}}$ pairs can be suppressed because of the limited energy and phase space available for pair creation.

The probability of a charged particle with $\ln\varepsilon$ and its variance $\sigma^2_{\ln\varepsilon}$ at a momentum p being of type k is given by the following expression:

$$P_k(\ln\varepsilon, \sigma_{\ln\varepsilon}|p) = \frac{1}{\sigma_{\ln\varepsilon}\sqrt{2\pi}} \exp\left[-\frac{(\ln\varepsilon - \langle\ln\varepsilon\rangle_k(p))^2}{2\sigma^2_{\ln\varepsilon}}\right]. \tag{28}$$

A particle-pair is identified of type hh if

$$P_{1,\mathrm{h}}P_{2,\mathrm{h}} > 10 \cdot P_{1,i}P_{2,i} \qquad \text{and} \qquad P_{1,\mathrm{h}}P_{2,\mathrm{h}} > 10 \cdot P_{1,j}P_{2,j}, \tag{29}$$

where ii and jj would be the other types of possible particle-pairs. If no type choice fulfils any of the above conditions, the particle-pair is left unidentified.

Signal events with identified $\pi^+\pi^-$, $\mathrm{K}^+\mathrm{K}^-$, and $\mathrm{p}\overline{\mathrm{p}}$ pairs (Fig. 59, middle and lower rows) indicate that their selection is efficient with high purity. The plot of unidentified pairs (bottom right) shows that these events usually contain pairs of high momentum particles, and for those the clear identification is not possible: these events are not used in data processing, but are corrected for.

For the calculation of two-track identification efficiencies, the knowledge of $\sigma_{\ln\varepsilon}$ is essential. Its distributions are extracted from data in bins of (η, p_T) where the η axis in the range $[-3, 3]$ is divided into 60 bins, while the p_T range $[0, 2\,\mathrm{GeV}]$ has 40 bins. Distributions of $\sigma_{\ln\varepsilon}$ as a function of transverse momentum p_T in some selected η ranges for charged reconstructed pions, kaons, and protons are shown in Figs. 60, 61, and 62.

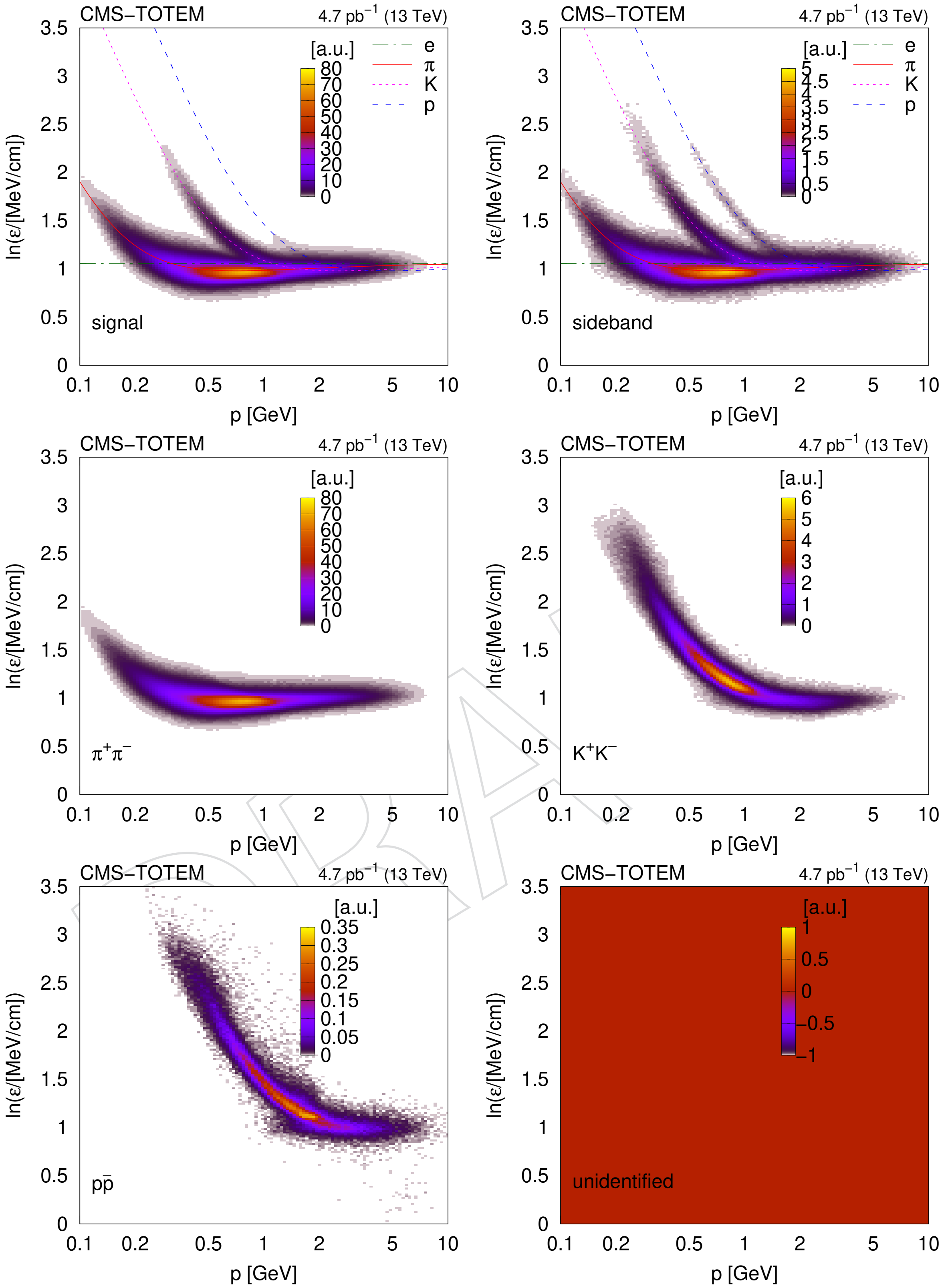

Figure 59: Distribution of $\ln \varepsilon$ as a function of total momentum p, for charged reconstructed particles in selected two-track events (signal, sideband, identified $\pi^+\pi^-$, K^+K^-, $p\bar{p}$, and unidentified). (ε is the most probable energy loss rate at a reference path length $l_0 = 450\ \mu$m). The colour scale is shown in arbitrary units and is linear. The curves show the expected $\ln \varepsilon$ for electrons, pions, kaons, and protons (Eq. (34.12) in Ref. [1]).

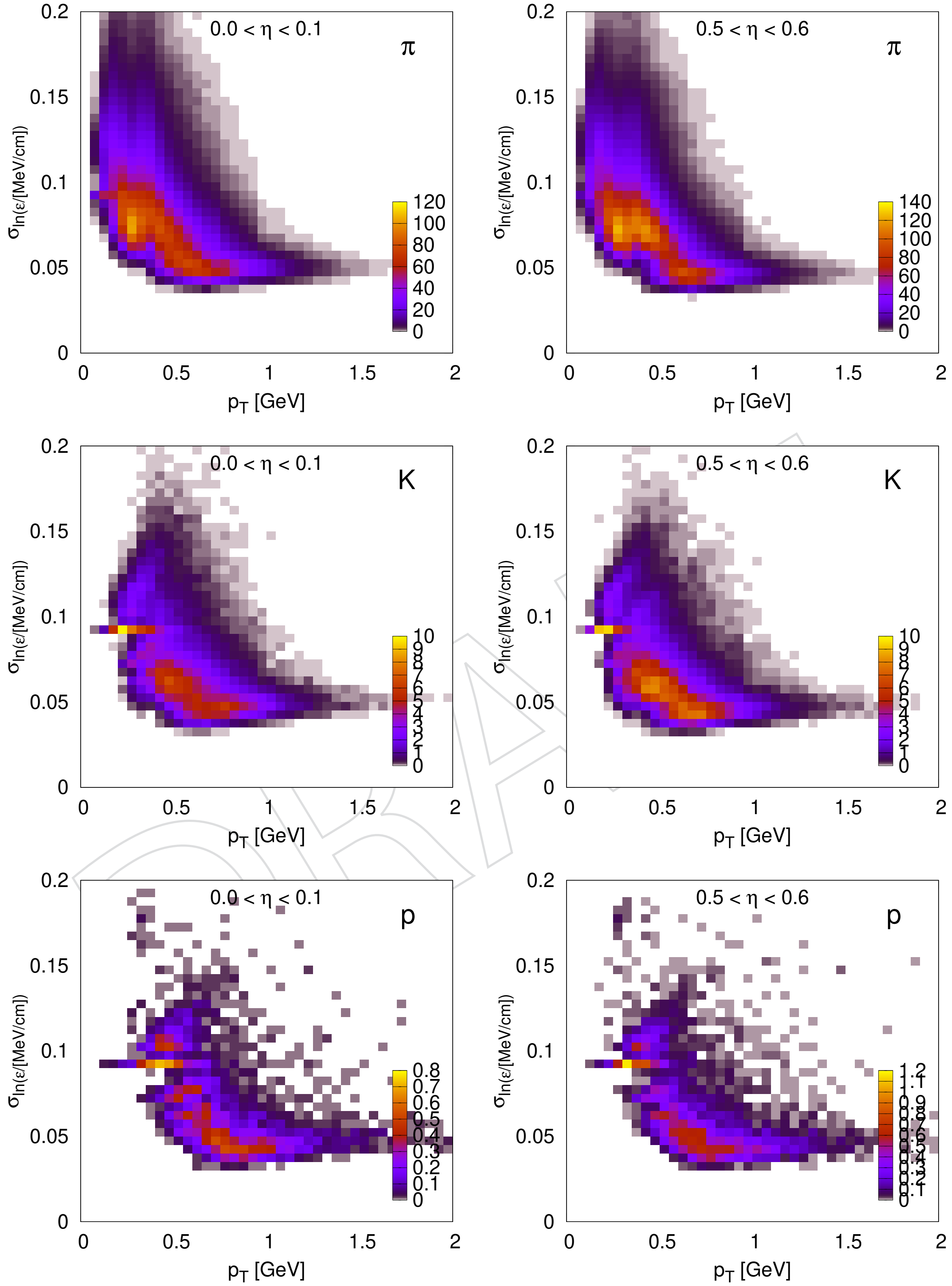

Figure 60: Distribution of $\sigma_{\ln \varepsilon}$ as a function of transverse momentum p_{T} in some selected η ranges ($0.0 < \eta < 0.1$ and $0.5 < \eta < 0.6$), for charged reconstructed particles pions, kaons, and protons. The colour scale is shown in arbitrary units and is linear.

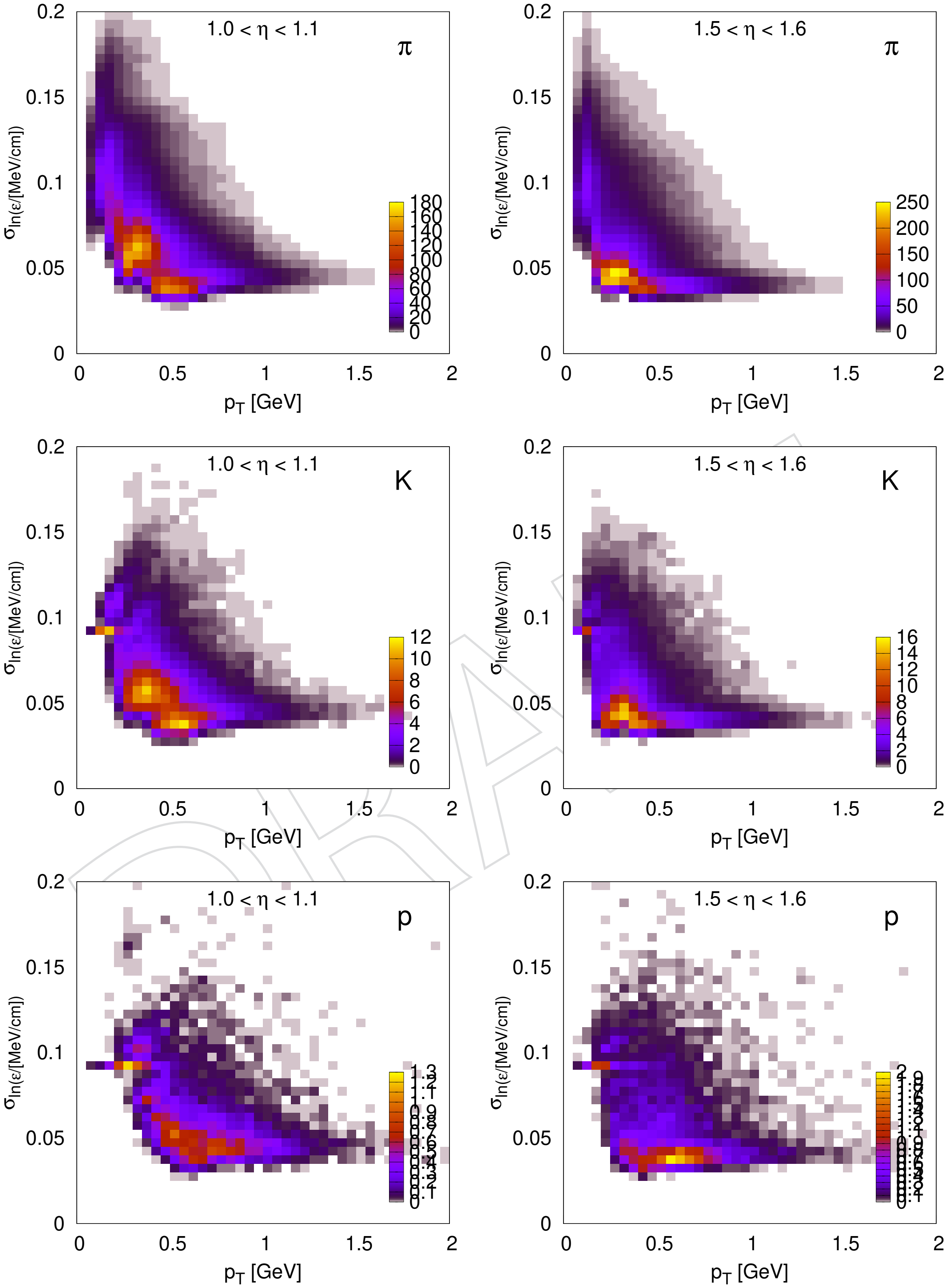

Figure 61: Distribution of $\sigma_{\ln\varepsilon}$ as a function of transverse momentum p_{T} in some selected η ranges ($1.0 < \eta < 1.1$ and $1.5 < \eta < 1.6$), for charged reconstructed particles pions, kaons, and protons. The colour scale is shown in arbitrary units and is linear.

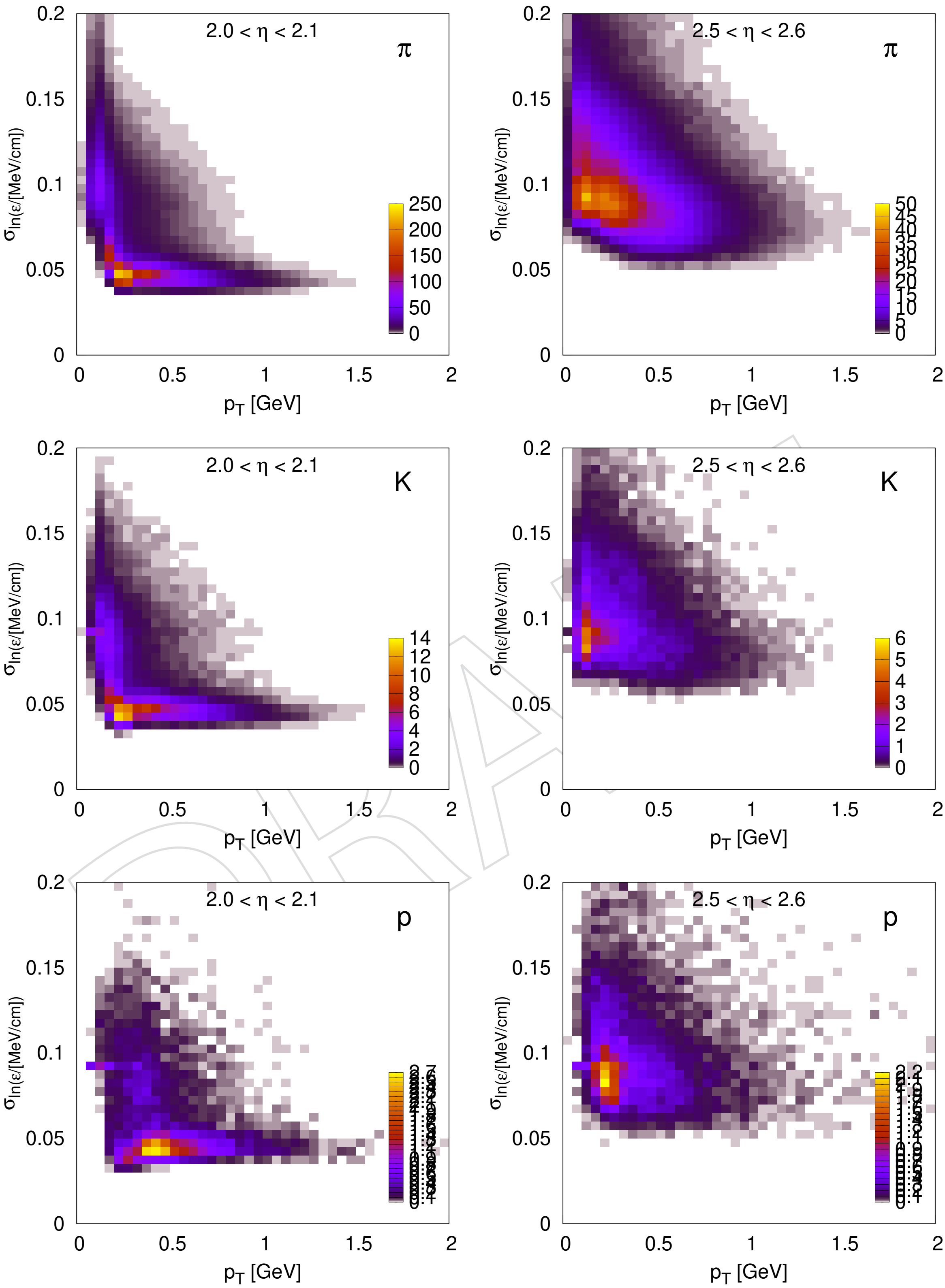

Figure 62: Distribution of $\sigma_{\ln \varepsilon}$ as a function of transverse momentum p_{T} in some selected η ranges ($2.0 < \eta < 2.1$ and $2.5 < \eta < 2.6$), for charged reconstructed particles pions, kaons, and protons. The colour scale is shown in arbitrary units and is linear.

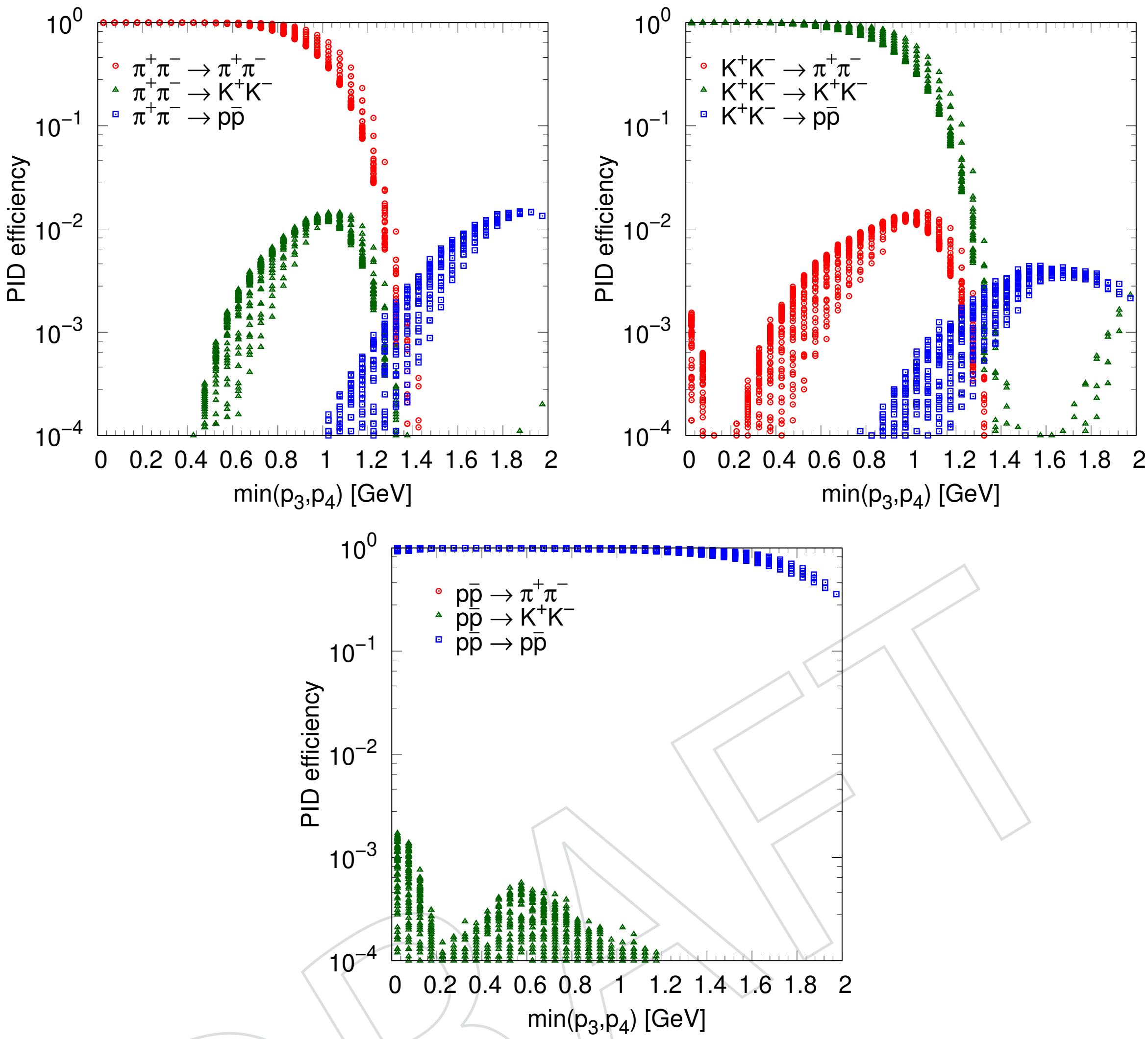

Figure 63: Demonstration of particle identification capabilities for particle-antiparticle hadron pairs. Identification (h^+h^- identified as $\to$ h^+h^-) and misidentification (h^+h^- identified as $\to$ i^+i^-) efficiencies as function of the minimal total momentum of the particle pair.

Identification efficiencies. In order to demonstrate particle identification capabilities for particle-antiparticle hadron pairs, a detailed simulation was set up, generating oppositely charged particles ($\pi^+\pi^-$, K^+K^-, and $p\bar{p}$) uniformly in the range $-2.5 < \eta < 2.5$ in narrow 50 MeV bins of total momentum (p_3, p_4) up to 2 GeV, 10^5 events each. While the most probable value of ε was taken from a model [1], using the density correction δ according to [29], its relative standard deviation was sampled from the measured distribution of $\sigma_{\ln\varepsilon}$ (Figs. 60-62). Identification (and misidentification) efficiencies as function of the minimal total momentum of the particle pair are shown in Fig. 63. (Instead of plotting as functions of (p_3, p_4), the minimal total momentum is a better variable to differentiate.) The efficiencies are close to 100% at low momenta, slowly reduced when going towards and past 1 GeV (pions and kaons) or 2 GeV (protons). The probability of misidentification is low, in the most populated low momentum regions it stays below a percent.

5.3 Calculation of the combined, silicon tracker-related corrections

The combined, silicon tracker-related, efficiencies with regard to high level trigger, detection, and identification are calculated in the four-dimensional space of $[\phi, m, (\cos\theta, \varphi)_{\text{GJ}}]$, separately for each (p_{1T}, p_{2T}) bin, using generated exclusive two-track events. Here

- ϕ is the azimuth angle between the transverse momentum vectors of the scattered protons,
- m is the invariant mass of the centrally produced h^+h^- system,
- $(\cos\theta, \varphi)_{\text{GJ}}$ are (cosine of the) polar and azimuthal angles of particle 3 (h^+) in the Gottfried-Jackson frame.

These events are generated with

- uniform y distribution in the range $[-y_{\max}, y_{\max}]$ (Sec. 1.3);
- uniform $p_{1,T}$ and $p_{2,t}$ distribution of the scattered protons in the range $[0.2, 0.8\,\text{GeV}]$ with 50 MeV binwidth;
- uniform ϕ distribution in the range $[0, \pi]$ in 18 bins;
- uniform m distribution in the range $[2m_{\pi,\text{K},\text{p}}, 4\,\text{GeV}]$ with 20 MeV binwidth;
- uniform $(\cos\theta, \varphi)_{\text{GJ}}$ distribution with 10 bins in $\cos\theta$ and with 10 bins in φ directions;
- using the above deduced single-track, two-track and identification efficiencies.

During event generation we use the kinematic relations deduced in Sec. 1.2, especially Eq. (14). In each generated event, the combined tracking, high level trigger and particle identification efficiencies are calculated (based on Secs. 5.1 and 5.2). For a better convergence the random values are obtained from Sobol's quasirandom sequence generator.[7]

The distributions of combined efficiency values based on the entire $[\phi, m, (\cos\theta, \varphi)_{\text{GJ}}]$ correction table for pions, kaons, and protons are shown in Fig. 64. The histograms indicate that the combined HLT-tracking-PID efficiencies are mostly in the range $0.2 - 0.8$. Events with combined tracker-related efficincies below 5% are not used in the analysis.

The coverage of the combined correction is explored in Figs. 65-68. Minimal and maximal values of combined efficiency in $[\phi, m, (\cos\theta, \varphi)_{\text{GJ}}]$ space for a given $(p_{1,T}, p_{2,T})$ bin, separately for each roman pot trigger configuration (TB, BT, TT, and BB). Plots for pions, kaons, and protons are shown in rows. (Plots for other $(p_{1,T}, p_{2,T})$ bins are similar.)

The efficiencies are nonzero, are usually above 10% reaching up to 90%, with small regions being below 1% which are

- the first 20 MeV wide mass bin at the threshold $2m_{\pi/\text{K}/\text{p}}$ at $\phi \approx \pi$;
- and in the case of kaons at $m > 2.5 - 2.7\,\text{GeV}$ because of narrowed particle identification capabilities are higher particle momenta.

In summary we have a nonzero coverage in $[\phi, m, (\cos\theta, \varphi)_{\text{GJ}}]$ space through most, but at least one, of the roman pot trigger configurations. During physics analysis a given event is weighted by the factor

[7] The necessary software taken from `https://github.com/DaanVanVugt/sobseq` with a set of direction numbers `new-joe-kuo-6.21201` from `https://web.maths.unsw.edu.au/~fkuo/sobol/`, based on [31].

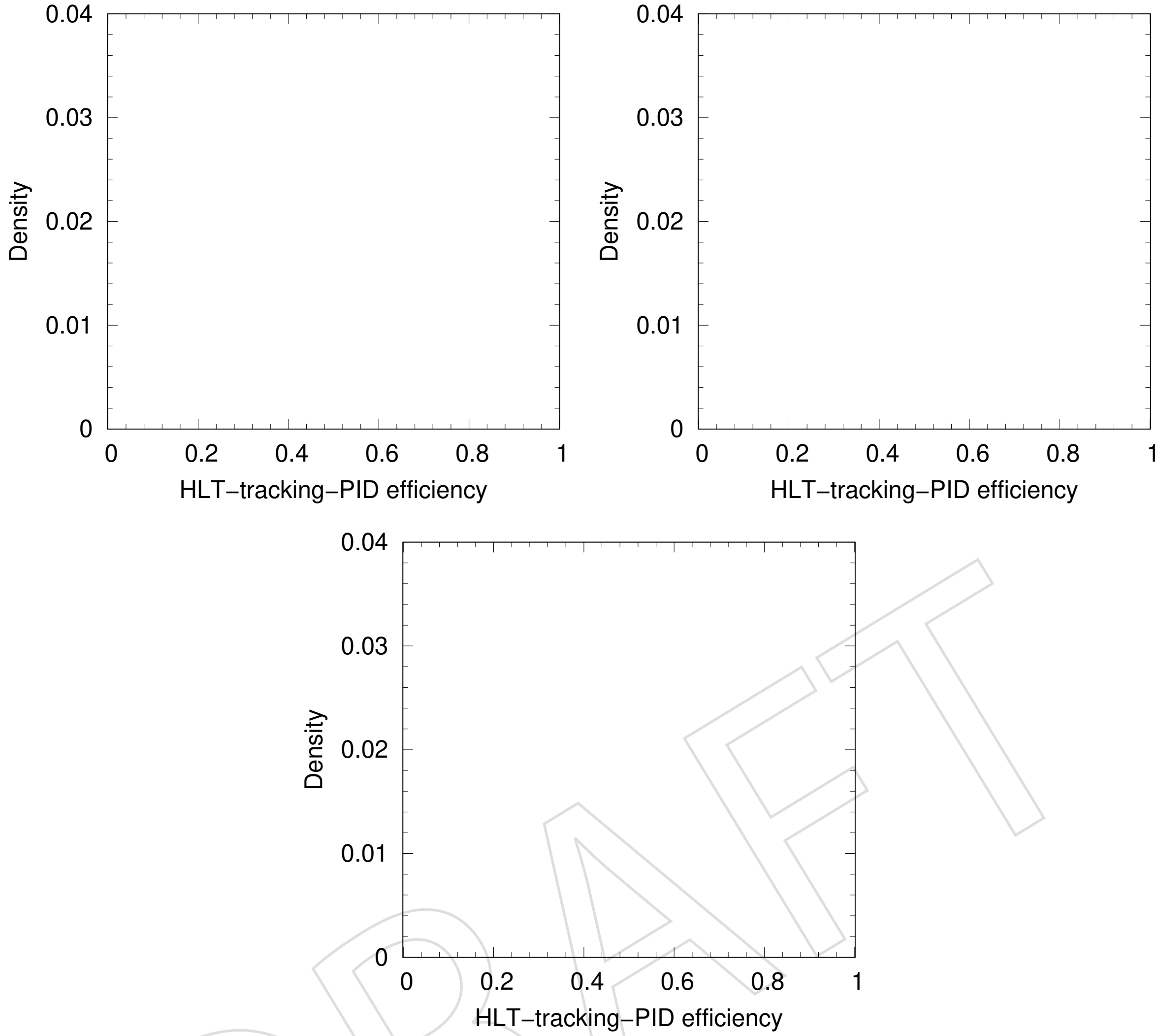

Figure 64: Distribution of combined efficiency values based on all $[\phi, m, (\cos\theta, \varphi)_{\text{GJ}}]$ correction tables in all $(p_{1,T}, p_{2,T})$ bins for pions, kaons, and protons.

$$\frac{\text{sign(classification)}}{L_{\text{int}}(\text{topology})} \times \frac{\prod \text{tracklet weights}}{\text{angular coverage}}_{\text{roman pots}} \times \frac{1}{\text{combined efficiency}}_{\text{tracker}}. \tag{30}$$

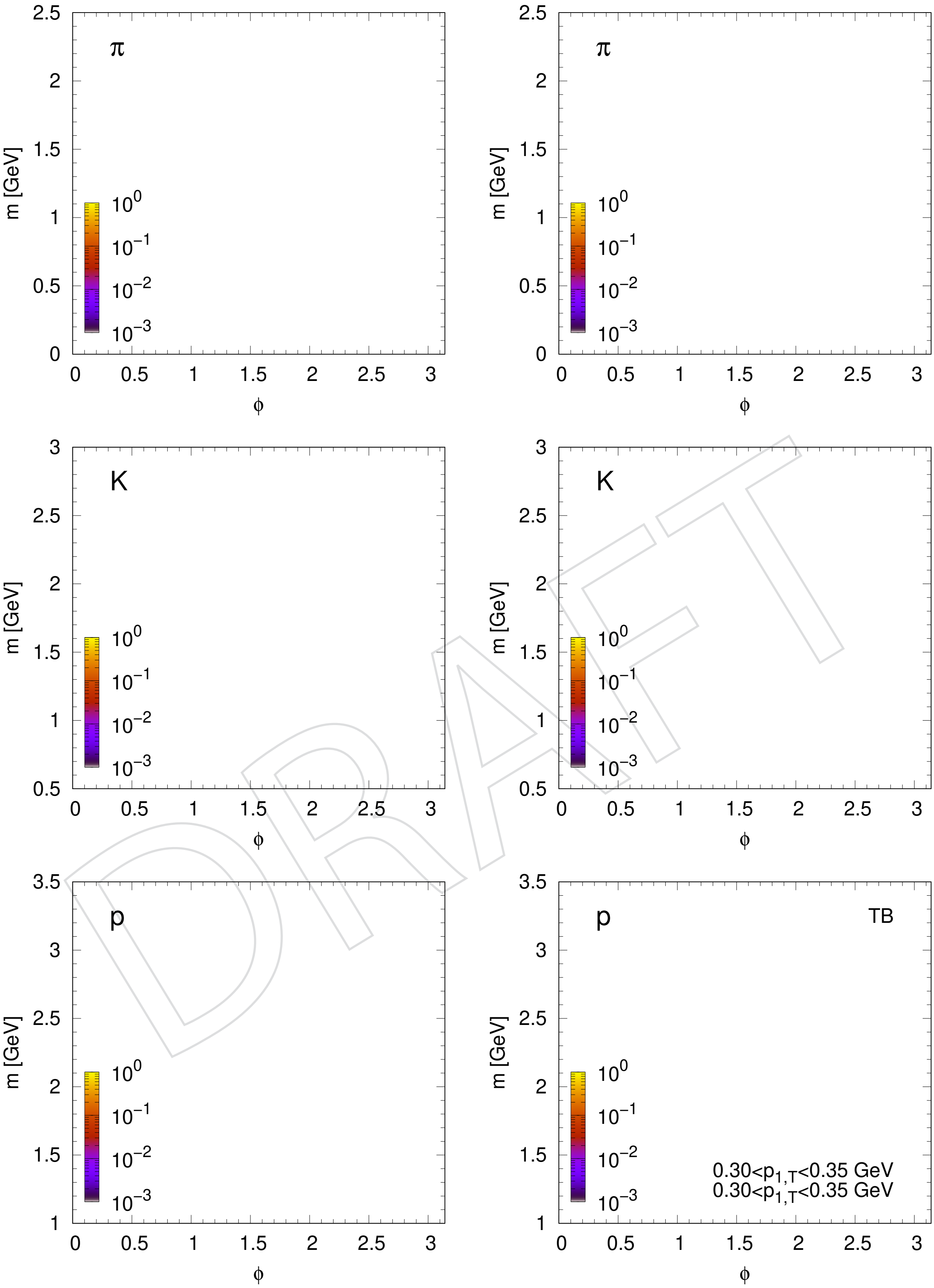

Figure 65: Minimal (left) and maximal (right) values of combined efficiency in $[\phi, m, (\cos\theta, \varphi)_{\mathrm{GJ}}]$ space for a given $(p_{1,T}, p_{2,T})$ bin and the TB roman trigger topology. Plots for pions, kaons, and protons are shown in rows.

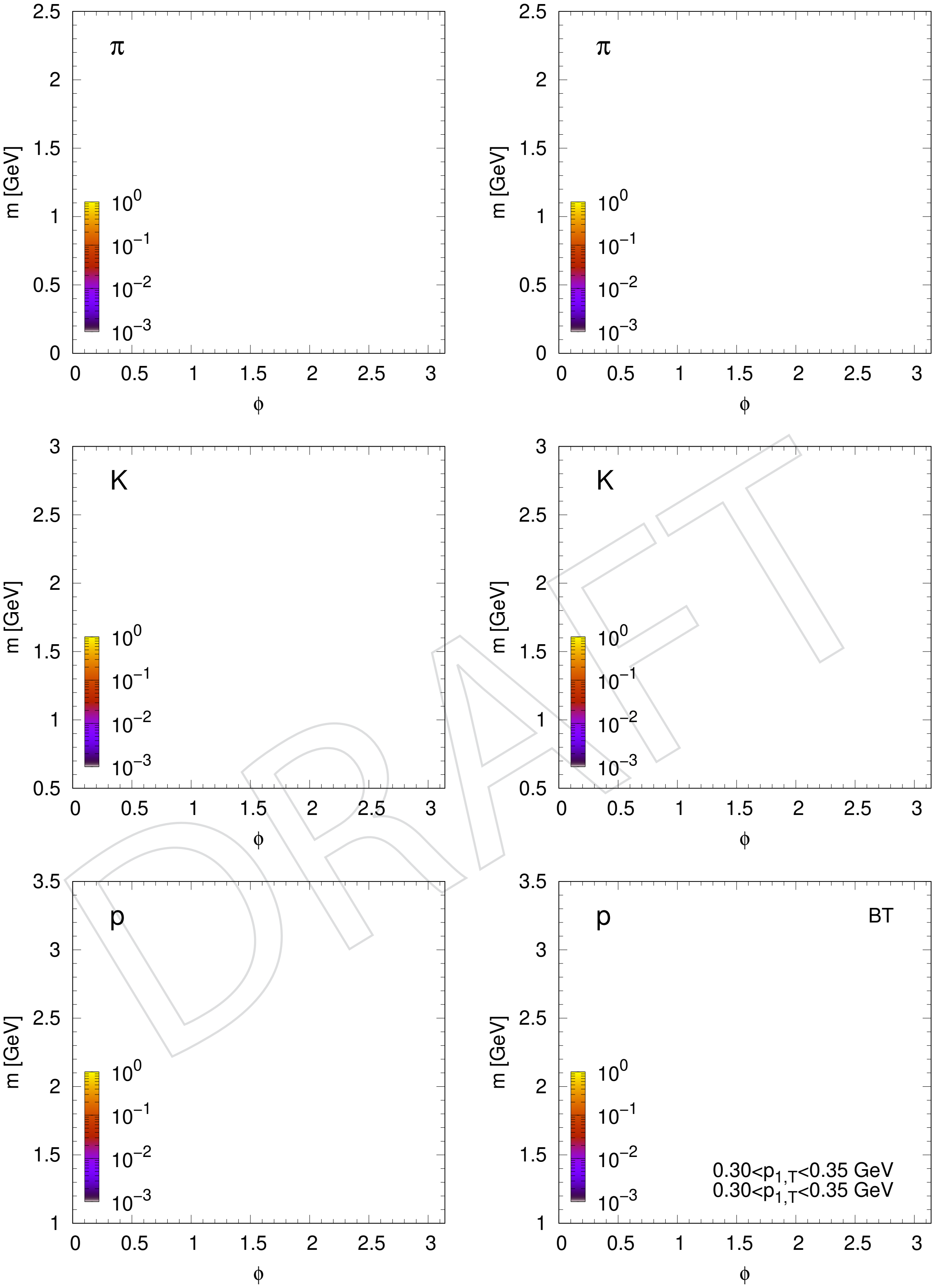

Figure 66: Minimal (left) and maximal (right) values of combined efficiency in $[\phi, m, (\cos\theta, \varphi)_{\mathrm{GJ}}]$ space for a given $(p_{1,T}, p_{2,T})$ bin and the BT roman trigger topology. Plots for pions, kaons, and protons are shown in rows.

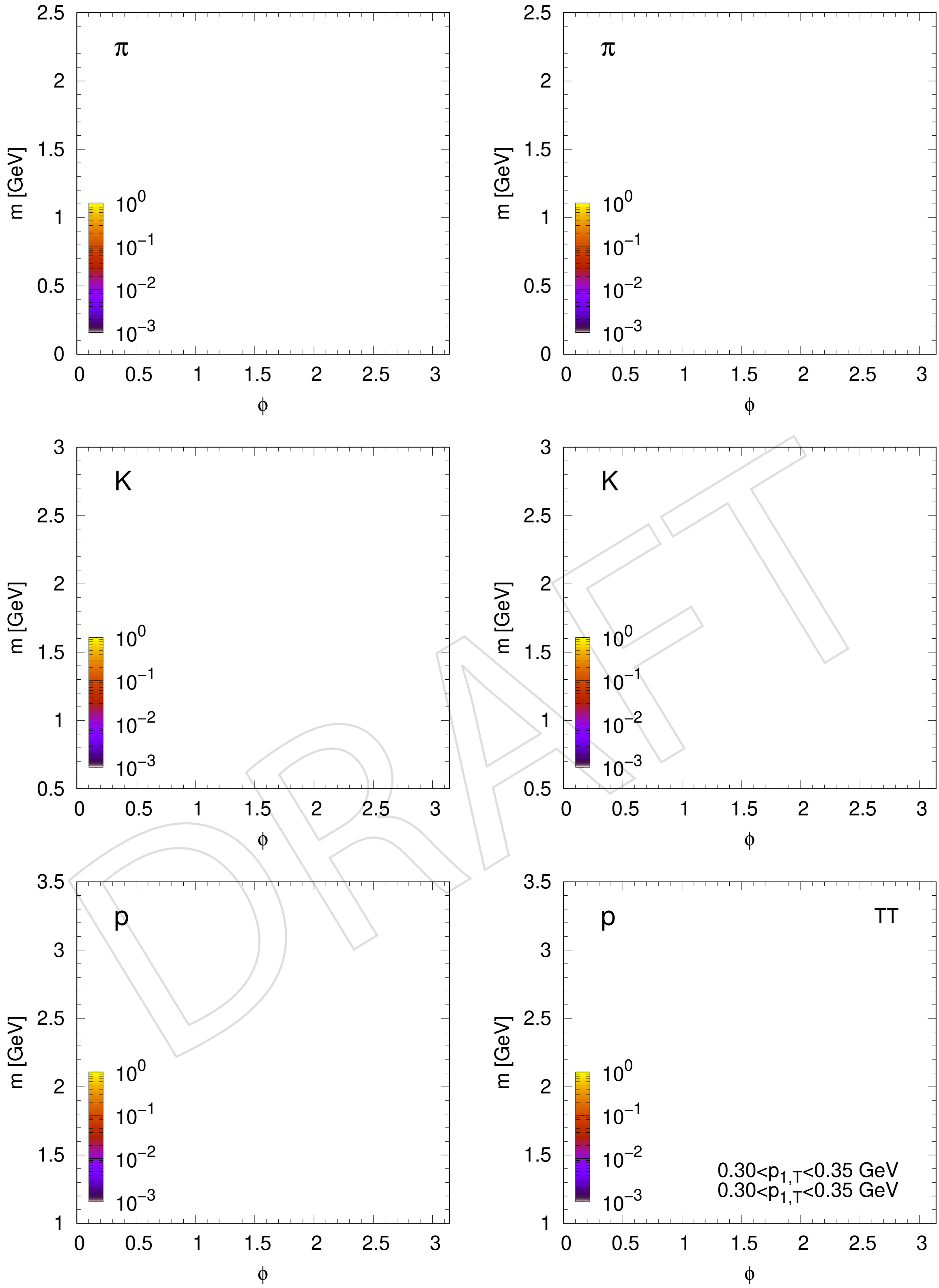

Figure 67: Minimal (left) and maximal (right) values of combined efficiency in $[\phi, m, (\cos\theta, \varphi)_{\mathrm{GJ}}]$ space for a given $(p_{1,T}, p_{2,T})$ bin and the TT roman trigger topology. Plots for pions, kaons, and protons are shown in rows.

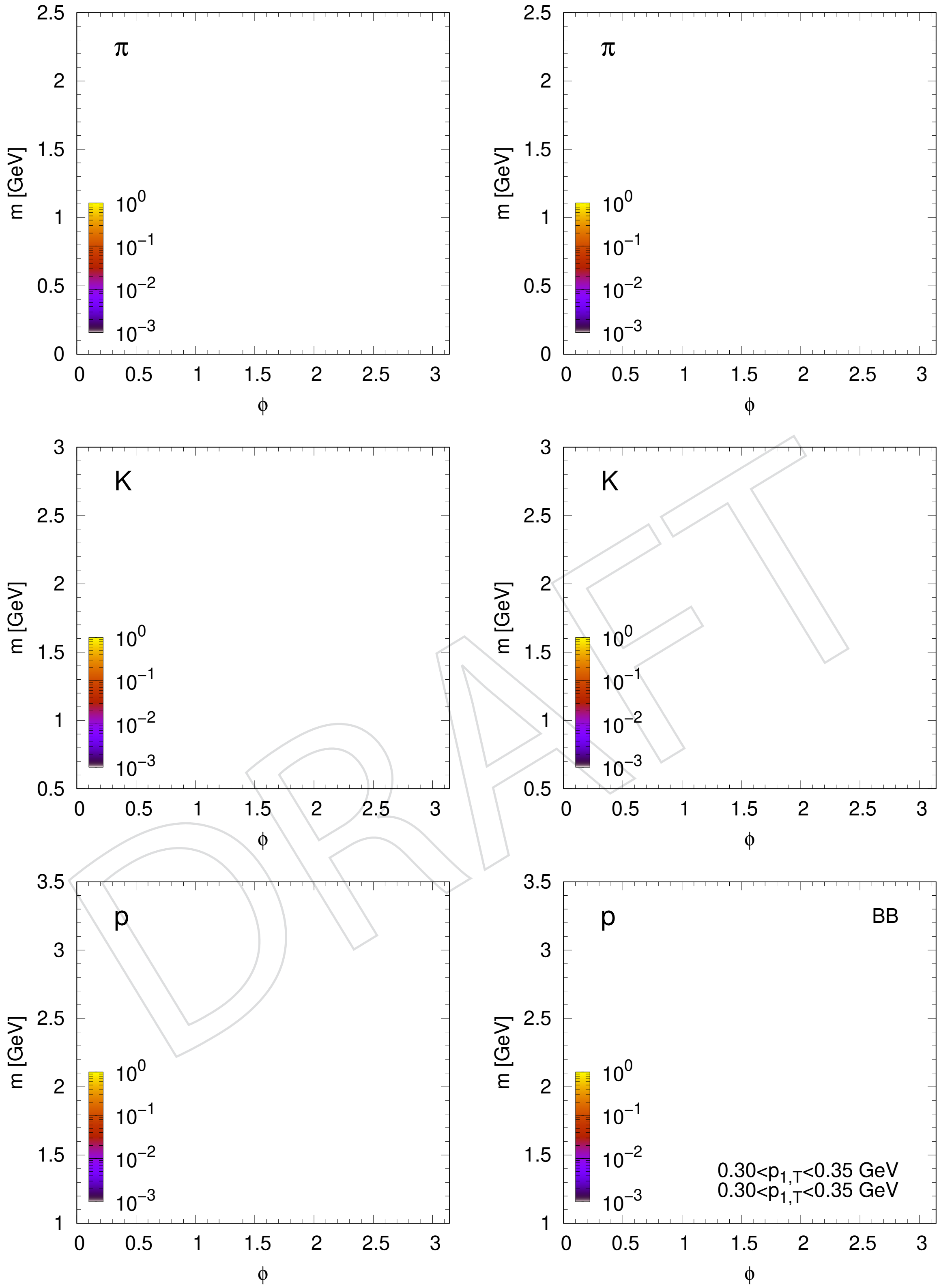

Figure 68: Minimal (left) and maximal (right) values of combined efficiency in $[\phi, m, (\cos\theta, \varphi)_{GJ}]$ space for a given $(p_{1,T}, p_{2,T})$ bin and the BB roman trigger topology. Plots for pions, kaons, and protons are shown in rows.

5.4 Momentum and mass resolutions

Transverse momentum. The mean shift Δp_{T} and the resolution $\sigma_{p_{\mathrm{T}}}$ of the p_{T} measurement for pions, kaons, and protons as a function of (η, p_{T}) are shown in Figs. 69 and 70. They are extracted from the simulation discussed in Sec. 5.1.

The bias for pions is very small, usually well below 5 MeV. For kaons the shift can reach to -10 MeV and $+5$ MeV, while for protons it is -15 MeV and 5 MeV. The shifts for kaons and protons are due to the fact that all particles are reconstructed with the pion mass assumption while the physical effects of particle passage through matter (energy loss and multiple scattering) is mass and momentum dependent. This way the shifts should depend on the total momentum ($p = p_{\mathrm{T}} \cosh \eta$), which is clearly visible in the plots.

The resolutions also show some variability. For pions they are mostly between $5 - 15$ MeV but reach up to 30 MeV at the high η and high p_{T} corner. For kaons the resolutions is mostly in the range $10 - 20$ MeV, whereas in the case of protons we find values of $15 - 25$ MeV. The increase with mass is the consequence of more multiple scattering.

Taking an approximate average value of $\sigma_{p_{\mathrm{T}}} \approx 10$ MeV, we can revisit the momentum sum distributions $\sum p_x$ and $\sum p_y$ (Sec. 6). There we have seen resolutions of $s_y \approx 75 - 85$ MeV and $s_x \approx 30$ MeV. The contribution from the central two-hadron system is in the range $10 -$ 15 MeV, a decisively smaller value. In conclusion, the uncertainties seen in momentum sum distributions mostly come from the proton momentum reconstruction of the roman pot system.

Invariant mass. Based on the previous study on the bias and resolution of the transverse momentum measurement, the bias and resolution of the invariant mass of the central two-hadron system is explored.

The mean shift Δm and the resolution σ_m of the invariant mass measurement as a function of daughter decay momentum $p^* = [(M/2)^2 - m^2_{\pi/\mathrm{K},/Pp}]^{1/2}$ for pions, kaons, and protons is shown for three selected $(p_{1,T}, p_{2,T})$ bins in Figs. 71-73. The plots are prepared using data with proper event weight, hence they reflect the true distribution of other kinematic variables.

For pions the shift is proportional to p^* and reaches $3 - 4$ MeV at 1 GeV, while it is in the region $(-2, 0)$ MeV for kaons and protons. The resolutions have a square-root-type dependence on p^* and reach 15 MeV at about 0.6 GeV, similarly for all particle types. In summary, the observed shifts are much smaller than the applied binwidth of 20 MeV, but the resolutions get comparable to the binwidth for higher masses. When studying quickly changing mass distributions (narrow resonances) these effects should be properly unfolded, but for slowly changing distributions (nonresonant continuum) an unfolding is not needed.

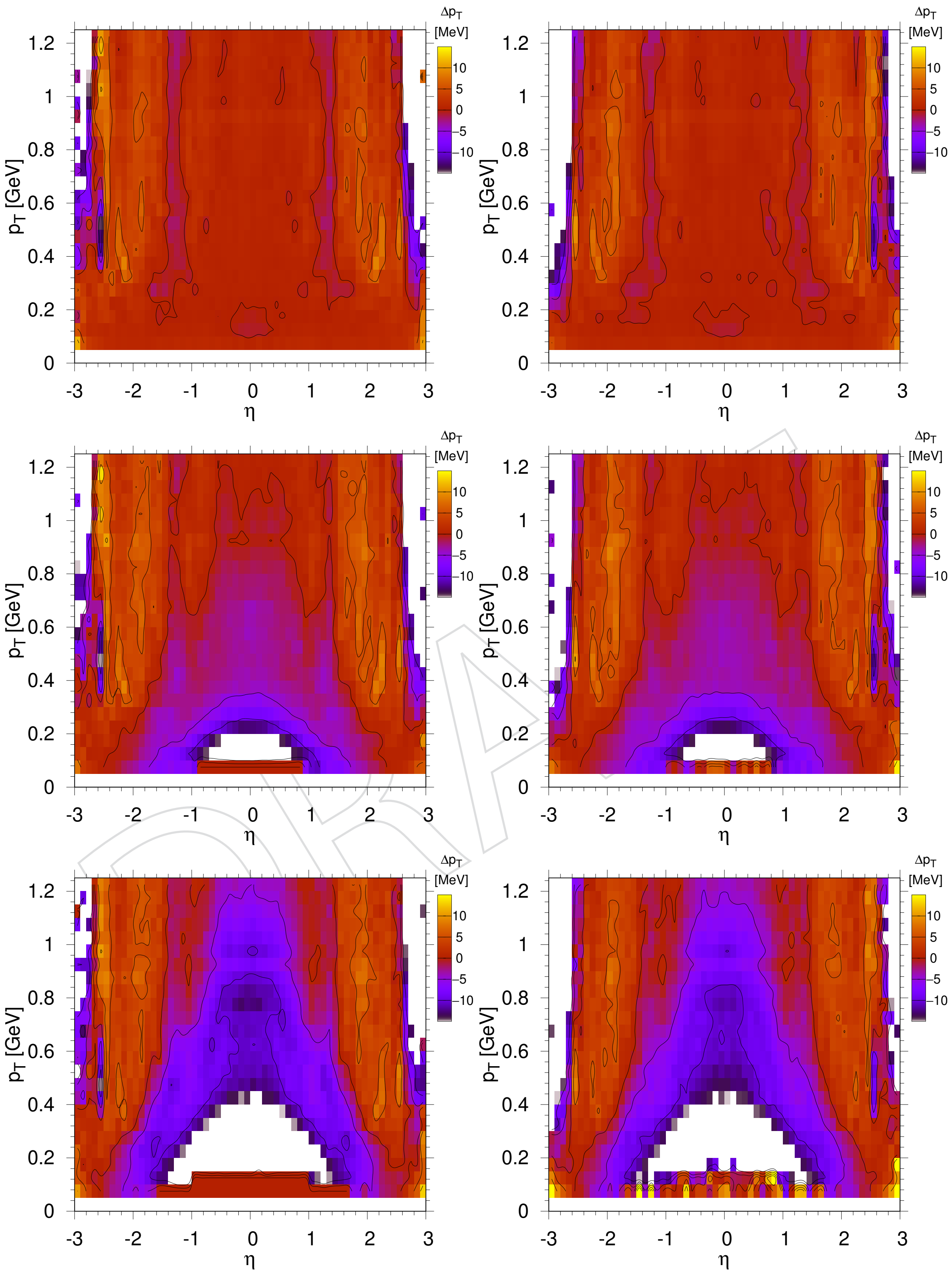

Figure 69: The mean shift Δp_{T} of the p_{T} measurement for pions (upper row), kaons (middle row), and protons (lower row) as a function of (η, p_{T}).

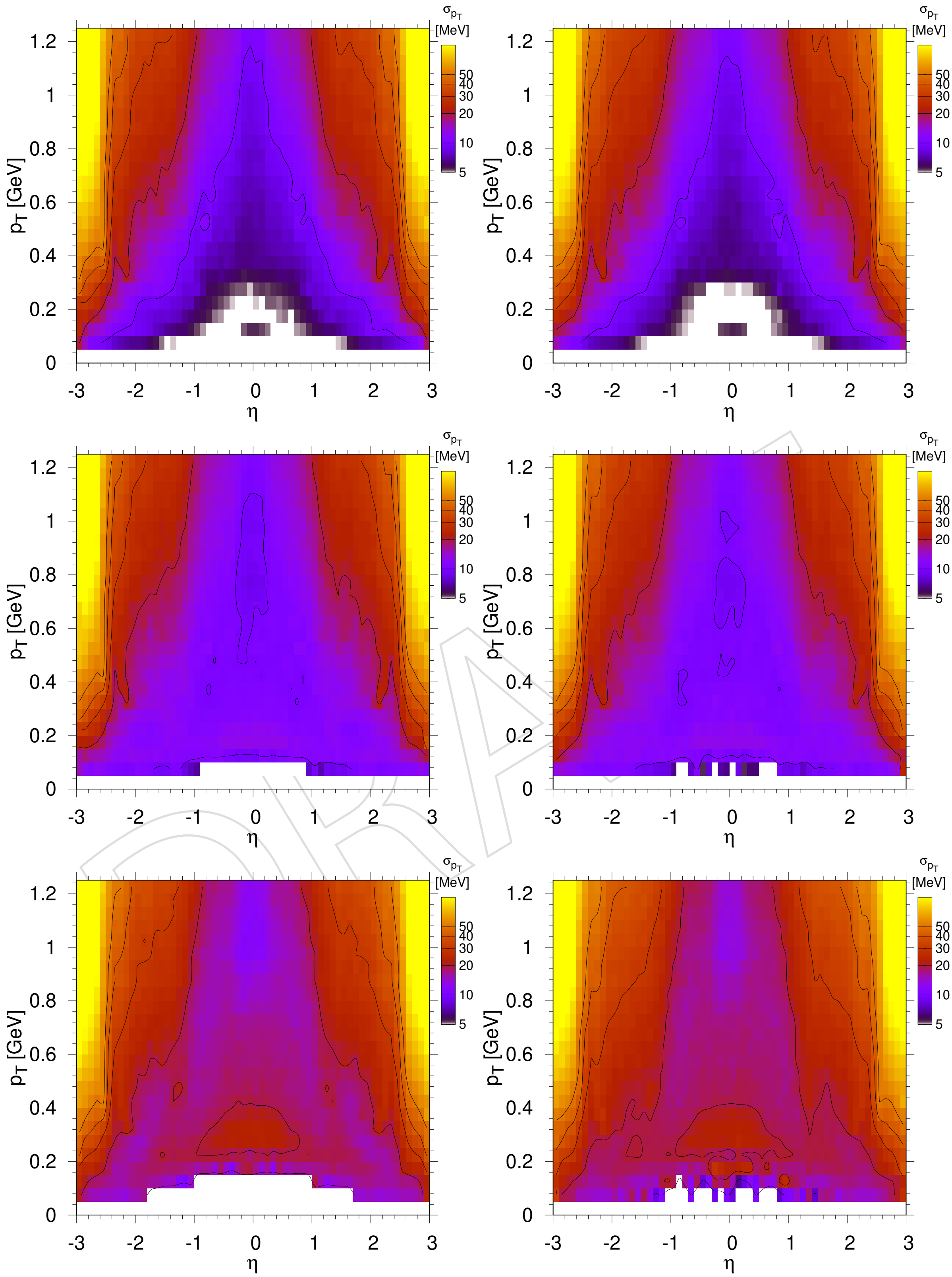

Figure 70: The resolution σ_{p_T} of the p_T measurement for pions (upper row), kaons (middle row), and protons (lower row) as a function of (η, p_T).

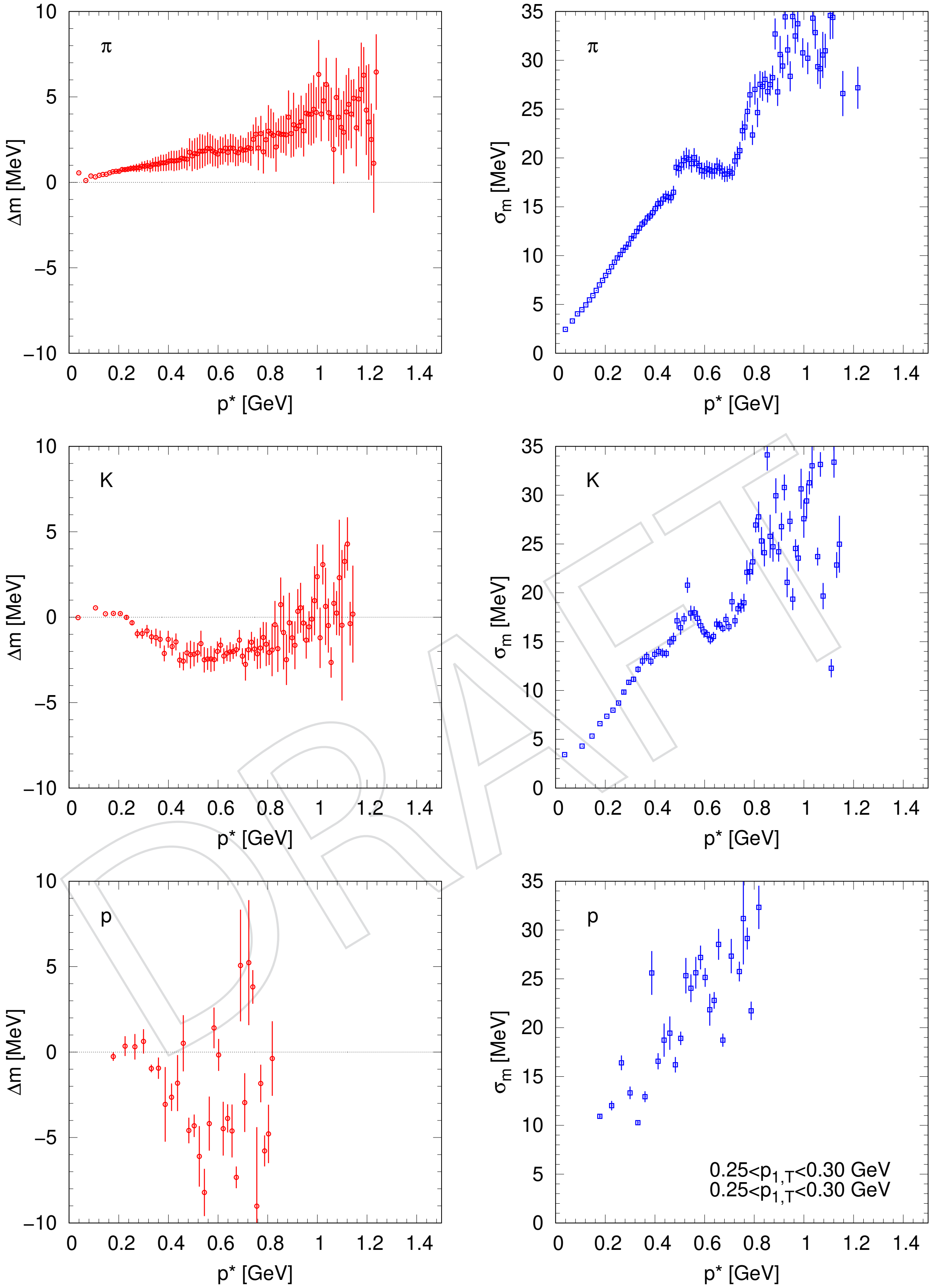

Figure 71: The mean shift Δm (left) and the resolution σ_m (right) of the invariant mass measurement as a function of daughter decay momentum q^* for pions, kaons, and protons for a selected $(p_{1,T}, p_{2,T})$ bin.

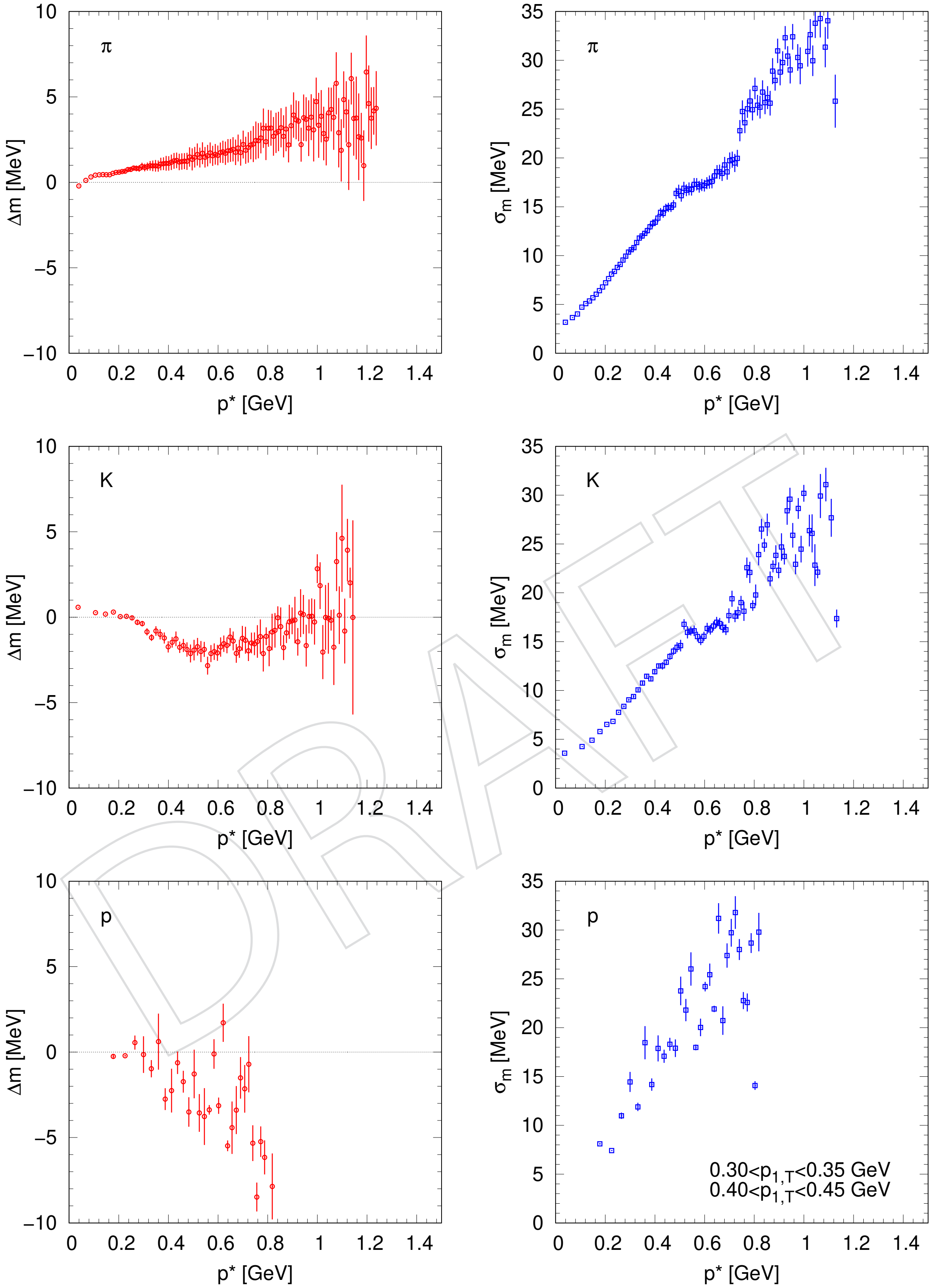

Figure 72: The mean shift Δm (left) and the resolution σ_m (right) of the invariant mass measurement as a function of daughter decay momentum q^* for pions, kaons, and protons for a selected $(p_{1,T}, p_{2,T})$ bin.

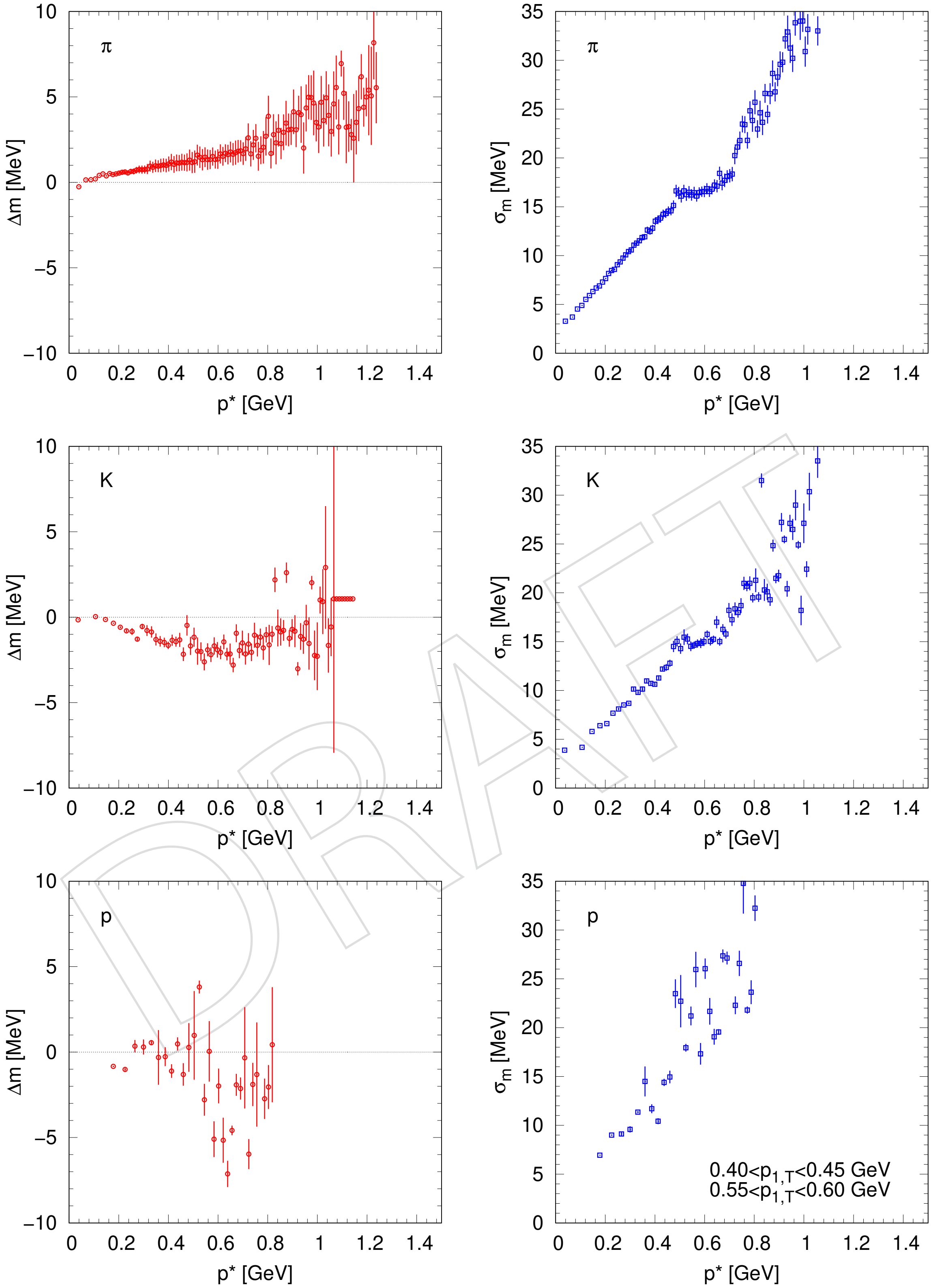

Figure 73: The mean shift Δm (left) and the resolution σ_m (right) of the invariant mass measurement as a function of daughter decay momentum q^* for pions, kaons, and protons for a selected $(p_{1,T}, p_{2,T})$ bin.

6 Event classification

The identification of exclusive events is based on momentum conservation in the transverse plane. In some way we need to require $\sum p_x \approx 0$ and $\sum p_y \approx 0$ for the sum on all four detected particles, since the incoming protons also had zero total momentum.

Momentum sums. Distributions of the sum of scattered proton momenta $(\sum_2 p_x, \sum_2 p_y)$ for diagonally triggered events are shown in Fig. 74-top. Distributions of the sum of scattered proton and central hadron momenta $(\sum_4 p_x, \sum_4 p_y)$ shown for each trigger configuration for 2-track events are shown in Fig. 74-bottom. Both distributions are well centred on $(0, 0)$.

Distribution of the sum of scattered proton momenta vs the sum of scattered proton and central hadron momenta ($\sum_4 p_x$ vs $\sum_2 p_x$, $\sum_4 p_y$ vs $\sum_2 p_y$) shown for each trigger configuration for 2-track events in Fig. 75. The contributions of true elastic (only two scattered protons, vertical band), true central exclusive (two scattered protons and two central charged hadrons, horizontal band) are very well visible. In addition, a slanted area of non-exclusive or inelastic background is present.

Selection variables. The event selection will be based on the value and covariance of momentum sums, more precisely by using the χ value defined as

$$\chi(\vec{s}) = (\vec{s}^T V^{-1} \vec{s})^{1/2} \tag{31}$$

where $\vec{s} = \sum \vec{p}_\mathrm{T}$, V is the covariance matrix. For two-dimensional vectors in the (s_x, s_y) plane it can be written out as

$$\chi(\vec{s}) = \left(\frac{V_{yy} s_x^2 - 2 V_{xy} s_x s_y + V_{xx} s_y^2}{V_{xx} V_{yy} - V_{xy}^2} \right)^{1/2} \tag{32}$$

The $\chi[\mathrm{pp}]$ values are based on $\sum_2 \vec{p}_\mathrm{T}$, while $\chi[\mathrm{p(h^+h^-)p}]$ are computed from $\sum_4 \vec{p}_\mathrm{T}$. They follow the χ-distribution[8] with a parameterless probability density function $P(\chi) = \chi \exp(-\chi^2/2)$ and cumulative distribution function $1 - \exp(-\chi^2/2)$, in two dimensions.

[8] https://en.wikipedia.org/wiki/Chi_distribution

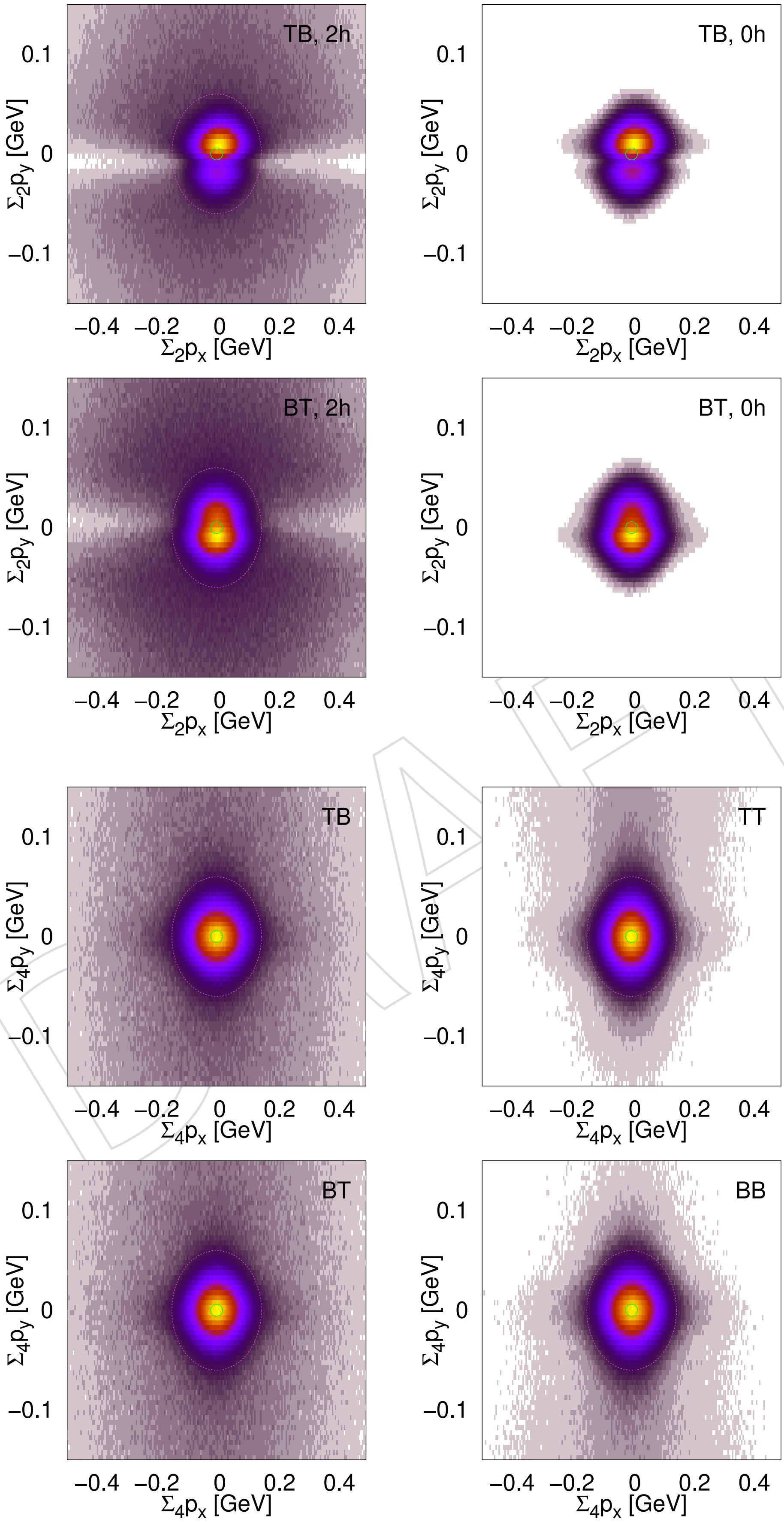

Figure 74: Top: Distribution of the sum of scattered proton momenta $(\sum_2 p_x, \sum_2 p_y)$ for diagonally triggered events (TB, BT). The two left column refers to the 2-track data set, while the right one displays the distribution based on the 0-track data set. Bottom: Distribution of the sum of scattered proton and central hadron momenta $(\sum_4 p_x, \sum_4 p_y)$ shown for various trigger configurations (TB, BT, TT, and BB) for 2-track events.

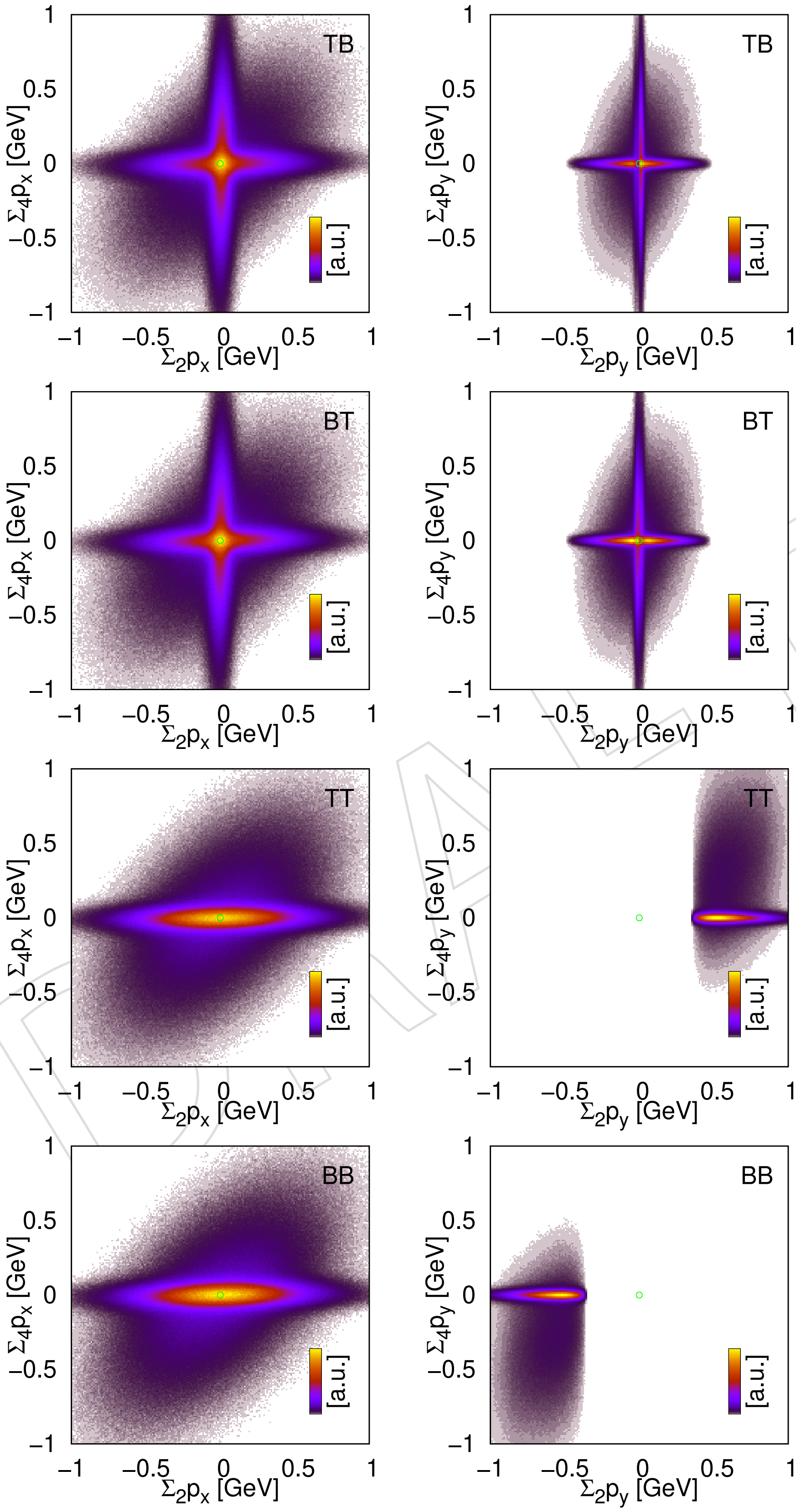

Figure 75: Distribution of the sum of scattered proton momenta vs the sum of scattered proton and central hadron momenta ($\sum_4 p_x$ vs $\sum_2 p_x$, $\sum_4 p_y$ vs $\sum_2 p_y$) shown for various trigger configurations (TB, BT, TT, and BB) for 2-track events.

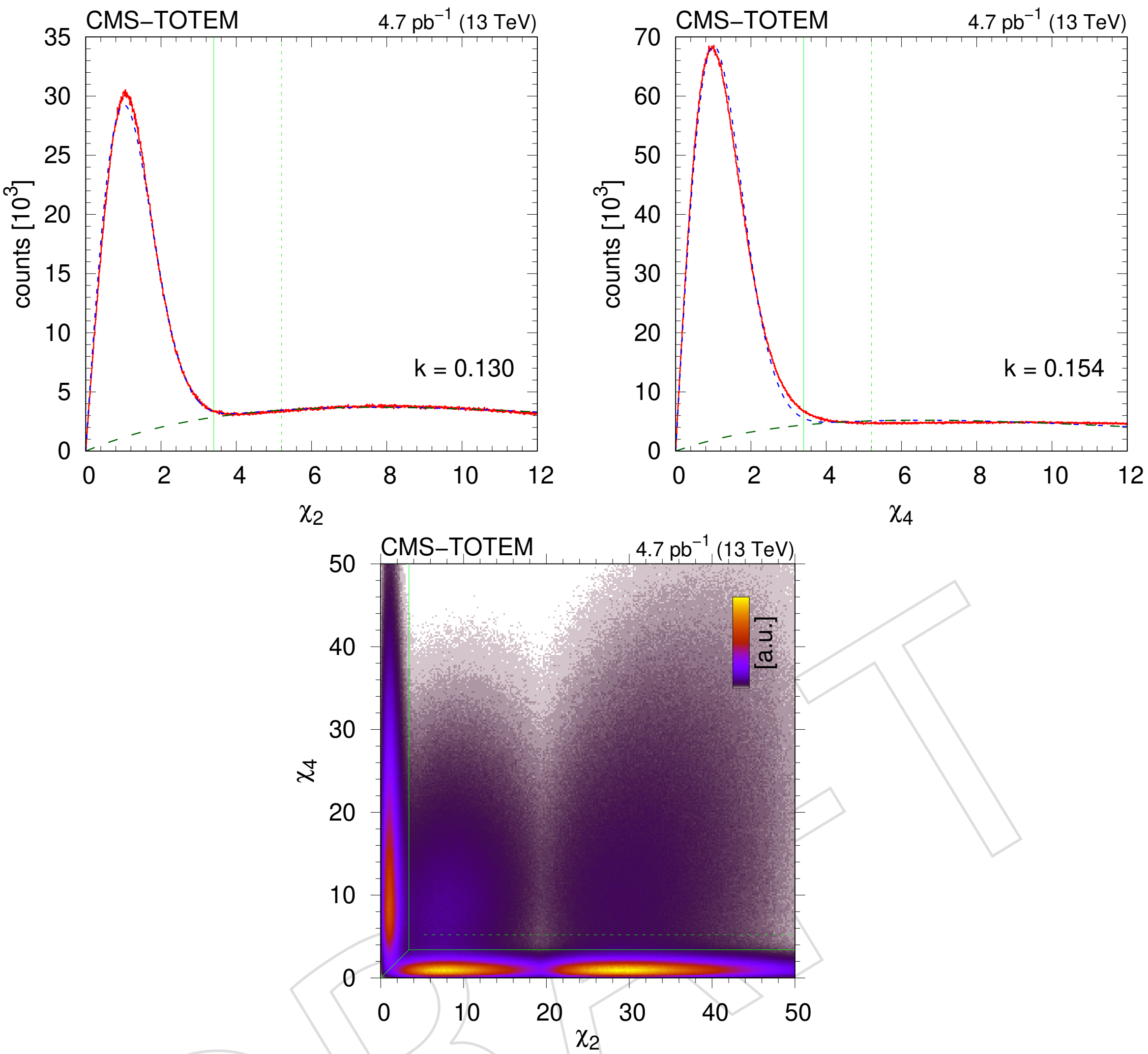

Figure 76: Top: Distribution of the selection variables $\chi[\text{pp}]$ (left) and $\chi[\text{p}(\text{h}^+\text{h}^-)\text{p}]$ (right). Fits using a two-component model (Eq. (33)) are indicated, the sum and the background component are plotted. Bottom: Joint distributions of selection variables $(\chi[\text{pp}], \chi[\text{p}(\text{h}^+\text{h}^-)\text{p}])$. Selection lines at 3.4 (green solid) and 5.2 (green dotted) are also plotted. Central exclusive signal events are at the bottom while elastic events are at the left margin. In all three plots the distributions are integrated over the angle between the scattered protons ϕ.

Distributions and joint distributions of the selection variables $\chi[\text{pp}]$ and $\chi[\text{p}(\text{h}^+\text{h}^-)\text{p}]$ are shown in Fig. 76-top, without any preselection (integrated over the angle between the scattered protons ϕ in the transverse plane). The distributions are fitted with a two-component model: a sum of a χ-distribution (signal) and phase-space motivated term (background) as

$$A\chi \exp(-\chi^2/2) + B\chi \exp(-k\chi). \tag{33}$$

The functional form fits the measured distribution quite well, with two relevant parameters only (B/A and k). Note that the first term (the χ-distribution) does not have an adjustable parameter, it is fixed.

Sideband events with weight of -1 are used to compensate for non-exclusive events in the signal region. In order for this subtraction scheme to work, we must have equal number of non-exclusive events in the signal and sideband regions. Hence the proper determination of n_{side} is crucial, discussed in the following.

We need to

- select almost all of the signal events. If the upper cut is placed at $n_{\text{top}} = 3.4$, it translates to a loss of $\exp(-n_{\text{top}}^2/2) \approx 0.0031$, well below half a percent;
- select as many sideband events as there are background in the signal region, hence for a chosen n_{top} value we need such a n_{side} which solves

$$\int_0^{n_{\text{top}}} \chi \exp(-k\chi) \mathrm{d}\chi = \int_{n_{\text{top}}}^{n_{\text{side}}} \chi \exp(-k\chi) \mathrm{d}\chi. \tag{34}$$

An event is classified (Fig. 76-bottom) if it more likely comes from signal than from the elastic+pileup background,

$$\chi[\mathrm{p(h^+h^-)p}] < \chi[\mathrm{pp}], \tag{35}$$

and within this,

- it is signal, if $\chi[\mathrm{p(h^+h^-)p}] < n_{\text{top}}$,
- it is sideband, if $n_{\text{top}} \le \chi[\mathrm{p(h^+h^-)p}] < n_{\text{side}}$.

***ϕ*-dependence.** While the choice on n_{top} is fixed at 3.4, the value of n_{side} depends on the actual distribution of $\chi[\mathrm{p(h^+h^-)p}]$ through Eq. (34). Distributions of selection variable $\chi[\mathrm{p(h^+h^-)p}]$ in bins of the angle between the scattered protons ϕ in the plane transverse to the beam direction are shown in Fig. 77. The fitted coefficient k and the position of the upper cut n_{top} for the description of the background component as a function ϕ are shown in Fig. 78 with their values listed in Table 8.

Joint distributions of selection variables $(\chi[\mathrm{pp}], \chi[\mathrm{p(h^+h^-)p}])$ are plotted in Fig. 79.

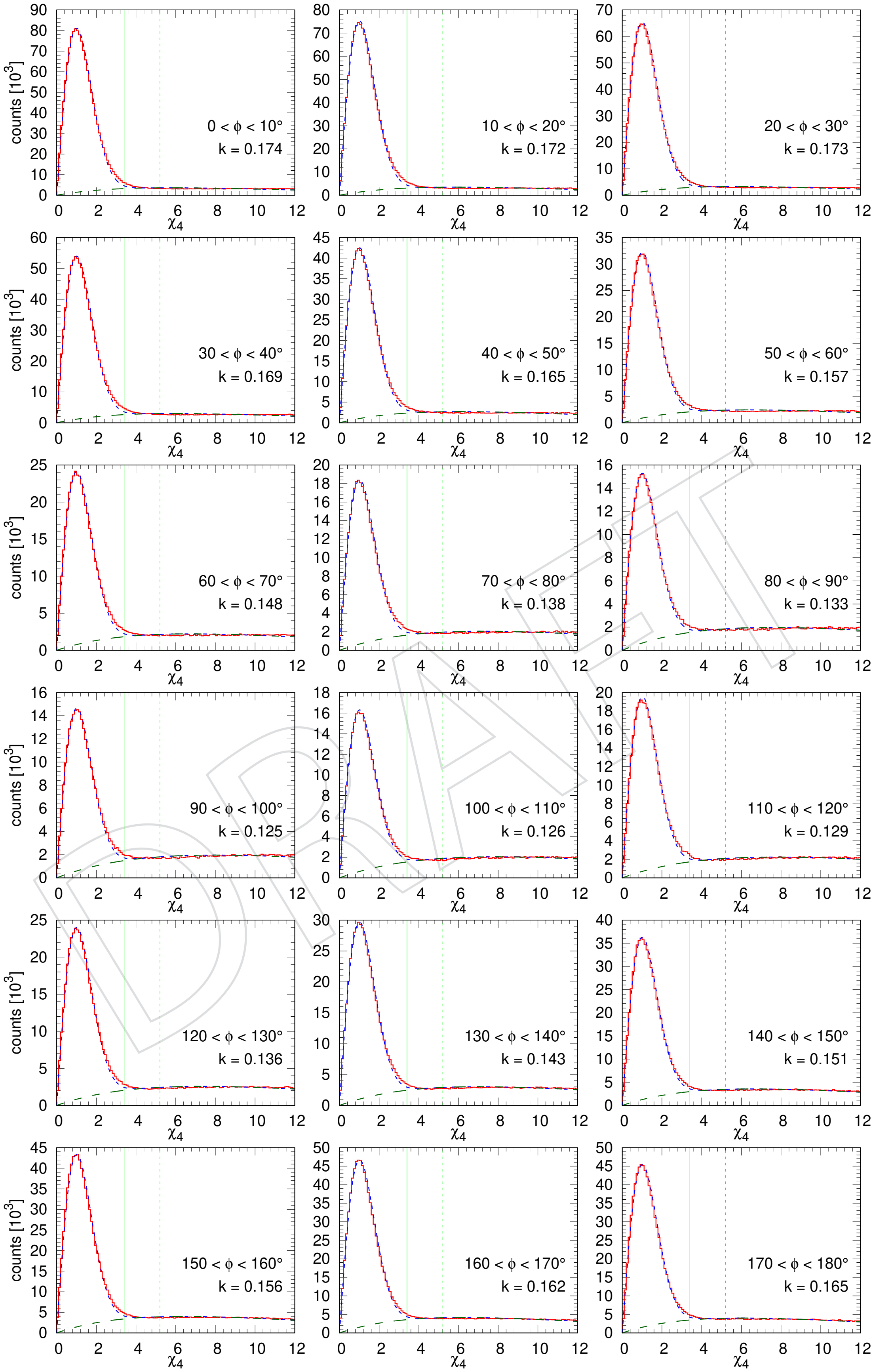

Figure 77: Distributions of selection variable $\chi[\mathrm{p}(\mathrm{h}^+\mathrm{h}^-)\mathrm{p}]$ in bins of the angle between the scattered protons ϕ in the plane transverse to the beam direction. The coefficient k is indicated in the plots.

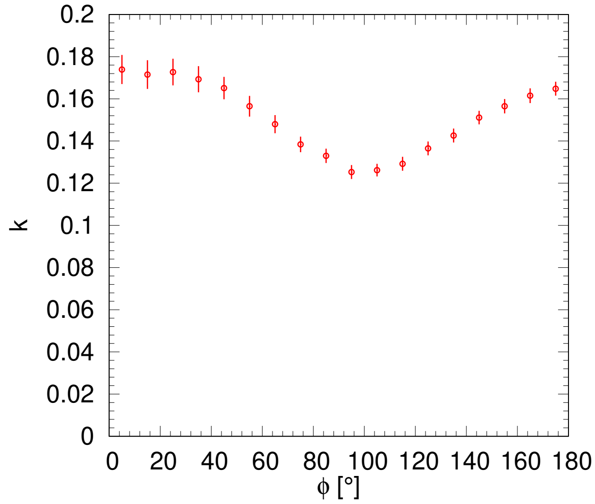

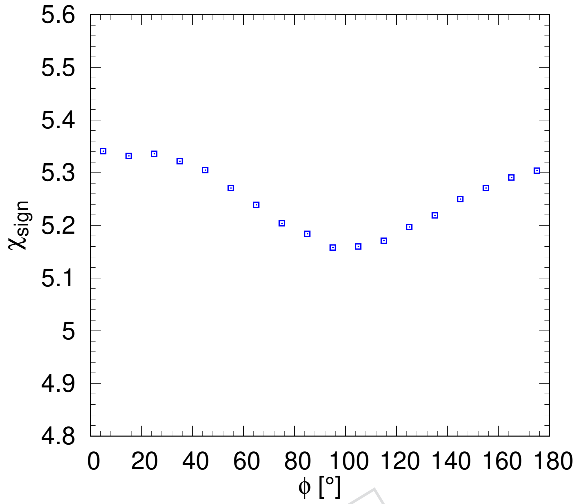

Figure 78: Coefficient k (left) and the position of the upper cut n_{top} (right) for the description of the background component as a function of the angle between the scattered protons ϕ in the plane transverse to the beam direction.

Table 8: The coefficient k and the position of the upper cut n_{top} for the description of the background component as a function of the angle between the scattered protons ϕ in the plane transverse to the beam direction.

$\Delta\phi[^\circ]$	k	n_{top}
$0-10$	0.1739 ± 0.0069	5.341
$10-20$	0.1715 ± 0.0068	5.332
$20-30$	0.1727 ± 0.0063	5.336
$30-40$	0.1693 ± 0.0062	5.322
$40-50$	0.1651 ± 0.0053	5.305
$50-60$	0.1565 ± 0.0049	5.271
$60-70$	0.1480 ± 0.0043	5.239
$70-80$	0.1384 ± 0.0037	5.204
$80-90$	0.1330 ± 0.0034	5.184
$90-100$	0.1253 ± 0.0033	5.158
$100-110$	0.1262 ± 0.0030	5.160
$110-120$	0.1292 ± 0.0033	5.171
$120-130$	0.1365 ± 0.0033	5.197
$130-140$	0.1426 ± 0.0033	5.219
$140-150$	0.1511 ± 0.0032	5.250
$150-160$	0.1565 ± 0.0034	5.271
$160-170$	0.1615 ± 0.0035	5.291
$170-180$	0.1648 ± 0.0033	5.304

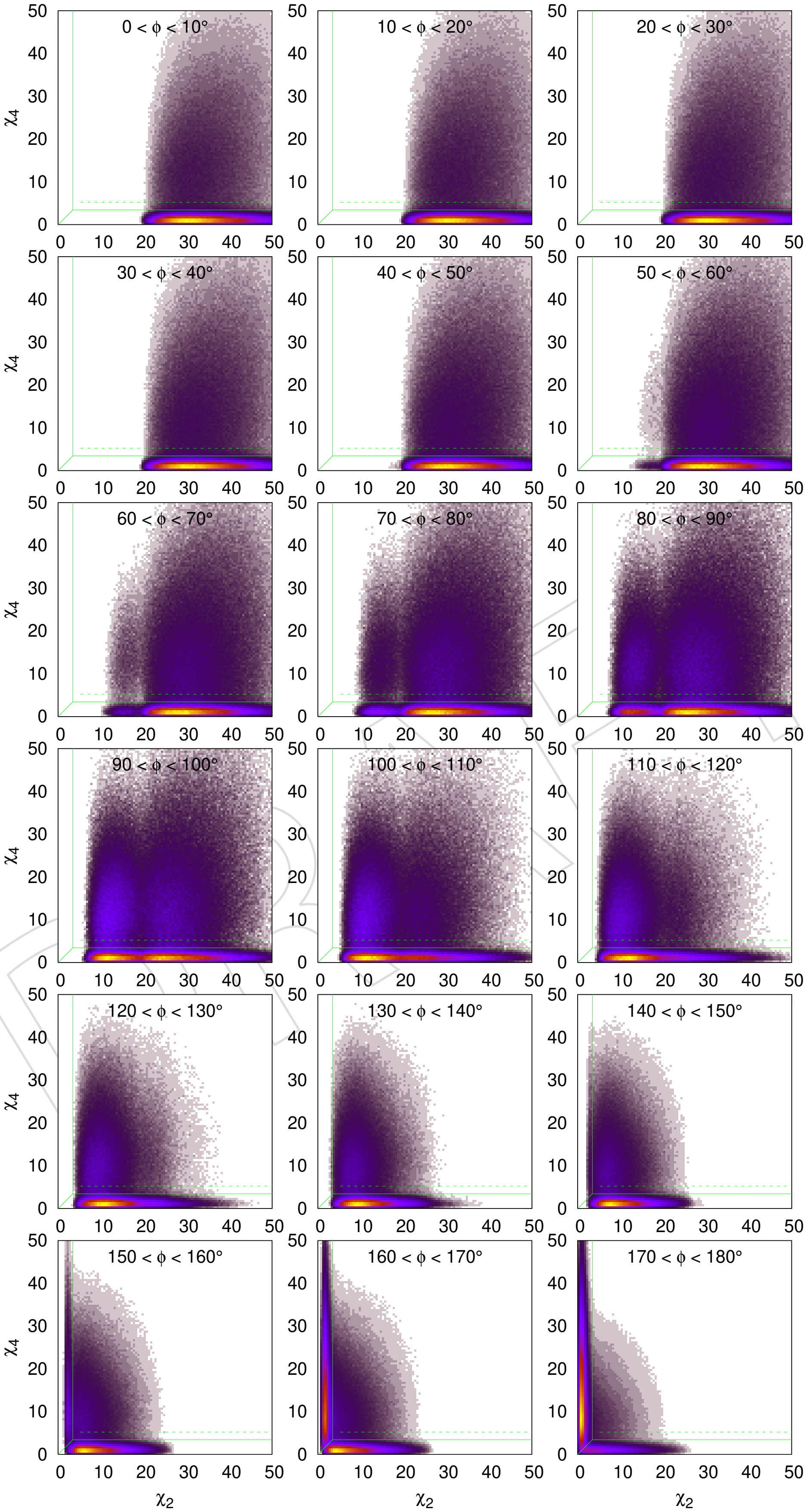

Figure 79: Joint distributions of selection variables $(\chi[\mathrm{pp}], \chi[\mathrm{p}(\mathrm{h}^+\mathrm{h}^-)\mathrm{p}])$ in bins of the angle between the scattered protons ϕ in the plane transverse to the beam direction.

7 Results

7.1 Systematic uncertainties

The relevant systematic uncertainties are listed in Table 9 where values propagated to the final differential cross sections are given: pileup correction (through the uncertainty of the visible cross section), lumisections with reduced roman pots availability, integrated luminosity, efficiency of the roman pot, removal of non-exclusive background, fraction of lost events during background removal and due to cut on looping particles, efficiency of single particle tracking, factorisation of tracking efficiency. The uncertainty related to roman pots and single particle tracking should be taken twice.

The estimated total systematic uncertainty of the differential cross section measurements has two components:

- the normalisation-type part includes all uncertainties but the roman pot and tracking efficiency related ones and amounts to 2.7%, if added in quadrature, dominated by uncertainty of integrated luminosity;
- the efficiency-type part has an estimated value of 4.7%, if added in quadrature, dominated by uncertainty of roman pot efficiencies.

When combined together these two components yield a total (correlated) systematic uncertainty of 5.4%.

The measured distributions are the following:

- distribution of the azimuth angle ϕ between the scattered proton momenta, $\mathrm{d}^3\sigma/\mathrm{d}p_{1,T}\,\mathrm{d}p_{2,T}\,\mathrm{d}\phi$,
- distribution of the two-hadron invariant mass m, $\mathrm{d}^3\sigma/\mathrm{d}p_{1,T}\,\mathrm{d}p_{2,T}\,\mathrm{d}m$,
- distribution of the squared four-momentum $\max(\hat{t},\hat{u})$ of the potential virtual meson, $\mathrm{d}^3\sigma/\mathrm{d}p_{1,T}\,\mathrm{d}p_{2,T}\,\mathrm{d}\max(\hat{t},\hat{u})$,

in the range $0.2 < p_{1,T}, p_{2,T} < 0.8\,\mathrm{GeV}$.

Table 9: List of systematic uncertainties: the sources and the systematic uncertainties propagated to the final differential cross sections.

Source	Value	Remark
Pileup correction	1.0%	through visible cross section (σ_{vis})
Lumisections with reduced RP availability	0.5%	
Integrated luminosity (L_{int})	2.5%	
HLT efficiency	small	neglected
Total normalisation-type	2.7%	
Roman pot efficiency	$\approx 3.0\%$	to be taken twice
Background removal	$< 0.5\%$	neglected
Lost events during background removal	-0.16%	neglected
Lost events due to looper cut	small	neglected
Single particle tracking efficiency	1.4%	to be taken twice
Particle identification efficiency	small	neglected
Total efficiency-type	4.7%	
Total systematics	5.4%	

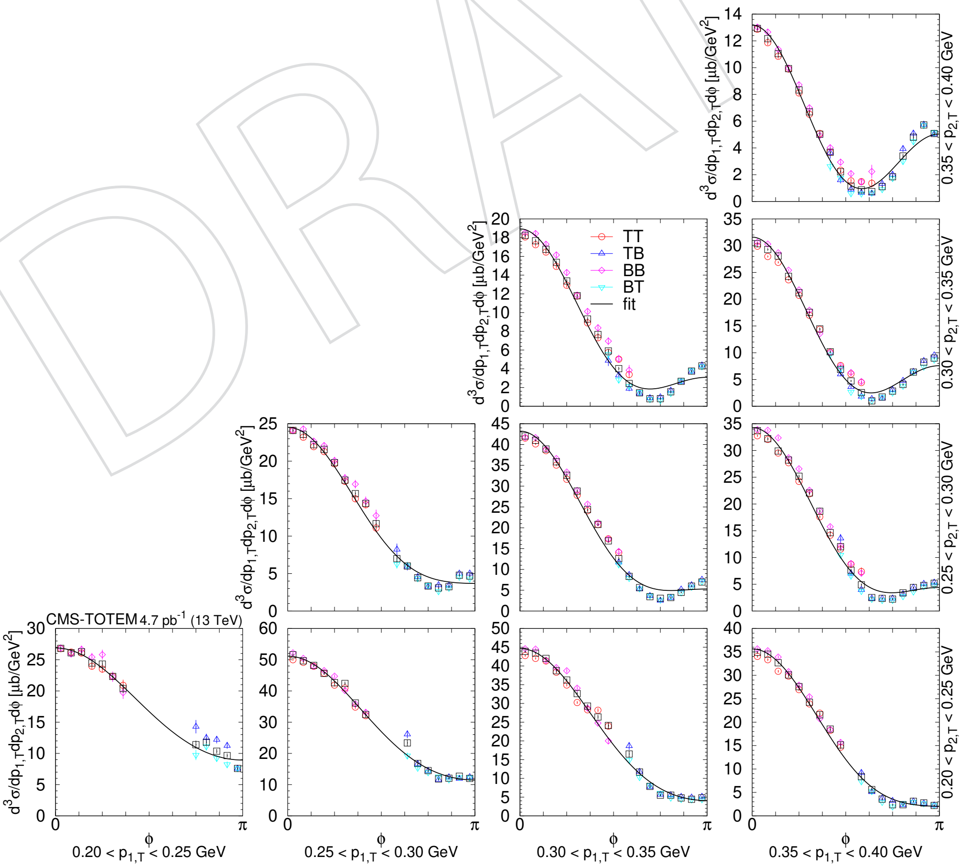

Figure 80: Distribution of $d^3\sigma/dp_{1,T}dp_{2,T}d\phi$ as a function of ϕ in the $\pi^+\pi^-$ nonresonant region ($0.35 < m < 0.65$ GeV) in several $(p_{1,T}, p_{2,T})$ bins, in units of μb/ GeV^2. Values based on data from each roman pots trigger configurations (TB, BT, TT, and TT) are shown separately with coloured symbols, while the weighted average is shown with black symbols. Results of fits with the form $[A(R - \cos\phi)]^2 + c^2$ are plotted with curves. The error bars indicate the statistical uncertainties.

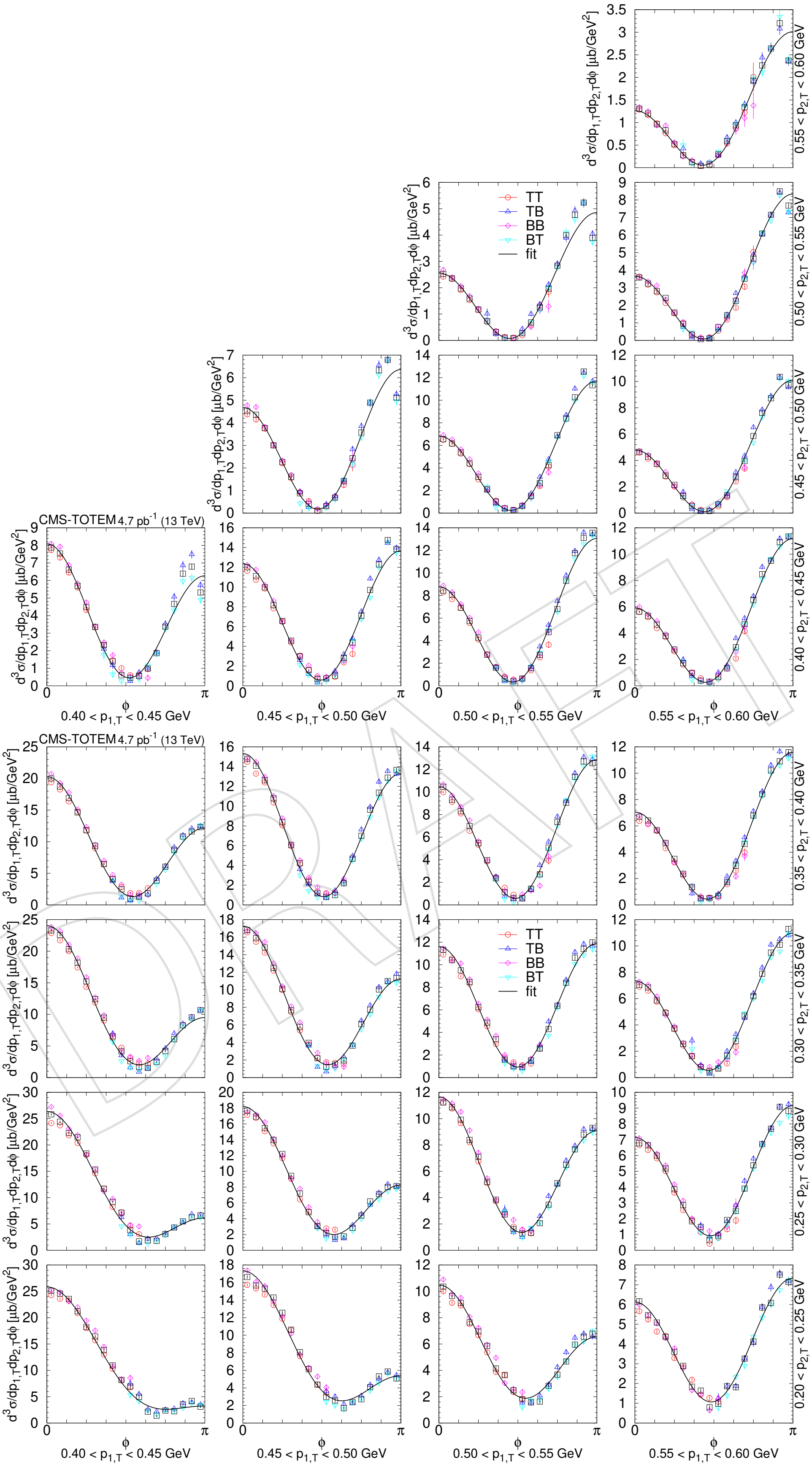

Figure 81: Distribution of $d^3\sigma/dp_{1,T}dp_{2,T}d\phi$ as a function of ϕ in the $\pi^+\pi^-$ nonresonant region ($0.35 < m < 0.65\,\text{GeV}$) in several $(p_{1,T}, p_{2,T})$ bins, in units of μb/ GeV^2. Values based on data from each roman pots trigger configurations (TB, BT, TT, and TT) are shown separately with coloured symbols, while the weighted average is shown with black symbols. Results of fits with the form $[A(R - \cos\phi)]^2 + c^2$ are plotted with curves. The error bars indicate the statistical uncertainties.

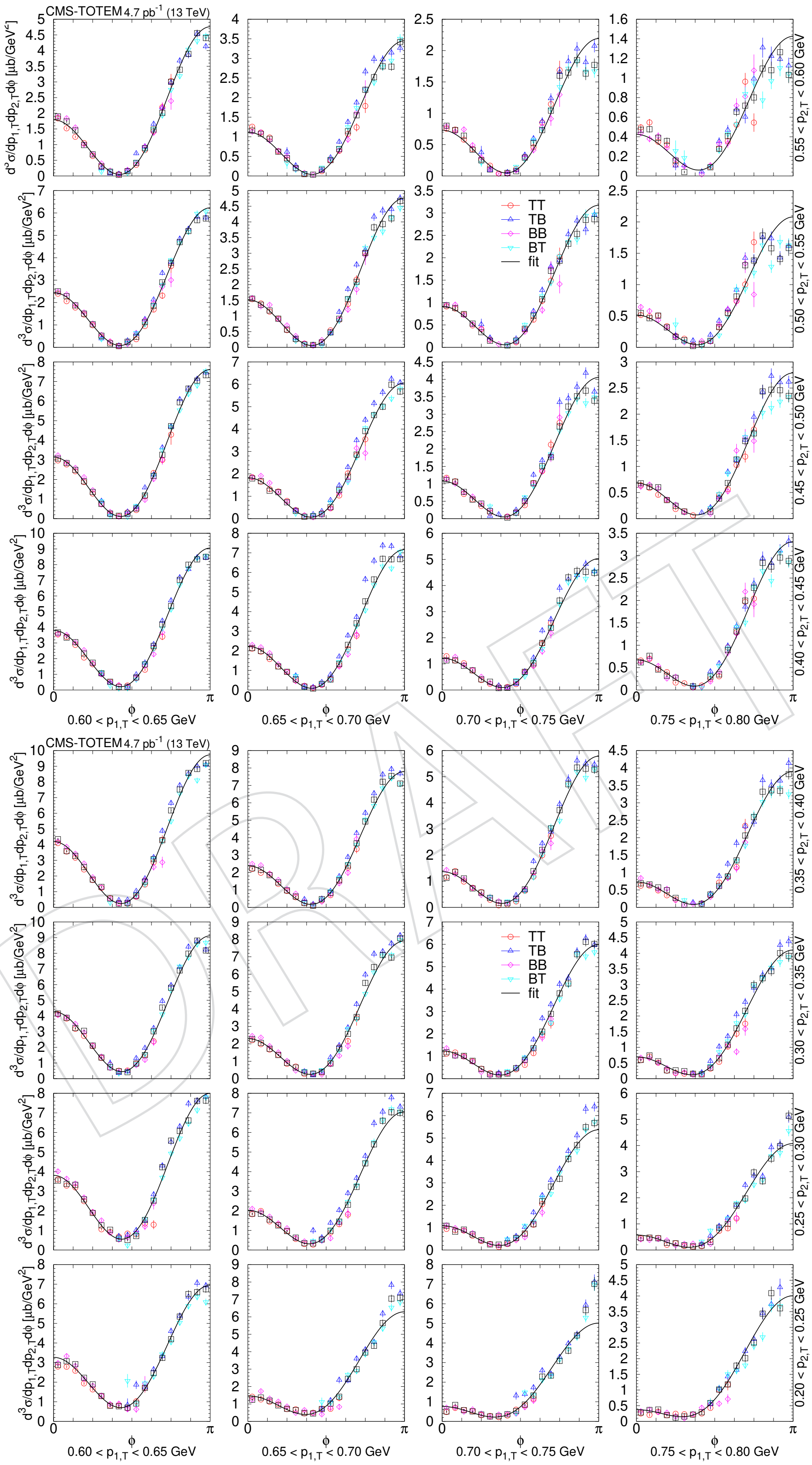

Figure 82: Distribution of $d^3\sigma/dp_{1,T}dp_{2,T}d\phi$ as a function of ϕ in the $\pi^+\pi^-$ nonresonant region ($0.35 < m < 0.65$ GeV) in several $(p_{1,T}, p_{2,T})$ bins, in units of μb/ GeV^2. Values based on data from each roman pots trigger configurations (TB, BT, TT, and TT) are shown separately with coloured symbols, while the weighted average is shown with black symbols. Results of fits with the form $[A(R - \cos\phi)]^2 + c^2$ are plotted with curves. The error bars indicate the statistical uncertainties.

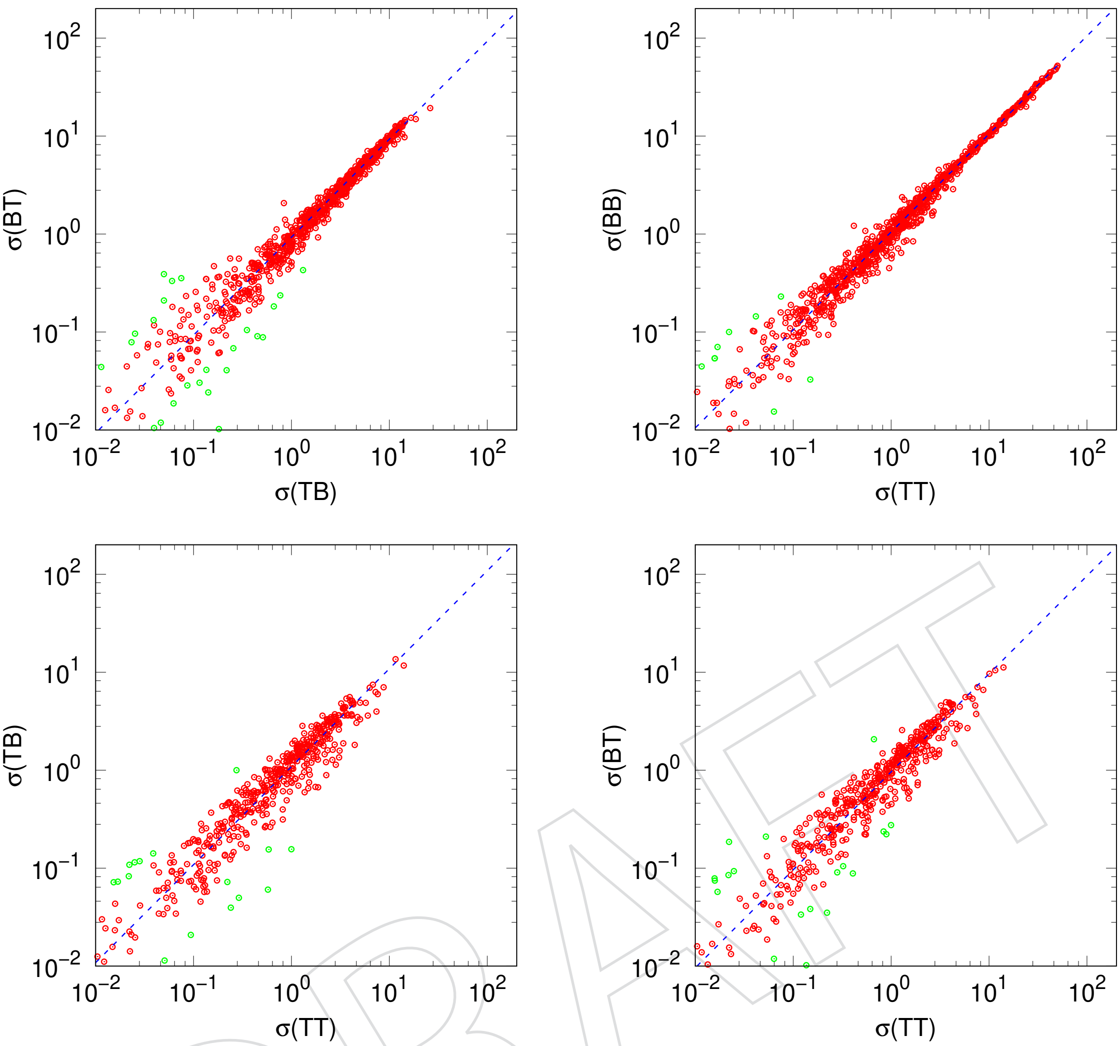

Figure 83: Comparison of measured differential cross section values, based on different roman pot trigger configurations (BT vs TB, BB vs TT, TB vs TT, and BT vs TT). In order to keep a clarity, error bars are omitted from the plot.

7.2 ϕ distributions

We deal with $\pi^+\pi^-$ pairs only. The distribution of $\mathrm{d}^3\sigma/\mathrm{d}p_{1,T}\mathrm{d}p_{2,T}\mathrm{d}\phi$ as a function of ϕ in several $(p_{1,T}, p_{2,T})$ bins are shown in Figs. 80-82. The differential cross sections are given in units of μb/ GeV^2, altogether 68 plots are included. Values based on data from each roman pots trigger configurations (TB, BT, TT, and BB) are shown separately with coloured symbols, while the weighted average is shown with black symbols. The error bars indicate the statistical uncertainties.

As an important cross-check of the whole analysis procedure comparisons of measured differential cross section values, based on different roman pot trigger configurations, are shown in Fig. 83. We can say that measurements made in differing conditions are compatible with each other (seen also in Figs. 80-82). In conclusion, their values can be averaged using the inverse variances of the individual measurements.

The distributions of the differential cross section can be fitted with a remarkably simple functional form

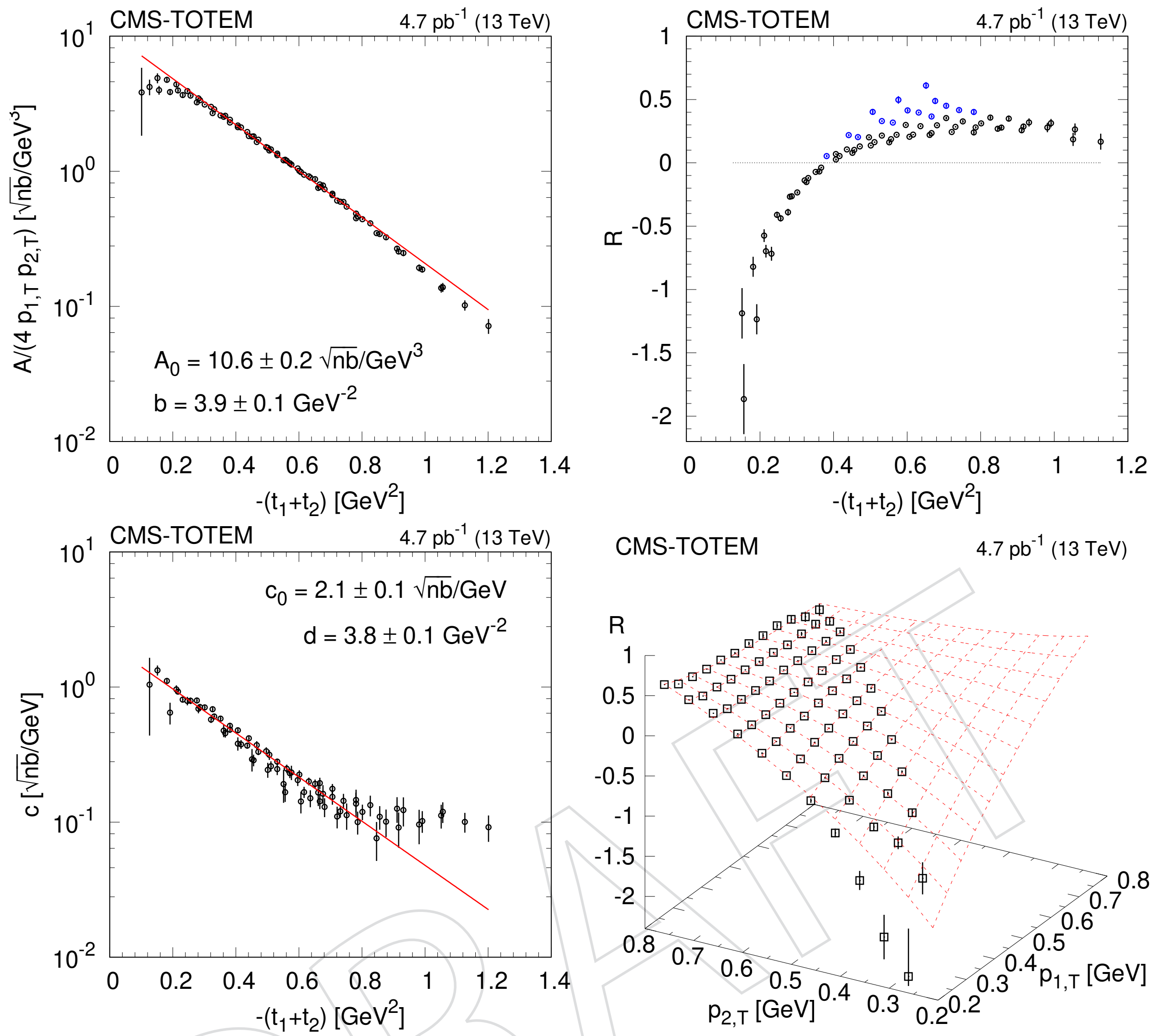

Figure 84: Dependence of the parameters A, R, and c (Eq. (36)) on (t_1, t_2). The fits correspond to the functional forms displayed in Eq. (39).

$$\left.\frac{d^3\sigma}{\mathrm{d}p_{1,T}\mathrm{d}p_{2,T}\mathrm{d}\phi}\right|_{0.35<m<0.65\,\mathrm{GeV}} = [A(R-\cos\phi)]^2 + c^2, \tag{36}$$

where A, R, and c are functions of $(p_{1,T}, p_{2,T})$. The formula features a sum of squared amplitudes and is inspired by former theoretical and experimental studies [9, 11], where $A(R-\cos\phi)$ is connected to the quantum mechanical amplitude of the process. The term containing c is added incoherently, it is small and is present to enhance the goodness of fit. The parabolic minimum, or dip, (at $\phi = \arccos R$) can be understood as an effect of additional pomeron exchanges between the incoming protons, resulting from the interference the bare and the rescattered (screened) amplitudes [25]. If the total amplitude crosses zero at a given ϕ, its squared value will have a parabolic minimum. The dependence of the parameters A, R, and c on (t_1, t_2) are shown in Fig. 84. The applied functional forms are

Table 10: Default DIME values of parameters for the meson-pomeron form factor and the coefficient for emission of secondaries.

Parameter	DIME	Remark
b_{exp} $[\mathrm{GeV}^{-2}]$	$1/2.2$	meson-pomeron form factors
b_{pow} $[\mathrm{GeV}^{-2}]$	1.7	
a_{or} $[\mathrm{GeV}]$	$1/1.1$	
b_{or} $[\mathrm{GeV}^{-1}]$	$\sqrt{0.5}$	
c_{sec}	0.7	coefficient for emission of secondaries

$$A(t_1,t_2) = 4\sqrt{t_1 t_2} \cdot A_0 e^{b(t_1+t_2)}, \tag{37}$$

$$R(t_1,t_2) \approx \frac{1.2(\sqrt{-t_1}+\sqrt{-t_2}) - 1.6\sqrt{t_1 t_2} - 0.8}{\sqrt{t_1 t_2}+0.1}, \tag{38}$$

$$c(t_1,t_2) = c_0 e^{d(t_1+t_2)}. \tag{39}$$

With that, the invariant triple differential cross section is

$$\frac{\mathrm{d}^3\sigma}{\mathrm{d}t_1\mathrm{d}t_2\mathrm{d}\phi} = 4\sqrt{t_1 t_2} \cdot A_0^2 \cdot e^{2b(t_1+t_2)}[R(t_1,t_2) - \cos\phi]^2 + \frac{1}{4\sqrt{t_1 t_2}} \cdot c_0^2 \cdot e^{2d(t_1+t_2)}, \tag{40}$$

where $A_0 \approx 10.6\sqrt{\mathrm{nb}}/\,\mathrm{GeV}^3$, $b \approx 3.9\,\mathrm{GeV}^{-2}$, while $c_0 \approx 2.1\sqrt{\mathrm{nb}}/\,\mathrm{GeV}$, $d \approx 3.8\,\mathrm{GeV}^{-2}$.

7.3 Available MC event generators

DIME [25] (v1.07) is a MC event generator for exclusive meson pair production via double pomeron exchange, cited in previous STAR [14] and CMS [15] publications. It can generate events for central exclusive nonresonant $\pi^+\pi^-$ and $\mathrm{K}^+\mathrm{K}^-$ production via the double pomeron exchange mechanism. The event generator is based on previous work on proton opacity [32], and the two-channel model [33] (Good-Walker approach), further details are given below. Although still available only in Fortran, the parameters of DIME are clear and the generator is well tunable. The list of tunable parameters of DIME MC are given in Tables 10 and 11.

Table 11: The four parameter sets of soft hadronic models in DIME used for the calculation of opacity, eikonal survival factor, and for the characterisation of diffractive proton eigenstates (Good-Walker formalism).

Parameter	DIME -1	DIME -2	DIME -3	DIME -4	Remark
σ_P $[\mathrm{mb}]$	23	33	60	50	pomeron strength
α_P	1.13	1.115	1.093	1.11	pomeron intercept, $= 1+\Delta$
α'_P $[\mathrm{GeV}^{-2}]$	0.08	0.11	0.075	0.06	pomeron slope
γ_i	1 ± 0.55	1 ± 0.4	1 ± 0.42	1 ± 0.47	dim'less coupling to state i
$2\,\lvert a_i \rvert^2$	1 ∓ 0.08	1 ± 0.5	1 ± 0.52	1 ± 0.5	a_i is the amplitude of state i
b_1 $[\mathrm{GeV}^{-2}]$	8.5	8	5.3	7.2	pomeron coupling to states
b_2 $[\mathrm{GeV}^{-2}]$	4.5	6	3.8	4.2	
c_1 $[\mathrm{GeV}^2]$	0.18	0.18	0.35	0.53	
c_2 $[\mathrm{GeV}^2]$	0.58	0.58	0.18	0.24	
d_1	0.45	0.63	0.55	0.6	
d_2	0.45	0.47	0.48	0.48	

SuperChic2 [34] can be regarded as a continuation of the work started with Dime , but only provides events with hadron-pair invariant masses above 2 GeV, hence it is not used in the data-MC comparisons.

GenEx [35] follows an approach very similar to that of Dime, but does not take into account the absorption corrections. The model developers estimated the corresponding suppression factor to be large, of the order of $2-5$, and cross sections have to be scaled down for lower masses ($m < 1.2\,\mathrm{GeV}$). The generator uses an exponential meson form factor with value of $\Lambda_{\mathrm{off}} = 1.0\,\mathrm{GeV}$. Since the differences between GenEx and Dime are almost entirely due to the absorption effects [14], it is not worthwhile to employ this generator as an independent one in this study.

Graniitti [36] (v1.051) is an algorithmic engine and MC event generator for high energy diffraction. It includes differential screening, an expendable set of scattering amplitudes with adaptive MC sampling, spin systematics and modern computational technology. First tests show that this generator misses the dip and the $(a + b\cos\phi)^2$ feature strongly present in $\mathrm{d}\sigma/\mathrm{d}\phi$ data, hence Graniitti is not used in the data-MC comparisons.

7.4 Tuning with Professor

For the tuning the tool Professor [37] (v2.3.3) is employed. It parametrises the per-bin generator response to parameter variations and numerically optimises the parametrised behaviour. Such an approach reduces the exponentially expensive process of brute-force tuning to a scaling closer to a power law in the number of parameters. It allows for massive parallelisation and systematically improves the scan results by use of a deterministic parametrisation of the generator response to changes in the steering parameters.

The measured distributions included in model tuning are

- distribution of the azimuth angle between the scattered proton momenta, $\mathrm{d}^3\sigma/\mathrm{d}p_{1,T}\,\mathrm{d}p_{2,T}\,\mathrm{d}\phi$, if $0.35 < m < 0.65\,\mathrm{GeV}$;
- distribution of the two-hadron invariant mass at low masses, $\mathrm{d}^3\sigma/\mathrm{d}p_{1,T}\,\mathrm{d}p_{2,T}\,\mathrm{d}m$, if $m < 0.7\,\mathrm{GeV}$;
- distribution of the two-hadron invariant mass at high masses, $\mathrm{d}^3\sigma/\mathrm{d}p_{1,T}\,\mathrm{d}p_{2,T}\,\mathrm{d}m$, if $1.8 < m < 2.2\,\mathrm{GeV}$;
- distribution of the squared four-momentum of the potential virtual meson, $\mathrm{d}^3\sigma/\mathrm{d}p_{1,T}\,\mathrm{d}p_{2,T}\,\mathrm{d}\max(\hat{t},\hat{u})$, if $1.8 < m < 2.2\,\mathrm{GeV}$.

in the range $0.2 < p_{1,T}, p_{2,T} < 0.8\,\mathrm{GeV}$.

Details on model tuning can be found in CMS AN-22-092.

The tuning, the minimisation of the global goodness-of-fit, converges to unique minima for all three form factor options. The χ^2/ndf values are displayed in Table. 12. They are in the range 1.6-2.0 (empirical), 1.2-1.5 (one-channel), and 1.0-1.3 (two-chanel).

Good fits are achieved with the one-channel or the two-channel models using exponential or Orear-type form factors, while the numerically best one is the *two-channel model with exponential parametrisation of the proton-pomeron form factor*.

Values and raw statistical uncertainties of the parameters tuned with the Professor tool, for the empirical, one-channel, and two-channel model are shown in Table 13 using the exponential, power-law, and the Orear-type parametrisations of the proton-pomeron form factor. Goodness-of-fit (χ^2/ndf) values are also listed. It is often recommended to multiply the uncer-

Table 12: Goodness-of-fit values (χ^2/ndf) of model tuning as functions of model and choice of form factor parametrisation.

Model	Form factor		
	exponential	Orear-type	power-law
empirical	10889/5803	11211/5802	12632/5803
one-channel	9393/5800	9043/5799	10597/5800
two-channel	8297/5793	9286/5792	11375/5793

tainties by the factor $\sqrt{\chi^2/\mathrm{ndf}}$.

The values of best parameters for the empirical, one-channel, and two-channel models with several choices of the proton-pomeron form factor (exponential, Orear-type, power-law) are shown in Fig. 85. In the case of the two-channel model, parameter values of models 1 and 2 describing the elastic differential proton-proton cross section from Ref. [33] are also indicated.

The matrix of correlation coefficients for the two-channel model are displayed in Fig. 86, shown separately for several choices of the proton-pomeron form factor.

Table 13: Values and raw statistical uncertainties of the parameters tuned with the PROFESSOR tool, given for the empirical, one-channel, and two-channel model with thethe exponential, power-law, and the Orear-type parametrisations of the proton-pomeron form factor. Goodness-of-fit (χ^2/ndf) values are also listed.

Parameter	Exponential	Orear-type	Power-law
empirical model			
a_{ore}	—	0.735 ± 0.015	—
$b_{\mathrm{exp/ore/pow}}[\mathrm{GeV}^{-2}]$	1.084 ± 0.004	1.782 ± 0.014	1.356 ± 0.001
$B_{\mathbb{P}}\ [\mathrm{GeV}^{-2}]$	3.757 ± 0.033	3.934 ± 0.027	4.159 ± 0.019
χ^2/dof	9470/5796	10059/5795	11409/5796
one-channel model			
$\sigma_0[\mathrm{mb}]$	34.99 ± 0.79	27.98 ± 0.40	26.87 ± 0.30
$\alpha_P - 1$	0.129 ± 0.002	0.127 ± 0.001	0.134 ± 0.001
$\alpha'_P\ [\mathrm{GeV}^{-2}]$	0.084 ± 0.005	0.034 ± 0.002	0.037 ± 0.002
a_{ore}	—	0.578 ± 0.022	—
$b_{\mathrm{exp/ore/pow}}[\mathrm{GeV}^{-2}]$	0.820 ± 0.011	1.385 ± 0.015	1.222 ± 0.004
$B_{\mathbb{P}}\ [\mathrm{GeV}^{-2}]$	2.745 ± 0.046	4.271 ± 0.021	4.072 ± 0.017
χ^2/dof	7356/5793	7448/5792	8339/5793
two-channel model			
$\sigma_0[\mathrm{mb}]$	20.97 ± 0.48	22.89 ± 0.17	23.02 ± 0.23
$\alpha_P - 1$	0.136 ± 0.001	0.129 ± 0.001	0.131 ± 0.001
$\alpha'_P\ [\mathrm{GeV}^{-2}]$	0.078 ± 0.001	0.075 ± 0.001	0.071 ± 0.001
a_{ore}	—	0.718 ± 0.012	—
$b_{\mathrm{exp/ore/pow}}[\mathrm{GeV}^{-2}]$	0.917 ± 0.007	1.517 ± 0.008	0.931 ± 0.002
$\Delta\|a\|^2$	0.070 ± 0.026	-0.058 ± 0.009	0.042 ± 0.011
$\Delta\gamma$	0.052 ± 0.042	0.131 ± 0.018	0.273 ± 0.023
$b_1\ [\mathrm{GeV}^2]$	8.438 ± 0.108	8.951 ± 0.041	8.877 ± 0.040
$c_1\ [\mathrm{GeV}^2]$	0.298 ± 0.012	0.278 ± 0.004	0.266 ± 0.006
d_1	0.472 ± 0.007	0.465 ± 0.002	0.465 ± 0.003
$b_2\ [\mathrm{GeV}^2]$	4.982 ± 0.133	4.222 ± 0.052	4.780 ± 0.060
$c_2\ [\mathrm{GeV}^2]$	0.542 ± 0.015	0.522 ± 0.006	0.615 ± 0.006
d_2	0.453 ± 0.009	0.452 ± 0.003	0.431 ± 0.004
χ^2/dof	5741/5786	6415/5785	7879/5786

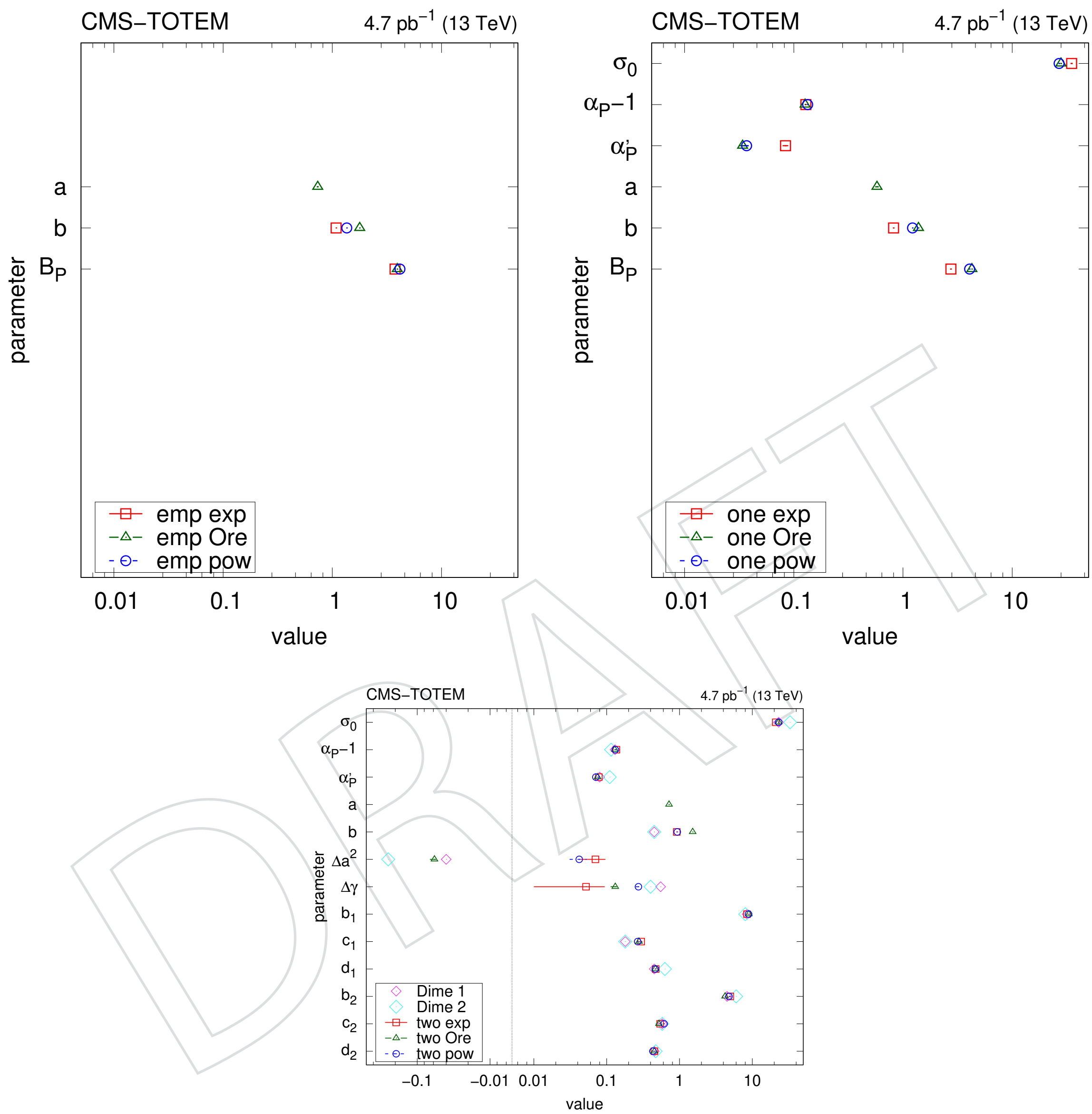

Figure 85: Values of best parameters for the empirical (top left), one-channel (top right), and two-channel (bottom) models with several choices of the proton-pomeron form factor (exponential, Orear-type, power-law). In the case of the two-channel model, parameter values of models 1 and 2 describing the elastic differential proton-proton cross section from Ref. [33] are also indicated.

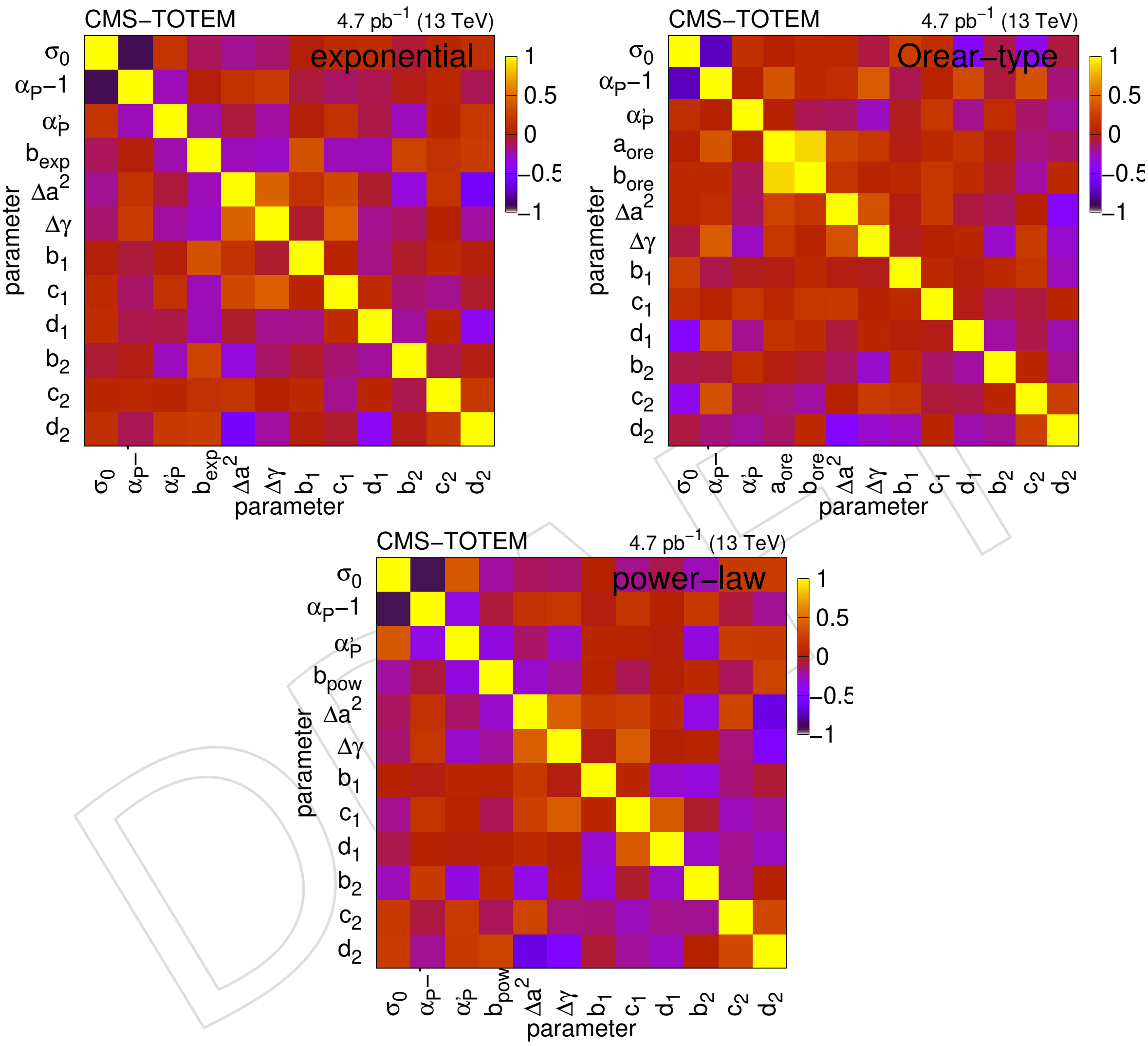

Figure 86: Correlation coefficients among values of best parameters for the two-channel model, in the case of exponential (top left), Orear-type (top right), and power-law (bottom) parametrisations of the proton-pomeron form factor.

7.5 Data-MC comparisons

ϕ distributions. The distributions of $\mathrm{d}^3\sigma/\mathrm{d}p_{1,T}\mathrm{d}p_{2,T}\mathrm{d}\phi$ in the nonresonant region ($0.35 < m < 0.65\,\mathrm{GeV}$) as a function of ϕ in several $(p_{1,T}, p_{2,T})$ bins are shown in Figs. 87-89. Measured values are shown together with the predictions of the empirical and the two-channel models using the tuned parameters for the exponential proton-pomeron form factors. The differential cross sections are given in units of μb/ GeV^2, altogether 68 plots are included.

m distributions. The distributions of $\mathrm{d}^3\sigma/\mathrm{d}p_{1,T}\mathrm{d}p_{2,T}\mathrm{d}m$ as a function of m in several $(p_{1,T}, p_{2,T})$ bins are shown for $\pi^+\pi^-$ in Figs. 90-92 with linear vertical scale, and with logarithmic vertical scale out to higher masses in Figs. 93-95, and for $\mathrm{K}^+\mathrm{K}^-$ in Figs. 96-98. (The mass spectra for $\mathrm{p}\overline{\mathrm{p}}$ pairs are not displayed.) Measured values are shown together with the predictions of the empirical and the two-channel models using the tuned parameters for the exponential proton-pomeron form factors. The differential cross sections are given in units of μb/ GeV^2, altogether 68 plots are included.

Some known resonances are well visible in both $\pi^+\pi^-$ and $\mathrm{K}^+\mathrm{K}^-$ channels ($f_0(980)$, $f_2(1270)$, $f_0(1500)$, $f_0(1710)$), while some are only present the $\mathrm{K}^+\mathrm{K}^-$ channel ($f_2'(1525)$) in line with the branching ratios. Resonance production will be examined in a subsequent study.

$\max(\hat{t}, \hat{u})$ distributions. The distributions of the squared momentum transfer of the virtual meson at invariant masses ($1.8 < m < 2.2\,\mathrm{GeV}$) in several $(p_{1,T}, p_{2,T})$ bins are shown for $\pi^+\pi^-$ in Figs. 99-100. Measured values are shown together with the predictions of the empirical and the two-channel models using the tuned parameters for the exponential proton-pomeron form factors. In addition, a theory-motivated curve of the form $\exp(4b_{exp}(t - m^2))/(t - m^2)^2$ is also plotted. The differential cross sections are given in units of μb/ GeV^2, altogether 46 plots are included.

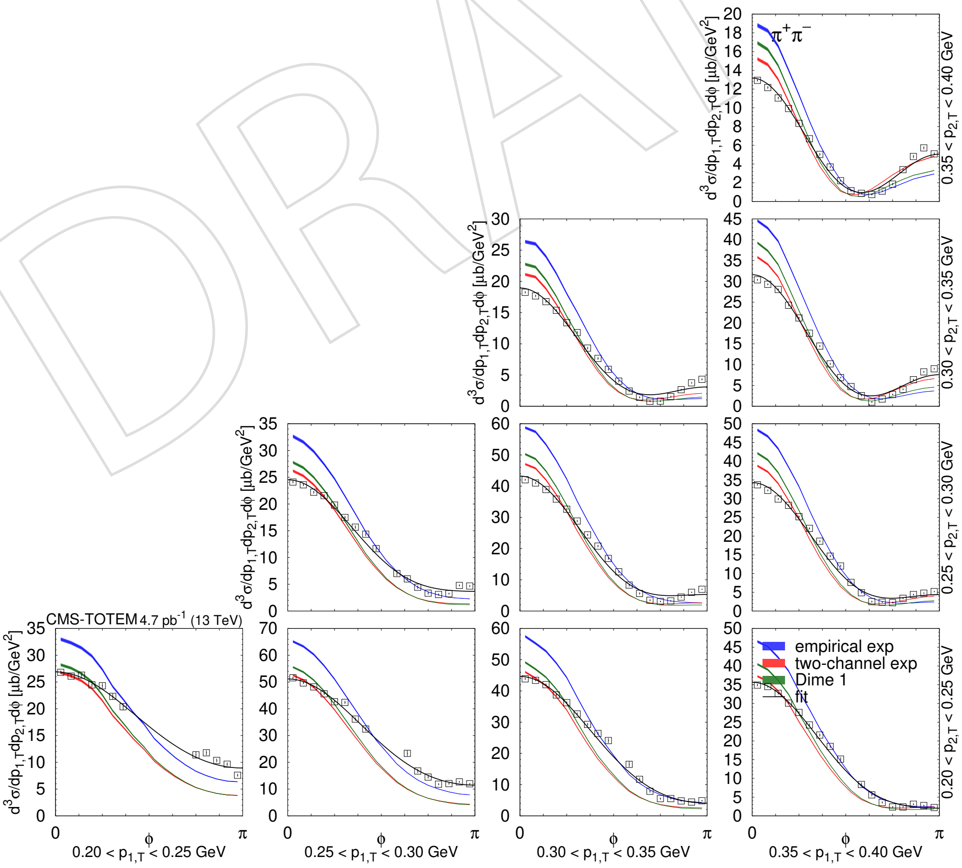

Figure 87: Distribution of $d^3\sigma/dp_{1,T}dp_{2,T}d\phi$ as a function of ϕ in the $\pi^+\pi^-$ nonresonant region ($0.35 < m < 0.65$ GeV in several $(p_{1,T}, p_{2,T})$ bins, in units of μb/ GeV^2. Measured values (black symbols) are shown together with the predictions of the empirical and the two-channel models (coloured symbols) using the tuned parameters for the exponential proton-pomeron form factors (see text for details). Curves corresponding to DIME (model 1) are also plotted. The error bars indicate the statistical uncertainties.

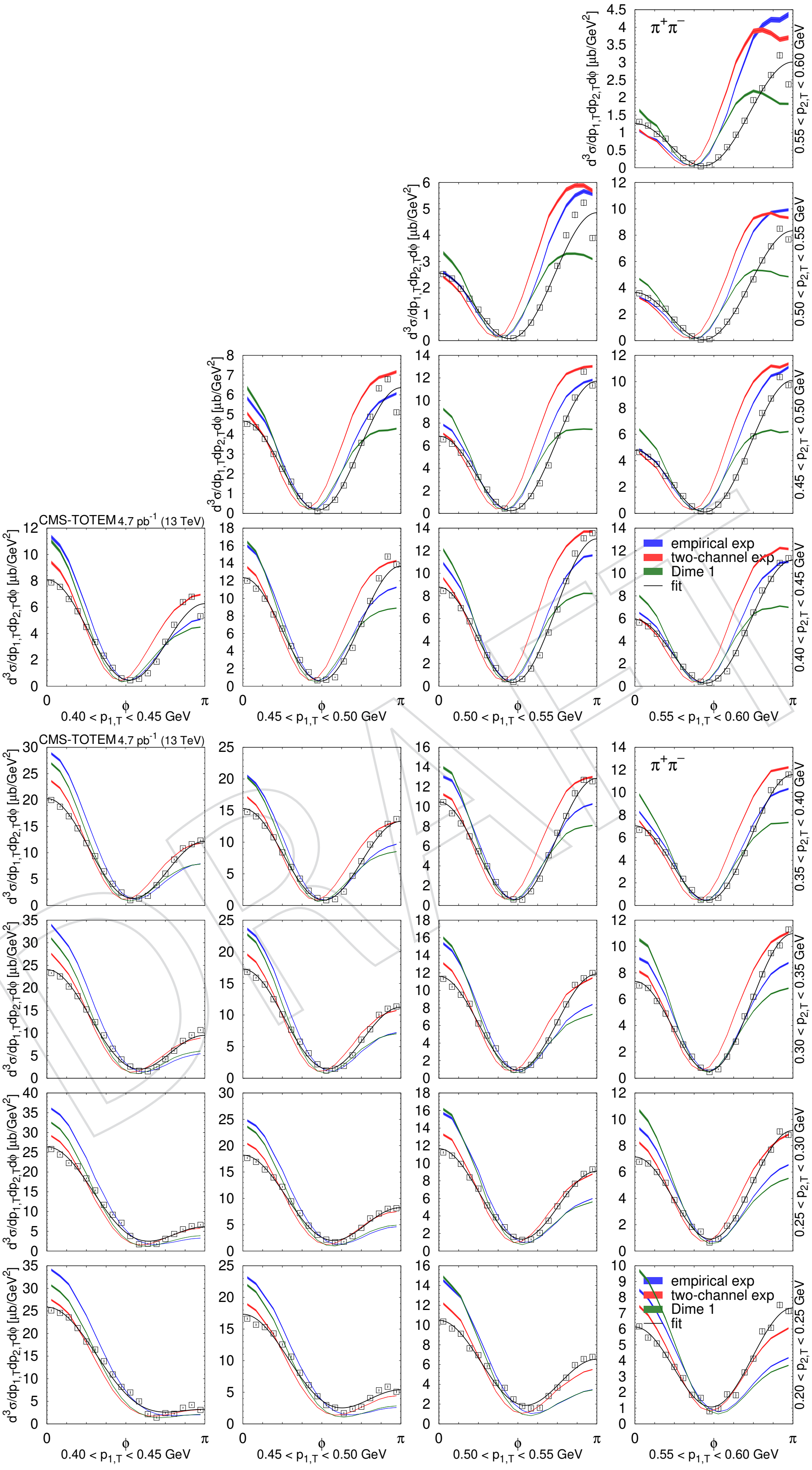

Figure 88: Distribution of $d^3\sigma/dp_{1,T}dp_{2,T}d\phi$ as a function of ϕ in the $\pi^+\pi^-$ nonresonant region ($0.35 < m < 0.65$ GeV in several ($p_{1,T}, p_{2,T}$) bins, in units of μb/GeV^2. Measured values (black symbols) are shown together with the predictions of the empirical and the two-channel models (coloured symbols) using the tuned parameters for the exponential proton-pomeron form factors (see text for details). Curves corresponding to DIME (model 1) are also plotted. The error bars indicate the statistical uncertainties.

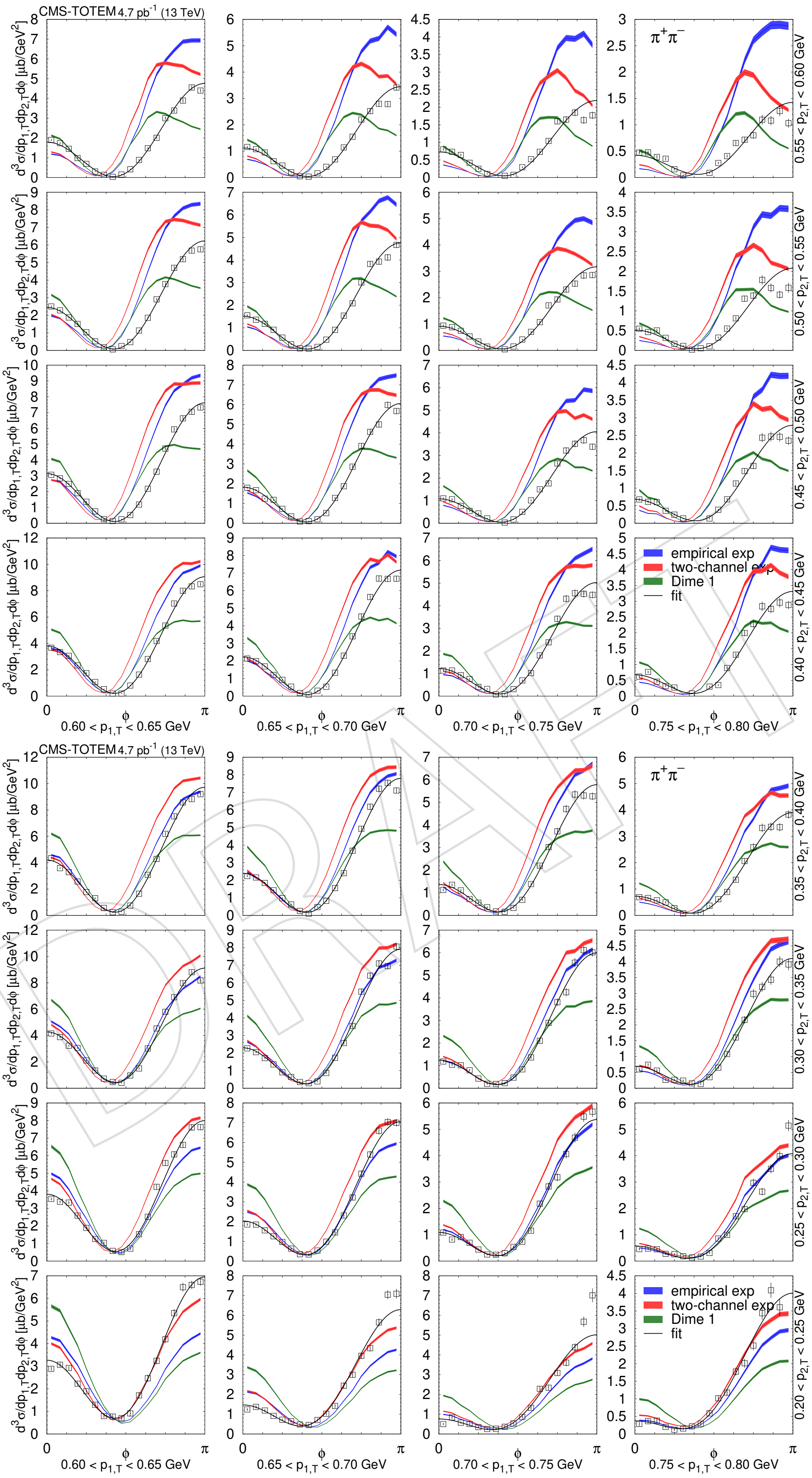

Figure 89: Distribution of $d^3\sigma/dp_{1,T}dp_{2,T}d\phi$ as a function of ϕ in the $\pi^+\pi^-$ nonresonant region ($0.35 < m < 0.65$ GeV in several $(p_{1,T}, p_{2,T})$ bins, in units of μb/GeV^2. Measured values (black symbols) are shown together with the predictions of the empirical and the two-channel models (coloured symbols) using the tuned parameters for the exponential proton-pomeron form factors (see text for details). Curves corresponding to DIME (model 1) are also plotted. The error bars indicate the statistical uncertainties.

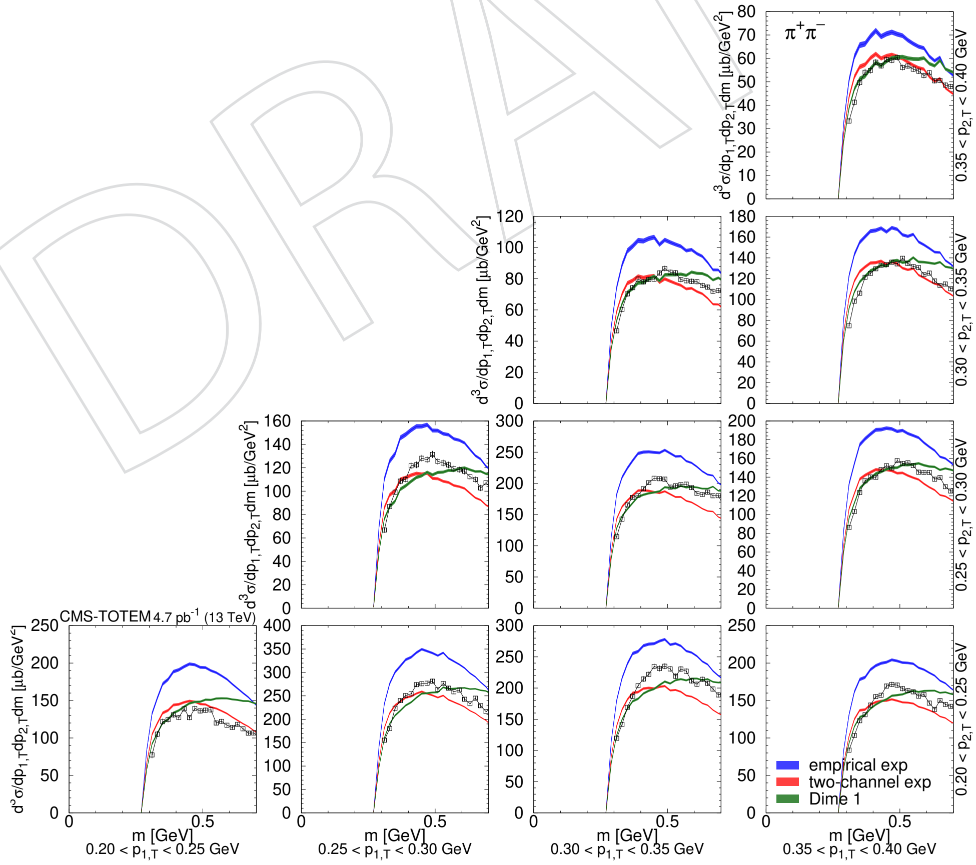

Figure 90: Distribution of $\mathrm{d}^3\sigma/\mathrm{d}p_{1,T}\mathrm{d}p_{2,T}\mathrm{d}m$ as a function of m for $\pi^+\pi^-$ pairs in several $(p_{1,T}, p_{2,T})$ bins, in units of μb/ GeV^3. Measured values (black symbols) are shown together with the predictions of the empirical and the two-channel models (coloured symbols) using the tuned parameters for the exponential proton-pomeron form factors (see text for details). Curves corresponding to DIME (model 1) are also plotted. The error bars indicate the statistical uncertainties.

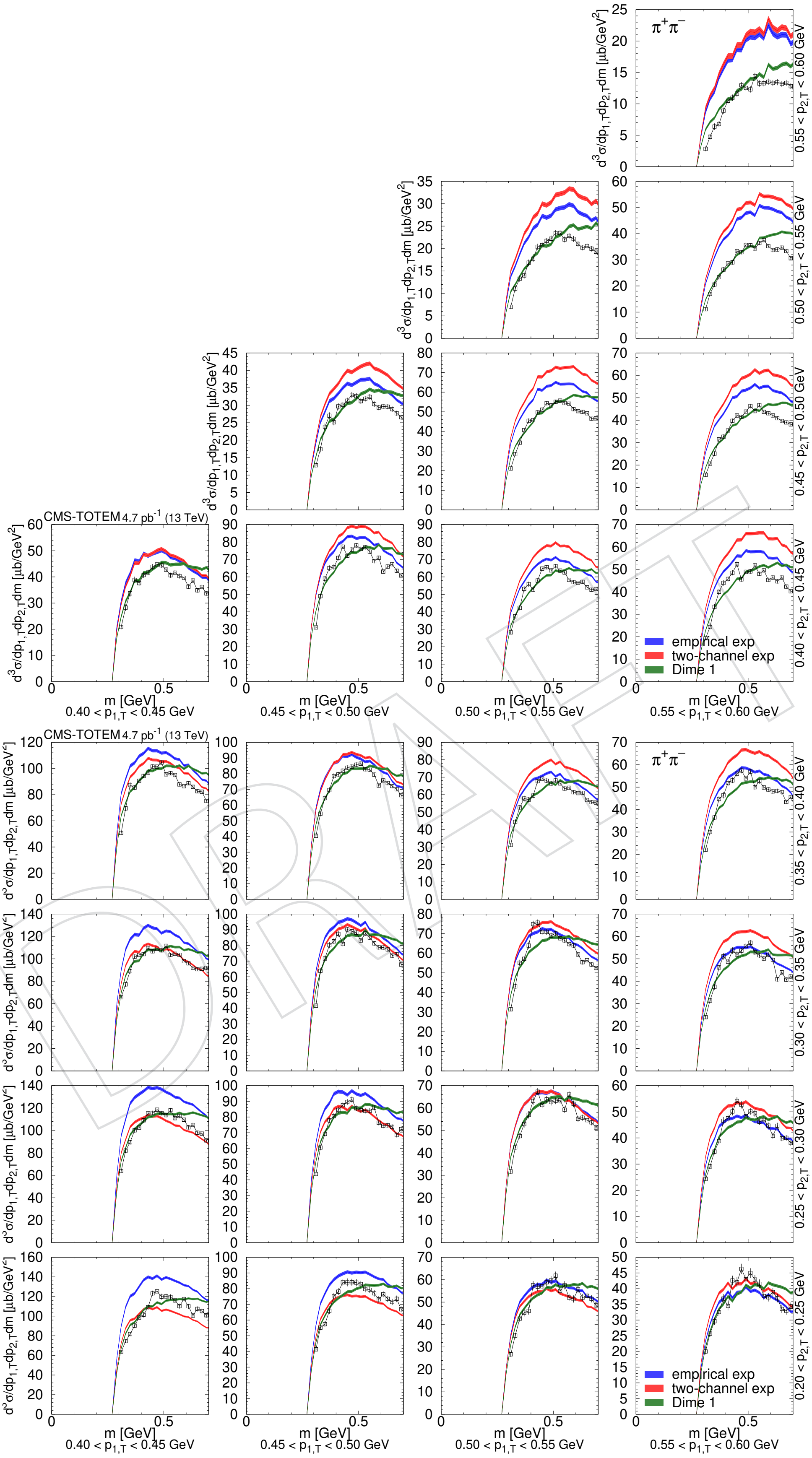

Figure 91: Distribution of $d^3\sigma/dp_{1,T}dp_{2,T}dm$ as a function of m for $\pi^+\pi^-$ pairs in several $(p_{1,T}, p_{2,T})$ bins, in units of μb/ GeV^3. Measured values (black symbols) are shown together with the predictions of the empirical and the two-channel models (coloured symbols) using the tuned parameters for the exponential proton-pomeron form factors (see text for details). Curves corresponding to DIME (model 1) are also plotted. The error bars indicate the statistical uncertainties.

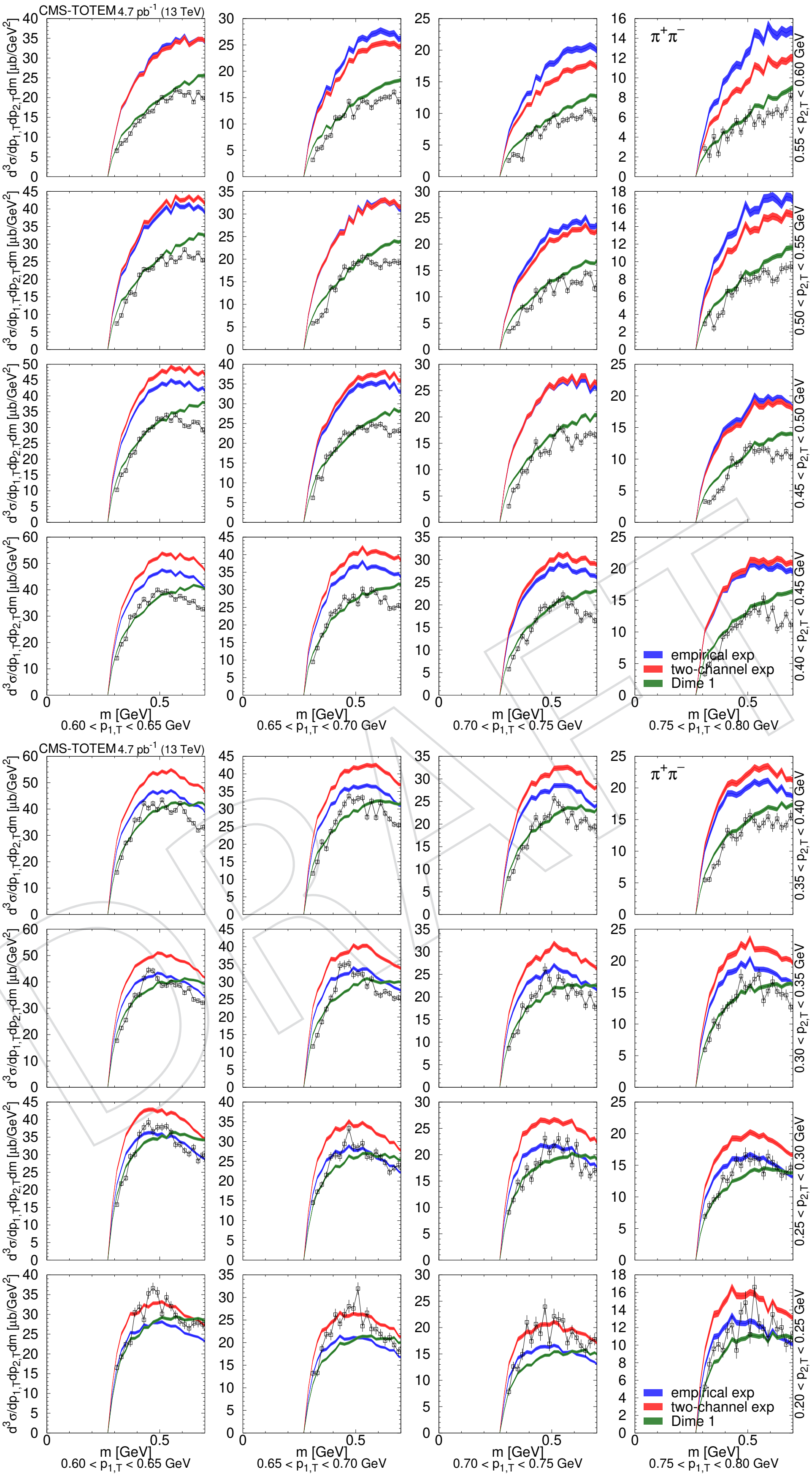

Figure 92: Distribution of $\mathrm{d}^3\sigma/\mathrm{d}p_{1,T}\mathrm{d}p_{2,T}\mathrm{d}m$ as a function of m for $\pi^+\pi^-$ pairs in several $(p_{1,T}, p_{2,T})$ bins, in units of μb/ GeV^3. Measured values (black symbols) are shown together with the predictions of the empirical and the two-channel models (coloured symbols) using the tuned parameters for the exponential proton-pomeron form factors (see text for details). Curves corresponding to DIME (model 1) are also plotted. The error bars indicate the statistical uncertainties.

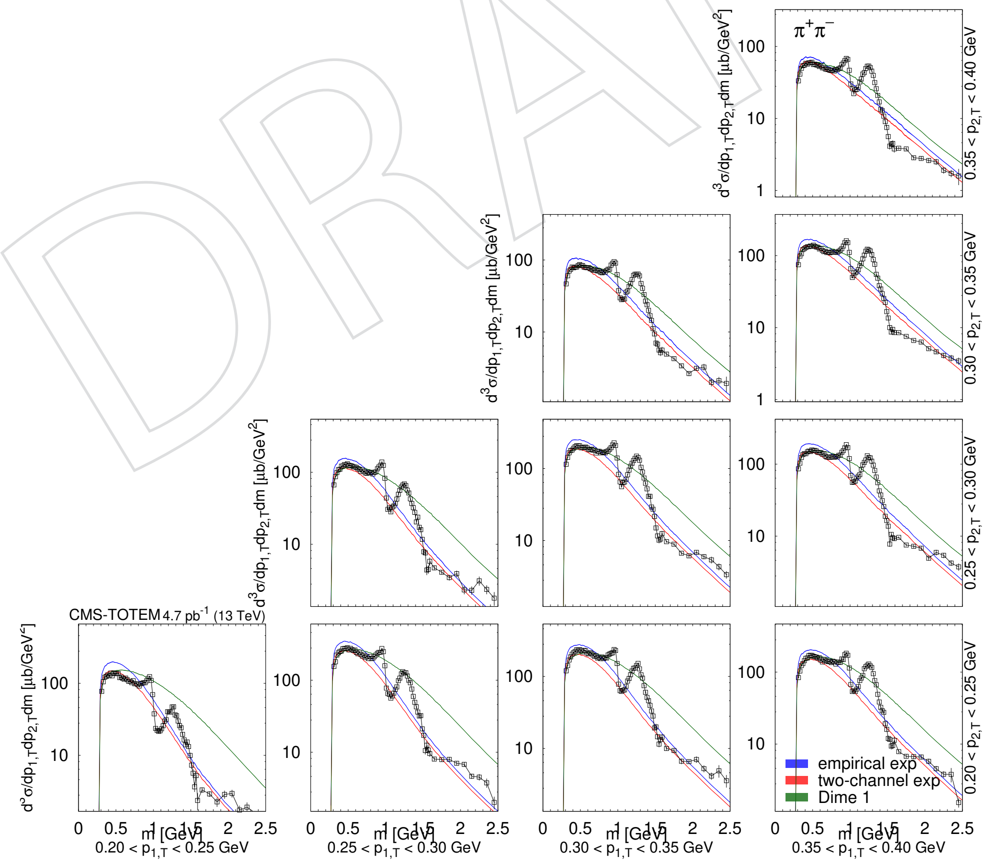

Figure 93: Distribution of $\mathrm{d}^3\sigma/\mathrm{d}p_{1,T}\mathrm{d}p_{2,T}\mathrm{d}m$ as a function of m for $\pi^+\pi^-$ pairs in several $(p_{1,T}, p_{2,T})$ bins, in units of μb/ GeV^3. Measured values (black symbols) are shown together with the predictions of the empirical and the two-channel models (coloured symbols) using the tuned parameters for the exponential proton-pomeron form factors (see text for details). Curves corresponding to DIME (model 1) are also plotted. The error bars indicate the statistical uncertainties.

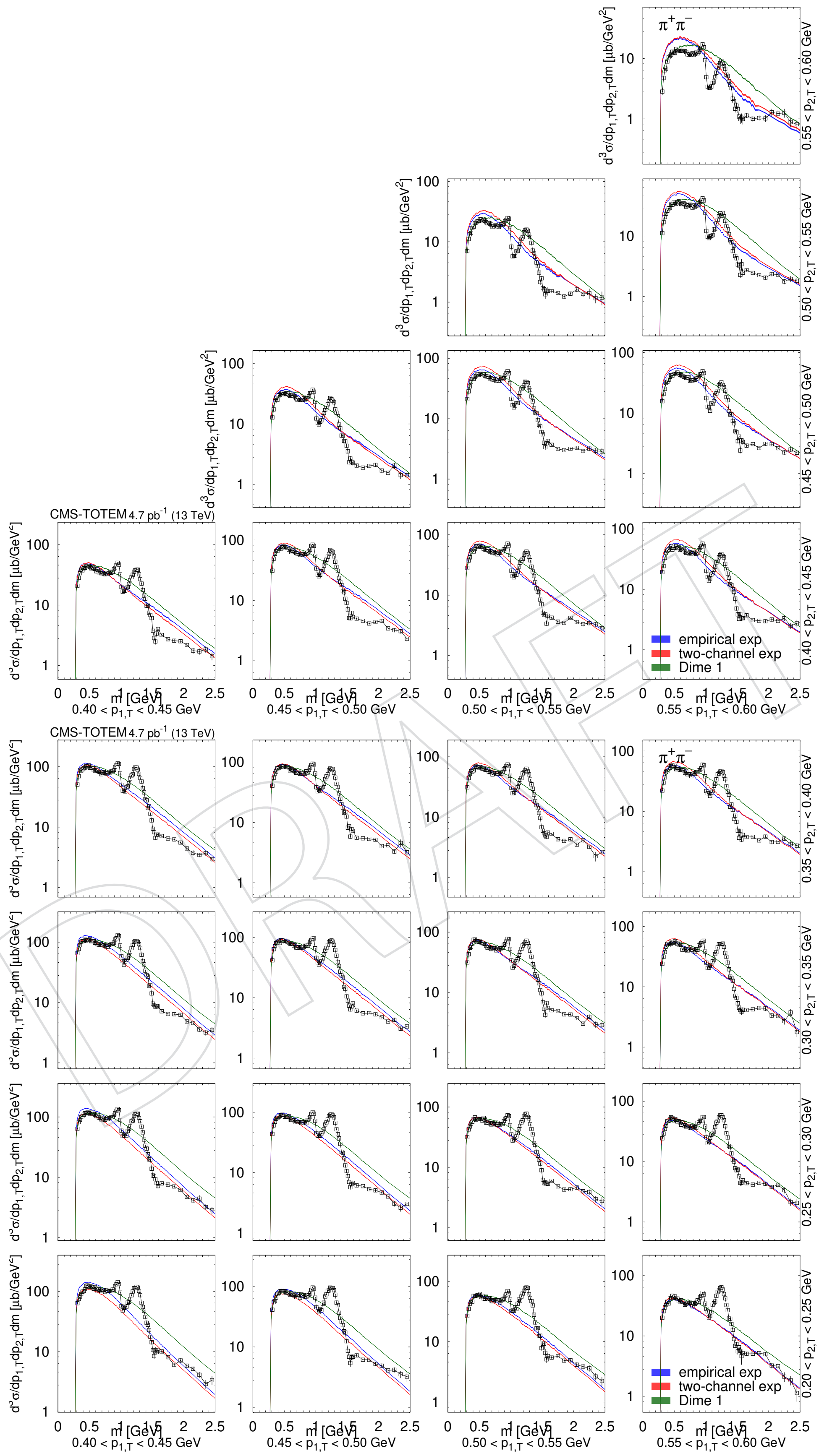

Figure 94: Distribution of $\mathrm{d}^3\sigma/\mathrm{d}p_{1,T}\mathrm{d}p_{2,T}\mathrm{d}m$ as a function of m for $\pi^+\pi^-$ pairs in several $(p_{1,T}, p_{2,T})$ bins, in units of μb/ GeV^3. Measured values (black symbols) are shown together with the predictions of the empirical and the two-channel models (coloured symbols) using the tuned parameters for the exponential proton-pomeron form factors (see text for details). Curves corresponding to DIME (model 1) are also plotted. The error bars indicate the statistical uncertainties.

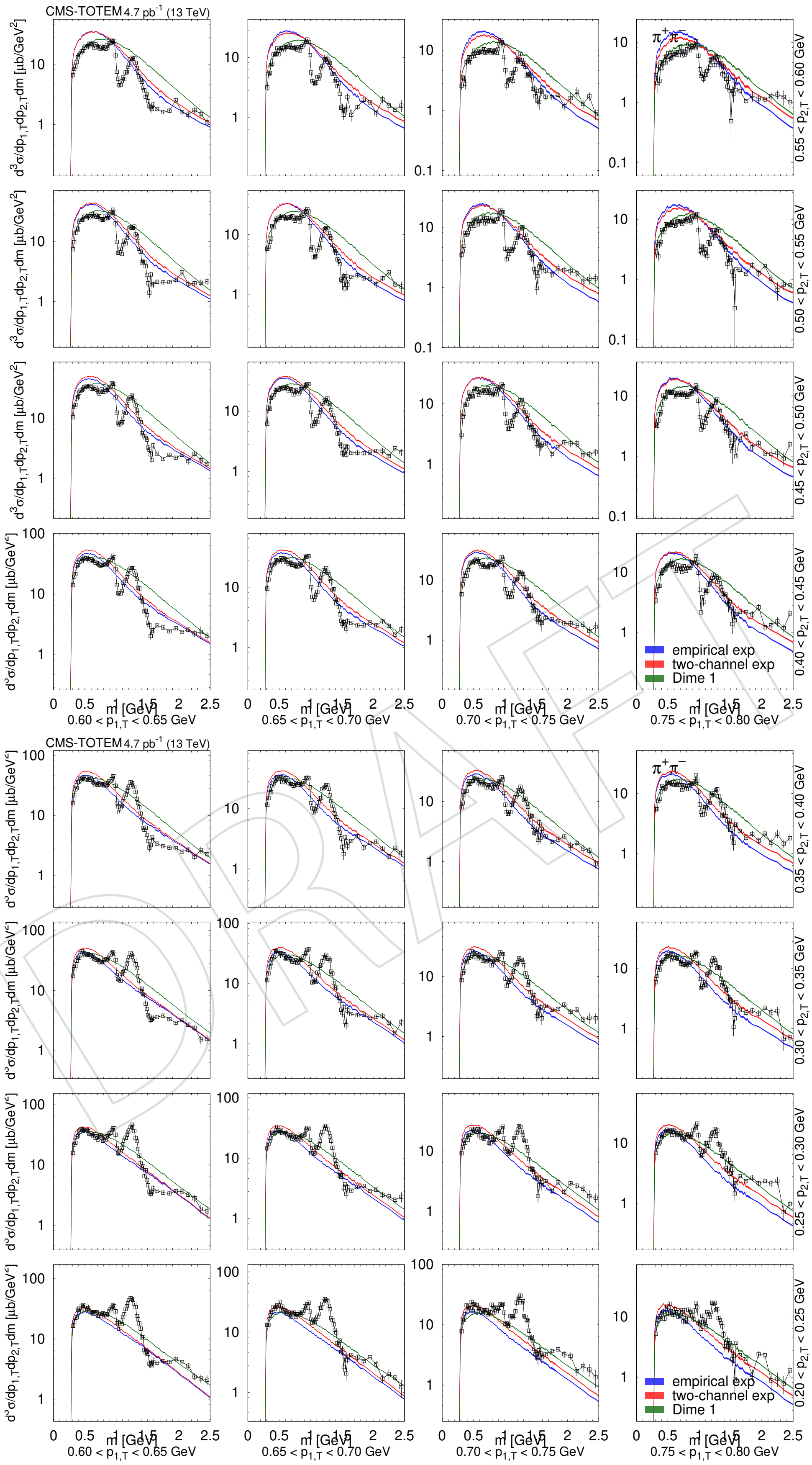

Figure 95: Distribution of $d^3\sigma/dp_{1,T}dp_{2,T}dm$ as a function of m for $\pi^+\pi^-$ pairs in several $(p_{1,T}, p_{2,T})$ bins, in units of μb/ GeV^3. Measured values (black symbols) are shown together with the predictions of the empirical and the two-channel models (coloured symbols) using the tuned parameters for the exponential proton-pomeron form factors (see text for details). Curves corresponding to DIME (model 1) are also plotted. The error bars indicate the statistical uncertainties.

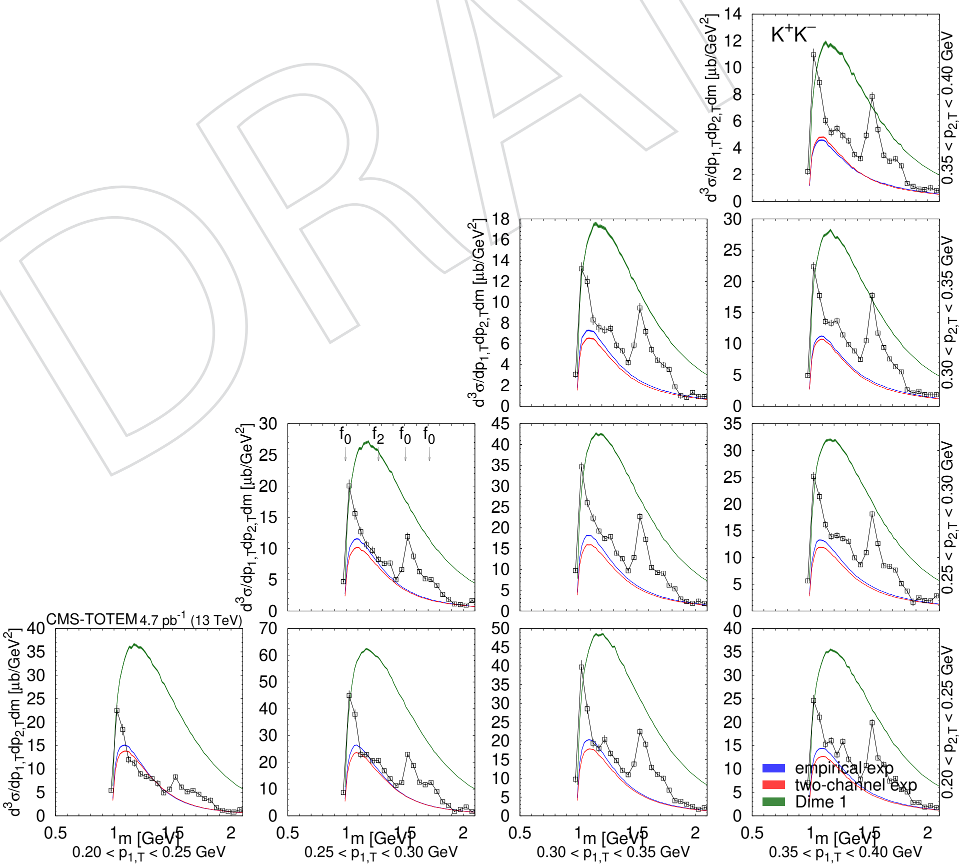

Figure 96: Distribution of $\mathrm{d}^3\sigma/\mathrm{d}p_{1,T}\mathrm{d}p_{2,T}\mathrm{d}m$ as a function of m for $\mathrm{K}^+\mathrm{K}^-$ pairs in several $(p_{1,T}, p_{2,T})$ bins, in units of μb/ GeV^3. Measured values (black symbols) are shown together with the predictions of the empirical and the two-channel models (coloured symbols) using the tuned parameters for the exponential proton-pomeron form factors (see text for details). Curves corresponding to DIME (model 1) are also plotted. The error bars indicate the statistical uncertainties.

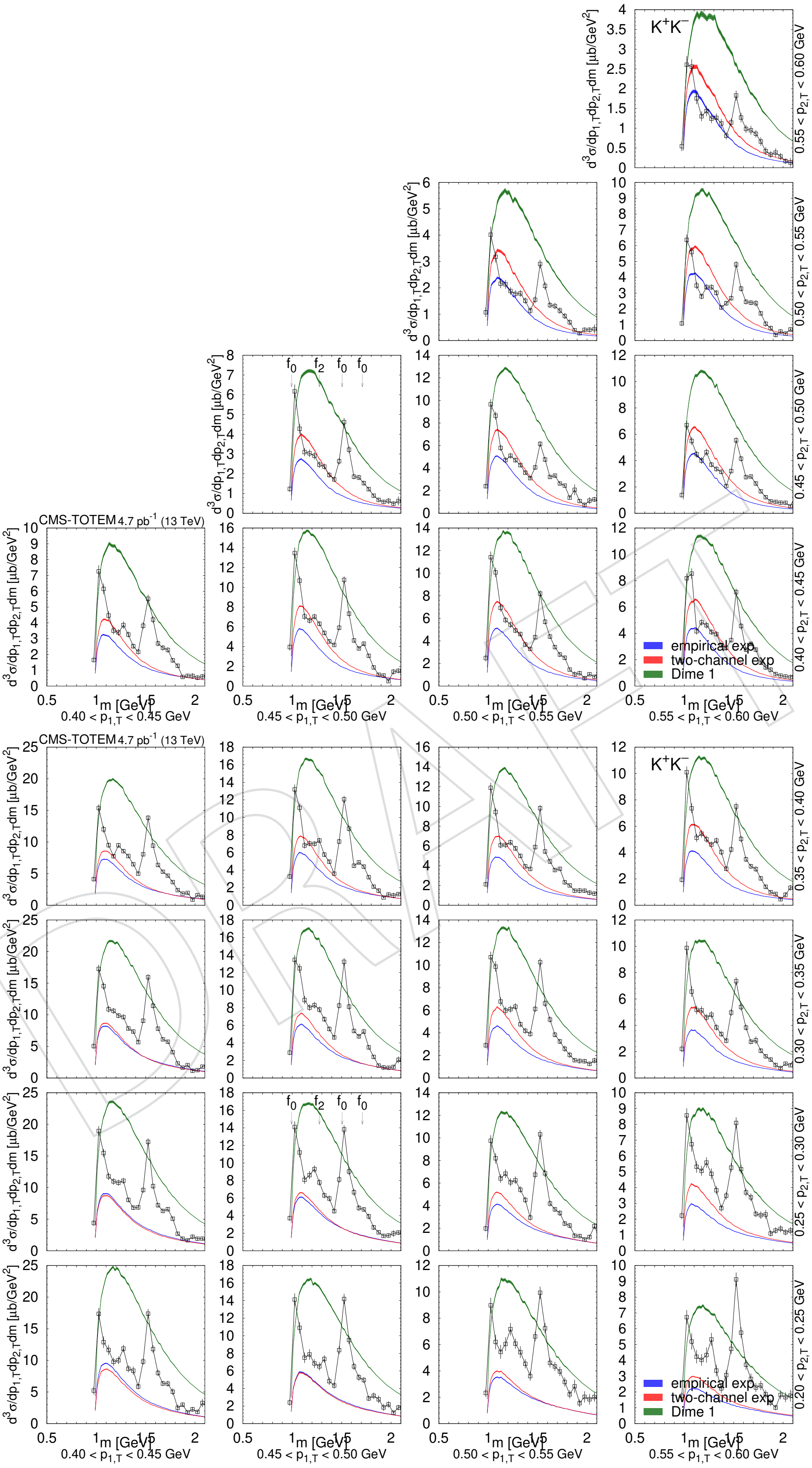

Figure 97: Distribution of $d^3\sigma/dp_{1,T}dp_{2,T}dm$ as a function of m for K^+K^- pairs in several $(p_{1,T}, p_{2,T})$ bins, in units of $\mu b/\,GeV^3$. Measured values (black symbols) are shown together with the predictions of the empirical and the two-channel models (coloured symbols) using the tuned parameters for the exponential proton-pomeron form factors (see text for details). Curves corresponding to DIME (model 1) are also plotted. The error bars indicate the statistical uncertainties.

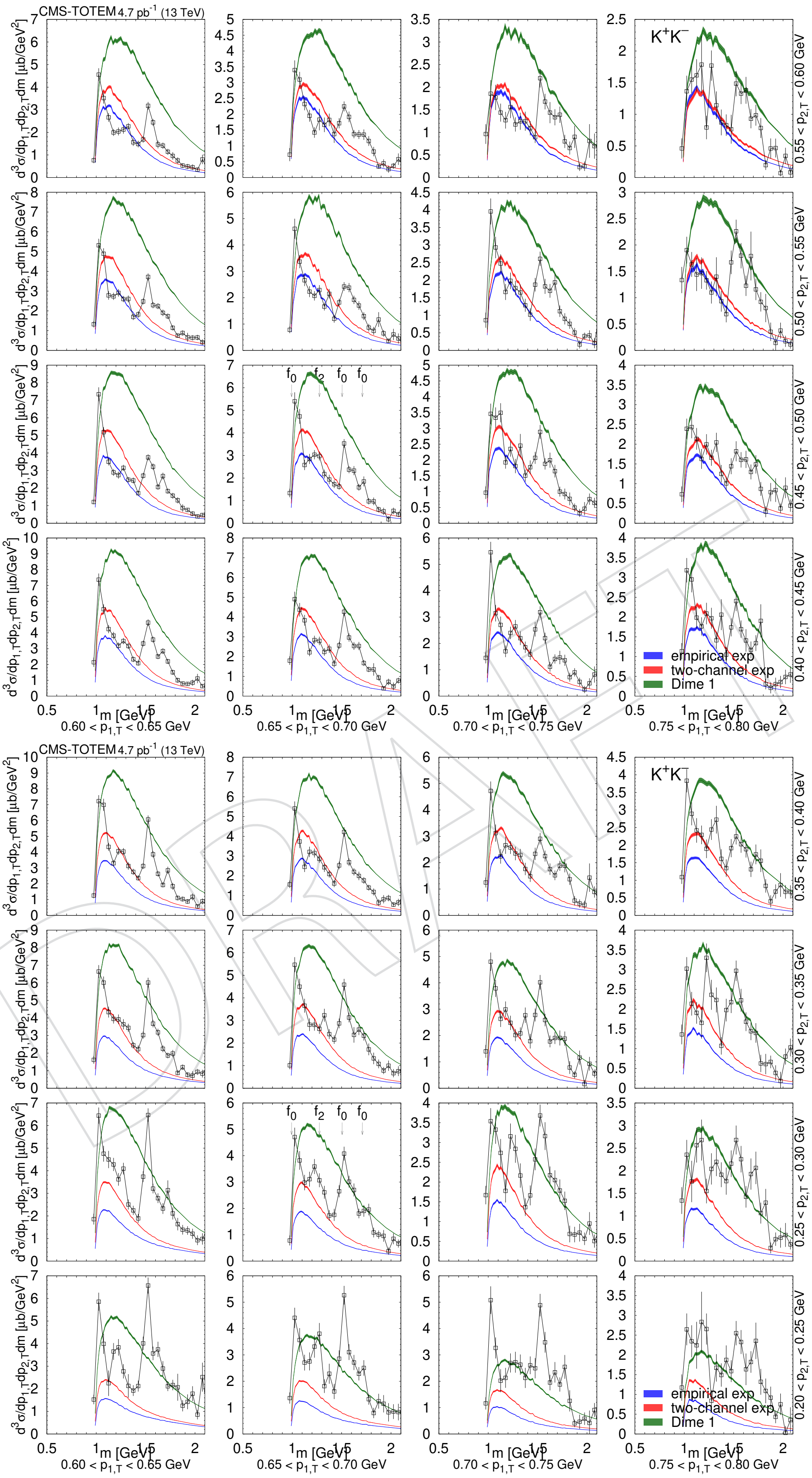

Figure 98: Distribution of $d^3\sigma/dp_{1,T}dp_{2,T}dm$ as a function of m for K^+K^- pairs in several $(p_{1,T}, p_{2,T})$ bins, in units of $\mu b/\,GeV^3$. Measured values (black symbols) are shown together with the predictions of the empirical and the two-channel models (coloured symbols) using the tuned parameters for the exponential proton-pomeron form factors (see text for details). Curves corresponding to DIME (model 1) are also plotted. The error bars indicate the statistical uncertainties.

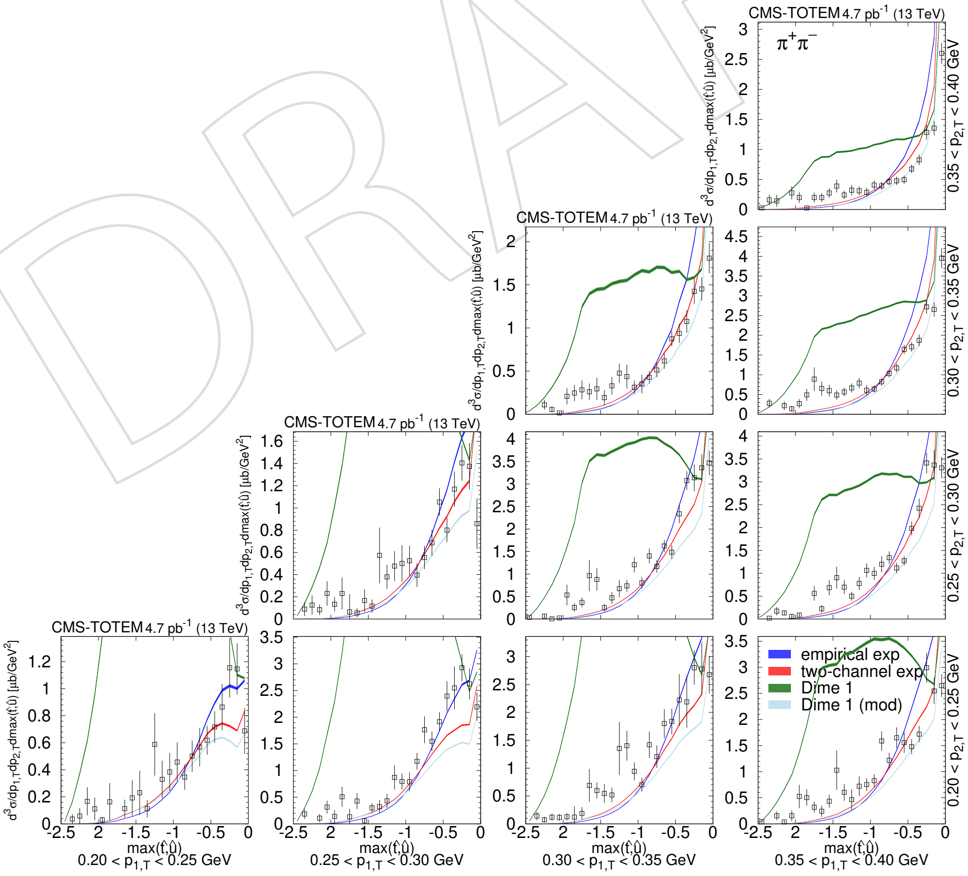

Figure 99: Distribution of the squared momentum transfer of the virtual meson in several $(p_{1,T}, p_{2,T})$ bins, in units of μb/ GeV^3. Measured values (black symbols) are shown together with the predictions of the empirical and the two-channel models (coloured symbols) using the tuned parameters for the exponential proton-pomeron form factors (see text for details). Curves corresponding to DIME (model 1) are also plotted. The error bars indicate the statistical uncertainties.

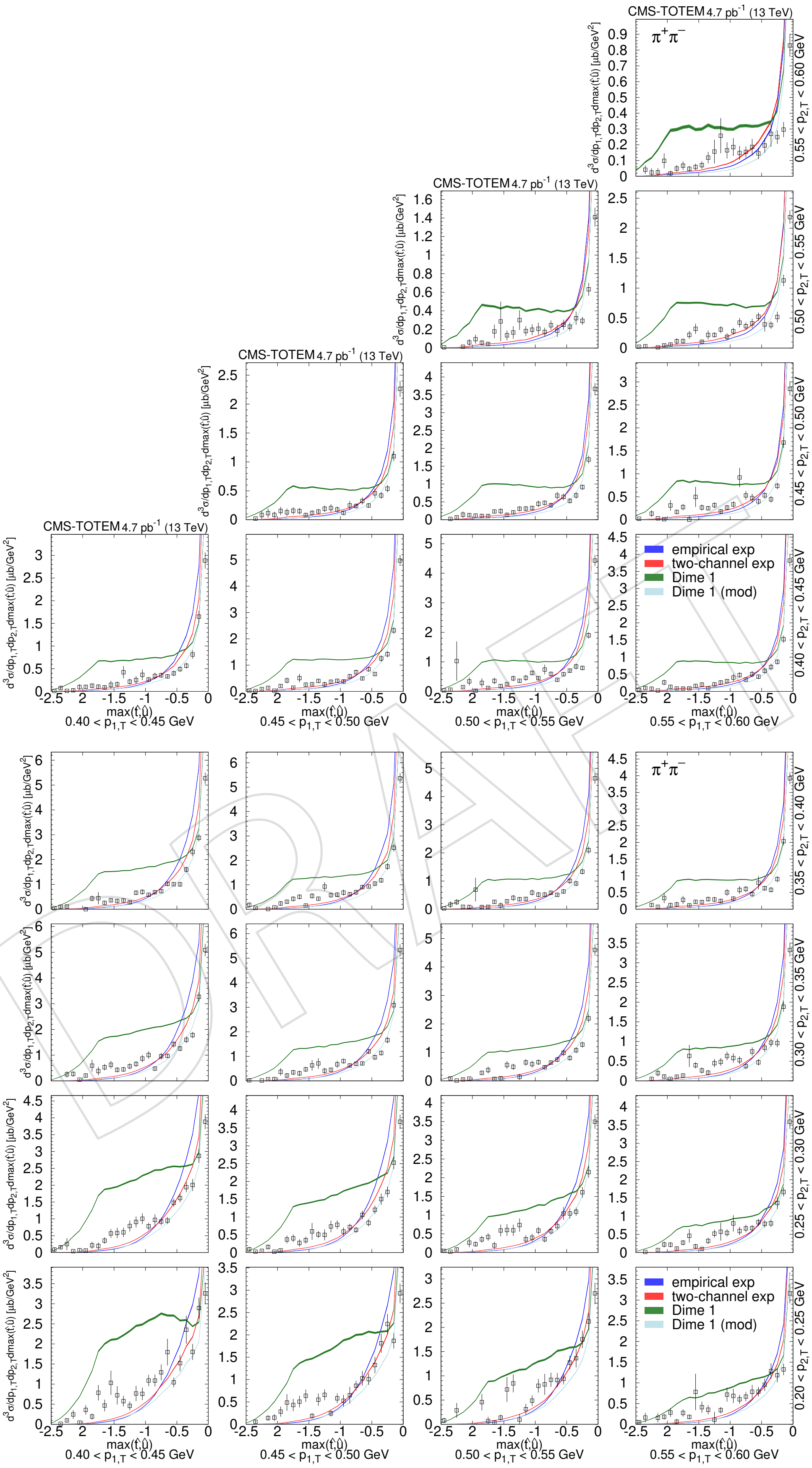

Figure 100: Distribution of the squared momentum transfer of the virtual meson in several $(p_{1,T}, p_{2,T})$ bins, in units of μb/ GeV^3. Measured values (black symbols) are shown together with the predictions of the empirical and the two-channel models (coloured symbols) using the tuned parameters for the exponential proton-pomeron form factors (see text for details). Curves corresponding to DIME (model 1) are also plotted. The error bars indicate the statistical uncertainties.

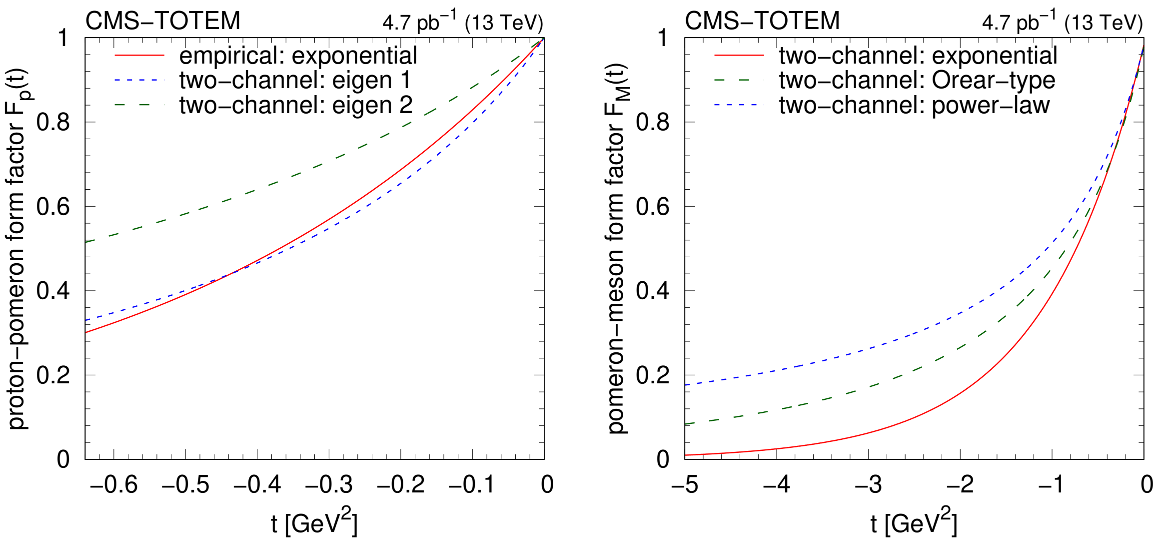

Figure 101: Left: The plain exponential proton-pomeron form factor compared to those of the two diffractive proton eigenstates. Right: Various options of the meson-pomeron form factor after tuning, shown for the exponential, power-law, and the Orear-type parametrisations.

Form factors. The plain exponential proton-pomeron form factor (from the fit with the empirical model) and those of the two diffractive proton eigenstates are shown in Fig. 101-left. One of the eigenstates is quite close to the exponential form.

Various options of the meson-pomeron form factor after tuning the two-channel model, for the exponential, power-law, and the Orear-type parametrisations are shown in Fig. 101-right.

Acknowledgments

This work was supported by the National Research, Development and Innovation Office of Hungary (K 128786).

References

[1] Particle Data Group Collaboration, “Review of Particle Physics”, *PTEP* **2022** (2022) 083C01, `doi:10.1093/ptep/ptac097`.

[2] V. Berestetsky and I. Pomeranchuk, “On the asymptotic behaviour of cross sections at high energies”, *Nucl. Phys.* **22** (1961) 629–639, `doi:10.1016/0029-5582(61)90473-4`.

[3] D. Amati, A. Stanghellini, and S. Fubini, “Theory of high-energy scattering and multiple production”, *Nuovo Cim.* **26** (1962) 896–954, `doi:10.1007/BF02781901`.

[4] S. Donnachie, H. G. Dosch, O. Nachtmann, and P. Landshoff, “Pomeron physics and QCD”, volume 19. Cambridge University Press, 12, 2004. ISBN 978-0-511-06050-2, 978-0-521-78039-1, 978-0-521-67570-3.

[5] M. Albrow, T. Coughlin, and J. Forshaw, “Central Exclusive Particle Production at High Energy Hadron Colliders”, *Prog. Part. Nucl. Phys.* **65** (2010) 149–184, `doi:10.1016/j.ppnp.2010.06.001`, `arXiv:1006.1289`.

[6] W. Ochs, "The Status of Glueballs", *J. Phys. G* **40** (2013) 043001, doi:10.1088/0954-3899/40/4/043001, arXiv:1301.5183.

[7] WA76 Collaboration, "Study of the centrally produced $\pi\pi$ and $K\overline{K}$ systems at 85-GeV/c and 300-GeV/c", *Z. Phys. C* **51** (1991) 351–364, doi:10.1007/BF01548557.

[8] WA91 Collaboration, "A further study of the centrally produced $\pi^+\pi^-$ and $\pi^+\pi^-\pi^+\pi^-$ channels in pp interactions at 300 and 450 GeV/c", *Phys. Lett. B* **353** (1995) 589–594, doi:10.1016/0370-2693(95)00629-Y.

[9] F. E. Close and G. A. Schuler, "Evidence that the pomeron transforms as a nonconserved vector current", *Phys. Lett. B* **464** (1999) 279–285, doi:10.1016/S0370-2693(99)00875-8, arXiv:hep-ph/9905305.

[10] WA102 Collaboration, "Experimental evidence for a vector like behavior of Pomeron exchange", *Phys. Lett. B* **467** (1999) 165–170, doi:10.1016/S0370-2693(99)01186-7, arXiv:hep-ex/9909013.

[11] F. E. Close, A. Kirk, and G. Schuler, "Dynamics of glueball and $q\overline{q}$ production in the central region of pp collisions", *Phys. Lett. B* **477** (2000) 13–18, doi:10.1016/S0370-2693(00)00235-5, arXiv:hep-ph/0001158.

[12] A. Kirk, "Resonance production in central pp collisions at the CERN Omega spectrometer", *Phys. Lett. B* **489** (2000) 29–37, doi:10.1016/S0370-2693(00)00944-8, arXiv:hep-ph/0008053.

[13] CDF Collaboration, "Measurement of central exclusive $\pi^+\pi^-$ production in $p\bar{p}$ collisions at $\sqrt{s} = 0.9$ and 1.96 TeV at CDF", *Phys. Rev. D* **91** (2015), no. 9, 091101, doi:10.1103/PhysRevD.91.091101, arXiv:1502.01391.

[14] STAR Collaboration, "Measurement of the central exclusive production of charged particle pairs in proton-proton collisions at $\sqrt{s} = 200$ GeV with the STAR detector at RHIC", *JHEP* **07** (2020), no. 07, 178, doi:10.1007/JHEP07(2020)178, arXiv:2004.11078.

[15] CMS Collaboration, "Study of central exclusive $\pi^+\pi^-$ production in proton-proton collisions at $\sqrt{s} = 5.02$ and 13 TeV", *Eur. Phys. J. C* **80** (2020), no. 8, 718, doi:10.1140/epjc/s10052-020-8166-5, arXiv:2003.02811.

[16] CMS Collaboration, "Track impact parameter resolution for the full pseudo rapidity coverage in the 2017 dataset with the CMS Phase-1 Pixel detector", Oct, 2020. CMS-DP-2020-049.

[17] CMS Collaboration, "The CMS experiment at the CERN LHC", *JINST* **3** (2008) S08004, doi:10.1088/1748-0221/3/08/S08004.

[18] TOTEM Collaboration, "The TOTEM experiment at the CERN Large Hadron Collider", *JINST* **3** (2008) S08007, doi:10.1088/1748-0221/3/08/S08007.

[19] TOTEM Collaboration, "Performance of the TOTEM Detectors at the LHC", *Int. J. Mod. Phys. A* **28** (2013) 1330046, doi:10.1142/S0217751X13300469, arXiv:1310.2908.

[20] ATLAS Collaboration, "Measurement of the Inelastic Proton-Proton Cross Section at $\sqrt{s} = 13$ TeV with the ATLAS Detector at the LHC", *Phys. Rev. Lett.* **117** (2016), no. 18, 182002, doi:10.1103/PhysRevLett.117.182002, arXiv:1606.02625.

[21] CMS Collaboration, “Measurement of the inelastic proton-proton cross section at $\sqrt{s} = 13$ TeV”, *JHEP* **07** (2018) 161, `doi:10.1007/JHEP07(2018)161`, `arXiv:1802.02613`.

[22] LHCb Collaboration, “Measurement of the inelastic pp cross-section at a centre-of-mass energy of 13 TeV”, *JHEP* **06** (2018) 100, `doi:10.1007/JHEP06(2018)100`, `arXiv:1803.10974`.

[23] TOTEM Collaboration, “First measurement of elastic, inelastic and total cross-section at $\sqrt{s} = 13$ TeV by TOTEM and overview of cross-section data at LHC energies”, *Eur. Phys. J. C* **79** (2019), no. 2, 103, `doi:10.1140/epjc/s10052-019-6567-0`, `arXiv:1712.06153`.

[24] CMS Collaboration, “CMS luminosity measurement for the 2018 data-taking period at $\sqrt{s} = 13$ TeV”, 2019. CMS-PAS-LUM-18-002.

[25] L. A. Harland-Lang, V. A. Khoze, and M. G. Ryskin, “Modelling exclusive meson pair production at hadron colliders”, *Eur. Phys. J. C* **74** (2014) 2848, `doi:10.1140/epjc/s10052-014-2848-9`, `arXiv:1312.4553`.

[26] CMS Collaboration, “Particle identification by ionization energy loss in the CMS silicon strip tracker”, *Int. J. Mod. Phys. E* **20** (2011) 1646, `doi:10.1142/S0218301311020022`.

[27] F. Siklér, “A parametrisation of the energy loss distributions of charged particles and its applications for silicon detectors”, *Nucl. Instrum. Meth. A* **691** (2012) 16, `doi:10.1016/j.nima.2012.06.064`, `arXiv:1111.3213`.

[28] F. Siklér, “Spectra of charged hadrons in pp collisions at $\sqrt{s} = 0.9$, 2.76 and 7 TeV identified via tracker energy loss”, *CMS AN* **2010/143** (2011).

[29] R. Sternheimer, M. Berger, and S. Seltzer, “Density effect for the ionization loss of charged particles in various substances”, *Atom. Data Nucl. Data Tabl.* **30** (1984) 261.

[30] CMS Collaboration, “Measurement of Tracking Efficiency”, 2010. CMS-PAS-TRK-10-002.

[31] S. Joe and F. Y. Kuo, “Constructing sobol sequences with better two-dimensional projections”, *SIAM J. Sci. Comput.* **30** (2008), no. 5, 2635–2654, `doi:10.1137/070709359`.

[32] M. Ryskin, A. Martin, and V. Khoze, “Proton Opacity in the Light of LHC Diffractive Data”, *Eur. Phys. J. C* **72** (2012) 1937, `doi:10.1140/epjc/s10052-012-1937-x`, `arXiv:1201.6298`.

[33] V. Khoze, A. Martin, and M. Ryskin, “Diffraction at the LHC”, *Eur. Phys. J. C* **73** (2013) 2503, `doi:10.1140/epjc/s10052-013-2503-x`, `arXiv:1306.2149`.

[34] L. A. Harland-Lang, V. A. Khoze, and M. G. Ryskin, “Exclusive physics at the LHC with SuperChic 2”, *Eur. Phys. J. C* **76** (2016), no. 1, 9, `doi:10.1140/epjc/s10052-015-3832-8`, `arXiv:1508.02718`.

[35] R. Kycia, J. Chwastowski, R. Staszewski, and J. Turnau, “GenEx: A simple generator structure for exclusive processes in high energy collisions”, *Commun. Comput. Phys.* **24** (2018), no. 3, 860–884, `doi:10.4208/cicp.OA-2017-0105`, `arXiv:1411.6035`.

[36] M. Mieskolainen, “GRANIITTI: A Monte Carlo Event Generator for High Energy Diffraction”, `arXiv:1910.06300`.

[37] A. Buckley et al., “Systematic event generator tuning for the LHC”, *Eur. Phys. J. C* **65** (2010) 331–357, doi:10.1140/epjc/s10052-009-1196-7, arXiv:0907.2973.